

# CONTROL OF ELECTRON TRANSFER KINETICS AT BORON-DOPED DIAMOND ELECTRODES BY SPECIFIC SURFACE MODIFICATION

THÈSE N° 2732 (2003)

PRÉSENTÉE À LA FACULTÉ SCIENCES DE BASE

SECTION DE CHIMIE ET GÉNIE CHIMIQUE

ÉCOLE POLYTECHNIQUE FÉDÉRALE DE LAUSANNE

POUR L'OBTENTION DU GRADE DE DOCTEUR ÈS SCIENCES

PAR

**Ilaria DUO**

laurea in chimica, Università degli Studi di Ferrara, Italie  
et de nationalité italienne

acceptée sur proposition du jury:

Prof. C. Comninellis, directeur de thèse

Prof. A. De Battisti, rapporteur

M. W. Haenni, rapporteur

Prof. C. Lévy-Clément, rapporteur

Prof. H. van den Bergh, rapporteur

Lausanne, EPFL  
2003



*Deep down, I don't believe it takes  
any special talent for a person to  
lift himself off the ground and  
hover in the air. You must stop  
being yourself. That's where it  
begins, and everything else follows  
from that. You must let yourself  
evaporate. Let your muscles go  
limp, breathe until you feel your  
soul pouring out of you, and then  
shut your eyes. That's how it's  
done. The emptiness inside your  
body grows lighter than the air  
around you. Little by little you  
begin to weigh less than nothing.  
You shut your eyes; you spread  
your arms; you let yourself  
evaporate. And then, little by little,  
you lift yourself off the ground.  
Like so.*

*Paul Auster "Mr. Vertigo" (1994)*



---

## Acknowledgements



---

I am grateful to Professor Christos Comninellis for giving me the opportunity to work in his research group, for his precious advice and helpful discussions. I have learn a lot collaborating with him.

I would like to thank the CSEM Centre Suisse d'Electronique et de Microtechnique SA, Neuchâtel, Switzerland, for providing diamond electrodes and for the financial support. I am particularly thankful to Mr Werner Haenni for the many interesting discussions.

Thanks to all the members of the jury: Professor Claude Lévy-Clément, Professor Achille De Battisti, Professor Hubert van den Bergh, and Engineer Werner Haenni for reading my thesis and for the very helpful remarks and Professor Claude Friedli for being the president of the jury.

Thanks to Professor De Battisti for establishing the contact with Professor Comninellis. It was the first step for my coming in Switzerland and starting a Ph.D.

I thank Professor Akira Fujishima for accepting me in his research group in Japan for three months. It has been a very important professional and personal experience. Ivan-san, Sarada-san, Tata-san thank you very much for your warm welcome, help and interesting discussion.

Many thanks to Dr. György Fóti and Dr. Boris Correa, for being to help at any time.

---

---

I'm particular thankful to Klaus Müller: his english correction and the stimulating remarks about the subject have been extremely precious.

I would like to thank all the technical staff and in particular Pierre-André Perroud, Gérard. Bovard, Jean-Claude Rapit and Alfred Neuenschwander for the technical support.

Thanks to Mrs Paule Anken, Lionel et Sara for being to help in solving administration problems.

I'm very grateful to my colleagues and friends for welcome me with enthusiasm. Thank to them, I had a lot of fun during these four years. Boltzi, Valérie & Vincent, Nele & Volker, Benoît, Leonardo, Jian, Gipi, Christian, Lukas & Géraldine, Daniela & Thomas, Adona & José, Marie & Peter, Béatrice & Christophe, Pierre, Justyna & Sean, Elena, Valia, Pascal, Nicolas, Eric, Chrystèle, Ivan, Pierre-Alain, Lassiné, Assunta and Carla, thank you.

Barbara and Carmem, thank you. You have been my first friends in Switzerland.

Non posso dimenticare gli amici in Italia per avermi sostenuto dall'inizio con costante affetto: Gisella, Umberto, Sergio, Tatiana & Paolo, Elena. Grazie mille.

Grazie Stefan per le tue risate, il tuo sostegno e il tuo amore.

Grazie mamma Germana e papà Sauro, per avermi sostenuto sempre. Il vostro esempio è una guida in tutte le mie scelte.

Grazie a tutta la mia famiglia.

---

---

# Abstract

---

Diamond films with different levels of doping have been the subject of applications and fundamental research in electrochemistry, opening up a new branch known as the electrochemistry of diamond. The electrochemical properties of diamond mostly depend on the operating conditions during the deposition of the film and on the treatment of the surface. The absence so far of a standard procedure in the production and treatment of diamond films has created a wide range of diamond quality and properties. This work would try to clarify some aspects of the electrochemical activity of boron-doped diamond electrodes in light of the results obtained in our and other laboratories.

Boron-doped diamond (BDD) electrodes, both as-grown and polarised anodically under different conditions, were prepared in order to study the chemical and electrochemical changes of diamond and clarify the rule played by the surface-state density. Many different treatments were employed, but only the most relevant results will be presented in this work, *viz.*, those obtained with four kinds of surface treatment: as-grown (BDD<sub>ag</sub>), mildly polarised (BDD<sub>mild</sub>), strongly polarised in perchloric acid (BDD<sub>severe</sub>), and strongly polarised in a sulphuric acid-acetic acid mixture (BDD<sub>AcOH</sub>). Charge transfer processes at the electrode surface were studied by steady-state (polarisation) and dynamic (cyclic voltammetry) potential step methods. Simple electron transfer processes such as the outer-sphere redox system ferri/ferrocyanide (Fe(CN)<sub>6</sub>III/II) and complex charge transfer reactions such as the inner-sphere 1,4-benzoquinone/hydroquinone (Q/H<sub>2</sub>Q) redox reaction were chosen to test the electrochemical properties of the electrodes. The properties of the diamond electrodes were found to undergo strong modification as a function of surface treatment. The reaction rate constants decreased significantly upon anodic polarisation. Important drops in the carrier surface concentration and in true surface area led to hindrance of electron transfer at the electrode surface.

The concept of non-diamond ( $sp^2$ ) impurities as charge transfer mediators on a diamond surface was suggested as an explanation for the electrochemical behaviour of diamond electrodes after surface oxidation treatment. To verify this concept, graphite particles were deposited on mildly polarised diamond electrodes (BDD<sub>mild</sub>) so as to prepare diamond-graphite composite electrodes (BDD-g), and their properties were compared with those of as-grown (BDD<sub>ag</sub>) diamond and carbon electrodes. The  $sp^2$  coverage on BDD was estimated by cyclic voltammetry. A strong analogy existed between as-grown diamond electrodes and diamond-graphite composite electrodes. In fact, by depositing graphite particles on diamond after its deactivation by anodic polarisation it was possible to restore the initial properties of

---

the as-grown diamond electrode. In the potential region of electrolyte decomposition,  $sp^2$  was eliminated from the BDD-graphite composite surface by oxidation to  $CO_2$ . BDD itself behaved as an 'non-active' electrode. In this case the oxidation of organic compounds was mediated by hydroxyl radicals formed during water discharge, without any participation of the electrode surface.

The behaviour of 'non-active' diamond in organic oxidation processes occurring in the potential region of water discharge was described in greater detail in the chapter about electrochemical oxidation of ethylenediaminetetraacetic acid (EDTA). The theoretical model developed for organic oxidation at 'non-active' anodes was used to predict results for the oxidation of EDTA at boron-doped diamond electrodes. The very good fit between experimental results and theoretical values confirmed that EDTA oxidation at diamond in the potential region of electrolyte decomposition was a fast reaction involving free electrogenerated hydroxyl radical intermediates formed at the anode during water discharge.

Nanoparticles of  $IrO_2$  were deposited by thermal decomposition on boron-doped diamond electrodes (BDD- $IrO_2$ ) in order to improve and better understand their electrocatalytic activity toward redox processes and the oxygen evolution reaction (OER). Electrodes with different  $IrO_2$  loadings were prepared and their electrochemical properties tested. The reaction rate constants of redox processes increased by several orders of magnitude, the overpotential of the oxygen evolution reaction decreased by about one volt. The  $IrO_2$  deposition completely altered the electrochemical properties of diamond from an 'non-active' to an 'active' material. The high electrocatalytic activity of BDD- $IrO_2$  electrodes toward the OER was also confirmed in an indirect way by the observation that the oxidation of organic substances and the production of peroxodisulphate are inhibited. The high degree of dispersion of the  $IrO_2$  particles led to a high electrocatalytic activity, even at extremely low  $IrO_2$  loadings.

On the basis of experimental results a phenomenological model was proposed. Boron-doped diamond was defined as a degenerated semiconductor material because of the quite high charge density on its surface due to the boron doping ( $> 10^{21}$  boron atoms  $cm^{-3}$ ), to the non diamond ( $sp^2$ ) carbon and in general to surface species. This distribution of charges on the surface promoted processes of electron transfer across the interface diamond/electrolyte. Deposition of particles on the diamond surface (graphite or  $IrO_2$ ) increased further this surface charge density until reaching a perfectly metallic behaviour. Since charge transfer processes occurred on the deposited particles at lower overpotential than on diamond sites, surface modified diamond electrodes showed the electrochemical properties of the deposited material.

---



---

# Version Abrégée

---

Le diamant de niveaux de dopage différents a été l'objet d'applications et d'études fondamentales en électrochimie ouvrant les portes à une nouvelle branche appelée électrochimie du diamant. Les propriétés électrochimiques du diamant dépendent principalement des conditions opératoires lors du processus de déposition du film et du type de traitement de la surface. L'absence d'une procédure standard pour la production et le traitement des films de diamant a créé une grande variété dans les propriétés et la qualité de ce type d'électrode. Ce travail clarifie quelques aspects de l'activité électrochimique des électrodes en diamant dopé au bore sur la base des résultats obtenus dans notre laboratoire et dans d'autres groupes de recherche.

Des électrodes de diamant dopé au bore (BDD), nouvelles et polarisées anodiquement sous différentes conditions ont été préparées pour étudier les modifications chimiques et électrochimiques du diamant et expliquer le rôle joué par la densité des états de surface. Bien que plusieurs traitements aient été effectués, seuls les résultats concernant quatre électrodes différemment traitées seront présentés dans ce travail: nouvelle électrode de diamant ( $BDD_{ag}$ ), diamant après faible polarisation ( $BDD_{mild}$ ), après forte polarisation dans l'acide perchlorique ( $BDD_{severe}$ ) et après forte polarisation dans un mélange d'acide sulfurique et d'acide acétique ( $BDD_{AcOH}$ ). Le processus de transfert de charge à la surface des électrodes a été étudié par échelons de potentiel de type stationnaire (polarisation) et dynamique (voltamétrie cyclique). Des transferts électroniques simples comme dans le cas du couple redox 'outer-sphere' ferri/ferrocyanure ( $Fe(CN)_6^{III/II}$ ) et complexes comme la réaction redox 'inner-sphere' 1,4-benzoquinone/hydroquinone ( $Q/H_2Q$ ) ont été choisis pour tester les propriétés électrochimiques des électrodes. Nous avons démontré que les propriétés du diamant sont considérablement modifiées avec le traitement de la surface. Les constantes de vitesse de réaction diminuent fortement après polarisation. La diminution importante de la concentration des transporteurs de charge inhibent le processus de transfert électronique à la surface des électrodes.

Le comportement électrochimique du diamant après oxydation de sa surface, peut être expliqué par le rôle des impuretés du carbone non-diamant ( $sp^2$ ) en tant que médiateur du transfert de charge sur la surface du diamant. De manière à vérifier notre hypothèse, des particules de graphite ont été déposées sur la surface du diamant faiblement polarisé ( $BDD_{mild}$ ) afin de préparer des électrodes de diamant-graphite ( $BDD-g$ ) et leurs propriétés ont été comparées avec celles d'une électrode nouvelle de diamant ( $BDD_{ag}$ ) et avec celles du carbone. Le taux de

---

recouvrement du BDD par  $sp^2$  a été estimé par voltamétrie cyclique. Nous avons trouvé une forte analogie entre la nouvelle électrode de diamant et celle de composition diamant-graphite. En effet, en déposant des particules de graphite sur le diamant et après l'avoir désactivé par polarisation anodique, l'électrode présentait les propriétés initiales typiques d'une nouvelle électrode. Dans la région du potentiel d'instabilité de l'électrolyte, le carbone  $sp^2$  est éliminé de la surface par oxydation en  $CO_2$ . Le diamant seul (BDD) se comporte comme une électrode 'non-active'. Dans ce cas, l'oxydation des produits organiques est assistée par les radicaux hydroxyles formés lors de la décharge de l'eau, sans aucune participation de la surface du diamant.

Le comportement 'non-actif' du diamant dans l'oxydation des produits organiques, dans la région du potentiel de décomposition de l'eau, est décrit en détail dans le chapitre de l'oxydation électrochimique de l'acide éthylènediaminetétraacétique (EDTA). Le modèle théorique développé pour l'oxydation des composés organiques sur des anodes 'non-actives' a été utilisé afin de prévoir les résultats de l'oxydation de l'EDTA sur le diamant. Les résultats expérimentaux corrént bien les valeurs théoriques confirmant ainsi que l'oxydation de l'EDTA sur le diamant, dans la région du potentiel de décomposition de l'électrolyte, est une réaction rapide qui implique, comme intermédiaires de réaction, des radicaux hydroxyles libres électrogénérés à l'anode pendant la décharge de l'eau.

Des nanoparticules de  $IrO_2$  ont été déposées, par décomposition thermique, sur des électrodes en diamant (BDD- $IrO_2$ ) afin d'améliorer et de mieux comprendre leur activité électrocatalytique envers le processus redox et la réaction de dégagement d'oxygène (OER). Nous avons préparé des électrodes avec une différente quantité de  $IrO_2$  et nous avons testé leurs propriétés électrochimiques. Les constantes de vitesse de réaction des couples redox augmentent de plusieurs ordres de grandeur et la surtension pour le dégagement d'oxygène diminue d'environ un volt. La déposition de  $IrO_2$  modifie complètement les propriétés électrochimiques du diamant, son comportement passe d'une électrode 'non-active' à 'active'. La haute activité électrocatalytique des électrodes BDD- $IrO_2$  envers l'OER a été confirmée par le fait que l'oxydation des produits organiques et la production du peroxydisulfate sont inhibées. L'importante dispersion des particules de  $IrO_2$  entraîne une grande activité électrocatalytique, même pour de très faibles dépôts de  $IrO_2$ .

Sur la base des résultats expérimentaux, nous avons proposé un modèle phénoménologique. Le diamant est défini comme un semiconducteur dégénéré étant donné sa relative grande densité de charge sur sa surface, due au dopage de bore ( $> 10^{21}$  atome de bore  $cm^{-3}$ ), au carbone non-diamant ( $sp^2$ ) et en général aux impuretés de surface. Cette distribution de charge sur la surface facilite le processus de transfert électronique à travers l'interface diamant/électrolyte. La déposition de

---

---

particules sur la surface de diamant (graphite ou IrO<sub>2</sub>) augmente encore cette densité de charge jusqu'à atteindre un comportement parfaitement métallique du diamant. Les électrodes de diamant, dont la surface est modifiée, présentent les propriétés électrochimiques typiques du matériel déposé jusqu'à ce que le transfert de charge se produise à la surface des molécules déposées à un surpotentiel plus bas que celui nécessaire aux sites de diamant.

---

---

# Table of symbols

---

---

## 1. Roman symbols

---

$A$	Surface area	$\text{cm}^2$
$C^* = C_j$	Concentration of specie j in the bulk	$\text{mol cm}^{-3}$
$C_j(0,t)$	Concentration of specie j at the surface	$\text{mol cm}^{-3}$
$C_{\text{dl}}$	Double layer capacitance	$\mu\text{F cm}^{-2}$
$D_j^0$	Diffusion coefficient of specie j	$\text{cm}^2 \text{s}^{-1}$
$COD$	Chemical oxygen demand	$\text{mol}(\text{O}_2) \text{cm}^{-3}$
$COD^0$	Initial value chemical oxygen demand	$\text{mol}(\text{O}_2) \text{cm}^{-3}$
$e$	Electronic charge	C
$E$	Potential of an electrode vs a reference	V
$\dot{E}$	Potential phasor	V
$E^0$	Standard potential	V
$E^{0'} = E_{\text{app}}^0$	Formal potential or apparent potential	V
$E_{\text{ac}}$	ac component of potential	V
$E_{\text{dc}}$	dc component of potential	V
$f$	Frequency of sinusoidal oscillation	$\text{s}^{-1}$
$F$	Faraday's constant	$\text{C mol}^{-1}$
$i$	Current intensity	A
$\dot{i}$	Current phasor	A
$ICE$	Instantaneous current efficiency	none
$j$	Current density	$\text{A cm}^{-2}$

---

$j_0$	Exchange current density	$A\text{ cm}^{-2}$
$j_{\text{lim}}$	Limiting current density	$A\text{ cm}^{-2}$
$k^0$	Standard rate constant	$\text{cm s}^{-1}$
$k_b$	Rate constant of oxidation (backward)	$\text{cm s}^{-1}$
$k_f$	Rate constant of reduction (forward)	$\text{cm s}^{-1}$
$k_m$	Mass transport coefficient	$\text{cm s}^{-1}$
$n$	Electron numbers	none
O	Oxidised form of a specie	none
OH*	Hydroxyl radical specie	none
$q^*$	Voltammetric charge	C
$r_i$	Rate of the reaction i	$\text{mol m}^{-2}\text{ s}^{-1}$
R	Reduced form of a specie	none
R	Gas constant	$\text{J mol}^{-1}\text{ K}^{-1}$
R	Resistance	$\Omega$
$R_{\text{ct}}$	Charge transfer resistance	$\Omega$
$R_S = R_\Omega$	Ohmic solution resistance	$\Omega$
SHE	Standard hydrogen electrode	none
$t$	Time	s
$T$	Absolute temperature	K
TOC	Total organic carbon	$\text{mol(C)}\text{ cm}^{-3}$
$TOC^0$	Initial value total organic carbon	$\text{mol(C)}\text{ cm}^{-3}$
$v$	Potential scan rate	$\text{V s}^{-1}$
$V$	Volume	$\text{m}^3$
$\dot{V}$	Flow rate	$\text{m}^3\text{ s}^{-1}$
x	Number atoms of carbon	none
y	Number atoms of hydrogen	none
z	Number atoms of oxygen	none
Z	Impedance	$\Omega$

---

## 2. Greek symbols

---

$\alpha$	Transfer coefficient of reduction reaction	none
$\beta$	Transfer coefficient of oxidation reaction	none
$\gamma$	Distribution coefficient	none
$\Gamma$	IrO <sub>2</sub> loading	molec. cm <sup>-2</sup>
$\Gamma$	Saturation surface concentration	mol m <sup>-2</sup>
$\eta$	Overpotential	V
$\eta$	Current efficiency	none
$\lambda$	Wavelength	nm
$\lambda$	Switching time in cyclic voltammetry	s
$\Lambda$	Parameter in cyclic voltammetry	
$\theta$	Relative surface coverage	none
$\rho$	Resistivity	$\Omega$ cm
$\psi$	Rate parameter in cyclic voltammetry	none
$\omega$	Angular frequency of rotation	s <sup>-1</sup>

---

## 3. Superscript

---

0	Initial or standard value
E	Relative to the electrode
S	Relative to the solution

---

---

## 4. Subscript

---

cr	Critic value
E	Relative to the electrode
in	Inlet
lim	Limiting value
l	Low value
h	High value
m	Relative to the mass
O	Relative to the oxidised specie
out	Outlet
R	Relative to the reduced specie
R	Relative to the reservoir
S	Relative to the solution

---

---

# Table of Contents



---

<b>CHAPTER 1 Introduction .....</b>	<b>1</b>
1. References .....	3
<b>CHAPTER 2 Bibliography.....</b>	<b>5</b>
1. Electrode processes.....	6
1.1 The electrical double layer .....	6
1.2 Faradaic processes .....	8
1.2.1 <i>Outer-sphere and inner-sphere charge transfer reactions</i> .....	9
1.2.2 <i>Mediated electrode reactions (surface redox catalysis)</i> .....	11
1.2.3 <i>Mediated solution reactions (solution redox catalysis)</i> .....	11
1.2.4 <i>The Butler-Volmer equation</i> .....	11
1.3 Electrochemical characterisation techniques .....	17
1.3.1 <i>Steady-state polarisation</i> .....	17
1.3.2 <i>Cyclic voltammetry</i> .....	17
1.3.3 <i>Impedance spectroscopy</i> .....	21
2. Synthetic boron-doped diamond in electrochemistry.....	26
2.1 History of a synthesis .....	27
2.1.1 <i>The substrate</i> .....	27
2.1.2 <i>Nucleation mechanism</i> .....	28
2.1.3 <i>Doping process</i> .....	29
2.1.4 <i>Diamond growth mechanism</i> .....	30
2.2 Hot-filament CVD .....	31
2.2.1 <i>The HF-CVD reactor</i> .....	31
2.3 Microwave CVD .....	32
2.4 Electrochemical processes on diamond .....	32
2.4.1 <i>Electrochemical characterisation</i> .....	32
2.4.2 <i>Outer-sphere and inner-sphere reactions at diamond electrodes</i> .....	34

---



2.5 The oxygen evolution reaction and organic oxidation on ‘non-active’ and ‘active’ electrodes.....	35
2.5.1 <i>The oxygen evolution reaction and the oxidation of organic substances on ‘non-active’ diamond electrodes</i> .....	37
2.5.2 <i>The oxygen evolution reaction and the oxidation of organic substances on ‘active’ IrO<sub>2</sub> electrodes</i> .....	43
3. References.....	47
<b>CHAPTER 3 Results: BDD surface treatment.....</b>	<b>51</b>
1. Introduction.....	52
2. Experimental.....	53
3. Results and discussion .....	55
3.1 Morphological characterisation.....	55
3.2 Surface redox processes on BDD surfaces.....	59
3.3 Electrochemical behaviour of soluble redox systems at BDD electrodes .....	63
3.3.1 <i>Outer-sphere electron transfer reactions</i> .....	64
3.3.2 <i>Inner-sphere electron transfer reactions</i> .....	70
4. Conclusions .....	76
5. Acknowledgement.....	79
6. References.....	80
<b>CHAPTER 4 Results: Graphite deposition on BDD surfaces .....</b>	<b>83</b>
1. Introduction.....	84
2. Experimental.....	84
3. Results and discussion.....	85
3.1 Morphological characterisation.....	85
3.2 Surface redox processes on BDD-graphite surfaces.....	86
3.3 Electrochemical behaviour of soluble redox systems at BDD-graphite electrodes .....	89
3.3.1 <i>Outer-sphere electron transfer reactions</i> .....	89
3.3.2 <i>Inner-sphere electron transfer reactions</i> .....	94
3.4 Oxygen evolution reaction .....	99
4. Conclusions .....	100
5. Acknowledgement.....	102
6. References.....	102
<b>CHAPTER 5 Results: Electrochemical oxidation of EDTA on BDD. Application to waste water treatment .....</b>	<b>105</b>
1. Introduction.....	106

---

---

1.1 Theoretical model for oxidation of EDTA at BDD electrodes .....	107
2. Experimental.....	<b>108</b>
3. Results and discussion .....	<b>111</b>
3.1 Cyclic voltammetry.....	111
3.2 Bulk electrolysis.....	114
4. Conclusions .....	<b>119</b>
5. Acknowledgment.....	<b>120</b>
6. References.....	<b>120</b>

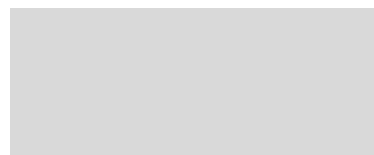
## **CHAPTER 6 Results: Iridium dioxide-modified BDD electrodes ..... 123**

1. Introduction.....	<b>124</b>
2. Experimental.....	<b>126</b>
3. Results and discussion .....	<b>128</b>
3.1 Morphological characterisation.....	128
3.2 Surface redox processes on BDD surfaces.....	131
3.3 Electrochemical behaviour of soluble redox systems at BDD electrodes .....	137
3.3.1 <i>Outer-sphere electron transfer reactions</i> .....	138
3.3.2 <i>Inner-sphere electron transfer reactions</i> .....	142
3.4 Oxygen evolution reaction (an inner-sphere reaction.....	149
3.5 Peroxodisulphate production (an inner-sphere reaction) .....	153
3.6 Oxidation of organic compounds (an inner-sphere reaction) .....	155
3.7 Stability of BDD-IrO <sub>2</sub> electrodes.....	160
4. Conclusions .....	<b>161</b>
5. Acknowledgment.....	<b>163</b>
6. References.....	<b>164</b>

## **CHAPTER 7 General discussion ..... 167**

1. Boron-doped diamond electrodes.....	<b>168</b>
1.1 Literature results.....	168
1.2 Results obtained in this work.....	171
2. The phenomenological model .....	<b>177</b>
3. References.....	<b>182</b>

---



---

Diamond is an extremely hard crystalline form of carbon and it is considered an excellent material for many applications due to its unusual physical and chemical properties such as high electrical resistivity, high thermal conductivity, high corrosion resistance, low coefficient of friction, chemical inertness, and optical transparency. These are important properties for several technical applications such as high-power electronic devices (heat spreader), coatings for cutting tools and electro-optical devices. For this reason it has long attracted the attention of scientists and the public. Interest in diamond has been further increased by the recent discovery that it is possible to produce polycrystalline diamond films with mechanical and electronic properties comparable to those of natural diamond. Diamond films with different levels of doping have been the subject of applications and fundamental research in electrochemistry, opening up a new branch known as the electrochemistry of diamond.

Among the factors that can influence the electrochemical behaviour of boron-doped diamond electrodes, the crystallographic structure [1, 2], the surface functional groups [3-5], the boron doping level [6, 7], and the presence of non-diamond carbon impurities ( $sp^2$ ) [1, 8] probably are the most important ones [9]. From an electrochemical point of view, the preparation and treatment of the diamond films will affect the stability of the electrode's response, the values of the background currents, the width of the potential window between hydrogen and oxygen evolution, the reversibility of redox reactions at diamond, and the current efficiency during the oxidation of organic compounds. The current lack of a standard procedure for the preparation and treatment of diamond films is responsible for the wide range of variation of diamond quality and properties reported in the literature. The conflicting conclusions as to effects of surface treatments on the charge transfer process across the interface diamond/electrolyte

---

further contribute to the confusion and make it even more difficult to compare results from different laboratories. This work aims at clarifying some aspects of the electron transfer kinetics at boron-doped diamond electrodes in light of the results obtained in our and other laboratories.

Boron-doped diamond (BDD) electrodes, both as-grown and polarised anodically under different conditions, were prepared in order to study the chemical and electrochemical changes of diamond and clarify the rule played by the surface-state density (Chapter 3). Many different treatments were employed, but only the most relevant results will be presented in this work, *viz.*, those obtained with four kinds of surface treatment: as-grown (BDD<sub>ag</sub>), mildly polarized (BDD<sub>mild</sub>), strongly polarised in perchloric acid (BDD<sub>severe</sub>), and strongly polarised in a sulphuric acid-acetic acid mixture (BDD<sub>AcOH</sub>). Charge transfer processes at the electrode surface were studied.

The concept of non-diamond ( $sp^2$ ) impurities as charge transfer mediators on a diamond surface was suggested as an explanation for the electrochemical behaviour of diamond electrodes after surface oxidation treatment. To verify this concept, graphite particles were deposited on mildly polarised diamond electrodes (BDD<sub>mild</sub>) so as to prepare diamond-graphite composite electrodes (BDD-g), and their properties were compared with those of as-grown (BDD<sub>ag</sub>) diamond and carbon electrodes (Chapter 4). By depositing graphite particles on diamond after its deactivation by anodic polarisation it was possible to restore the initial properties of the as-grown diamond electrode. In the potential region of electrolyte decomposition,  $sp^2$  was eliminated from the BDD-graphite composite surface by oxidation to CO<sub>2</sub>. BDD itself behaved as a 'non-active' electrode. In this case the oxidation of organic compounds was mediated by hydroxyl radicals formed during water discharge, without any participation of the electrode surface.

The behaviour of 'non-active' diamond in organic oxidation processes occurring in the potential region of water decomposition was described in greater detail in the chapter about electrochemical oxidation of ethylenediaminetetraacetic acid (EDTA) (Chapter 5). The theoretical model developed for organic oxidation at 'non-active' anodes was used to predict results for the oxidation of EDTA at boron-doped diamond electrodes. The very good fit between experimental results and theoretical values confirmed that EDTA oxidation at diamond in the potential region of electrolyte decomposition was a fast reaction involving free electrogenerated hydroxyl radical intermediates formed at the anode during water discharge.

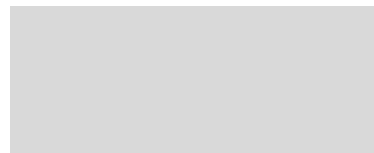
Nanoparticles of IrO<sub>2</sub> were deposited (Chapter 6) by thermal decomposition on boron-doped diamond electrodes (BDD-IrO<sub>2</sub>) in order to improve and better understand their electrocatalytic activity toward redox processes and the oxygen evolution reaction (OER). The IrO<sub>2</sub> deposition completely altered the electrochemical properties of diamond from an ‘non-active’ to an ‘active’ material. The high electrocatalytic activity of BDD-IrO<sub>2</sub> electrodes toward the OER was also confirmed in an indirect way by the observation that the oxidation of organic substances and the production of peroxodisulphate are inhibited. The high degree of dispersion of the IrO<sub>2</sub> particles led to a high electrocatalytic activity, even at extremely low IrO<sub>2</sub> loadings.

On the basis of experimental results a phenomenological model was proposed (Chapter 7). Boron-doped diamond was defined as a degenerated semiconductor material because of the quite high charge density on its surface due to the boron doping ( $> 10^{21}$  boron atoms cm<sup>-3</sup>), to the non diamond (*sp*<sup>2</sup>) carbon and in general to surface impurities. This distribution of charges on the surface promoted processes of electron transfer across the interface diamond/electrolyte. Deposition of particles on the diamond surface (graphite or IrO<sub>2</sub>) increased further this surface charge density until reaching a perfectly metallic behaviour.

---

## 1. References

1. H. B. Martin, A. Argoitia, J. C. Angus, and U. Landau, *J. Electrochem. Soc.*, **146** (1999) 2959.
2. T. Kondo, Y. Einaga, B. V. Sarada, T. N. Rao, D. A. Tryk, and A. Fujishima, *J. Electrochem. Soc.*, **149** (2002) E179.
3. K. Hayashi, S. Yamanaka, H. Okushi, and K. Kajimura, *Appl. Phys. Lett.*, **68** (1996) 376.
4. I. Yagi, H. Notsu, T. Kondo, D. A. Tryk, and A. Fujishima, *J. Electroanal. Chem.*, **473** (1999) 173.
5. D. A. Tryk, K. Tsunozaki, T. N. Rao, and A. Fujishima, *Diamond Relat. Mater.*, **10** (2001) 1804.
6. R. J. Zhang, S. T. Lee, and Y. W. Lam, *Diamond Relat. Mater.*, **5** (1996) 1288.
7. C. Lévy-Clément, F. Zenia, N. A. Ndao, and A. Deneuveille, *New Diamond Front. Carbon Technol.*, **9** (1999) 189.
8. G. M. Swain, A. B. Anderson, and J. C. Angus, *MRS Bull.*, **23** (1998) 56.
9. M. C. Granger and G. M. Swain, *J. Electrochem. Soc.*, **146** (1999) 4551.



---

A review of electrochemical processes taking place at electrode surfaces was presented. A distinction was made between inner and outer-sphere processes, mediated electrode reactions (on '*active*' electrodes) and mediated solution electrochemical reactions (on '*non-active*' electrode). Particular attention was paid to simple outer-sphere and complex inner-sphere electron transfer reactions as a system model for testing electrochemical properties of electrode/electrolyte interfaces. The fundamentals of the techniques of steady-state polarisation, cyclic voltammetry and impedance were presented as powerful methods for the electrochemical investigation of electrode materials. A general description of diamond properties was also given, ranging from the preparation methods to the morphological and electrochemical characterisation of diamond electrodes, and emphasising the several electrochemical applications of the material. A theoretical model was developed to predict chemical oxygen demand (COD) and instantaneous current efficiency (ICE) during the electrochemical oxidation of organic compounds on '*non-active*' diamond electrodes. A kinetic model also was developed to predict the current efficiency of oxidation of organic compounds on '*active*' IrO<sub>2</sub> electrodes.

## 1. Electrode processes

An active electrochemical system is characterised by charge transfer across an interface generally between an electronic conductor (electrode) and an ionic conductor (electrolyte). Through the electrode, the charge is usually transported by electrons. The most common electrode materials are metals (Au, Pt, etc.), oxides ( $\text{IrO}_2$ ,  $\text{PbO}_2$ ,  $\text{RuO}_2$ ) supported on Ti base metal and referred to as dimensionally stable electrodes (DSA), and carbon (graphite). In the electrolyte, the charge transport is provided by the movement of ions. The electrolytes used most often are liquid solutions composed of ionic species in either water or a nonaqueous solvent. Less conventional electrolytes are fused salts and ionically conductive polymers.

Studying charge transfer phenomena experimentally at a single interface is not possible. All system properties result from a combination of many interfaces (electrochemical cell). Such a system usually consists of at least two electrodes in contact with an electrolyte. The reaction taking place in an electrochemical cell is the result of two half-reactions which separately describe the charge transfer at the two electrodes. Because most often the attention is turned to only one of these reactions (at the working electrode), the other half of the cell is standardised by using an electrode/electrolyte phase with a constant composition (reference electrode). The internationally accepted primary reference electrode is the standard hydrogen electrode (SHE), which has all the components at unit activity. Since the potential of the reference electrode is fixed, any change in the cell is related to the phenomena at the working electrode.

Two types of processes occur at electrodes. One kind involves electron transfer across the metal/electrolyte interface (*faradaic* processes). When the metal/electrolyte interface changes because of adsorption or desorption phenomena, *nonfaradaic* processes are said to be involved in the electrical double layer. Both faradaic and nonfaradaic processes take place at an electrode during electrochemical reactions. Although the faradaic processes are of primary interest when studying an electrochemical reaction, the nonfaradaic processes must be considered by studying the nature of the electrode/electrolyte interface.

### 1.1. The electrical double layer [1]

When charge transfer cannot occur across the metal/solution interface, even if an external potential difference is imposed, the electrode is called an *ideally polarizable electrode* (IPE). Some real electrode/solution interfaces can approach this ideal behaviour within a particular potential range. A mercury electrode in contact

with a deaerated solution of potassium chloride is a typical example of IPE over a two volts wide range of potential.

Since charge does not cross the interface during potential changes at IPE, the interface behaves like a capacitor. For a given applied potential, charge is stored in equal measure on the electrode ( $q^M$ ) and in the solution ( $-q^S$ ). In the case of a metallic electrode, the excess or deficiency of electrons is limited to a very thin surface layer ( $< 1$  Angstrom), while the charge in solution is distributed in the proximity of the electrode surface. This charge distribution at the interface is called an *electrical double layer* with which a double-layer capacitance,  $C_{dl}$ , is associated.

The double-layer region is described by a model which assumes a solution side distribution of charge over several 'layers' (Fig. 2.1).

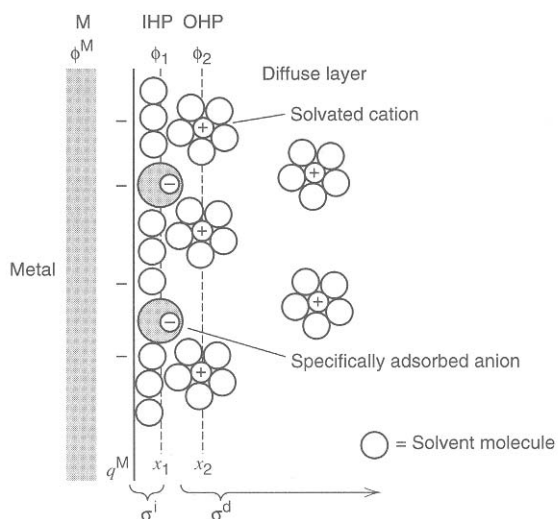


**FIGURE 2.1.** Proposed model of the double layer region. Case of specifically and nonspecifically adsorbed ions [2].

The region next to the electrode is made up of solvent molecules and, sometimes, specifically adsorbed species. This is called *compact*, *Helmholtz*, or *Stern layer*. The electrical centres of these specifically adsorbed species form the *inner Helmholtz plane* (IHP). Solvated ions present in the solution can approach the electrode surface only to a distance from the IHP that corresponds to the diameter of the solvent molecules. The electrical centres of the nearest solvated ions form the *outer Helmholtz plane* (OHP).

These ions, which interact with the electrode through long-range electrostatic forces, are called *nonspecifically adsorbed* species. Because of the electrostatic nature of these interactions, ions are distributed in a 3D region called the *diffuse layer* which extends from the OHP to the bulk of the solution. The thickness of the diffuse layer



depends on the total ionic concentration in the solution. Sometimes the double layer can be neglected while studying electrode reaction kinetics. Nevertheless, the fact that the structure of the double layer could affect the reaction rate on the electrode must be taken in account.

## 1.2. Faradaic processes [1]

Faradaic processes involve electron transfer occurring across the electrode/electrolyte interface. Whereas a general electrode reaction such as  $O + ne^- \rightarrow R$  can be written to summarise the steps occurring in the electrochemical cell, many processes are really involved and influence the reaction rate:

- a. mass transfer from the bulk to the electrode surface and *vice versa*
- b. electron transfer at the electrode surface
- c. homogeneous (in the bulk) or heterogeneous (at the electrode surface) chemical reactions
- d. surface phenomena such as adsorption, crystallisation, etc.

Some of these steps have potential-dependent rates. The simplest reaction only involves mass transfer of the reactant molecule from the bulk to the electrode, heterogeneous charge transfer across the interface without adsorption, and mass transfer of the product molecule to the bulk of the solution. The electrode's response to current flow corresponds to an overpotential that is the sum of different terms associated with the reaction steps occurring with a finite rate in the electrochemical cell. Accordingly, a reaction can be represented by a series of resistances (or impedances). A fast reaction step is represented by a small resistance, while a slow step is described by a high one. Except for very low current or potential perturbations, these resistances are functions of the applied potential. The kinetics of a system is strongly influenced by the applied potential. This is true for all faradaic processes. By controlling the potential at the electrode, one can control the reactivity and study the relation between the rate constant and the applied potential.

Based on the nature of the interactions between reactants and electrode surface, electrochemical faradaic processes can be classified [3] as (1) outer-sphere, (2) inner-sphere, (3) mediated electrode and (4) mediated solution reactions (Fig. 2.2).

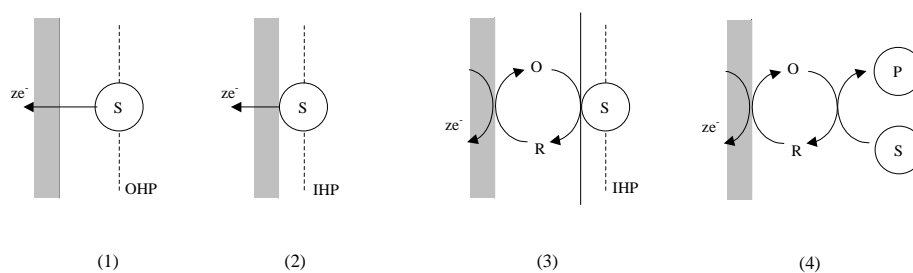


**FIGURE 2.2.** Schematic representation of faradaic oxidation processes: (1) outer-sphere reaction, (2) inner-sphere reaction, (3) mediated electrode reaction (the mediator couple O/R is fixed on the electrode) and (4) mediated solution reaction (the mediator couple O/R is in solution). Electrode surface in gray, S = reactant in solution, P = product in solution, IHP = inner Helmholtz plane, OHP = outer Helmholtz plane.

**1.2.1. Outer-sphere and inner-sphere charge transfer reactions.** The kinetics of a reaction is influenced by the nature and structure of the reacting species, the solvent, the electrode material and adsorbed layers on the electrode. To clarify these influences, microscopic theories have been developed. Two key concepts in this discussion are the *inner-sphere* and the *outer-sphere* electron transfer reaction [1]. The term ‘outer-sphere’ is used to designate a reaction in which the activated complex maintains the coordination sphere originally present in the reactant species. With the term ‘inner-sphere’, a reaction is described in which the reactants share a ligand in the activated complex. In other words, an outer-sphere reaction occurs with weak interaction between the electrode and the reactant, which maintains a distance of at least one solvent layer from the electrode surface (Fig. 2.3).

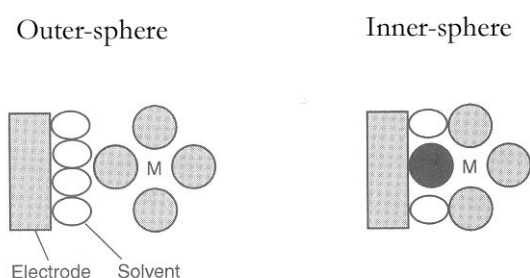


**FIGURE 2.3.** Outer-sphere and inner-sphere reactions. M = metal ion surrounded by ligands. The ligand in dark represents the shared ligand in an inner-sphere reaction.

In the case of an inner-sphere reaction, both the reactant and the product species as well as the activated complex are involved in very strong interactions with the electrode surface (specific adsorption). Obviously, the kinetics of outer-sphere reactions is less dependent on the electrode material than that of inner-sphere electron transfer reactions. Nevertheless, the electrode material could influence the

kinetics even in the case of outer-sphere charge transfer, by affecting the electrical double layer and the Helmholtz layer structure. A distribution of electronic states on the electrode surface can influence as well the electron transfer kinetics in outer-sphere reactions. Anyway, outer-sphere reactions can be treated in a more general way than inner-sphere reactions, and the theory is much more developed [4, 5]. For this reason the discussion that follows pertains to this kind of reactions.

#### *Outer-sphere reactions*

Redox systems such as  $\text{Fe}^{2+}/\text{Fe}^{3+}$ ,  $\text{Fe}(\text{CN})_6^{3-}/\text{Fe}(\text{CN})_6^{4-}$ ,  $\text{MnO}_4^-/\text{MnO}_4^{2-}$ , etc. have been taken as model redox reactions because of their supposedly outer-sphere electron transfer mechanism. Particularly, the outer-sphere  $\text{Fe}(\text{CN})_6^{3-}/\text{Fe}(\text{CN})_6^{4-}$  reaction has been frequently used to check the interface properties of different electrode materials. Nevertheless, many investigations have shown the extremely complex nature of this reaction. Its kinetics is influenced by the nature of the electrode material, and this has been attributed to different functional groups on the surface [6, 7]. The influence of electrolyte concentration and of valency of the associated cation were investigated by Kuta *et al*, who revealed a strong interaction between the cation of the supporting electrolyte and the electroactive anion during electron transfer, which is promoted by an increase in the cation concentration and valency [8]. On the basis of similar results obtained previously [9], it was suggested that a three-body collision probably was responsible for the creation of the activated complex during the charge transfer step. The decrease in reaction rate caused by a concentration increase of the redox couple has been explained in terms of a partial blocking of the surface by poorly soluble species [10]. Because of the formation of Prussian blue  $\text{Fe}[\text{Fe}^{3+}\text{Fe}^{2+}(\text{CN})_6]_3$  observed in acidic solutions, an interaction between  $\text{Fe}(\text{CN})_6^{3-}$  or  $\text{Fe}(\text{CN})_6^{4-}$  with  $\text{Fe}^{2+}$  or  $\text{Fe}^{3+}$  was proposed by the authors to explain this blocking phenomenon. The presence of adsorbed species preceding and following the electron transfer was demonstrated by Fleischmann *et al*, by using Raman spectroscopy. This work showed that the nature of these adsorbed species changed with the supporting electrolyte cation, with the applied potential, and with the nature of the electrode material [11]. The exchange current and the transfer coefficients of the reaction were calculated and correlated with those obtained for a one-electron reaction with two partial charge transfer steps [12]. The nature of the electrode material and the presence of surface states on the surface seemed to play an important role [13]. McCreery attributed the change in kinetics to surface interactions of the redox couple, but no hypotheses were advanced as to their nature, and the redox system appeared to be insensitive to the carbon-oxygen functionalities of the active sites.

### *Inner-sphere reactions*

Several inner-sphere redox reactions have been studied so far to test the electrochemical properties of electrodes. The benzoquinone/hydroquinone reaction was one of these inner-sphere redox reactions, because it involves a complex electron and proton transfer reaction. The kinetics and mechanism of this reaction on platinum electrodes have been discussed in many papers, and several hypotheses have been proposed [14-17]. It has been demonstrated that hydroquinone and *p*-benzoquinone were irreversibly adsorbed as a monolayer on the platinum surface [14, 15]. Studies carried out in different media showed that the nature of the charge transfer depended on the pH value [18]. Vetter in particular demonstrated that in acidic media the protonation was fast, while the electrochemical steps were rate-controlling by a mechanism of the type:  $H, e, H, e$  in which a consecutive transfer of protons ( $H$ ) and electrons ( $e$ ) was involved. The redox couple was also sensitive to the nature of the surface. In particular, a surface pretreatment in the case of carbon electrodes had a positive influence on the reversibility of the system [19].

**1.2.2. Mediated electrode reactions (surface redox catalysis).** Here, electron transfer occurs through heterogeneous redox catalysis. The electrode surface is directly involved in the redox process, by exchanging electrons with the reactants in solution. In this case the mediator couple O/R is fixed on the electrode surface, and the process can only take place at the inner Helmholtz plane (case (3) in Fig. 2.2). The  $\text{IrO}_2$  electrode is a typical example. These electrodes have been referred to as active electrodes (see § 2.5.2).

**1.2.3. Mediated solution reactions (solution redox catalysis).** In this case the mediated couple O/R is in solution but is electrogenerated at the electrode surface (case (4) in Fig. 2.2). Depending on the reactivity of the mediator, two extreme cases can be distinguished: reaction of the mediator in a very thin reaction layer close to the electrode (high reactivity) or reaction in the bulk solution (low reactivity). A typical example of high-reactivity intermediate is the formation of active hydroxyl radicals by water discharge on boron-doped diamond. This electrode has been referred to as an ‘non-active’ electrode (see § 2.5.1).

**1.2.4. The Butler-Volmer equation.** The potential of an electrode strongly affects the kinetics of all faradaic processes occurring on its surface. The phenomenological model of Butler and Volmer is able to relate the reaction rate (current density) with the applied electrode potential using two parameters ( $k^0$  or  $j_0$

and  $\alpha$ ). A one-step, one-electron process can be considered as the simplest electrode process (reaction 2.1):



where  $k_f$  and  $k_b$  represent the heterogeneous rate constants of the reduction and oxidation reaction, respectively.

Qualitatively, the model can be summarised by Figure 2.4. The reaction can be visualised in terms of progress along a reaction coordinate, connecting the reactant configuration to the product configuration on an energy surface. The reaction coordinate can be taken as the distance between the reactant nuclei. The free energy profile can be discussed along the reaction coordinate. The curves corresponding to the reactant and the product configuration intersect at the transition state, and the heights of the barriers to oxidation and reduction determine their relative rates. When the rates are equal (Fig. 2.4a), the system is at equilibrium ( $E_{\text{eq}}$ ). For positive potential values, the energy of the reactant electron is lower, the energy curve drops with respect to the energy of O. The reduction barrier rises and the net effect is the conversion of O to R (Fig. 2.4b). The cathodic component,  $i_a$ , to the total current is defined as:

$$i_a = F A k_b C_R(0,t) \quad 2.2$$

where  $C_R(0,t)$  is the concentration ( $\text{mol m}^{-3}$ ) of the reduced form at the electrode surface and at time  $t$ . For potentials more negative than the equilibrium value, the situation is inverted, and a net cathodic flow of current is obtained (Fig. 2.4c). The anodic component  $i_c$ , to the total current is defined as:

$$i_c = F A k_f C_O(0,t) \quad 2.3$$

where  $C_O(0,t)$  is the concentration ( $\text{mol m}^{-3}$ ) of the reduced form at the electrode surface and at time  $t$ .

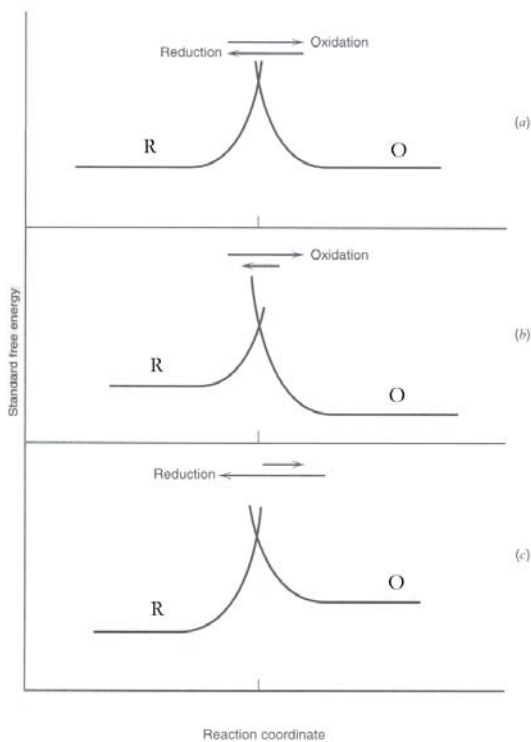


**FIGURE 2.4.** Simple representation of standard free energy changes during a faradaic process. (a) potential corresponding to equilibrium; (b) potential higher than the equilibrium value; (c) potential lower than the equilibrium value, O/R redox couple.

The influence of the potential on the rate (current) of an electrode reaction has been determined quantitatively. The relation obtained is known as the *Butler-Volmer* kinetic equation (Eq. 2.4):

$$i = FAk^0 \left\{ C_O(0,t) \exp \left[ -\alpha \frac{F}{RT} (E - E^{0'}) \right] - C_R(0,t) \exp \left[ -(1 - \alpha) \frac{F}{RT} (E - E^{0'}) \right] \right\} \quad 2.4$$

where  $F$  is the Faraday constant,  $A$  is the electrode surface area,  $C_O(0,t)$  and  $C_R(0,t)$  are the concentrations ( $\text{mol m}^{-3}$ ) of the oxidised and reduced form at the electrode surface and at time  $t$ ,  $\alpha$  is the transfer coefficient, and  $E^{0'}$  is defined as the potential where reduction and oxidation rate constants  $k_f$  and  $k_b$  have the same value, which corresponds to the *standard rate constant*,  $k^0$  ( $k_f = k_b = k^0$ ).

The reaction rate constants at other potentials can be simply expressed in terms of  $k^0$  (Eqs. 2.5 and 2.6):

$$k_f = k^0 \exp \left[ -\alpha \frac{F}{RT} (E - E^{0'}) \right] \quad 2.5$$

$$k_b = k^0 \exp\left[(1 - \alpha) \frac{F}{RT} (E - E^{0'})\right] \quad 2.6$$

A system with a large  $k^0$  will reach equilibrium on a short time scale, while small  $k^0$  are typical of very slow reactions. The largest values of  $k^0$  have been measured in the range of 1 to 10 cm s<sup>-1</sup> and are associated with outer-sphere transfer processes. Even if  $k^0$  of a reaction is quite small, the  $k_f$  and  $k_b$  value can be made quite large by using a sufficiently high potential relative to the  $E^{0'}$  value (Eqs. 2.5 and 2.6).

At equilibrium ( $E = E_{eq}$ ) the net current is zero, the bulk concentrations are found also at the surface:  $C^* = C(0,t)$ , thus from Eq. 2.4 it is possible to obtain the Nernst equation (Eq. 2.7):

$$E_{eq} = E^{0'} + \frac{RT}{F} \ln \frac{C_O^*}{C_R^*} \quad 2.7$$

At equilibrium, the oxidation and the reduction reaction take place with the same rate. The anodic and the cathodic current,  $i_a$  and  $i_c$  (Eqs. 2.2 and 2.3), will be equal in absolute value, and can be expressed in terms of *exchange current*  $i_0$  (Eq. 2.8):

$$i_0 = F A k^0 C_O^* \exp\left[-\alpha \frac{F}{RT} (E_{eq} - E^{0'})\right] = F A k^0 C_O^{*(1-\alpha)} C_R^{*\alpha} \quad 2.8$$

In the particular case where  $C_O^* = C_R^* = C$ , the combination of Equations 2.7 and 2.8 gives:

$$i_0 = F A k^0 C \quad 2.9$$

Dividing the Butler-Volmer formulation (Eq. 2.4) by the expression for  $i_0$  (Eq. 2.8), the following equation is obtained:

$$i = i_0 \left[ \frac{C_O(0,t)}{C_O^*} e^{-\alpha \frac{F}{RT} \eta} - \frac{C_R(0,t)}{C_R^*} e^{(1-\alpha) \frac{F}{RT} \eta} \right] \quad 2.10$$

where the overpotential is defined as  $\eta = E - E_{eq}$ .

*No mass transfer effect*

If the solution is well stirred or the current is so low that the surface concentration does not differ from the bulk value, the last equation, Eq. 2.10, becomes:

$$i = i_0 \left[ e^{-\alpha \frac{F}{RT} \eta} - e^{(1-\alpha) \frac{F}{RT} \eta} \right] \quad 2.11$$

which is known as the *Butler-Volmer equation* (Eq. 2.11). The transfer coefficient  $\alpha$  for the reduction reaction also is called  $\alpha_{\text{red}}$ , while the term  $(1-\alpha)$  corresponds to the transfer coefficient of the oxidation reaction and it is often represented by a  $\beta_{\text{ox}}$ . Using  $\alpha$  and  $\beta$ , the equation 2.11 becomes:

$$i = i_0 \left[ e^{-\alpha_{\text{red}} \frac{F}{RT} \eta} - e^{\beta_{\text{ox}} \frac{F}{RT} \eta} \right] \quad 2.12$$

Depending on the overpotential value, two cases, a and b, can be distinguished:

*a) Small overpotentials ( $\eta < 10$  mV)*

For small values of the overpotential,  $|\eta < 10 \text{ mV}|$  at 25 °C, the equation can be simplified to the linear relation:

$$i = i_0 \frac{F}{RT} \eta \quad 2.13$$

which shows that the net current is linearly related to the overpotential within a narrow potential range near  $E_{\text{eq}}$ . The ratio  $\eta/i$  has the units of a resistance, and is often called the charge transfer resistance,  $R_{\text{ct}}$ .

$$R_{\text{ct}} = \frac{RT}{Fi_0} \quad 2.14$$

This parameter is the negative reciprocal slope of the  $i$ - $\eta$  curve at the point where this curve passes through the origin (Fig. 2.5). It can be evaluated directly in some experiments, and serves as a convenient index of the kinetic ease.



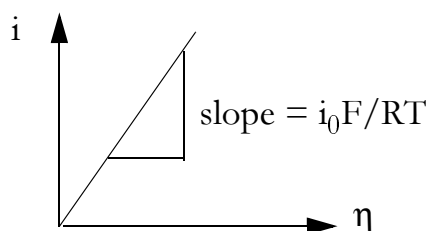


**FIGURE 2.5.** Linearised  $i$ - $\eta$  curve for small overpotentials; one-step, one-electron redox reactions.

*B) Large overpotentials ( $\eta > 118$  mV)*

For large values of the overvoltage,  $|\eta| > 118$  mV at 25 °C, one of the terms in the brackets in Eq. 2.11 becomes negligible:

$$\eta = \frac{RT}{\alpha F} \ln i_0 - \frac{RT}{\alpha F} \ln i \quad 2.15$$

The plot of  $\log i$  vs  $\eta$ , known as *Tafel plot*, is a useful device for evaluating the kinetic parameters. The Tafel form can be expected to hold whenever the back reaction contributes less than 1% of the total net current. Tafel plots (Fig. 2.6) are represented by two branches, one with a positive (anodic) and one with a negative (cathodic) slope.

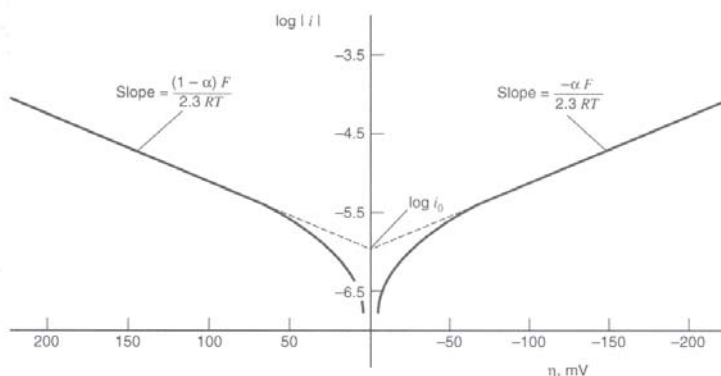


**FIGURE 2.6.** Tafel plots for anodic and cathodic branches of the current-overpotential curve for the reaction  $O + e = R$  with  $\alpha = 0.5$  at 298.15 K and with a  $j_0 = 10^{-6}$  A cm $^{-2}$ .

Both linear segments extrapolate to a common intercept which corresponds to  $\log i_0$ . The plot deviates from linear behaviour as  $\eta$  approaches zero, because the back reaction can no longer be neglected. From this kind of representation, values

of  $i_0$  and  $\alpha$  are easily accessible. When the electrode kinetics is sluggish and a significant activation overpotential is required, good Tafel relationships can be seen.

### 1.3. Electrochemical characterisation techniques

The following paragraphs refer to electrochemical methods in which the working electrode is subjected to potential perturbations, and the electrode's response is recorded. The view is here restricted to the methods of steady-state polarisation, cyclic voltammetry and impedance spectroscopy, as simple and powerful techniques for studying the kinetic parameters in electrochemical systems.

**1.3.1. Steady-state polarisation.** This potential step method involves applying a potential difference between the working and the reference electrode and recording a current response when a steady state is reached. Current-potential curves provide information about kinetic parameters of the redox reaction investigated.

If the applied overpotential is small ( $\eta < 10$  mV) and both redox forms are present (so that an equilibrium potential exists), the current and the potential are linked by a linearised  $i$ - $\eta$  relation (Eq. 2.13 for one-step, one-electron reactions). In this case kinetic information about  $k^0$  and the charge transfer resistance (Eqs. 2.13 and 2.14) is directly available from some experiments, as shown in Figure 2.5.

With large potential perturbations ( $\eta > 118$  mV), since the mass-transfer-controlled region is not involved, the kinetics of sluggish reactions can be investigated. In this potential region the back reaction (corresponding to one of the two branches in Fig. 2.6) can be neglected. In this case the current-potential relation provides information about the kinetic parameters (Eq. 2.15).

**1.3.2. Cyclic voltammetry.** Cyclic voltammetry has become a very popular technique for initial electrochemical studies of new systems. Particular attention has been paid to systems in which the mass transport of electroactive species occurs only by diffusion. The next paragraph will describe the solution of the diffusion equations with the appropriate boundary conditions for electrode reactions with heterogeneous rate constants.

#### *Nernstian systems*

The reaction  $O + e^- \leftrightarrow R$  is considered, assuming semi-infinite linear diffusion and a solution initially containing only the species O, with the electrode at an initial

potential  $E_i$  where no electrode reaction occurs. The potential is varied linearly at a scan rate  $v$  so that the potential at any time is:

$$E(t) = E_i - vt \quad 2.16$$

If we can assume that the rate of electron transfer is high at the electrode surface so that the species O and R immediately adjust to the ratio dictated by the Nernst equation, then the surface concentration ratio is time (potential) dependent.

For a Nernstian system the peak current,  $i_p$ , can be written as:

$$i_p = (2.69 \times 10^5) A D_O^{1/2} C_O^* v^{1/2} \quad (\text{for a mono-electronic reaction } n = 1) \quad 2.17$$

at 25 °C for  $A$  in  $\text{cm}^2$ ,  $D_O$  in  $\text{cm}^2 \text{ s}^{-1}$ ,  $C_O^*$  in  $\text{mol cm}^{-3}$ ,  $v$  in  $\text{V s}^{-1}$ , and  $i_p$  in A.

The peak potential,  $E_p$ , can be expressed as:

$$E_p = E_{1/2} - 1.109 \frac{RT}{nF} = 28.5 \text{ mV at } 25^\circ\text{C} \quad (n = 1) \quad 2.18$$

Because the peak sometimes is broad so that the peak potential may be difficult to determine, it will be convenient to report the *half-peak potential*  $E_{p/2}$ , which corresponds to the potential at a current equal to  $i_p/2$ .  $E_{1/2}$  is located midway between  $E_p$  and  $E_{p/2}$ , so that a convenient diagnostic for a Nernstian wave is given by:

$$|E_p - E_{p/2}| = 2.2 \frac{RT}{nF} = 56.5 \text{ mV at } 25^\circ\text{C} \quad (n = 1) \quad 2.19$$

For a reversible wave,  $E_p$  is independent of the scan rate, and  $i_p$  is proportional to  $v^{1/2}$ . The latter property indicates a diffusion-controlled process.

The shape of a curve in the return sweep depends on the ‘switching potential’  $E_\lambda$ , or on how far beyond the cathodic peak the scan was allowed to proceed before reversal of the potential scan (Fig. 2.7). However, if  $E_\lambda$  is at least 35 mV ( $n = 1$ ) past the cathodic peak, the peaks in the reverse scan all have the same general shape as in the forward  $i$ - $E$  curve, only in the opposite direction on the current scale (curves 1, 2, and 3 in Fig. 2.7), and with the decaying current of the cathodic wave taken as a baseline (curves 1', 2', and 3' in Fig. 2.7). When the cathodic sweep is stopped and the current is allowed to decay to zero (curve 4 in Fig. 2.7), a subsequent anodic wave will then be identical to the cathodic one, only plotted in the opposite direction on both the  $i$  and  $E$  axes.

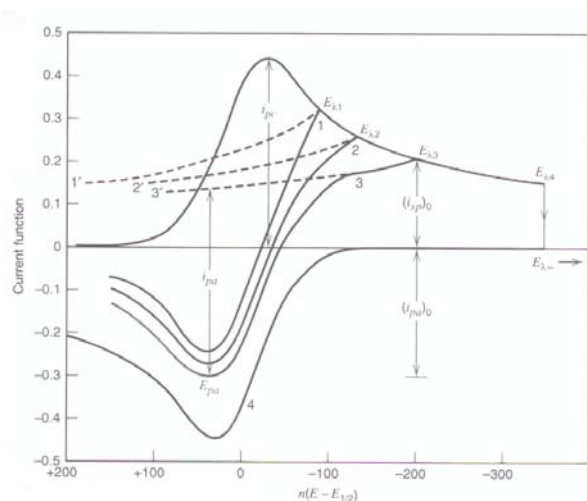


**FIGURE 2.7.** Cyclic voltammograms for different switching potential values,  $E_{\lambda}$ .

Two experimental parameters of interest are the ratio of the peak currents,  $i_{pa}/i_{pc}$ , and the separation of the peak potentials,  $E_{pa}-E_{pc}$ . For a Nernstian system with stable product,  $i_{pa}/i_{pc} = 1$  regardless of the scan rate, switching potential and diffusion coefficients. The power of cyclic voltammetry lies in its diagnostic strength, which derives from the ease of interpreting the qualitative and semi-quantitative behaviour. The difference between  $E_{pa}$  and  $E_{pc}$  ( $\Delta E_p$ ) is a useful diagnostic test for a Nernstian reaction. Although  $\Delta E_p$  slightly depends on  $E_{\lambda}$ , it is always close to 59 mV at 25 °C ( $n = 1$ ).

### Irreversible systems

Here we consider an irreversible one-step, one-electron reaction  $O + e^- \rightarrow R$ . The peak current is written as:

$$i_p = (2.99 \times 10^5) \alpha^{1/2} A C_O^* D_O^{1/2} \nu^{1/2} \quad 2.20$$

where the units are the same as for Eq. 2.17. For a totally irreversible couple,  $E_p$  is a function of the scan rate, shifting in a negative (reduction) or positive (oxidation) direction with increasing scan rate. The peak potential is given by:

$$E_p = E^{0'} - \frac{RT}{\alpha F} \left[ 0.78 + \ln \left( \frac{D_O^{1/2}}{k^0} \right) + \ln \left( \frac{\alpha F \nu}{RT} \right)^{1/2} \right] \quad 2.21$$

Introducing the *half-peak potential*  $E_{p/2}$ , the following equation is obtained:

$$|E_p - E_{p/2}| = 1.857 \frac{RT}{\alpha F} = 47.7/\alpha \text{ mV at } 25^\circ\text{C} \quad 2.22$$

### *Quasi-reversible systems*

Quasi-reversible reactions exhibit kinetic electron transfer limitations where the reverse reaction has to be considered. For the one-step, one-electron case the peak current is given by

$$i_p = i_p(\text{rev})K(\Lambda, \alpha)$$

where  $i_p(\text{rev})$  is the reversible peak value (Eq. 2.17). The shape of the peak and the various peak parameters are a function of  $\alpha$  and of a parameter  $\Lambda$  defined as:

$$\Lambda = \frac{k^0}{\left(D_O^{1-\alpha} D_R^\alpha \frac{RT}{F} v\right)^{1/2}} \quad 2.23$$

In this case the wave shape is a function of  $k^0$ ,  $\alpha$ , the switching potential  $E_\lambda$  and  $v$ . If  $E_\lambda$  is at least 90 mV ( $n = 1$ ) beyond the cathodic peak, the effect of  $E_\lambda$  is small. In this case the curves are a function of the parameter  $\Psi$  defined as:

$$\Psi = \frac{\left(\frac{D_O}{D_R}\right)^{\alpha/2} k^0}{\left(\pi D_O \frac{RT}{F} v\right)^{1/2}} \quad 2.24$$

For  $0.3 < \alpha < 0.7$ ,  $\Delta E_p$  is independent of  $\alpha$ , and only depends on  $\Psi$ . Table 2.1, which provides data linking  $\Psi$  and  $k^0$ , is the basis for a widely used method (*method of Nicholson*) for estimating  $k^0$  in quasi-reversible systems. By this method the variation of  $\Delta E_p$  with  $v$  can be determined, and from this variation the value of  $\Psi$  can be found.

**TABLE 2.1.** Variation of  $\Delta E_p$  with  $\psi$  at 25 °C for one-step, one-electron transfer reactions with  $E_\lambda = E_p - 112.5/n$  mV and  $\alpha = 0.5$ .

$\psi$	$\Delta E_p$ [mV]
20	61
6	64
4	66
2	72
1	84
0.75	92
0.50	105
0.25	141
0.10	212

**1.3.3. Impedance spectroscopy.** By imposing potential steps, the electrode can be driven to a condition far from equilibrium, and subjected to large perturbations. The response obtained usually is a transient signal (as in cyclic voltammetry). Another approach is that of perturbing the cell with an alternating signal of small magnitude, and observing the way the system follows the perturbations at steady state. The advantages of this technique are:

- a. high-precision measurements, because of an indefinitely stable response that can be averaged over a long period of time
- b. theoretical treatment of the experimental response by linearised or simplified current-potential characteristics
- c. measurements over a very wide range of time or frequencies ( $10^4$  to  $10^{-6}$  s or  $10^{-4}$  to  $10^6$  Hz)

Since one is working close to equilibrium, details about the current-potential response are not required. This leads to important simplifications in treating kinetic and diffusion phenomena.

The technique where the cell or electrode impedance is studied as a function of frequency of the ac source is called *electrochemical impedance spectroscopy* (EIS). Theory can interpret the equivalent resistance and capacitance values in terms of

interfacial phenomena. The mean potential of the working electrode (dc potential) is the equilibrium potential determined by the ratio of oxidised and reduced forms of the redox couple. Measurements can be made at different potentials by preparing solutions having different concentration ratios. This technique is capable of high precision, and it is frequently used to evaluate heterogeneous charge transfer parameters and to study the double-layer structure.

A variant of electrochemical impedance spectroscopy is *ac voltammetry*. In this case a three-electrode cell is used in the conventional manner, and the potential program imposed on the working electrode is the sum of a dc value,  $E_{dc}$ , which is slowly scanned as a function of time, plus a sinusoidal component,  $E_{ac}$ , usually with a 5-mV peak-to-peak amplitude. The measured responses are the magnitude of the ac component of current at the frequency of  $E_{ac}$  and its phase angle relative to  $E_{ac}$ . The role of the dc potential is that of setting the surface concentrations of O and R. The dc potential usually differs from the true equilibrium value, because the bulk and surface concentrations of the species are not the same and a double layer exists. However, since this potential is a steady potential, the diffusion layer soon becomes so thick that its dimension greatly exceeds that of the diffusion zone affected by the rapid perturbation of  $E_{ac}$ . Thus, to the ac part of the experiment the surface concentrations look like bulk concentrations.

The impedance,  $Z$ , is a kind of generalised resistance that links the voltage to the current in the phasor notation (generalised Ohm's law):

$$\vec{E} = \vec{I}Z \quad 2.25$$

and can be represented as

$$Z(\omega) = Z_{Re} - jZ_{Im} \quad 2.26$$

In a general sense, an electrochemical cell behaves as an impedance to a sinusoidal excitation. It should then be possible to represent its behaviour by an equivalent circuit of resistors and capacitors that pass current with the same amplitude and phase angle as the real cell does under a given excitation. A circuit frequently used is called the Randles equivalent circuit (Fig. 2.8). All current passes through the solution resistance, thus  $R_s$  is inserted as a series element. The parallel elements are introduced because the total current through the working interface is the sum of a faradaic process and of double-layer charging. The double-layer capacitance is regarded as a pure capacitance represented in the circuit by a capacitor of capacitance  $C_{dl}$ . The faradaic process is represented by an impedance,  $Z_f$ . In one

of the representations, this impedance is separated into a pure resistance due to charge transfer,  $R_{ct}$ , and a general impedance called Warburg impedance,  $Z_W$ , which is related to the mass transfer resistance. In contrast to  $R_s$  and  $C_{dl}$  which are nearly ideal circuit elements, the faradaic impedance usually changes with the frequency.

The equivalent circuit of an electrochemical cell is not unique. A given equivalent circuit will represent cell behaviour at a given frequency. The chief objective of a faradaic impedance experiment is that of discovering frequency dependence. Theory is then applied to transform these functions into chemical information. It is only in the simplest cases that individual circuit elements can be identified with processes occurring in the electrochemical cell.

Many other circuits have been devised to account for more complex phenomena such as adsorption, multistep charge transfer, or homogeneous chemistry.

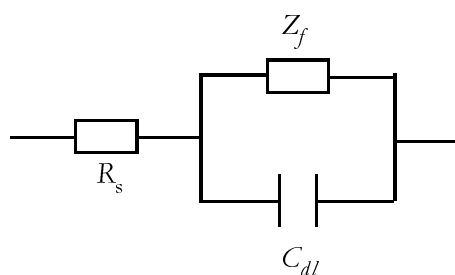


**FIGURE 2.8.** Equivalent circuit of an electrochemical cell. Randles circuit. Solution resistance,  $R_s$ ; faradaic impedance,  $Z_f$ ; and double layer capacitance,  $C_{dl}$ .

The variation of impedance  $Z$  with frequency is often of interest, and can be displayed in different ways. In a *Bode plot*,  $\log|Z|$  and the phase  $\phi$  are both plotted against  $\log \omega$ . An alternative representation, called the *Nyquist plot*, displays  $Z_{Im}$  vs  $Z_{Re}$  for different values of  $\omega$ . Important chemical information can be obtained from this kind of representation. A Nyquist plot for an electrochemical system with the regions of mass-transfer and kinetic control at low and high frequencies, respectively, is shown in Fig. 2.9.



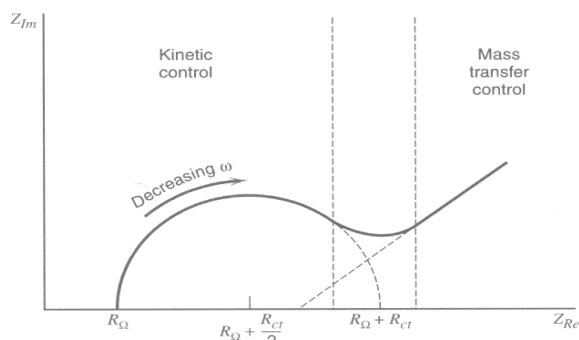


**FIGURE 2.9.** Impedance plot for an electrochemical system. Regions of mass-transfer and kinetic control are found at low and high frequencies, respectively. Ohmic or solution resistance,  $R_{\Omega} = R_S$ .

This representation corresponds to the Randles equivalent circuit in which the faradaic impedance,  $Z_F$ , is separated into the charge-transfer term  $R_{ct}$  and the Warburg term  $Z_W$ .

*Low-frequency limit*

For  $\omega \rightarrow 0$  the plot of  $Z_{Im}$  vs  $Z_{Re}$  should become linear and have unit slope, as shown in Figure 2.10. In this region the frequency dependence only comes from Warburg impedance terms.

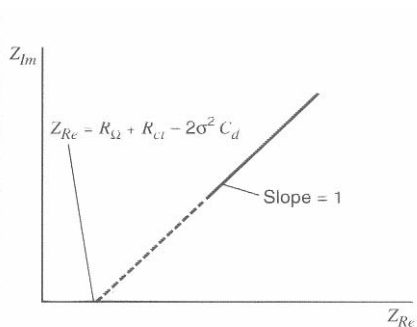


**FIGURE 2.10.** Impedance plane plot for low frequencies.

*High-frequency limit*

At very high frequencies, the Warburg impedance becomes unimportant in relation to  $R_{ct}$ , and the equivalent circuit converges to that shown in Figure 2.11.A. The imaginary component of  $Z$  becomes a pure capacitance  $C_{dl}$  that constitutes zero impedance at high frequencies. All of the current is charging current, the only

impedance being due to the charge-transfer resistance,  $R_{ct}$ . At lower frequencies the capacitance makes an impedance contribution that becomes very important at very low frequencies; hence none of the current will go through  $C_{dl}$  and the imaginary impedance falls off again. The resulting general feature of the  $Z_{Im}$  vs  $Z_{Re}$  plot is a semicircle as shown in Fig. 2.11.B.

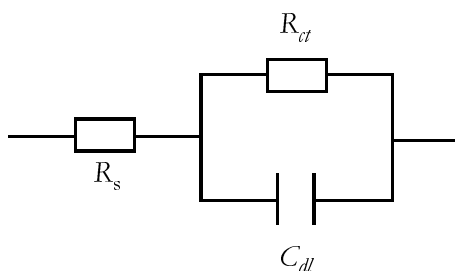


**FIGURE 2.11.A** Equivalent circuit at high frequencies. The Warburg impedance is unimportant.

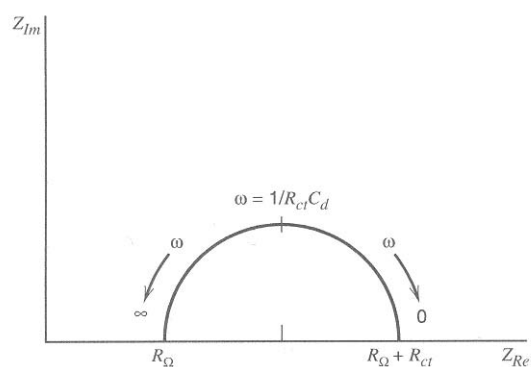


**FIGURE 2.11.B** Impedance plane plot for the equivalent circuit in Fig. 2.11.A.

### Real systems

The impedance plot for a real system combines the two limiting cases explained previously. The features will depend more particularly on the charge-transfer resistance and its relation to the Warburg impedance (Fig. 2.9). If the system is kinetically sluggish, it will have a large  $R_{ct}$  but only a limited region where mass transfer is an important factor. In other cases,  $R_{ct}$  can be extremely small relative to the solution resistance and to the Warburg element over a wide range of frequencies. The kinetics of the system is so fast that mass transfer only is seen and the circular region is not well defined.

Working at high frequencies, a mathematical treatment of results for the simple circuit in Fig. 2.11.A can be performed in terms of admittance,  $Y$ , instead of impedance values,  $Z$  [20]. Before recalculation, the resistance of the solution,  $R_s$ , is subtracted from the measured impedance,  $Z_{meas}$ , and only the term related to the electrode,  $Z_{el}$  (Eq. 2.27), is retained:

$$Z_{el} = Z_{meas} - R_s = \frac{R_{ct}}{1 + i\omega R_{ct} C_{dl}} \quad 2.27$$

where  $C_{dl}$  is the capacitance of the double layer. The electrode admittance,  $Y_{el}$ , as the inverse of the electrode impedance,  $Z_{el}$ , can be expressed by Equation 2.28:

$$Y_{el} = \frac{1}{R_{ct}} + i\omega C_{dl} = Re(Y) + iIm(Y) \quad 2.28$$

Plotting the real part of admittance,  $Re(Y)$ , as a function of  $\log \omega$ , one obtains an intercept that is the inverse of electrode resistance. Plotting the imaginary part of impedance divided by the  $\omega$  value, one obtains an intercept that corresponds to the double-layer capacity of electrode (Figs. 2.12.A and 2.12.B).

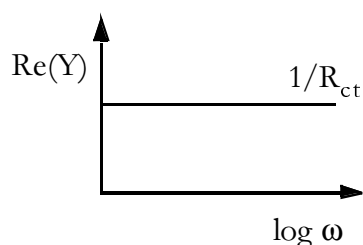


**FIGURE 2.12.A** Representation of the real part of electrode admittance as a function of frequency for the circuit in Fig. 2.11.A.

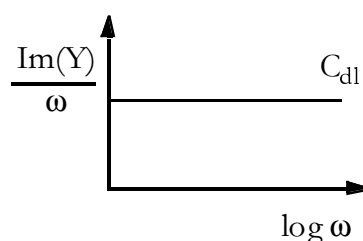


**FIGURE 2.12.B** Representation of the imaginary part of electrode admittance as a function of frequency for the circuit in Fig. 2.11.A.

By this mathematical treatment, the different elements of the equivalent circuit can be calculated. Thus, important information about the electrochemical properties of the electrode material can be obtained.

## 2. Synthetic boron-doped diamond in electrochemistry

Diamond is a material with unique properties: it is a perfect dielectric with an extremely high atomic density and hardness, has the lowest coefficient of thermal expansion, has a high thermal conductivity, is an electric insulator, is transparent from the ultraviolet to the far infrared, and is chemically inert. For this reason it has long attracted the attention of scientists and the public. Interest in diamond has been further increased by the recent discovery that it is possible to produce polycrystalline diamond films with mechanical and electronic properties comparable to those of natural diamond. Diamond films with different levels of doping have

been the subject of applications and fundamental research in electrochemistry, opening up a new branch known as the electrochemistry of diamond. The following paragraphs will try to give a short review on diamond materials, summarise the history of its synthesis, illustrate the mechanisms proposed for the process, and summarise the recent advances in diamond electrochemistry.

## 2.1. History of a synthesis [21]

Synthetic diamond was first produced in the laboratory in 1905 by C. V. Burton [22], but it was only in 1963 that boron was incorporated in diamond to obtain a semiconducting material by the “high-pressure, high-temperature” technique (HPHT) [23]. In 1982 a new technique was developed in Japan at the National Institute for Research in Inorganic Materials (NIRIM) to produce good-quality diamond films on non-diamond substrates from hydrocarbon-hydrogen mixtures [24]. The procedure was described as a “hot-filament chemical vapour deposition” (HF-CVD). One year later [25] the same research group reported another method called “microwave-plasma chemical vapour deposition” (MW-CVD). Since these first innovations, a number of CVD methods have been developed for diamond film growth. They differ more particularly in the way in which the hydrogen dissociation is activated. A limitation of the methods is the relatively small coating area: HF-CVD can treat samples of  $0.5 \text{ m}^2$ . However, CVD is one of the best-known methods for diamond production, and CVD diamond-based components are manufactured and sold commercially.

**2.1.1. The substrate.** The nature of the substrate is an important factor in diamond production, because it determines directly or indirectly the feasibility of the whole process. The chosen material must have a melting point at the process pressure higher than the temperature required for diamond growth. Two other parameters are the thermal expansion coefficient and the chemical/metallurgical stability. A small thermal coefficient assures a good adhesion between substrate and diamond coating that is relatively unaffected by temperature changes. Chemical stability is required to avoid any reaction between the substrate and the carbon or the other gas-phase components during diamond growth. Different groups of materials can be identified:

*Cu, Ag, Zn, Cd, Hg, Ga, In, Tl, C (graphite), Ge, Sn, Pb.* These metals do not react with carbon. However, the rather low solubility of diamond in these elements prevents formation of a carbide interlayer at the diamond/substrate interface. Thus, the diamond film is not expected to have a good adherence on these materials.

*Fe, Ru, Os, Co, Rh, Ir, Ni, Pd, Pt.* These materials act as carbon sinks dissolving the graphite deposit and forming a solid solution. Large amounts of carbon are incorporated in the bulk leading to important chemical and mechanical changes of the substrate surface.

*Ti, Zr, Nb, Ta, Mo W, B, Si.* This class of elements comprises the carbide-forming materials. They are the elements most often employed as substrate materials for diamond deposition. The carbide interlayer that is formed improves the adhesion between diamond and substrate and enhances the diamond nucleation rate. The configuration of this kind of electrodes is similar to that of dimensionally stable anodes (DSA). In particular, the deposition of diamond on titanium base metal has been tested to obtain mechanically stable electrodes on a highly conductive metal substrate [26]. The formation of a conductive TiC interlayer assures good adhesion of the diamond coating and a good electrical contact between Ti and diamond. However, the carbide layer can severely modify the substrate's mechanical properties, influence diamond nucleation, and modify the final quality of the diamond film.

Another important aspect is the availability of geometric forms. Metallic substrates are available in a large variety of forms (plates, discs, grids, etc.), while ceramic substrates can only be prepared as plates, discs, rings, and fibres. This limitation is also reflected in the costs. For these reasons, common metals have been the focus of attention and of efforts to overcome the practical problems related to the deposition of diamond on these materials. The choice of the substrate remains an important problem today, in particular because of its influence on the nucleation, growth, and final quality of the diamond film.

**2.1.2. Nucleation mechanism.** Diamond is the best substrate material for diamond deposition. Based on the idea that defects on the substrate surface will enhance the nucleation density, all substrates usually are pretreated by mechanical polishing with a diamond powder. In this way scratches are created on the surface which act as high-energy sites for diamond nucleation, and moreover, diamond particles remain on the substrate surface supplying nucleation sites for diamond growth. In the last stage of film growth, after cessation of gas-phase activation, a thin layer (several nanometers) of non-diamond carbon is formed. To remove it, the samples are treated by strong oxidising processes which eliminate it as CO<sub>2</sub>.

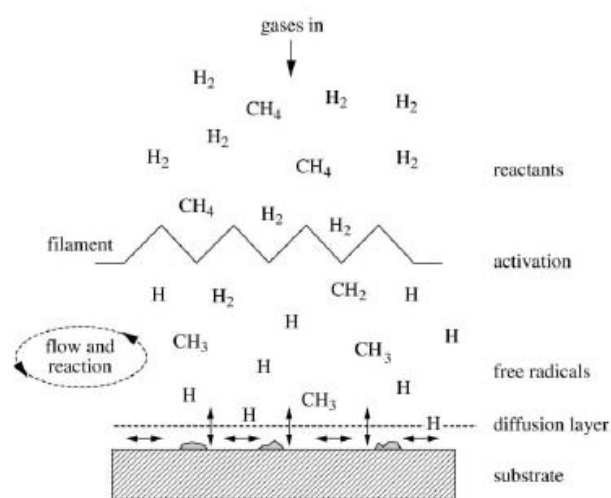


FIGURE 2.13. CVD process for diamond [21].

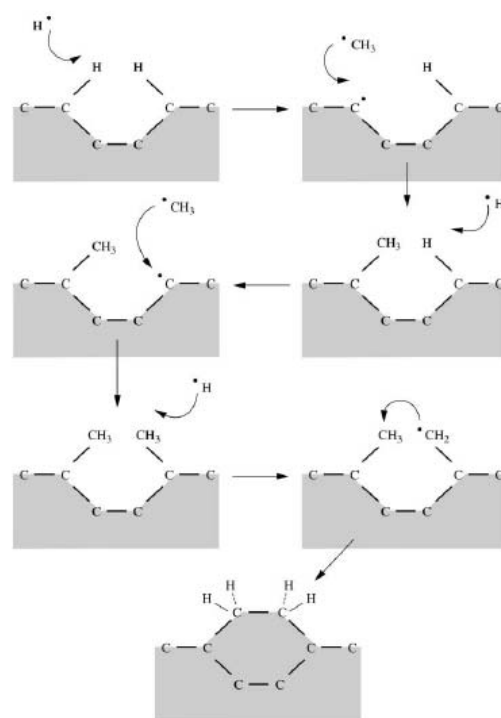


FIGURE 2.14. Diamond growth at a {110} site [21].

**2.1.3. Doping process.** A boron source is usually introduced into the gas-phase for doping of the diamond lattice during its growth, in order to make conductive diamond. Trimethylboron is added to the gas mixture in a concentration between 10 and 10 000 ppm, depending on the desired doping level. In fact, the content of boron in the diamond film is proportional to its content in the gas phase [27]. The resistivity of diamond depends on the boron content and can vary from  $10^4 \Omega \text{ cm}$  ( $10^{18}$  atoms of boron  $\text{cm}^{-3}$ ) to  $10^{-3} \Omega \text{ cm}$  ( $10^{21}$  atoms of boron  $\text{cm}^{-3}$ ). As its resistivity decreases, the dielectric diamond successively acquires the properties of a *p*-type semiconductor and then of a semimetal ( $> 5 \times 10^{20}$  atoms of boron  $\text{cm}^{-3}$ ).

The boron content in the gas phase also determines the texture of the growing film [27]. More particularly, boron appears to stabilise the  $\langle 111 \rangle$  texture; a decrease in growth rate was also noticed and was attributed to a rearrangement to an atomically smooth surface [28].

*n*-Type doping of diamond can be induced by introduction of nitrogen ( $\text{N}_2$ ,  $\text{N}_2\text{O}$ ,  $\text{N}(\text{CH}_3)_3$  and  $\text{NH}_3$ ) into the gas phase. At low nitrogen concentrations the growth rate is enhanced while the film quality remains high. Nitrogen incorporation

into the diamond surface, however, is still difficult to achieve because of the unavoidable formation of HCN that inhibits further diamond growth. Furthermore, a high level of nitrogen in the gas phase strongly decreases the film quality [29].

Recently, successful *n*-type doping has been achieved by using PH<sub>3</sub> as an additive [30]. Small amounts of phosphine enhance the film growth, probably because P deposition onto the filament catalyses hydrogen dissociation. A high PH<sub>3</sub> level and, consequently, an excessive deposition of P onto the filament, to the contrary, could be responsible for the progressive deactivation of the process that was noticed. Relative to these new doping procedures, boron-doped diamond so far remains the best-known diamond material in the electrochemical field, which is due to the excellent reproducibility of film preparation.

**2.1.4. Diamond growth mechanism.** Many papers have been published about gas-phase compositions in different CVD processes, but so far the results have been inconclusive with respect to the mechanism of diamond growth. A mechanism frequently reported is that suggested by Ashfold *et al* [31]. According to this mechanism, the precursor gases (CH<sub>4</sub> and H<sub>2</sub>) are dissociated by the thermal energy of the hot filament. Reactive species diffuse towards the substrate surface where they adsorb to form a carbon film. Under favourable conditions, the film grows as diamond (Fig. 2.13). The activation of the gas is tied to the dissociation of hydrogen molecules into atoms. Atomic hydrogen abstracts an hydrogen atom from the surface of diamond (diamond particles are present on the substrate from the polishing powder) leaving a surface radical. A methyl group then adds to the carbon radicals, and these steps are repeated building up the diamond lattice (Fig. 2.14).

The CVD process in Fig. 2.14 is based on the deposition of less stable diamond and simultaneous etching (or consumption) of the more stable graphite. The mechanism proposed assumes that hydrogen attacks graphite much faster than diamond, in contradiction with the second law of thermodynamics. For this reason another mechanism [32] was considered in which, to solve the paradox, diamond is assumed to nucleate in the gas phase forming charged clusters. Because of surface charge on the substrate, the clusters cannot coagulate but maintain a nanometer size which, in turn, provides a high capillary pressure and contributes to stabilise diamond over graphite. In this case the etching and the deposition are two opposite processes which cannot take place simultaneously.

## 2.2. Hot-filament CVD [21]

The first boron-doped diamond thin film has been synthesised with the HF-CVD technique. The most important aspects of the deposition technique are explained here, giving particular attention to the parameters that are important for preparing the boron-doped diamond samples (BDD) used in the present work.

**2.2.1. The HF-CVD reactor.** The reactor (Fig. 2.15) is a vacuum chamber supplied with a carefully controlled flow of process gases. A heater (1 in Fig. 2.15) is used to keep the sample at the target temperature. The substrate sample (2) sits on the heater a few millimetres away from a filament (3) electrically heated to a temperature usually in excess of 2000 °C. The process gases are a mixture of CH<sub>4</sub> and H<sub>2</sub> containing an appropriate chemical species for providing *p* or *n*-type doping.

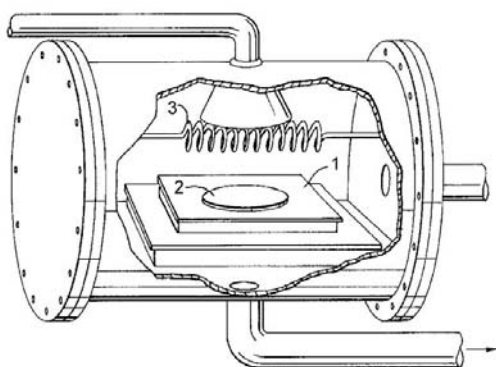


**FIGURE 2.15.** Schematic representations of a hot filament CVD reactor: 1) heater, 2) substrate and 3) filament.

Tungsten is commonly used as a filament material because of its high melting point of 3410 °C and lower costs as compared to other suitable materials such as rhenium (3180 °C) and tantalum (2996 °C). A considerable property of some of these metals is their reactivity with respect to carbon; the carburisation of the filament is a consequence of gaseous specie activation and significantly modifies the physical properties of the filament material. Accordingly, tantalum might be preferred because it forms a carbide with a melting point of 3880 °C and the lowest vapour pressure of all known materials. The role of the filament in the process is not clear so far. The filament acting as an energy supplier or as a catalyst in the dissociation of molecular hydrogen are two of the hypotheses proposed. Redman *et al* [33] suggested that heated hydrogen molecules become adsorbed on the hot filament surface which then promotes the molecular dissociation.



## 2.3. Microwave CVD

In microwave chemical vapour deposition (MW-CVD), synthesis conditions quite similar to those described for HF-CVD are employed. A microwave energy supplier substitutes the hot filament device in activating the carbon-containing gas phase. Different compositions of the gas mixture have been tested. A gas phase composed of 1% CH<sub>4</sub> in H<sub>2</sub> usually is used as the process gas. The deposition is performed at a pressure of 10 - 100 Torr with the substrate at a temperature of around 850-1000 °C. Figure 2.16 schematically illustrates the reactors used in HF-CVD and MW-CVD.

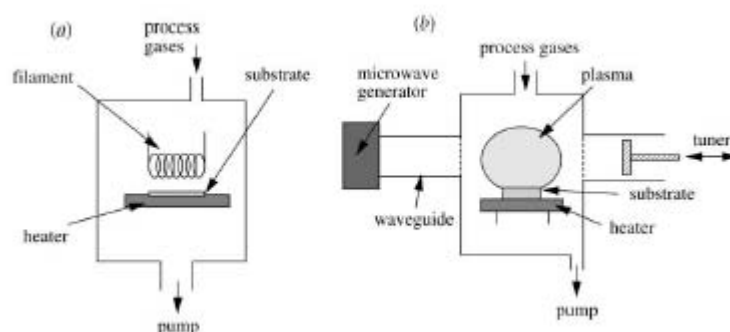


FIGURE 2.16. Schematic representation of two low-pressure CVD reactor: (a) hot-filament and (b) microwave plasma reactor [21].

## 2.4. Electrochemical processes on diamond

Electrochemical studies of diamond were started more than fifteen years ago with the first publication on diamond electrochemistry [34]. After that, work started in Japan, the USA, France and other countries. Over the last few years, the number of publications has increased dramatically. In this Section an attempt will be made to summarise the most important advances in diamond electrochemistry.

**2.4.1. Electrochemical characterisation.** The quality of conducting diamond films usually is investigated by recording the background cyclic voltammetric  $j$ - $E$  curves of the electrodes. In fact, the magnitude of the background current, the working potential window and the features of the curves are sensitive to the presence of non-diamond carbon impurities [35-37]. Typically, high quality diamond film has a flat, featureless voltammetric response in the potential range between -0.3 and 1.2 V vs SHE, with a background current 10 times lower than polished glassy carbon [38, 39, 40 and references therein]. Non-diamond surface impurities are more active than diamond and cause a higher background current. The increased

surface charge density is evident from a larger double-layer charging current [40]. Acid washing, oxygen plasma and other techniques will oxidise the  $sp^2$  carbon and eliminate impurities from the diamond surface without any change in morphology or damage to the microstructure. Cyclic voltammetry can detect  $sp^2$  impurities and their removal with a higher sensitivity than Raman spectroscopy. This is because (i) impurities exist at very low level and are randomly distributed on the surface and (ii) spectroscopic measurements are the average of the response of both subsurface and surface microstructure.

Another important property of high-quality diamond is the wide potential window between hydrogen and oxygen evolution. A total region of around four volts is available within which rather low background currents are recorded.

With its combination of a low background current, an extremely high overvoltage for oxygen and hydrogen evolution, and an extremely high stability, diamond is a suitable material for many industrial applications.

Three classes of electrochemical applications may be identified:

- a. synthesis of chemicals
- b. electroanalysis
- c. destruction of pollutants

The diamond surface is not favourable for adsorption, so that electrochemical processes that involve adsorbed intermediates ( $H_2$ ,  $O_2$  and  $X_2$  evolution) are hindered on diamond. They will require very high overpotentials in order to proceed at an appreciable rate. The wide potential window without electrolyte decomposition and the high stability of diamond allow electrochemical reactions to be carried out at potentials otherwise difficult to reach. Direct synthetic reactions have been carried out, such as the production of ammonia, chlorine,  $Ag^{2+}$  and peroxodisulfate [41-45]. Diamond has been tested in the oxidation of many organic compounds for waste water treatment, and an extremely high current efficiency was obtained [46-49].

The low background currents on diamond lead to an improved signal-to-background ratio as compared with glassy carbon [50, 51]. Stable signals for several redox systems have been detected on diamond, with detection limits as low as a few ppb [47, 52-54]. The linear response found as a function of concentration of the redox system indicates that diamond can be used for analytical purposes [38]. Negligible adsorption phenomena have been found on diamond surfaces for a wide

range of compounds [38 and references therein, 53]. After partial surface fouling, the response of electrodes could be restored by simple electrochemical oxidation without modifying the morphological properties of the polycrystalline film [47, 49]. Anodic oxidation of the surface has been often used as a pretreatment in order to increase the sensitivity, stability and selectivity of the diamond's electrochemical response [38, 55].

#### **2.4.2. Outer-sphere and inner-sphere reactions at diamond electrodes.**

Studies of the behaviour of redox systems on diamond electrodes can yield important information concerning the electrochemical properties of the electrodes. Because of the variations in film composition, morphology, preparation and pretreatment conditions, it has been very difficult so far to compare results from different laboratories. For the same reason, a fundamental understanding of the diamond electrode/electrolyte interface is still lacking.

Modestov et al. focused their studies on the kinetics of the outer-sphere  $\text{Fe}(\text{CN})_6(\text{III})/(\text{II})$  redox system on a diamond electrode material [56, 57]. By Auger measurements, they demonstrated the absence of adsorption phenomena and suggested an increase in the surface-state density on the diamond surface in order to explain an enhancement of the electrochemical reaction rate. They compared the calculated kinetic constants with results obtained by impedance measurements, and correlated the values with the doping level in the electrodes. Surface states which are responsible for increasing metallic properties of the samples were described in terms of boron concentration on the diamond material. The concept of an intrinsic resistivity of the diamond material due to its semiconductor character was introduced to explain the low reaction rate of ferri/ferrocyanide on diamond electrodes.

The effect of the pretreatment was also investigated [58]. In the paper, Granger et Swain pointed out that anodic oxidation of the electrode could cause a deactivation of diamond owing to the introduction of oxygen terminations on the surface. Increasing reversibility of the system after rehydrogenation confirmed a higher activity of the hydrogen-terminated surface and excluded any influence of non-diamond carbon (which is completely removed by anodic oxidation of the surface and not reintroduced by hydrogenation). Electrostatic interactions as well as a possible surface blocking occurring on the oxygen-terminated active sites were proposed as an explanation for deactivation by anodic treatment.

A wide range of boron doping levels in the samples and different conditions used in the preparation of electrodes are found in literature reports. If it is considered that different electrolytes, pH, and concentrations were also used in the experiments, then the discrepancies in observed electrochemical properties of the diamond electrodes are completely justified. The most important factors that can influence the electrochemical behaviour of diamond electrodes could be summarised as follows: the doping type and its concentration, the morphological feature of the crystals, the surface terminations (H, O), and the presence of non-diamond amorphous carbon impurities ( $sp^2$ ).

Other papers have reported investigations of the inner-sphere benzoquinone/hydroquinone system on diamond. This redox reaction is extremely irreversible ( $\Delta E > 1$  V), and it was found to strongly depend on the physical and chemical properties of the diamond surface [57, 59-61].

Generally, outer-sphere processes are insensitive to the nature of the electrode surface, however, in the case of diamond a relation between kinetics and surface treatment was noticed. Furthermore, the kinetic parameters have extremely small values, indicating an extremely slow electron transfer process on diamond. In the case of inner-sphere processes, the irreversibility of the systems is even more important, and a fouling process was also noticed [49] in the potential region of electrolyte stability.

The BDD electrodes are characterised by very slow kinetics of inner-sphere reactions such as  $O_2$  evolution. In fact, very high overpotentials are required for this kind of processes. The very weak bond between the diamond surface and active intermediates (hydroxyl radicals) is the cause of the slow kinetics of this kind of a reaction. However, the weakly bonded hydroxyl radicals are chemically extremely active, and at potentials close to oxygen evolution, the oxidation of organics results in a complete combustion incineration of the organic species. In this potential region all fouling effects are avoided, and a very high current efficiency is obtained.

## **2.5. The oxygen evolution reaction and organic oxidation on ‘non-active’ and ‘active’ electrodes [62]**

It has been found that frequently, electrochemical oxidation of certain organics in aqueous media occurs without any loss of electrochemical activity, only at high potential values, with concomitant evolution of oxygen [63-67]. Furthermore, it has been found that the nature of the electrode material strongly influences, both the selectivity and the efficiency of the process [63, 68-70]. In order to interpret these

observations, a comprehensive model has been proposed [63, 68-70]. This model allows two different cases to be distinguished: ‘non-active’ and ‘active’ anodes.

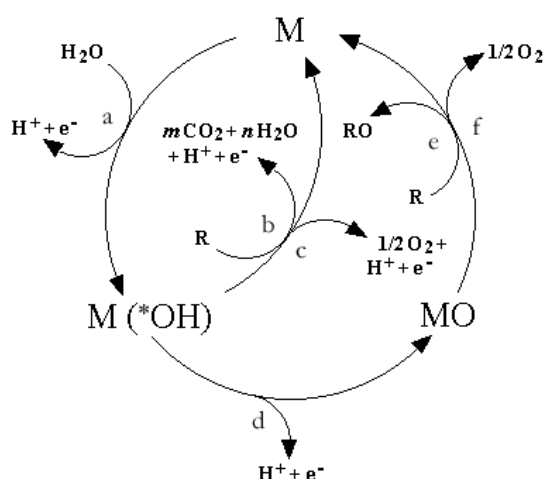


**FIGURE 2.17.** Mechanistic scheme of anodic oxidation of organic compounds with simultaneous oxygen evolution on *non-active* anodes (reactions a, b and e) and on *active* anodes (reactions a, c, d and f). (a) water discharge to hydroxyl radicals,  $\text{OH}^*$ ; (b) combustion of the organic compound,  $\text{R}$ , *via* hydroxyl radicals; (c) oxygen evolution by electrochemical oxidation of hydroxyl radicals; (d) formation of the higher metal oxide,  $\text{MO}$ ; (e) partial (selective) oxidation of the organic compound; (f) oxygen evolution by chemical decomposition of the higher metal oxide.

Figure 2.17 illustrates the reaction scheme in acidic media, where  $\text{M}$  designates an active site at the anode surface. The first step in all cases is the discharge of water molecules to hydroxyl radicals (reaction a). The electrochemical and chemical activity of hydroxyl radicals strongly depends on the nature of the electrode material used. Two extreme classes of electrodes can be defined: ‘non-active’ and ‘active’ anodes.

At ‘non-active’ electrodes there is a weak interaction between electrode  $\text{M}$  and hydroxyl radicals ( $*\text{OH}$ ). In this case the oxidation of organics is mediated by hydroxyl radicals (reaction b in Fig. 2.17 with  $\text{M} = \text{BDD}$ ). This reaction occurs in competition with oxygen evolution by hydroxyl radical discharge (reaction c in Fig. 2.17 with  $\text{M} = \text{BDD}$ ), which occurs without any participation of the anode surface.

At ‘active’ electrodes there is a strong interaction between electrode  $\text{M}$  and hydroxyl radicals ( $*\text{OH}$ ). In this case the hydroxyl radicals may interact with the anode, with a possible transfer of oxygen from the hydroxyl radicals to the anode surface and the formation of so-called higher oxide (reaction d in Fig. 2.17 with  $\text{M} = \text{IrO}_2$ ). The surface redox couple  $\text{MO}/\text{M}$  can act as a mediator in the partial (selective) oxidation of organics (reaction e in Fig. 2.17 with  $\text{M} = \text{IrO}_2$ ). This

reaction occurs in competition with oxygen evolution due to chemical decomposition of the higher oxide (reaction f in Fig. 2.17 with  $M = \text{IrO}_2$ ).

In the following paragraphs, the electrochemical oxidation of organic compounds is examined on diamond and  $\text{IrO}_2$  electrodes in acidic media, these electrodes being examples of 'non-active' and 'active' electrodes, respectively.

**2.5.1. The oxygen evolution reaction and the oxidation of organic substances on 'non-active' diamond electrodes.** Diamond electrodes have been defined as 'non-active' electrodes. In fact, they do not provide any catalytically active site for the adsorption of reactants and/or products in aqueous media. Intermediates such as hydroxyl radicals produced by water decomposition at 'non-active' anodes (reaction a in Fig. 2.17) are considered to be involved in the oxidation of organics in aqueous media. These intermediates are responsible for the electrochemical combustion of the organic compounds (reaction e in Fig. 2.17). The electrochemical activity (overpotential for oxygen evolution) and the chemical reactivity of adsorbed hydroxyl radicals (rate of oxidation of the organic substances by electrogenerated hydroxyl radicals) are strongly related to the strength of interaction between anode (M) and hydroxyl radicals ( $\text{OH}^*$ ). As a general rule, the weaker the M- $\text{OH}^*$  interaction, the lower will be the anode's activity toward oxygen evolution (high overvoltage anodes), and the higher its reactivity for the oxidation of organics (fast chemical reaction).

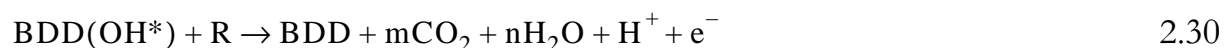
At high anodic potentials close to the potential of water decomposition, the activity of BDD electrodes is considerably enhanced, and there is no evidence for a loss of electrode activity [42, 46, 47, 49, 71]. In the case of aromatic compounds, it has been found that the polymeric film formed in the region of water stability can be destroyed by subjecting the electrode to high anodic potentials ( $E > 2.3 \text{ V vs SHE}$ ) in the region of  $\text{O}_2$  evolution. This treatment can restore the electrode's activity. In fact, the applied potential is located in the region of water discharge at BDD electrodes, and this involves the production of reactive intermediates (hydroxyl radicals,  $\text{OH}^*$ ) which oxidise the polymeric film on the anode surface.

A model has been developed [48, 63, 68-70] to describe the combustion of organics (R) on BDD anodes. It assumes that both the oxidation of organics and the oxygen evolution reaction take place exclusively through mediation by hydroxyl radicals, *i.e.* the electrode itself does not exhibit any 'active' character. This assumption simplifies the general mechanism presented above (Fig. 2.17), so that a reaction scheme involving three different reactions is obtained.

The first reaction is the electrochemical discharge of water leading to hydroxyl radical formation (reaction a, Fig 2.17):



These hydroxyl radicals are then consumed by two competing reactions: combustion of organics (reaction b in Fig. 2.17 with  $M = \text{BDD}$ ):



and oxygen evolution (reaction c in Fig. 2.17 with  $M = \text{BDD}$ ):



Dioxygen very probably also participates in the combustion of organics according to the following reaction scheme:

1) Formation of organic radicals,  $\text{R}^*$ , by a dehydrogenation mechanism:



2) Reaction of the organic radical with dioxygen:



3) Further abstraction of a hydrogen atom with the formation of an organic hydroperoxide ( $\text{ROOH}$ ):



Since the organic hydroperoxides are relatively unstable, decomposition of such intermediates often leads to molecular breakdown and formation of subsequent intermediates with lower carbon numbers. These scission reactions continue rapidly until the organic substance has been completely transformed to  $\text{CO}_2$  and  $\text{H}_2\text{O}$ .

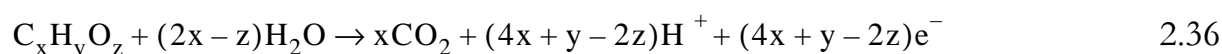
A kinetic model can be developed for this reaction scheme by making the following further assumptions: (i) adsorption of the organic compounds at the electrode surface is negligible; (ii) the overall rate of electrochemical combustion of organics (involving hydroxyl radicals and the formation of hydroperoxide) is a fast reaction and is controlled by mass transport of organics to the anode surface. Under

these conditions, the limiting current density of electrochemical combustion of a given organic compound can be described by the equation:

$$j_{lim} = n \cdot F \cdot k_m \cdot C \quad 2.35$$

where  $j_{lim}$  ( $A\ m^{-2}$ ) is the limiting current density of the combustion of organics,  $n$  is the number of electrons,  $F$  is the Faraday constant ( $C\ mol^{-1}$ ),  $k_m$  is the mass transport coefficient ( $m\ s^{-1}$ ), and  $C$  is the concentration in solution ( $mol\ m^{-3}$ ).

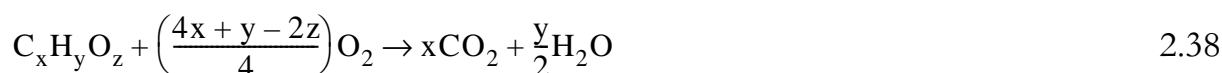
For the combustion of a generic organic compound, the number of electrons exchanged can be calculated by considering the following reaction:



Replacing the value of  $n = (4x+y-2z)$  in Equation 2.35, the limiting current will become:

$$j_{lim} = (4x + y - 2z) \cdot F \cdot k_m \cdot C \quad 2.37$$

From the equation for the chemical combustion of organic compounds (reaction 2.38):



the relation between the concentration of the organic substance ( $C_xH_yO_z$ ,  $mol\ m^{-3}$ ) and the chemical oxygen demand ( $O_2$ ,  $mol\ m^{-3}$ ) is obtained:

$$C = \frac{4}{(4x + y - 2z)} COD \quad 2.39$$

From Equations 2.37 and 2.39, the limiting current density of the combustion of organics can be related to the COD value at any time during electrolysis:

$$j_{lim}(t) = 4 \cdot F \cdot k_m \cdot COD(t) \quad 2.40$$

At the beginning of electrolysis ( $t = 0$ ), the initial limiting current density is given by:

$$j_{lim}^0 = 4 \cdot F \cdot k_m \cdot COD^0 \quad 2.41$$

where  $COD^0$  is the initial value of COD.



Working under galvanostatic conditions, two different operating regimes can be identified:

$$j < j_{lim} \text{ for reactions controlled by the applied current}$$

$$j > j_{lim} \text{ for reactions under mass transport control}$$

*Electrolysis under current control*

In this operating regime, the current efficiency is 100% while the rate of COD removal is constant and can be expressed as:

$$r = \alpha j_{lim}^0 / 4F \tag{2.42}$$

where the parameter  $\alpha$  is a dimensionless term defined as:

$$\alpha = j / j_{lim}^0 \quad \text{with} \quad 0 < \alpha < 1 \tag{2.43}$$

Using Equation 2.41, the constant rate of COD removal (Eq. 2.42) can be expressed as

$$r = \alpha k_m COD^0 \tag{2.44}$$

To describe COD as a function of time, the mass balance over the electrochemical cell and the reservoir of a batch-recirculated reactor system considered (Fig. 2.18).

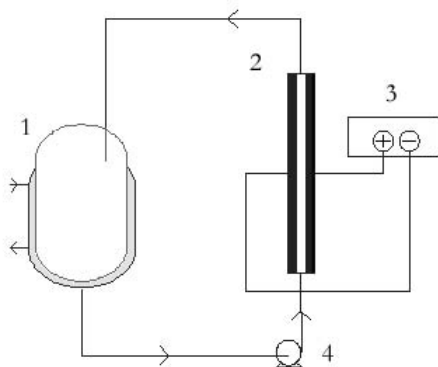


**FIGURE 2.18.** Electrochemical setup: (1) thermoregulated reservoir, (2) electrochemical flow-through cell, (3) current supply and (4) magnetic pump.

Since the volume of the electrochemical reactor ( $V_E$ ) is much smaller than the reservoir volume ( $V_R$ ), the mass balance for COD in the electrochemical cell can be calculated by:

$$\dot{V}COD_{out} = \dot{V}COD_{in} - \alpha Ak_m COD^0 \quad 2.45$$

where  $\dot{V}$  is the flow rate ( $\text{m}^3 \text{s}^{-1}$ ) through the electrochemical cell,  $COD_{in}$  and  $COD_{out}$  are the chemical oxygen demand ( $\text{O}_2$ ,  $\text{mol m}^{-3}$ ) at the inlet and outlet of the reactor, respectively, and  $A$  is the anode surface area ( $\text{m}^2$ ). For a well mixed reservoir, the mass balance for COD is:

$$\dot{V}(COD_{out} - COD_{in}) = \dot{V} \cdot \frac{dCOD_{in}}{dt} \quad 2.46$$

where outlet and inlet are referred to the electrochemical cell. Obviously the inlet of the cell means the outlet of the reservoir and *vice versa* (Fig. 2.18). Combining Equations 2.45 and 2.46 and writing  $COD_{in}$  as a function of time, the following equation is obtained:

$$\frac{dCOD}{dt} = -\frac{\alpha Ak_m COD^0}{V_R} \quad 2.47$$

Remembering that  $COD(t=0) = COD^0$ , the integration of Eq. 2.47 between the limits of 0 and  $t$  gives:

$$COD(t) = COD^0 \left( 1 - \frac{\alpha \cdot A \cdot k_m}{V_R} \cdot t \right) \quad 2.48$$

This behaviour persists up to a critical time  $t_{cr}$  corresponding to the time at which the applied current density is equal to the limiting current density ( $j = j_{lim}$ )

At the critical time, the COD critical value can be calculated from:

$$COD_{cr} = \alpha \cdot COD^0 \quad 2.49$$

A critical time of  $t_{cr} = \frac{1-\alpha}{\alpha} \cdot \frac{V_R}{A \cdot k_m}$  is obtained.

*Electrolysis under mass transport control*

When the applied current exceeds the limiting current, a secondary reaction (oxygen evolution) takes place resulting in a decrease of the instantaneous current efficiency, ICE:

$$ICE = \frac{j_{lim}}{j} = \frac{COD(t)}{\alpha \cdot COD^0} \quad 2.50$$

This regime is possible in two cases:

- (i) at  $j < j_{lim}^0$  ( $\alpha < 1$ ), when the electrolysis is continued beyond the critical time, or
- ii) at  $j > j_{lim}^0$  ( $\alpha > 1$ ), when the applied current density is higher than the initial limiting current density.

In these cases, the *COD* mass balances on the electrochemical cell and on the reservoir can be expressed as:

$$\frac{dCOD}{dt} = -\frac{A k_m COD}{V_R} \quad 2.51$$

Integration of this equation with the initial conditions of (i)  $COD = \alpha COD^0$  at a time  $t = t_{cr}$  and (ii)  $COD = COD^0$  at a time  $t = 0$  leads to

$$(i) \quad COD(t) = \alpha COD^0 \cdot \exp\left(-\frac{A \cdot k_m}{V_R} \cdot t + \frac{1 - \alpha}{\alpha}\right) \quad 2.52.a$$

$$(ii) \quad COD(t) = COD^0 \cdot \exp\left(-\frac{A \cdot k_m}{V_R} \cdot t\right) \quad 2.52.b$$

From Equations 2.50 and 2.49, the instantaneous current efficiency, ICE, is given by:

$$(i) \quad ICE = \exp\left(-\frac{A \cdot k_m}{V_R} \cdot t + \frac{1 - \alpha}{\alpha}\right) \quad 2.53.a$$

$$(ii) \quad ICE = \frac{1}{\alpha} \cdot \exp\left(-\frac{A \cdot k_m}{V_R} \cdot t\right) \quad 2.53.b$$

The model developed yields predictions of ICE and COD as functions of time during the oxidation of organic compounds. The predictive power of the model has

---

been confirmed by preparative electrolysis of different classes of organic compounds such as phenol [48, 72], 4-chlorophenol [49], 3-methylpyridine [42] and polyacrylates [73]. Table 2.2 summarises the most important equations in the form in which they will be used in the following chapters.

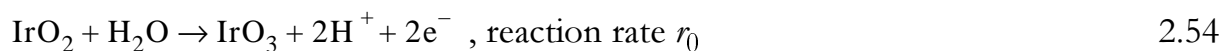
**TABLE 2.2.** Equations describing COD and ICE as functions of time during oxidation at BDD electrodes.  $COD^0 = COD(t = 0)$  (mol  $O_2$   $m^{-3}$ );  $V_R$ : reservoir volume ( $m^3$ );  $k_m$ : mass transport coefficient ( $m\ s^{-1}$ );  $A$ : electrode area ( $m^2$ );  $\alpha = j/j_{lim}$ ,  $t_{cr} = [(1 - \alpha)/\alpha] \cdot (V_R/Ak_m)$ .

	Instantaneous Current Efficiency ICE	Chemical Oxygen Demand COD( $t$ )
$j < j_{lim}$		
$t < t_{cr}$ current control	1	$COD^0 \left( 1 - \frac{\alpha \cdot A \cdot k_m}{V_R} \cdot t \right)$
$t > t_{cr}$ mass transport control	$\exp\left(-\frac{A \cdot k_m}{V_R} \cdot t + \frac{1 - \alpha}{\alpha}\right)$	$\alpha COD^0 \cdot \exp\left(-\frac{A \cdot k_m}{V_R} \cdot t + \frac{1 - \alpha}{\alpha}\right)$
$j > j_{lim}$ mass transport control	$\frac{1}{\alpha} \cdot \exp\left(-\frac{A \cdot k_m}{V_R} \cdot t\right)$	$COD^0 \cdot \exp\left(-\frac{A \cdot k_m}{V_R} \cdot t\right)$

**2.5.2. The oxygen evolution reaction and the oxidation of organic substances on ‘active’  $IrO_2$  electrodes.** The oxygen evolution reaction proceeds at metal oxide electrodes with kinetics dependent on solvent properties and on electrode surface treatment. It has been found that the electrochemical oxidation of organics in aqueous media will occur without any loss in electrode activity, only at high potentials with concomitant evolution of oxygen. It has further been found that the nature of the electrode material strongly influences, both the selectivity and the efficiency of the process. In order to interpret these observations, a comprehensive model [63, 68-70] has been proposed for the anodic oxidation of organics in acidic media including a competition with oxygen evolution (Fig. 2.17). This model allows a distinction to be made between two limiting cases: ‘active’ and ‘non-active’ anodes. Metal oxides such as  $IrO_2$  are classified as active electrode materials. They have a high electrocatalytic activity towards inner-sphere reactions

such as O<sub>2</sub> evolution occurring at rather low overpotentials. This is due to the strong bond that exists between the metal oxide and the reaction intermediates (hydroxyl radicals), and facilitates the initial water discharge process. The active intermediates formed have a rather low chemical activity, however, because of their strong interaction with the electrode surface. In the potential range close to the oxygen evolution overpotential, therefore, the electrochemical oxidation of organic compounds proceeds with a rather low instantaneous current efficiency, and the process is a partial oxidation of the organics rather than a complete combustion to CO<sub>2</sub> and water. A kinetic model has been developed [63, 68-70] to account for these phenomena.

In this model describing the oxidation of organics (R), it is assumed that both the oxidation of these organics and oxygen evolution exclusively proceed through mediation by the same surface sites, of the IrO<sub>3</sub> type; *i.e.* the electrode does not exhibit any ‘non-active’ character [69, 74]. This assumption simplifies the general mechanism presented above (Fig. 2.17), so that a reaction scheme involving three different reactions is obtained. The first reaction, consisting of two consecutive steps, is an electrochemical oxidation leading to the formation of the active species IrO<sub>3</sub> by discharge of water. Excluding all other reactions of the intermediates on IrO<sub>2</sub> (\*OH), the overall equation for this reaction can be formulated (reaction d in Fig. 2.17 with M = IrO<sub>2</sub>):



The active IrO<sub>3</sub> species is then consumed by two competing reactions: the selective oxidation of the organic compound (reaction e in Fig. 2.17 with M = IrO<sub>2</sub>):



and the side reaction of oxygen evolution (reaction f in Fig. 2.17 with M = IrO<sub>2</sub>):



both regenerating active electrode sites.

A kinetic model can be developed for this simplified reaction scheme by making the following further assumptions: (i) adsorption of all organic compounds (both R and RO) at the electrode surface is negligible; (ii) the oxidation reaction of the organics (reaction 2.55) is first order with respect to both the organics (R) and the active species (IrO<sub>3</sub>); (iii) the reaction of oxygen evolution (reaction 2.56) is first order with respect to IrO<sub>3</sub> [69, 74]. Under galvanostatic conditions, the rate of

formation of the active species IrO<sub>3</sub> (reaction 2.54),  $r_0$  (mol m<sup>-2</sup> s<sup>-1</sup>), at the electrode surface is given by the equation:

$$r_0 = \frac{j}{2F} \quad 2.57$$

where  $j$  is the applied current density (A m<sup>-2</sup>),  $F$  is the Faraday constant (C mol<sup>-1</sup>), and 2 is the number of electrons involved. The rate of oxidation of the organic substance (reaction 2.55),  $r_1$  (mol m<sup>-2</sup> s<sup>-1</sup>), can be written as:

$$r_1 = k_1 \theta \Gamma_s C_R^E \quad 2.58$$

where  $k_1$  is the rate constant of this oxidation reaction (m<sup>3</sup> mol<sup>-1</sup> s<sup>-1</sup>),  $\theta$  is the relative surface coverage by IrO<sub>3</sub>,  $\Gamma_s$  is the saturation surface concentration of this species (mol m<sup>-2</sup>), and  $C_R^E$  is the concentration of organic R near the electrode surface (mol m<sup>-3</sup>). The side reaction of oxygen evolution (reaction 2.56) follows the kinetics represented by the equation

$$r_2 = k_2 \theta \Gamma_s \quad 2.59$$

where  $r_2$  is the reaction rate (mol m<sup>-2</sup> s<sup>-1</sup>) and  $k_2$  is the rate constant (s<sup>-1</sup>) of oxygen evolution.

Using the steady-state assumption of  $r_0 = r_1 + r_2$ , the surface coverage by IrO<sub>3</sub> can be formulated as

$$\theta = \frac{j}{2F\Gamma_s(k_1 C_R^E + k_2)} \quad 2.60$$

This expression shows that the surface coverage by the active species depends on the electrode material ( $\Gamma_s$  and  $k_2$ ). At a given anode,  $\theta$  increases linearly with the applied current  $j$  and decreases with increasing reactivity and concentration of the organics ( $k_1$  and  $C_R^E$ ). Obviously, the relative surface coverage has a maximum value of unity, which means that in a given system (electrode material, composition, and nature of electrolyte) the current is limited. The current efficiency  $\eta$  is defined as the fraction of current consumed for oxidation of the organic substance, and can be written in terms of the reaction rates as follows:

$$\eta = \frac{r_1}{r_0} \quad 2.61$$

It can also be expressed as a function of the rate constants and organic concentration, and written in a convenient linear form [69, 74]:

$$\frac{1}{\eta} = 1 + \frac{k_2}{k_1} \cdot \frac{1}{C_R^E} \quad 2.62$$

For a given electrode material, the ratio  $k_2/k_1$  expresses the reactivity of organics to be oxidised: the lower this ratio, the stronger will be the competition of organics against oxygen evolution. It is also seen that an increasing concentration of the organic substance favours its oxidation, resulting in a higher current efficiency.

Equations 2.57 and 2.59, which are formulated as functions of the local concentration of organics at the electrode surface,  $C_R^E$ , are not directly applicable, since the variable is *a priori* unknown. Since adsorption of organics has been neglected in this model, mass transport in the liquid phase will determine the relation between local and bulk concentration.

At steady state, the mass transport rate is equal to the rate of oxidation of the organic substance:

$$k_m(C_R^S - C_R^E) = k_1 \theta \Gamma_S C_R^E \quad 2.63$$

where  $k_m$  is the mass transport coefficient ( $\text{m s}^{-1}$ ) and  $C_R^S$  is the concentration of the organic in the bulk solution. The local concentration is then related to the bulk concentration through the equation:

$$C_R^E = \frac{C_R^S}{1 + \phi} \quad 2.64$$

where the parameter  $\phi$  is defined as:

$$\phi = \frac{k_1}{k_m} \theta \Gamma_S \quad 2.65$$

From Equations 2.62 and 2.64, the following expression of current efficiency as a function of the bulk organic concentration can be obtained [69, 74]:

$$\frac{1}{\eta} = 1 + \frac{k_2}{k_1} (1 + \phi) \frac{1}{C_R^S} \quad 2.66$$

When using equation 2.66, it is important to remember that  $\phi$  depends on the organic concentration.

The model simplifies when concentration polarisation is neglected. In fact, when the rate of oxidation,  $r_1$ , is much lower than that of diffusion of organics towards the anode,  $\phi$  tends to zero and the organic concentration at the electrode is equal to the bulk concentration:  $C_R^E = C_R^S$ . Thus, when plotting the inverse of current efficiency against the inverse of bulk concentration, a straight line with a slope  $k_2/k_1$  is obtained. This provides a suitable experimental method for determining the ratio of the constants, by measuring the current efficiency for oxidation of the organics at different bulk concentrations. The current efficiency can be determined, either by analysing the oxidation products or by measuring the oxygen evolution rate. The effect of mass transport on current efficiency has also been treated assuming a concentration-independent  $\phi$  [69]. This description is limited to low surface coverages by the active species involving a strong limitation of the applicable current density.

---

### 3. References

1. A. J. Bard and L. R. Faulkner, 'Electrochemical methods - Fundamentals and applications', J. Wiley and Sons, Inc., New York, 2001.
2. J. O. M. Bockris, M. A. V. Devanathan, and K. Mueller, *Proc. Phys. Soc. Ser. A*, **274** (1963) 55.
3. F. Beck and H. Schulz, *Electrochim. Acta*, **29** (1984) 1569.
4. R. A. Marcus, *J. Chem. Phys.*, **24** (1956) 966.
5. R. A. Marcus, *Electrochim. Acta*, **13** (1968) 995.
6. R. J. Taylor and A. A. Humffray, *J. Electroanal. Chem.*, **42** (1973) 347.
7. W. J. Blaedel and G. W. Schieffer, *J. Electroanal. Chem.*, **80** (1977) 259.
8. J. Kuta and E. Yeager, *J. Electroanal. Chem.*, **59** (1975) 110.
9. P. Bindra, H. Gerischer, and L. M. Peter, *J. Electroanal. Chem.*, **57** (1974) 435.
10. J. Kawiak, T. Jedral, and Z. Galus, *J. Electroanal. Chem.*, **145** (1983) 163.
11. M. Fleischmann, P. R. Graves, and J. Robinson, *J. Electroanal. Chem.*, **182** (1985) 87.
12. L. Mueller and S. Dietzsch, *J. Electroanal. Chem.*, **121** (1981) 255.
13. R. L. McCreery, in *Interfacial Electrochemistry* (A. Wieckowski, ed.), Marcel Dekker, Inc., New York, 1999, p. 631.
14. J. H. White, M. P. Soriaga, and A. T. Hubbard, *J. Electroanal. Chem.*, **177** (1984) 89.



15. J. H. White, M. P. Soriaga, and A. T. Hubbard, *J. Electroanal. Chem.*, **185** (1985) 331.
16. G. Kokkinidis, *J. Electroanal. Chem.*, **172** (1984) 265.
17. E. Laviron, *J. Electroanal. Chem.*, **164** (1984) 213.
18. Vetter, *Z. Elektrochem.*, **56** (1952) 797.
19. K. Ravichandran and R. P. Baldwin, *Anal. Chem.*, **58** (1984) 1745.
20. L. Mészáros, B. Lengyel, T. Garai, and G. TrabANELLI, *Acta Chim. Hung.*, **127** (1990) 113.
21. S. Ferro, *J. Mater. Chem.*, **12** (2002) 2843.
22. C. V. Burton, *Nature*, **72** (1905) 397.
23. F. P. Bundy, *J. Chem. Phys.*, **38** (1963) 631.
24. S. Matsumoto, Y. Sato, M. Tsutsumi, and N. Setaka, *J. Mater. Sci.*, **17** (1982) 3106.
25. M. Kamo, Y. Sato, S. Matsumoto, and N. Setaka, *J. Cryst. Growth*, **62** (1983) 642.
26. V. Fisher, D. Gandini, S. Laufer, E. Blank, and C. Comninellis, *Electrochim. Acta*, **44** (1998) 521.
27. R. Locher, J. Wagner, F. Fuchs, M. Maier, P. Gonon, and P. Koidl, *Diamond Relat. Mater.*, **4** (1995) 678.
28. D. J. Poferl, N. C. Gardner, and J. C. Angus, *J. Appl. Phys.*, **44** (1973) 1428.
29. B. Atakan, M. Beuger, and K. Kohse-Hoinghaus, *Phys. Chem. Chem. Phys.*, (1999) 705.
30. R. S. Tsang, P. W. May, M. N. R. Ashfold, and K. N. Rosser, *Diamond Relat. Mater.*, **7** (1998) 1651.
31. M. N. R. Ashfold, *Chem. Soc. Rev.* (1994) 21.
32. I.-D. Jeon, C. J. Park, D.-Y. Kim, and N.M.Hwang, *J. Cryst. Growth*, **223** (2001) 6.
33. S. A. Redman, C. Chung, and M. N. R. Ashfold, *Diamond Relat. Mater.*, **8** (1999) 1383.
34. Y. V. Pleskov, A. Y. Sakharova, M. D. Krotova, L. L. Bouilov, and B. V. Spitsyn, *J. Electroanal. Chem.*, **228** (1987) 19.
35. Y. V. Pleskov, *Russ. Chem. Rev.*, **68** (1999) 381.
36. G. M. Swain, A. B. Anderson, and J. C. Angus, *MRS Bull.*, **23** (1998) 56.
37. R. Tenne and C. Lévy-Clément, *Isr. J. Chem.*, **38** (1998) 57.
38. T. N. Rao and A. Fujishima, *Diamond Relat. Mater.*, **9** (2000) 384.
39. I. Duo, P.-A. Michaud, W. Haenni, A. Perret, and C. Comninellis, *Electrochem. Solid-state Lett.*, **3** (2000) 325.
40. M. C. Granger, M. Witek, J. Xu, J. Wang, M. Hupert, A. Hanks, M. D. Koppang, J. E. Butler, G. Lucazeau, M. Mermoux, J. W. Strojek, and G. M. Swain, *Anal. Chem.*, **72** (2000) 3793.

41. S. Ferro, A. D. Battisti, I. Duo, C. Comninellis, W. Haenni, and A. Perret, *J. Electrochem. Soc.*, **147** (2000) 2614.
42. J. Iniesta, P.-A. Michaud, M. Panizza, and C. Comninellis, *Electrochem. Commun.*, **3** (2001) 346.
43. C. Reuben, E. Galun, H. Cohen, R. Tenne, R. Kalish, Y. Muraki, K. Hashimoto, A. Fujishima, J. M. Butler, and C. Lévy-Clément, *J. Electroanal. Chem.*, **396** (1995) 233.
44. M. Panizza, I. Duo, P.-A. Michaud, G. Cerisola, and C. Comninellis, *Electrochem. Solid-state Lett.*, **3** (2000) 550.
45. P.-A. Michaud, C. Comninellis, W. Haenni, A. Perret, and M. Fryda, in *International Patent*, 2001.
46. D. Gandini, E. Mahé, P.-A. Michaud, W. Haenni, A. Perret, and C. Comninellis, *J. Appl. Electrochem.*, **30** (2000) 1.
47. M. Panizza, P.-A. Michaud, G. Cerisola, and C. Comninellis, *J. Electroanal. Chem.*, **507** (2001) 206.
48. M. Panizza, P.-A. Michaud, G. Cerisola, and C. Comninellis, *Electrochem Commun.*, **3** (2001) 336.
49. M. A. Rodrigo, P.-A. Michaud, I. Duo, M. Panizza, G. Cerisola, and C. Comninellis, *J. Electrochem. Soc.*, **148** (2001) D60.
50. R. C. Engstrom and V. A. Strasser, *Anal. Chem.*, **56** (1984) 136.
51. I.-F. Hu, D. H. Karweik, and T. Kuwana, *J. Electroanal. Chem.*, **188** (1985) 59.
52. J. Xu and G. M. Swain, *Anal. Chem.*, **70** (1998) 1502.
53. T. N. Rao, I. Yagi, T. Miwa, D. A. Tryk, and A. Fujishima, *Anal. Chem.*, **71** (1999) 2506.
54. M. D. Koppang, M. Witek, J. Blau, and G. M. Swain, *Anal. Chem.*, **71** (1999) 1188.
55. I. Duo, S. Ferro, A. D. Battisti, and C. Comninellis, in *Catalysis at nanoparticles surfaces* (A. Wieckowski, E. R. Savinova, and C. G. Vayenas, eds.), Marcel Dekker Inc., New York, in press.
56. A. D. Modestov, Y. V. Pleskov, V. P. Varnin, and I. G. Teremetskaya, *Russ. J. Electrochem.*, **33** (1997) 60.
57. A. D. Modestov, Y. E. Evstefeeva, Y. V. Pleskov, V. M. Mazin, V. P. Varnin, and I. G. Teremetskaya, *J. Electroanal. Chem.*, **431** (1997) 211.
58. M. C. Granger and G. M. Swain, *J. Electrochem. Soc.*, **146** (1999) 4551.
59. S. Alehashem, F. Chambers, J. W. Strojek, G. M. Swain, and R. Ramesham, *Anal. Chem.*, **67** (1995) 2812.
60. R. Ramesham and M. F. Rose, *J. Mater. Sci. Lett.*, **16** (1997) 1693.
61. N. G. Ferreira, L. L. G. Silva, E. J. Corat, and V. J. Trava-Airoldi, *Diamond Relat. Mater.*, **11** (2002) 1523.

62. G. Fóti and C. Comninellis, in *Modern Aspects of Electrochemistry*, Vol. 37 (B. E. Conway, R. E. White, and C. G. Vayenas, eds.), Plenum Press, New York, in press.
63. C. Comninellis and A. D. Battisti, *J. Chim. Phys.*, **93** (1996) 673.
64. C. Comninellis and C. Pulgarin, *J. Appl. Electrochem.*, **21** (1991) 703.
65. C. Comninellis and E. Plattner, *Chimia*, **42** (1988) 250.
66. C. Comninellis and C. Pulgarin, *J. Appl. Electrochem.*, **23** (1993) 108.
67. C. Comninellis and A. Nerini, *J. Appl. Electrochem.*, **25** (1995) 23.
68. C. Comninellis, *Electrochim. Acta*, **39** (1994) 1857.
69. O. Simond, V. Shaller, and C. Comninellis, *Electrochim. Acta*, **42** (1997) 2009.
70. G. Fóti, D. Gandini, Ch. Comninellis, A. Perret, and W. Haenni, *Electrochem. Solid-state Lett.*, **2** (1999) 228.
71. L. Gherardini, P.-A. Michaud, M. Panizza, C. Comninellis, and N. Vatistas, *J. Electrochem. Soc.*, **148** (2001) D78.
72. J. Iniesta, P.-A. Michaud, M. Panizza, G. Cerisola, A. Aldaz, and C. Comninellis, *Electrochim. Acta*, **46** (2001) 3573.
73. R. Bellagamba, P.-A. Michaud, C. Comninellis, and N. Vatistas, *Electrochem. Commun.*, **4** (2002) 171.
74. G. Fóti, D. Gandini, and C. Comninellis, *Current Topics in Electrochem.*, **5** (1997) 71.

---

## Results: BDD surface treatment

---

Boron-doped diamond electrodes, both as-grown and polarised anodically under different conditions, were prepared in order to study the chemical and electrochemical changes of diamond and clarify the rule played by the surface-state density. Many different treatments were employed, but only the most relevant results will be presented in this work, *viz.*, those obtained with four kinds of surface treatment: as-grown (BDD<sub>ag</sub>), mildly polarised (BDD<sub>mild</sub>), strongly polarised in perchloric acid (BDD<sub>severe</sub>), and strongly polarised in a sulphuric acid-acetic acid mixture (BDD<sub>AcOH</sub>). Scanning electron microscopy was performed to study crystal structure and surface changes. The O/C ratio was measured by X-ray photoelectron spectroscopy in order to estimate the oxidation level of the surface. The voltammetric charge and the capacitance of the electrodes were calculated to determine the active surface area. Charge transfer processes at the electrode surface were studied by steady-state (polarisation) and dynamic (cyclic voltammetry) potential step methods. Simple electron transfer processes such as the outer-sphere redox system ferri/ferrocyanide (Fe(CN)<sub>6</sub>III/II) and complex charge transfer reactions such as the inner-sphere 1,4-benzoquinone/hydroquinone (Q/H<sub>2</sub>Q) redox reaction were chosen to test the electrochemical properties of the electrodes. The properties of the diamond electrodes were found to undergo strong modification as a function of surface treatment. The active surface area and the reaction rate constants decreased significantly upon anodic polarisation. Important drops in the carrier surface

concentration and in true surface area led to hindrance of electron transfer at the electrode surface.

---

## 1. Introduction

Among the factors that can influence the electrochemical behaviour of boron-doped diamond electrodes, the crystallographic structure [1, 2], the surface functional groups [3-5], the boron doping level [6, 7], and the presence of non-diamond amorphous carbon impurities ( $sp^2$ ) [1, 8] probably are the most important ones [9]. The preparation conditions and the surface treatment have a strong effect on the electrochemical behaviour of diamond electrodes [4, 10, 11]. Many kinds of surface treatment have been used so far, and the resulting changes in electrode properties have been investigated. Anodic polarisation, oxygen plasma oxidation and boiling in strong acid are some of these surface treatment techniques [4, 5, 9-11]. Among all the procedures employed, anodic oxidation is the simplest one. The most evident result of anodic polarisation is an improvement in reproducibility of the electrode's response [12]. For this reason anodic oxidation has been widely used as a surface treatment for the electrochemical investigation of diamond electrodes. Significant changes in crystal morphology have not been found, but the chemical changes occurring on the surface during anodic polarisation are still almost unknown. It was noticed that the background currents recorded in the window of electrolyte stability were higher at untreated diamond electrodes than at prepolarised ones [9], but no specific causes were pointed out to explain this feature. An important effect of the polarisation appears to be the elimination of  $sp^2$  species that can be more or less numerous on the diamond surface, depending on the fabrication conditions. The importance of non-diamond impurities for the electrode's activity is not completely understood as yet. In the present chapter it will be tried to clarify the influence of surface heterogeneity on the electronic properties of the diamond material, and particularly the importance of the  $sp^2$  impurities in electron-transfer reactions.

## 2. Experimental

### *Electrode preparation*

The boron-doped diamond (BDD) thin films employed during this work have been provided by the CSEM in the frame of collaboration with EPFL. Boron-doped diamond electrodes were prepared by hot-filament chemical vapour deposition (HF-CVD, see Chapter 2) on *p*-type, low-resistivity (1 to 3 m $\Omega$  cm), {100} silicon wafers (Siltronix, diameter 10 cm, thickness 0.5 and 1mm). Mainly tantalum has been used at CSEM as filament material. The Tantalum content in the diamond films was estimated to be less than 100 ppb, i.e. at the detectable limit of the measuring techniques like RBS, ERDA and GDOS (Rutherford Backscattering Spectrometry, Elastic Recoil Detection Analysis and Glow Discharge Optical Emission Spectroscopy) due to the fact that TaC has the lowest vapour pressure of all known materials. The distance between the filament and the silicon substrate was adjusted at 20 mm. During the heating of the filament between 2440 and 2560  $^{\circ}\text{C}$ , the temperature of the substrate was monitored from 780 to 870  $^{\circ}\text{C}$ . The process gas was a mixture of 1% CH<sub>4</sub> in H<sub>2</sub> containing trimethylboron (TMB) as a boron source (1 ppm, with respect to H<sub>2</sub>). A gas flow of 5 dm<sup>3</sup> min<sup>-1</sup> was supplied into the chamber while a pressure of 5000 to 10 000 Pa was maintained. Film growth occurred at a rate of 0.24  $\mu\text{m h}^{-1}$ , and polycrystalline films were grown to a thickness of 1  $\mu\text{m}$  with grain size from 200 to 800 nm. The boron/carbon ratio in the diamond films was 4500 to 5500 ppm, corresponding to a concentration of around  $9 \times 10^{20}$  boron atoms cm<sup>-3</sup> (the semiconductor-metal transition occurs at  $2 \times 10^{20}$  cm<sup>-3</sup>). The electrical resistivity,  $\rho$ , was 10-20 m $\Omega$  cm. The HF-CVD process, optimised at CSEM, allows to synthesise very thin diamond films (between 0.1 and 3  $\mu\text{m}$ ), as a result of a highly homogeneous growing. This result could be obtained by pretreating the silicon substrate with alcoholic water suspension of diamond nanoparticles (<10 nm) to reach a nucleation density higher than  $10^{12}$  sites cm<sup>-2</sup>.

As-grown boron-doped diamond electrodes (BDD<sub>ag</sub>) were simply washed once with 2-propanol and twice with Milli-Q water in an ultrasonic bath in order to clean the surface without changing its hydrophobic properties. BDD electrodes polarised under mild conditions were obtained by 30 min of anodic polarisation at 10 mA cm<sup>-2</sup> of as-grown electrodes in 1 M H<sub>2</sub>SO<sub>4</sub> (BDD<sub>mild</sub>). BDD electrodes polarised under severe conditions were obtained by 576 h of anodic polarisation at 1 A cm<sup>-2</sup> of as-grown electrodes in 1 M HClO<sub>4</sub> at 40  $^{\circ}\text{C}$  (BDD<sub>severe</sub>). Similar BDD electrodes polarised under severe conditions were also obtained by 16 h of anodic polarisation at 1 A cm<sup>-2</sup> of as-grown electrodes in 1 M H<sub>2</sub>SO<sub>4</sub> + 3 M CH<sub>3</sub>COOH (AcOH) at 40  $^{\circ}\text{C}$  (BDD<sub>AcOH</sub>).

### *Morphological characterisation*

The surface morphology was characterised by scanning electron microscopy (SEM) using a JEOL JMS-6300-F scanning electron microscope at up to 4000 times magnification. The BDD samples were analysed by x-ray photoelectron spectroscopy (XPS) in order to study the surface changes resulting from anodic treatments. The element analysis was carried out using a Kratos AXIS ULTRA system in order to calculate the O/C ratios on the sample surfaces after anodic treatments. A total area of  $700 \times 300 \mu\text{m}$  was analysed over a thickness of  $50 \div 100$  angstroms using a 15-kV Al-mono as the (monochromatic) x-ray source. Raman spectroscopy was performed with a T64000 Jobin Yvon spectrometer for structural characterisation of the diamond electrodes. Contact angles were measured by a Contact Angle Measuring System G10 (KRUS, D).

### *Electrochemical measurements*

Figure 3.1 shows the components used to accommodate the electrode sample, assure electrical contact, and obtain a geometrically well defined surface area of  $1 \text{ cm}^2$ . The cage was made of teflon (1 and 5), the gasket (4) was made of silicon material. The screws (6) were titanium. The diamond sample (3) was supported on a titanium plate (2) to assure electrical contact. A conventional three-electrode glass cell (0.1 L) was used for voltammetry (Fig. 3.2). The counterelectrode was a platinum spiral. A  $\text{Hg}/\text{Hg}_2\text{SO}_4$ ,  $\text{K}_2\text{SO}_4(\text{sat})$  electrode was used as the reference electrode. All values of potential are reported relative to a standard hydrogen electrode (SHE). Fluka Chemie chemicals and Milli-Q water were used to prepare solutions.

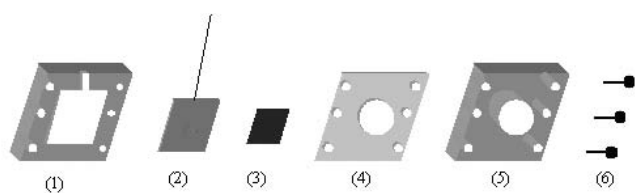


**FIGURE 3.1.** System for housing and mounting the diamond electrodes (3) in the electrochemical measurements. Cage made of teflon (1 and 5), gaskets of silicon material (4); screws (6) and metal support (2) of titanium.

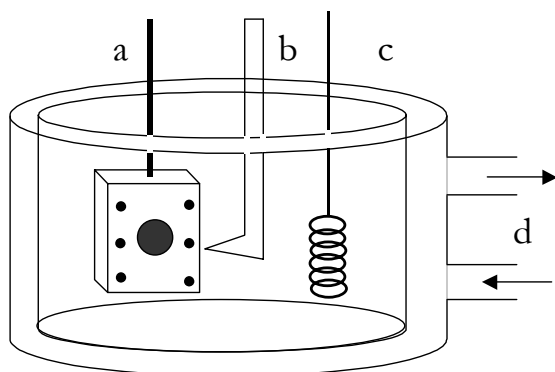


**FIGURE 3.2.** Scheme of a conventional three-electrode electrochemical glass cell: (a) working electrode (BDD), (b) reference electrode (Hg/Hg<sub>2</sub>SO<sub>4</sub>), (c) counter-electrode (Pt), (d) thermostat system.

Cyclic voltammetry and steady-state polarisation were performed with a computer-controlled Autolab PGstat30. Polarisation curves were recorded at 0.1 mV s<sup>-1</sup> over a 10 mV wide range around the equilibrium potential,  $E^{0'}$ , after conditioning the electrodes at the initial potential for 120 seconds.

## 3. Results and discussion

### 3.1. Morphological characterisation

Anodic polarisation is expected to modify the diamond surface in terms of chemical composition, wettability and crystal shape. The techniques of SEM and XPS were used in order to study effects of the treatment on the morphology of the electrode surface.

#### *Scanning electron microscopy (SEM)*

The SEM records showed that the diamond morphology had not changed after mild polarisation. In fact, diamond polarised under mild conditions (BDD<sub>mild</sub>) exhibited exactly the same crystal morphology as that seen at as-grown (BDD<sub>ag</sub>) diamond (Figs. 3.3.A and 3.3.B). After severe polarisation (BDD<sub>severe</sub> and BDD<sub>AcOH</sub>), however, important changes were visible. The colour of the surface had changed from blue to multicoloured (BDD<sub>severe</sub>) or mirrorlike (BDD<sub>AcOH</sub>). It was seen that after severe polarisation (BDD<sub>severe</sub> in Fig. 3.3.C) a diamond film was still present on the surface, but the morphology had completely changed: the



polycrystalline structure of diamond was no longer visible. After severe treatment in the presence of acetic acid ( $\text{BDD}_{\text{AcOH}}$ ), the crystal edges were smoother, and a strong change in crystal shape and size had occurred as the typical result of a polishing process (Fig. 3.3.D).

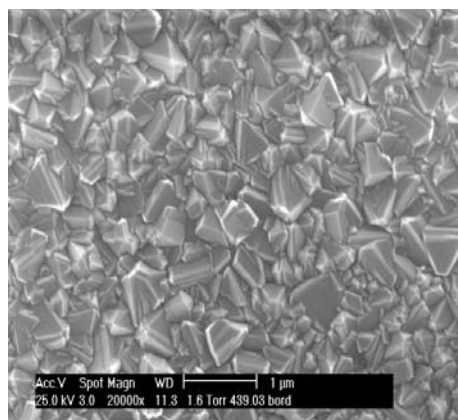


**FIGURE 3.3.A** SEM image of an as-grown BDD electrode ( $\text{BDD}_{\text{ag}}$ ).

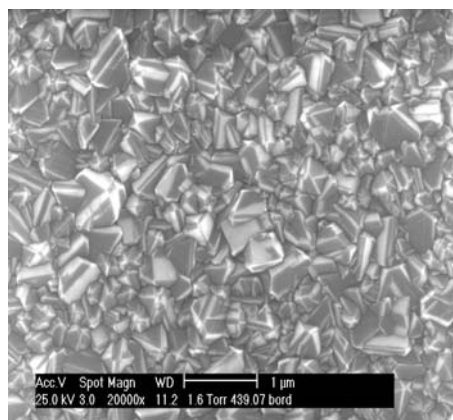


**FIGURE 3.3.B** SEM image of a diamond electrode after 30 min of mild anodic polarisation at  $10 \text{ mA cm}^{-2}$  in  $1 \text{ M H}_2\text{SO}_4$ ;  $T = 25 \text{ }^\circ\text{C}$  ( $\text{BDD}_{\text{mild}}$ ).

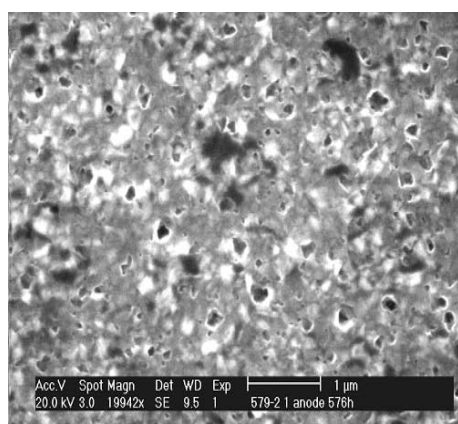


**FIGURE 3.3.C** SEM image of a BDD electrode after 576 h of severe anodic polarisation at  $1 \text{ A cm}^{-2}$  in  $1 \text{ M HClO}_4$ ;  $T = 40 \text{ }^\circ\text{C}$  ( $\text{BDD}_{\text{severe}}$ ).

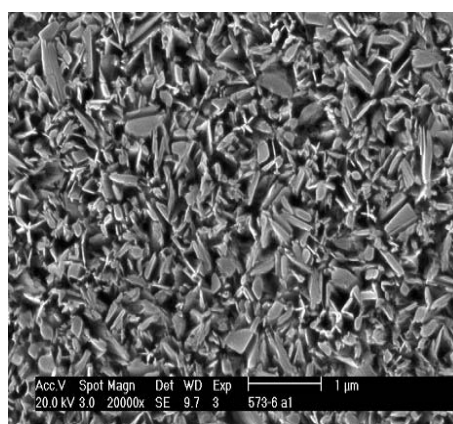


**FIGURE 3.3.D** SEM image of a BDD electrode after 16 h of severe anodic polarisation at  $1 \text{ A cm}^{-2}$  in  $1 \text{ M H}_2\text{SO}_4 + 3 \text{ M CH}_3\text{COOH}$ ;  $T = 40 \text{ }^\circ\text{C}$  ( $\text{BDD}_{\text{AcOH}}$ ).

### X-ray photoelectron spectroscopy (XPS) and contact angle measurements

Contact angle and XPS measurements were performed at all electrodes prepared in order to quantify the wettability of the samples and correlate it with the

O/C surface ratio (atomic %). Table 3.1 shows results for the oxygen/carbon ratio and the contact angles found after different treatments.

**TABLE 3.1.** Oxygen/carbon ratios and water contact angles found at BDD electrodes after different treatments.

Electrode	Oxygen/carbon	Contact angle (°)
BDD <sub>ag</sub>	0.08	102.5
BDD <sub>mild</sub>	0.22	57
BDD <sub>severe</sub>	0.26	53
BDD <sub>AcOH</sub>	2.06	76

Mild anodic polarisation (BDD<sub>mild</sub>) led to an increase in the oxygen/carbon ratio due to the introduction of oxygen-terminated functional groups on the diamond surface. Contact angle measurements by the goniometry technique were also made to characterise the solid/water interactions. Water on an as-grown diamond (BDD<sub>ag</sub>) had a contact angle higher than 90° and typical of a nonwetable material. Oxygen introduced by anodic polarisation increased the wettability of the surface, as shown by the decrease of the contact angle of water from BDD<sub>ag</sub> to BDD<sub>mild</sub>. The contact angle did not change significantly when going from BDD<sub>mild</sub> to a strong polarised diamond (BDD<sub>severe</sub>). Because of the relation between wettability and oxygen coverage, one can deduce that after mild polarisation already, the surface was completely oxidised and a severe polarisation treatment (BDD<sub>severe</sub>) could not increase the oxygen level any further. Quite different behaviour was the seen at BDD<sub>AcOH</sub>: the O/C ratio increased by one order of magnitude. The strong decrease in the carbon signal relative to the oxygen peak indicated a strong change in surface composition and morphology of the samples. The higher contact angle, in fact, indicated a higher degree of smoothness typical of a polished surface.

### *Raman spectroscopy*

Raman spectra were recorded for as-grown (BDD<sub>ag</sub>), mildly polarised (BDD<sub>mild</sub>), and severely treated (BDD<sub>severe</sub>) diamond (Fig. 3.4) for a crystallographic characterisation of the samples. The spectra were normalised to the diamond peak in order to be able to compare Raman intensity features.

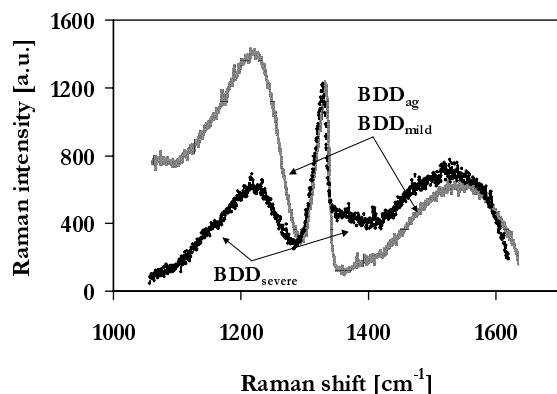


**FIGURE 3.4.** Raman spectra of as-grown ( $BDD_{ag}$ ) and mildly polarised ( $BDD_{mild}$ ) diamond as well as of diamond electrodes after severe polarisation ( $BDD_{severe}$ ).

The spectra revealed a one-phonon band at  $1332\text{ cm}^{-1}$  corresponding to the crystalline boron-doped diamond [6, 7, 13-16]. A wide band centred at  $1500\text{ cm}^{-1}$  was attributed to disordered graphite [16]. The Raman band centred at around  $1200\text{ cm}^{-1}$  represented a Fano-type interference resulting from degeneration of the diamond Fermi level within the valence band for high doping levels [6, 7, 14-16]. In fact, the boron concentration of  $BDD_{ag}$  electrodes was quite high, around  $10^{20}$ - $10^{21}$  atoms boron  $\text{cm}^{-3}$ . After mild polarisation ( $BDD_{mild}$ ) no changes were found in the Raman spectrum. To the contrary, large changes were recorded after severe polarisation. It can be seen in Figure 3.4 that the band at  $1200\text{ cm}^{-1}$  strongly decreased in the case of  $BDD_{severe}$  electrodes. The full width at half maximum (FWHM) of the peak ( $19.26\text{ cm}^{-1}$ ) did not change with the treatment, however, indicating some nonmodified quality of the film. A progressive decrease in charge carrier surface density appears to be the result of anodic treatments.

#### *Roughness factor and true surface area of BDD*

The SEM images were also used to estimate the true surface areas and roughness factors of BDD electrodes. Some approximation was made on the basis of the image obtained on a silicon substrate (Fig. 3.5).

For calculations, cubic and octahedral geometric shapes were chosen to represent the diamond crystals. The calculated roughness factor for diamond was around 5. This value corresponds to that found in the literature [17]. The same roughness factor value was calculated for  $BDD_{mild}$  electrodes, because the morphology of electrodes had not changed (Fig. 3.3.B). In case of severely treated electrodes ( $BDD_{severe}$ ) the polycrystalline structure of diamond was no longer visible and a roughness factor of around 1 was calculated. The roughness factor for

BDD<sub>AcOH</sub> electrodes also was considered equal to 1 because of the small crystal size.

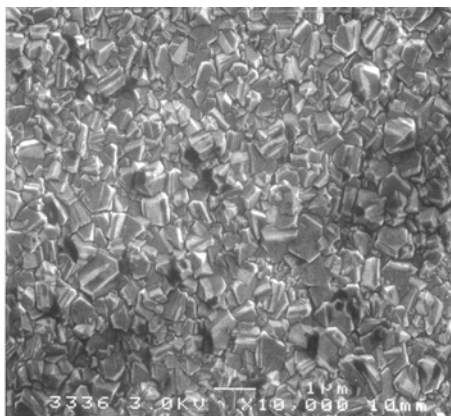


**FIGURE 3.5.** SEM image of a polycrystalline boron-doped diamond (BDD<sub>ag</sub>).

### 3.2. Surface redox processes on BDD surfaces

Cyclic voltammetry performed at the potentials of electrolyte stability provides an *electrochemical spectrum* of the surface redox transitions and is a measure of activity of the electrode surface. The diamond's behaviour was tested by cyclic voltammetry in 0.5 M H<sub>2</sub>SO<sub>4</sub>. The electrochemical response of the electrodes varied as a function of surface treatment (Figs. 3.6.A and 3.6.B). Untreated electrodes (BDD<sub>ag</sub>) exhibited the highest surface activity. The voltammogram revealed many surface redox transitions represented by overlapping current waves in the voltammetric curve (Fig. 3.6.A). The electrode's response decreased significantly after mild anodic polarisation. In fact, the voltammetric response of BDD<sub>mild</sub> electrodes revealed a decrease of surface activity, and only one well-defined irreversible pair of peaks was still visible (Fig. 3.6.B), probably to be attributed to surface redox functions. The peak current decreased and the irreversibility of the surface redox couple increased with increasing severity of the treatment (BDD<sub>severe</sub>). The lowest activity was recorded after the treatment in the presence of AcOH (BDD<sub>AcOH</sub>) (Fig. 3.6.B).

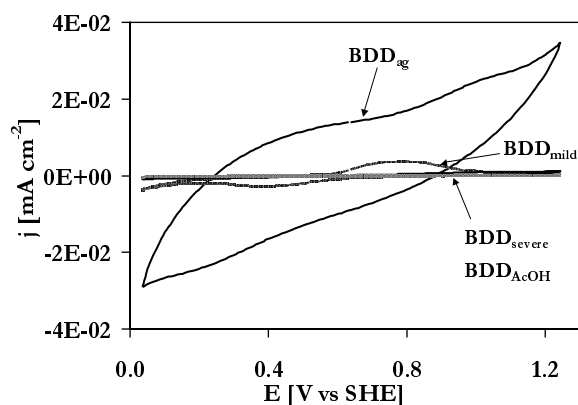


**FIGURE 3.6.A** Cyclic voltammograms of BDD electrodes in 0.5 M  $\text{H}_2\text{SO}_4$ . Scan rate  $0.05 \text{ V s}^{-1}$ ;  $T = 25 \text{ }^\circ\text{C}$ .

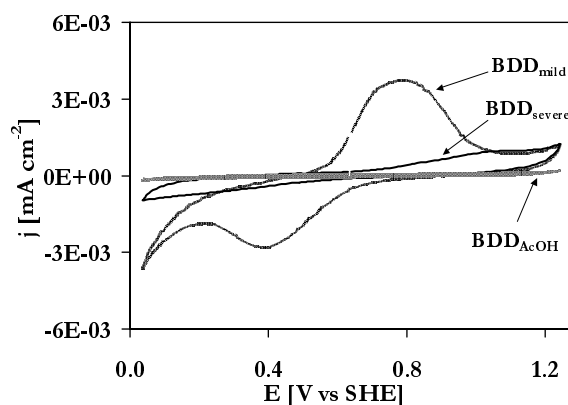


**FIGURE 3.6.B** Cyclic voltammograms of BDD electrodes in 0.5 M  $\text{H}_2\text{SO}_4$ . Scan rate  $0.05 \text{ V s}^{-1}$ ;  $T = 25 \text{ }^\circ\text{C}$ . Zoom of Fig. 3.6.A.

Cyclic voltammograms were recorded for all electrodes at different scan rates (Figs. 3.7.A to 3.7.D). The current did not increase as a linear function of scan rate, indicating the presence of irreversible redox surface processes [18]. The peak separation,  $\Delta E_p$ , increased with increasing severity of the treatment while the peak currents decreased.

From the measurements, the voltammetric charge was calculated at different scan rates as the integral of the anodic part of the voltammogram. The values of charge, which are a measure of surface activity of the electrodes, are shown in Table 3.2. If the voltammetric charge of  $\text{BDD}_{\text{AcOH}}$  electrodes is supposed to represent the activity of a totally clean diamond surface, then charge values normalized to the charge of  $\text{BDD}_{\text{AcOH}}$  ( $C_x/C_{\text{AcOH}}$ ) will provide a measure of active surface area of the electrodes. This ratio attains values higher than 200 for the  $\text{BDD}_{\text{ag}}$  electrodes (Table 3.2). This should be due to the presence of functional groups electrochemically active on the electrode surface. A first treatment would eliminate part of these surface groups while reducing the surface activity ( $\text{BDD}_{\text{mild}}$ ). A further, severe treatment then reduces the electrode's activity ( $\text{BDD}_{\text{severe}}$  and  $\text{BDD}_{\text{AcOH}}$ ) very significantly. The difference in voltammetric charge between the last two electrodes is related to changes in surface roughness resulting from the treatment (SEM images in Fig. 3.3), rather than to a different chemical modification of surface composition.

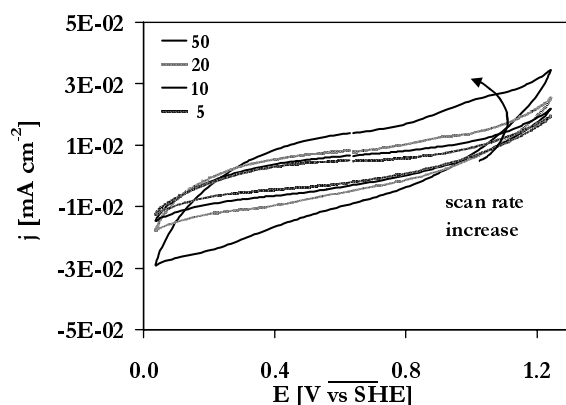


**FIGURE 3.7.A** Cyclic voltammograms of a  $\text{BDD}_{\text{ag}}$  electrode in 0.5 M  $\text{H}_2\text{SO}_4$  at different scan rates [ $\text{mV s}^{-1}$ ].  $T = 25\text{ }^\circ\text{C}$ .

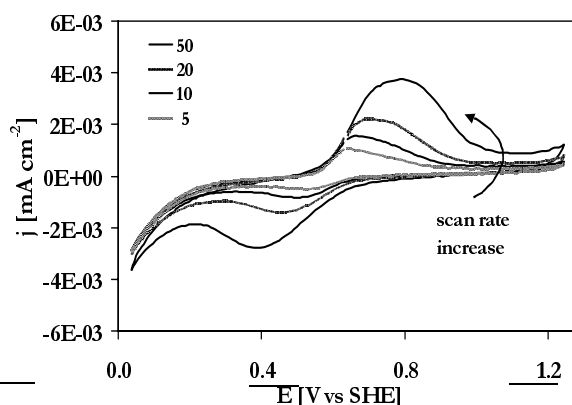


**FIGURE 3.7.B** Cyclic voltammograms of a  $\text{BDD}_{\text{mild}}$  electrode in 0.5 M  $\text{H}_2\text{SO}_4$  at different scan rates [ $\text{mV s}^{-1}$ ].  $T = 25\text{ }^\circ\text{C}$ .

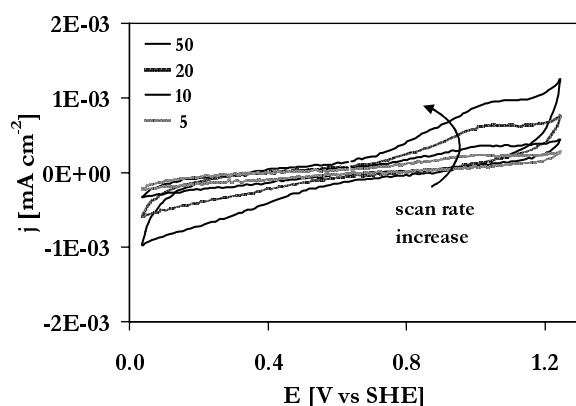


**FIGURE 3.7.C** Cyclic voltammograms of a  $\text{BDD}_{\text{severe}}$  electrode in 0.5 M  $\text{H}_2\text{SO}_4$  at different scan rates [ $\text{mV s}^{-1}$ ].  $T = 25\text{ }^\circ\text{C}$ .

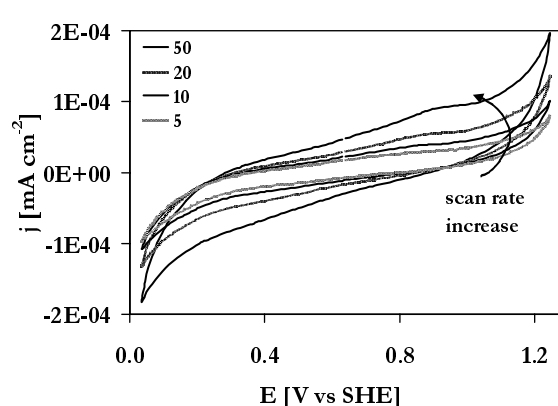


**FIGURE 3.7.D** Cyclic voltammograms of a  $\text{BDD}_{\text{AcOH}}$  electrode in 0.5 M  $\text{H}_2\text{SO}_4$  at different scan rates [ $\text{mV s}^{-1}$ ].  $T = 25\text{ }^\circ\text{C}$ .

By cyclic voltammetry, the double-layer capacitance,  $C_{\text{dl}}$ , can also be estimated (Eq. 3.1). Values of double-layer capacitance calculated via the total (anodic and cathodic) currents,  $i$ , as functions of the scan rate,  $\nu$ , are shown in Table 3.3 for different applied potentials. These values refer to the electrode's geometric surface area ( $1\text{ cm}^2$ ).

**TABLE 3.2.** Voltammetric charge and active surface ratio for BDD electrodes after different treatments. Values refer to the electrode's geometric surface area of  $1\text{cm}^2$ . Electrolyte:  $0.5\text{ M H}_2\text{SO}_4$ .  $T = 25\text{ }^\circ\text{C}$ .

Electr.	$5\text{ mV s}^{-1}$		$10\text{ mV s}^{-1}$		$20\text{ mV s}^{-1}$		$50\text{ mV s}^{-1}$	
	C $\text{mC cm}^{-2}$	$C_x/C_{\text{AcOH}}$	C $\text{mC cm}^{-2}$	$C_x/C_{\text{AcOH}}$	C $\text{mC cm}^{-2}$	$C_x/C_{\text{AcOH}}$	C $\text{mC cm}^{-2}$	$C_x/C_{\text{AcOH}}$
<b>BDD<sub>ag</sub></b>	1.5	238	$9.1 \times 10^{-1}$	236	$5.6 \times 10^{-1}$	222	$3.7 \times 10^{-1}$	244
<b>BDD<sub>mild</sub></b>	$1.2 \times 10^{-1}$	19	$7.3 \times 10^{-2}$	19	$4.8 \times 10^{-2}$	19	$3.2 \times 10^{-2}$	21
<b>BDD<sub>severe</sub></b>	$4.7 \times 10^{-2}$	7	$2.4 \times 10^{-2}$	6	$1.8 \times 10^{-2}$	7	$9.3 \times 10^{-3}$	6
<b>BDD<sub>AcOH</sub></b>	$6.3 \times 10^{-3}$	1	$3.8 \times 10^{-3}$	1	$2.5 \times 10^{-3}$	1	$1.5 \times 10^{-3}$	1

$$i_c = 2C_{dl} v \quad 3.1$$

The capacitance values vary with potential because of the presence of surface redox systems active at different values of potential. Following a severe treatment of the electrodes the capacitance values decreased significantly, and became almost potential independent. The capacitance of the BDD<sub>ag</sub> electrode/solution interface was much higher than the values found in the literature for a double-layer capacitance ( $10$  to  $40\text{ }\mu\text{F cm}^{-2}$ ) [19]. After anodic polarisation (BDD<sub>mild</sub>) the calculated capacitance was one order of magnitude lower than in the case of fresh electrodes. Severe polarisation processes led to an important further capacitance decrease at the interface (BDD<sub>severe</sub> and BDD<sub>AcOH</sub>). A strong change in the surface morphology is responsible for the activity decrease seen at BDD<sub>severe</sub> and BDD<sub>AcOH</sub> electrodes (Table 3.3). A true surface area five times larger than the geometric one was calculated for fresh diamond electrodes, and is attributed to the polycrystalline structure of the film (see § 3.1). After oxidising treatments the true surface area decreased significantly, as shown by the SEM images (Figs. 3.3.A to 3.3.D). The changes in capacitance occurring as a result of treatments have already been emphasized for BDD electrodes, but no explanation was found so far [9]. The very low capacitance values obtained for strongly treated BDD electrodes indicate that surface redox transitions were eliminated from the diamond surface, and only a true double-layer capacitance ( $C_{dl} = 10\text{ }\mu\text{F cm}^{-2}$ ) due to the charge distribution at the electrode/electrolyte interface can be calculated. Thus, in the case of BDD<sub>ag</sub> and

BDD<sub>mild</sub> electrodes, the capacitance values contain contributions of a true double-layer capacitance and of a pseudocapacitance associated with surface redox systems. To explain this behaviour, a nonnegligible amount of graphite ( $sp^2$ ) impurities may be assumed to be present on the surface of fresh electrodes (BDD<sub>ag</sub>). In fact, redox equilibria could exist and generate such a high electrode activity, only in the presence of unsaturated carbon bonds on the diamond surface. The fact that the capacitance value found for BDD<sub>AcOH</sub> electrodes is similar to that of a diamond single crystal ( $1 \mu\text{F cm}^{-2}$ ), on which no impurities are supposed to be present [9, 20], is an argument supporting the progressive elimination of the  $sp^2$  impurities from the diamond surface by anodic oxidation.

**TABLE 3.3.** Capacitance values,  $C$ , calculated by cyclic voltammetry at different potential values [V *vs* SHE] after treatment of the diamond surface. Investigations at two different scan rates:  $5 \text{ mV s}^{-1}$  and  $50 \text{ mV s}^{-1}$ . Geometric surface area:  $1 \text{ cm}^2$ . Electrolyte:  $0.5 \text{ M H}_2\text{SO}_4$ .  $T = 25 \text{ }^\circ\text{C}$ .

Electrode	Capacitance [ $\mu\text{F cm}^{-2}$ ]					
	$5 \times 10^{-3}$ [V $\text{s}^{-1}$ ]			$5 \times 10^{-2}$ [V $\text{s}^{-1}$ ]		
	0.64 [V]	0.8 [V]	1.1 [V]	0.64 [V]	0.8 [V]	1.1 [V]
BDD <sub>ag</sub>	749	497	180	231	206	100
BDD <sub>mild</sub>	117	55	43	22	38	10
BDD <sub>severe</sub>	7	10	11	3	4	7
BDD <sub>AcOH</sub>	2	2.6	2	1	0.8	0.7

### 3.3. Electrochemical behaviour of soluble redox systems at BDD electrodes

The electrochemical properties of diamond electrodes towards redox systems in the solution are quite sensitive to prior surface treatments. A decrease in surface conductivity following surface treatments had been observed in the past, however, the origin of this effect remains largely controversial. In many papers a modification of the carrier concentration at the diamond surface was suggested to occur as a result of the treatment [21-25]. Other research groups suggested that surface hydrogen or oxygen terminations may be responsible for the activity of the surface [4, 5, 11, 26]. The nature of the surface carriers was not unambiguously defined so



far; they could be boron states,  $sp^2$  impurities, or a near-surface hydrogen film promoting electron transfer at the surface. Hydrogen-terminated surface groups could be seen as an electron source in some redox processes. Several redox systems were studied at diamond electrodes in an attempt to correlate the electrochemical response of the electrodes with the surface treatments.

**3.3.1. Outer-sphere electron transfer reactions.** Many redox systems are very sensitive to the surface properties of the electrode, thus they could be used to check the surface state. The outer-sphere ferri/ferrocyanide ( $\text{Fe}(\text{CN})_6$ III/II) couple is a simple one-electron transfer process, yet its behaviour appears to be strongly influenced by the nature of the electrode surface. For this reason this redox system was investigated on BDD electrodes after their anodic oxidation, so as to elucidate the relation between electrochemical activity and chemical nature of the diamond electrode surface. A wide range of values (from  $10^{-5}$  to  $10^{-2}$   $\text{cm s}^{-1}$ ) was found in the literature for the reaction rate constant,  $k^0$ , in the ferri/ferrocyanide system on BDD electrodes [24, 27, 28]. When evaluating the results obtained, the fact that the quality of the diamond film, its doping level, the chemical composition of the diamond surface and its previous history can affect the electrochemical response of the electrode should be taken in account.

#### *Cyclic voltammetry*

Cyclic voltammetry was performed in order to study the behaviour of the outer-sphere ferri/ferrocyanide ( $\text{Fe}(\text{CN})_6$ III/II) redox system. The cathodic and the anodic transfer coefficients ( $\alpha_{\text{red}}$  and  $\beta_{\text{ox}}$  respectively), the apparent potential,  $E^{0'}_{\text{app}}$  (defined as the experimental equilibrium potential of the redox couple in solution), and the electrochemical rate constant  $k^0$ , were calculated. Considering the highly metallic character of boron-doped diamond electrodes ( $10^{20}$  to  $10^{21}$  boron atoms  $\text{cm}^{-3}$ ), equations developed for metal electrodes were used for the mathematical treatment of experimental results (Eqs. 2.20, 2.21, 2.22 for irreversible systems).

The voltammetric response of the electrodes changed with the surface treatment, as shown in Figures 3.8.A to 3.8.D. The largest currents were recorded at  $\text{BDD}_{\text{ag}}$  electrodes. At polarised electrodes ( $\text{BDD}_{\text{mild}}$  and  $\text{BDD}_{\text{severe}}$ ), the peak currents were only half as large. A very low response (ten times lower) was obtained at  $\text{BDD}_{\text{AcOH}}$  electrodes.

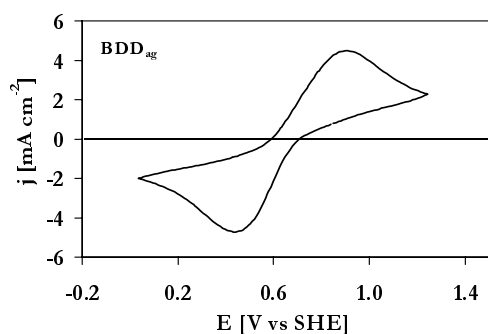


**FIGURE 3.8.A** Cyclic voltammogram of the redox couple  $\text{Fe}(\text{CN})_6^{3-}/\text{Fe}(\text{CN})_6^{4-}$   $12.5 \times 10^{-3} / 12.5 \times 10^{-3}$  M in 0.5 M  $\text{H}_2\text{SO}_4$ . Scan rate  $0.1 \text{ V s}^{-1}$ ,  $T = 25 \text{ }^\circ\text{C}$ .  $\text{BDD}_{\text{ag}}$ .

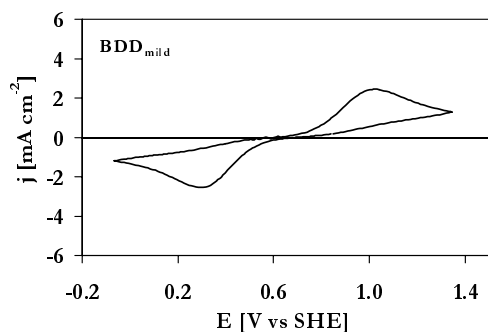


**FIGURE 3.8.B** Cyclic voltammogram of the redox couple  $\text{Fe}(\text{CN})_6^{3-}/\text{Fe}(\text{CN})_6^{4-}$   $12.5 \times 10^{-3} / 12.5 \times 10^{-3}$  M in 0.5 M  $\text{H}_2\text{SO}_4$ . Scan rate  $0.1 \text{ V s}^{-1}$ ,  $T = 25 \text{ }^\circ\text{C}$ .  $\text{BDD}_{\text{mild}}$ .

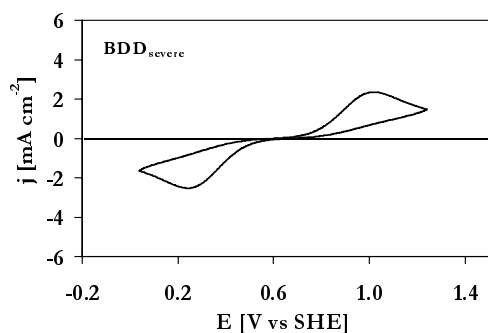


**FIGURE 3.8.C** Cyclic voltammogram of the redox couple  $\text{Fe}(\text{CN})_6^{3-}/\text{Fe}(\text{CN})_6^{4-}$   $12.5 \times 10^{-3} / 12.5 \times 10^{-3}$  M in 0.5 M  $\text{H}_2\text{SO}_4$ . Scan rate  $0.1 \text{ V s}^{-1}$ ,  $T = 25 \text{ }^\circ\text{C}$ .  $\text{BDD}_{\text{severe}}$ .

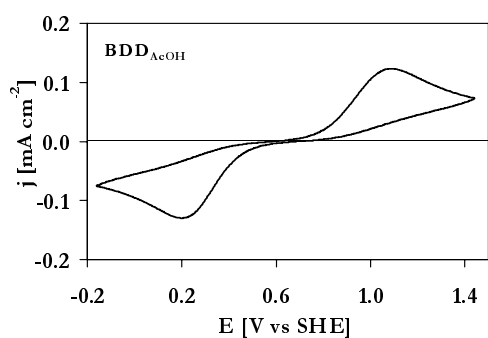


**FIGURE 3.8.D** Cyclic voltammogram of the redox couple  $\text{Fe}(\text{CN})_6^{3-}/\text{Fe}(\text{CN})_6^{4-}$   $12.5 \times 10^{-3} / 12.5 \times 10^{-3}$  M in 0.5 M  $\text{H}_2\text{SO}_4$ . Scan rate  $0.1 \text{ V s}^{-1}$ ,  $T = 25 \text{ }^\circ\text{C}$ .  $\text{BDD}_{\text{AcOH}}$ .

The couple's redox behaviour was tested at different scan rates at the four BDD electrodes (Figs. 3.9.A to 3.9.D) in order to calculate the kinetic parameters of the reaction.

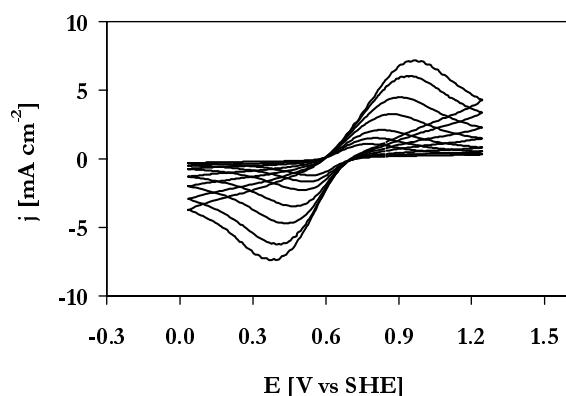


**FIGURE 3.9.A** Cyclic voltammograms for  $\text{Fe}(\text{CN})_6$  III/II  $12.5 \times 10^{-3} / 12.5 \times 10^{-3}$  M in 0.5 M  $\text{H}_2\text{SO}_4$  recorded at  $\text{BDD}_{\text{ag}}$  electrodes with different scan rates: 5, 10, 20, 50, 100, 200 and  $300 \text{ mV s}^{-1}$ ,  $T = 25^\circ\text{C}$ .

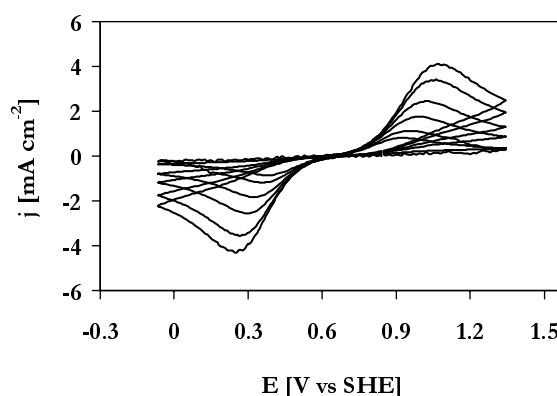


**FIGURE 3.9.B** Cyclic voltammograms for  $\text{Fe}(\text{CN})_6$  III/II  $12.5 \times 10^{-3} / 12.5 \times 10^{-3}$  M in 0.5 M  $\text{H}_2\text{SO}_4$  recorded at  $\text{BDD}_{\text{mild}}$  electrodes with different scan rates: 5, 10, 20, 50, 100, 200 and  $300 \text{ mV s}^{-1}$ ,  $T = 25^\circ\text{C}$ .

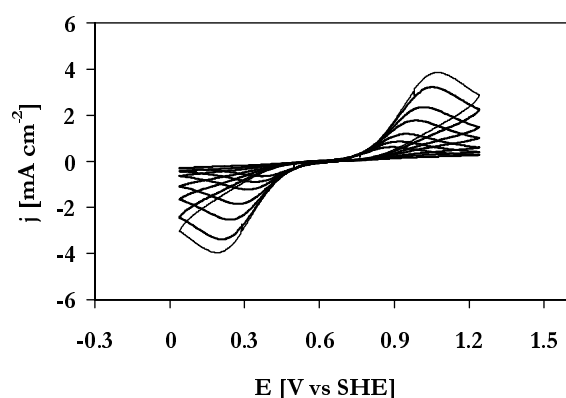


**FIGURE 3.9.C** Cyclic voltammograms for  $\text{Fe}(\text{CN})_6$  III/II  $12.5 \times 10^{-3} / 12.5 \times 10^{-3}$  M in 0.5 M  $\text{H}_2\text{SO}_4$  recorded at  $\text{BDD}_{\text{severe}}$  electrodes with different scan rates: 5, 10, 20, 50, 100, 200 and  $300 \text{ mV s}^{-1}$ ,  $T = 25^\circ\text{C}$ .

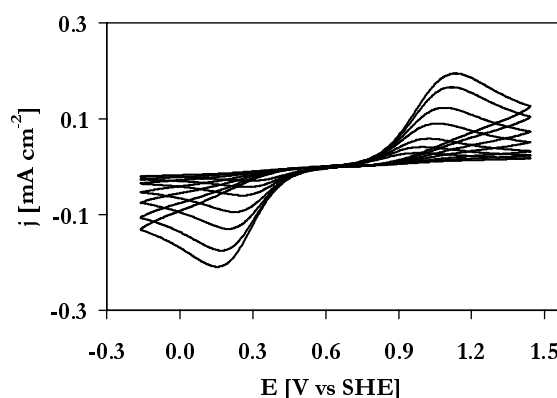


**FIGURE 3.9.D** Cyclic voltammograms for  $\text{Fe}(\text{CN})_6$  III/II  $12.5 \times 10^{-3} / 12.5 \times 10^{-3}$  M in 0.5 M  $\text{H}_2\text{SO}_4$  recorded at  $\text{BDD}_{\text{AcOH}}$  electrodes with different scan rates: 5, 10, 20, 50, 100, 200 and  $300 \text{ mV s}^{-1}$ ,  $T = 25^\circ\text{C}$ .

The redox system was irreversible at all BDD electrodes ( $\Delta E_p > 59 \text{ mV}$  for 1 electron). Both oxidation and reduction peaks exhibited the typical trend of irreversible systems following the equation that relates the peak potentials,  $E_p$ , and the half-peak potential,  $E_{p/2}$  (see § 1.2.4 of Chapter 2):

$$|E_p - E_{p/2}| = 1.857 \frac{RT}{\alpha F} = 47.7/\alpha \quad (\text{mV at } 25^\circ\text{C}) \quad \text{method (1)} \quad 3.2$$

From Equation 3.2, the transfer coefficients  $\alpha_{\text{red}}$  (cathodic reaction) and  $\beta_{\text{ox}}$  (anodic reaction) were calculated (method 1). Because of the dependence of the peak potentials on scan rate, the transfer coefficients were also calculated using the following equation (method 2):

$$E_p = E^0 + \frac{RT}{\alpha n F} \left( 0.78 - \ln k^0 + \ln \sqrt{D^0 \frac{\alpha n F}{RT}} \right) - \frac{RT}{2\alpha F} \ln v \quad \text{method (2)} \quad 3.3$$

The results were compared with those obtained with method 1 (Eq. 3.2). The reaction rate constants,  $k^0$ , were also calculated with Equation 3.3 while allowing for literature values of the diffusion coefficient,  $D^0$  ( $7.35 \times 10^{-6} \text{ cm}^2 \text{ s}^{-1}$  for  $\text{Fe}(\text{CN})_6\text{II}$  and  $6.7 \times 10^{-6} \text{ cm}^2 \text{ s}^{-1}$  for  $\text{Fe}(\text{CN})_6\text{III}$  [29]), one electron being involved in the electron transfer process.

Such a mathematical treatment was applied to the results from all electrodes investigated. Table 3.4 summarizes the calculated parameter values.

**TABLE 3.4.** Parameters of the redox system  $\text{Fe}(\text{CN})_6\text{III/II}$   $12.5 \times 10^{-3} / 12.5 \times 10^{-3} \text{ M}$  calculated from the results of cyclic voltammetry performed at different diamond electrodes. Electrolyte:  $0.5 \text{ M H}_2\text{SO}_4$ .  $T = 25^\circ\text{C}$ .

electrode	$\Delta E_p$	$E^{0'}_{\text{app}}$	$\beta_{\text{ox}}$	$\beta_{\text{ox}}$	$\alpha_{\text{red}}$	$\alpha_{\text{red}}$	$k^*$	$k^{**}$	$k^0$
	[V]	[V vs SHE]	(1)	(2)	(1)	(2)	[cm/s]	[cm/s]	[cm/s]
<b>BDD<sub>ag</sub></b>	0.24	0.67	0.3	0.3	0.4	0.3	$3 \times 10^{-4}$	$4 \times 10^{-4}$	$4 \times 10^{-4}$
<b>BDD<sub>mild</sub></b>	0.53	0.66	0.3	0.3	0.3	0.3	$1 \times 10^{-4}$	$6 \times 10^{-5}$	$8 \times 10^{-5}$
<b>BDD<sub>severe</sub></b>	0.52	0.63	0.3	0.3	0.3	0.3	$8 \times 10^{-5}$	$9 \times 10^{-5}$	$9 \times 10^{-5}$
<b>BDD<sub>AcOH</sub></b>	0.62	0.64	0.2	0.3	0.3	0.3	$4 \times 10^{-5}$	$1 \times 10^{-5}$	$3 \times 10^{-5}$

(1) determined from Eq. 3.2

$k^* = k^0$  determined from the oxidation peak

$k^0 = (k^* + k^{**})/2$

(2) determined from Eq. 3.3

$k^{**} = k^0$  determined from the reduction peak

The as-grown diamond had a high activity toward the redox couple, whereas the same electrode was deactivated after anodic polarisation. The reaction became more irreversible and the current peaks decreased significantly after oxidation of the electrode surface. The transfer coefficients,  $\alpha_{\text{red}}$  and  $\beta_{\text{ox}}$ , were not so sensitive to the

anodic treatment. The sum of the transfer coefficients did not add up to unity (as it should according to theory for metallic materials) at any of the diamond electrodes investigated. A semiconductor character of the diamond electrodes could explain such a behaviour. The values calculated for the reaction rate constant on BDD<sub>ag</sub> electrodes were consistent with those reported in the literature [24, 25]. The reaction rate constant values could be compared as all tested electrodes had similar transfer coefficients,  $\alpha_{\text{red}}$  and  $\beta_{\text{ox}}$ . For treated diamond electrodes, the values decreased by one order of magnitude relative to those found at BDD<sub>ag</sub>. A decrease in the  $sp^2$  density could explain the reduced activity of these electrodes.

### Steady-state polarisation curves

The kinetic parameters of the ferri/ferrocyanide redox process were also determined by polarising the electrode surfaces. The polarisation curves of Fig. 3.10 show a perfect symmetry between the anodic and the cathodic reaction. The polarisation curves were fitted to straight lines the slopes of which increased linearly with concentration of the species. The exchange currents,  $j_0$ , and the reaction rate constants,  $k^0$ , were calculated (Eqs. 3.4 and 3.5) in the low-overpotential approximation ( $\eta < 10$  mV) of the Butler-Volmer equation (Eq. 2.13 of Chapter 2):

$$j = j_0 \frac{F}{RT} \eta \quad (n = 1) \quad 3.4$$

$$k^0 = \frac{j_0}{FC} \quad 3.5$$

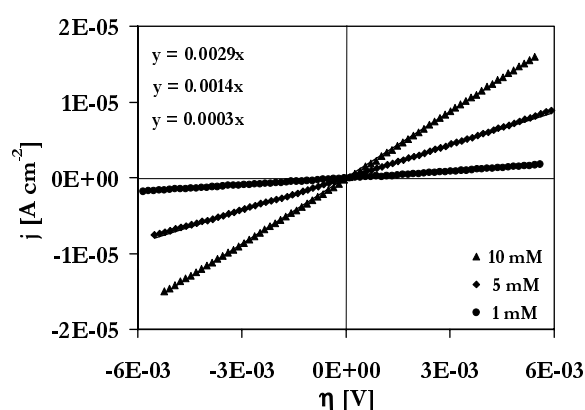


**FIGURE 3.10.A** Polarisation curves for the  $\text{Fe}(\text{CN})_6\text{III/II}$  system at BDD<sub>ag</sub> electrodes at different concentrations. Electrolyte: 0.5 M  $\text{H}_2\text{SO}_4$ ; scan rate 0.1  $\text{mV s}^{-1}$ ;  $T = 25$  °C.

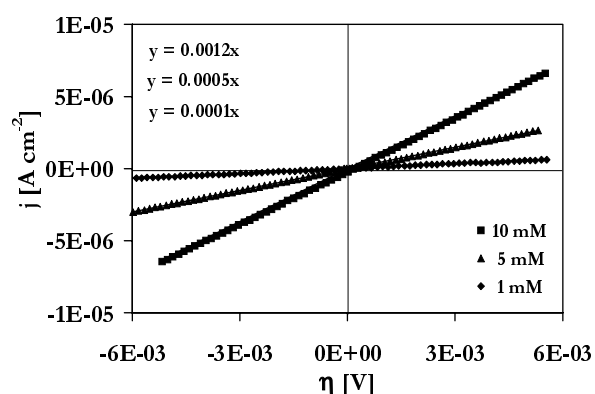


**FIGURE 3.10.B** Polarisation curves for the  $\text{Fe}(\text{CN})_6\text{III/II}$  system at BDD<sub>mild</sub> electrodes at different concentrations. Electrolyte: 0.5 M  $\text{H}_2\text{SO}_4$ ; scan rate 0.1  $\text{mV s}^{-1}$ ;  $T = 25$  °C.

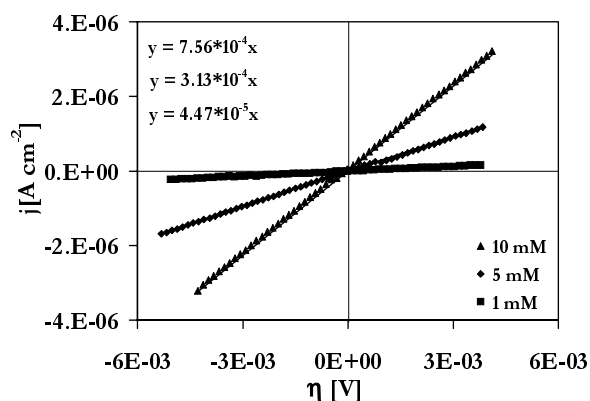


**FIGURE 3.10.C** Polarisation curves for the  $\text{Fe}(\text{CN})_6\text{III/II}$  system at  $\text{BDD}_{\text{severe}}$  electrodes at different concentrations. Electrolyte: 0.5 M  $\text{H}_2\text{SO}_4$ ; scan rate  $0.1 \text{ mV s}^{-1}$ ;  $T = 25 \text{ }^\circ\text{C}$ .

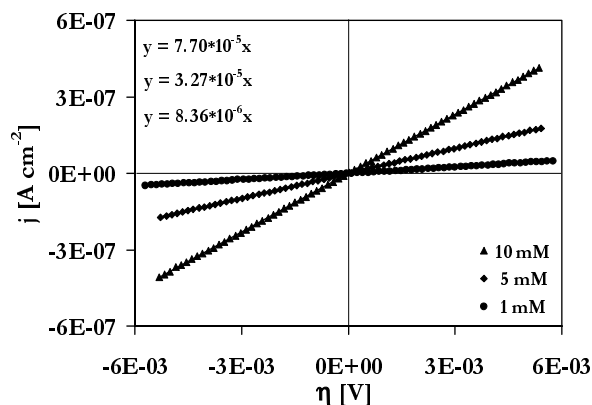


**FIGURE 3.10.D** Polarisation curves for the  $\text{Fe}(\text{CN})_6\text{III/II}$  system at  $\text{BDD}_{\text{AcOH}}$  electrodes at different concentrations. Electrolyte: 0.5 M  $\text{H}_2\text{SO}_4$ ; scan rate  $0.1 \text{ mV s}^{-1}$ ;  $T = 25 \text{ }^\circ\text{C}$ .

Equations 3.4 and 3.5 have been developed for the case of small overpotential values from the Butler-Volmer equation, supposing that the sum of  $\alpha$  and  $\beta$  was unity (see Chapter 2). In our case, previous measurements by cyclic voltammetry had demonstrated that  $\alpha$  and  $\beta$  have the same value but their sum is a constant value smaller than unity. It is possible to write the following relation:

$$\alpha + \beta = K < 1 \quad 3.6$$

When using the Butler-Volmer equation in the low-overpotential approximation ( $\eta < 1$ ) (Eq. 3.4), the relation  $\alpha + \beta = 1$  was supposed to be valid as a necessary approximation.

**TABLE 3.5.** Reaction rate constants of the redox system  $\text{Fe}(\text{CN})_6\text{III/II}$   $12.5 \times 10^{-3} / 12.5 \times 10^{-3} \text{ M}$  at diamond electrodes calculated from the results of polarisation measurements. Electrolyte: 0.5 M  $\text{H}_2\text{SO}_4$ .  $T = 25 \text{ }^\circ\text{C}$ .

Electrode	$k^0 [\text{cm s}^{-1}]$
$\text{BDD}_{\text{ag}}$	$8 \times 10^{-5}$
$\text{BDD}_{\text{mild}}$	$3 \times 10^{-5}$
$\text{BDD}_{\text{severe}}$	$2 \times 10^{-5}$
$\text{BDD}_{\text{AcOH}}$	$2 \times 10^{-6}$

The reaction rate constants were calculated from Equation 3.5 (Table 3.5). The low values of  $k^0$  were due to a slow electron transfer process. The irreversibility became more pronounced after oxidising treatment of the electrodes. Since the outer-sphere ferri/ferrocyanide system is known to be insensitive to oxide coverage of the electrode surface, a decrease in the concentration of the  $sp^2$  impurities as the electron transfer mediators on the diamond surface could explain an electrode deactivation upon oxidation. Nevertheless, the sensitivity of the redox system to elimination of these impurities was quite low. This observation can be explained by considering that usually an outer-sphere transfer process readily proceeds on both  $sp^2$  and  $sp^3$  carbon, thus no big differences should be noticed after  $sp^2$  carbon elimination. The fact that the real surface area changes after oxidising treatment of the electrodes (see roughness factor in paragraph 3.1) also could explain a decreasing in the rate constant values. The values calculated for the reaction rate constant from the polarisation measurements were lower than those obtained by cyclic voltammetry (Table 3.4).

**3.3.2. Inner-sphere electron transfer reactions.** The behaviour of the inner-sphere benzoquinone/hydroquinone redox system was investigated on BDD electrodes as an example of a more complex redox reaction. This redox system was particularly interesting because of the complexity of the aromatic molecular structure and because of a multistep process involving the consecutive transfer of two electrons and two protons. The reaction is classified as inner-sphere occurring through an adsorption step on the electrode surface. Its high sensitivity to the surface properties confirms this assumption. It was investigated at all the electrodes treated anodically. Even though no adsorption phenomena were detected during the experiments, the different treatments of the BDD electrodes strongly influenced the kinetics of the process.

#### *Cyclic voltammetry*

Cyclic voltammetry was performed to study the kinetics of the reaction. Figures 3.11.D illustrate the behaviour of 1,4-benzoquinone/hydroquinone at the different diamond electrodes. The reaction was slow on all diamond electrodes investigated. A first observation was an increase in irreversibility (estimated from the  $\Delta E_p$ ) of the redox couple from BDD<sub>ag</sub> to BDD<sub>AcOH</sub>. Another factor was the more important sensitivity of the cathodic part of the voltammograms to the surface treatment. This asymmetrical behaviour can be attributed to a semiconductor-type character (p-type) of diamond electrodes, even if the boron doping level is such as to give rise to a resistivity typical of a semimetal material.

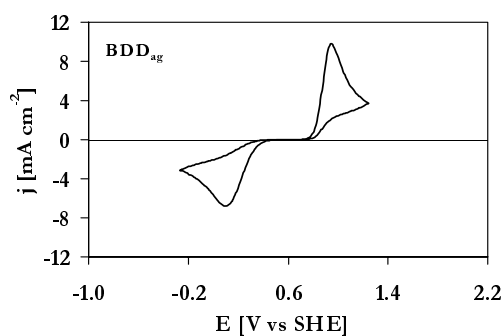


**FIGURE 3.11.A** Cyclic voltammogram of the Q/H<sub>2</sub>Q redox couple in 0.5 M H<sub>2</sub>SO<sub>4</sub>. Q/H<sub>2</sub>Q 12.5x10<sup>-3</sup>/12.5x10<sup>-3</sup> M. Scan rate 0.1 V s<sup>-1</sup>, T = 25 °C. BDD<sub>ag</sub>.

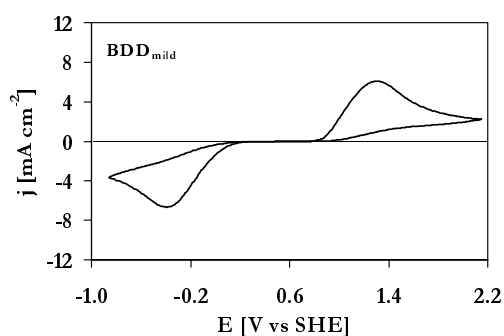


**FIGURE 3.11.B** Cyclic voltammogram of the Q/H<sub>2</sub>Q redox couple in 0.5 M H<sub>2</sub>SO<sub>4</sub>. Q/H<sub>2</sub>Q 12.5x10<sup>-3</sup>/12.5x10<sup>-3</sup> M. Scan rate 0.1 V s<sup>-1</sup>, T = 25 °C. BDD<sub>mild</sub>.

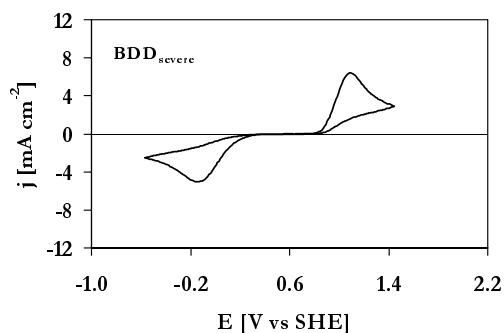


**FIGURE 3.11.C** Cyclic voltammogram of the Q/H<sub>2</sub>Q redox couple in 0.5 M H<sub>2</sub>SO<sub>4</sub>. Q/H<sub>2</sub>Q 12.5x10<sup>-3</sup>/12.5x10<sup>-3</sup> M. Scan rate 0.1 V s<sup>-1</sup>, T = 25 °C. BDD<sub>severe</sub>.

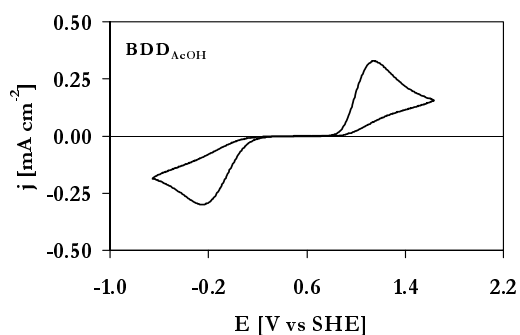


**FIGURE 3.11.D** Cyclic voltammogram of the Q/H<sub>2</sub>Q redox couple in 0.5 M H<sub>2</sub>SO<sub>4</sub>. Q/H<sub>2</sub>Q 12.5x10<sup>-3</sup>/12.5x10<sup>-3</sup> M. Scan rate 0.1 V s<sup>-1</sup>, T = 25 °C. BDD<sub>AcOH</sub>.



It had been expected that the redox system would be more irreversible on an oxygen-free diamond surface ( $\text{BDD}_{\text{ag}}$ ) where adsorption phenomena are hindered, while any oxygen present on the surface should facilitate an adsorption mechanism through hydrogen bonding with the oxygen groups at the aromatic molecule.

The opposite experimental finding implies that oxygen coverage of the diamond surface (table 3.1) did not influence the mechanism of the redox reaction. Elimination of non-diamond carbon ( $sp^2$ ) impurities (by oxidation to  $\text{CO}_2$ ) is a more likely explanation for the increase in irreversibility occurring with increasingly severe surface treatment.

Different redox couple concentrations were also investigated in order to see the effects of concentration on the equilibrium potential and reaction rate at BDD electrodes (Figs. 3.12.A to 3.12.B). Both the anodic and the cathodic currents exhibited a linear increase with increasing concentration, as expected for metallic systems.

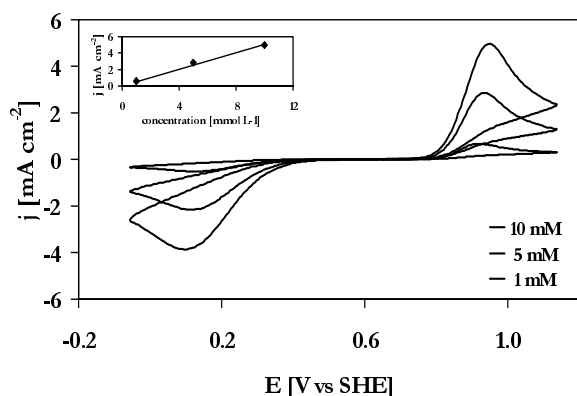


**FIGURE 3.12.A** Cyclic voltammograms of Q/ $\text{H}_2\text{Q}$  in 0.5 M  $\text{H}_2\text{SO}_4$  at  $\text{BDD}_{\text{ag}}$  electrodes and different concentrations: 1, 5, 10 mM. Scan rate  $0.1 \text{ V s}^{-1}$ ;  $T = 25 \text{ }^\circ\text{C}$ .

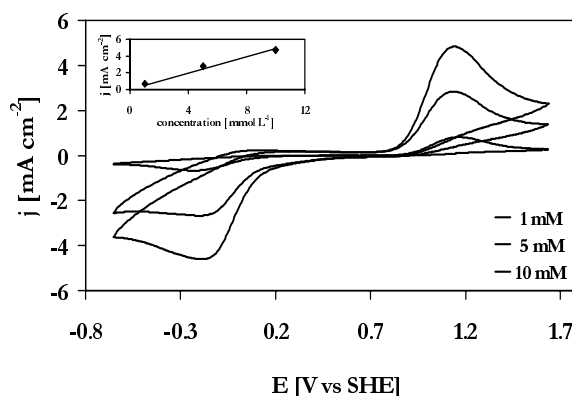


**FIGURE 3.12.B** Cyclic voltammograms of Q/ $\text{H}_2\text{Q}$  in 0.5 M  $\text{H}_2\text{SO}_4$  at  $\text{BDD}_{\text{mild}}$  electrodes and different concentrations: 1, 5, 10 mM. Scan rate  $0.1 \text{ V s}^{-1}$ ;  $T = 25 \text{ }^\circ\text{C}$ .

Voltammetry was performed at different scan rates in order to evaluate the kinetic parameters of the reaction (Figs. 3.13.A to 3.13.D). The mathematical treatment used was that for metal electrodes (Eqs. 3.2 and 3.3). Values of  $D^0 = 8.5 \times 10^{-6} \text{ cm}^2 \text{ s}^{-1}$  and  $9.8 \times 10^{-6} \text{ cm}^2 \text{ s}^{-1}$  were used for the diffusion coefficients of hydroquinone and benzoquinone, respectively [30]. Table 3.6 shows the calculated parameter values.

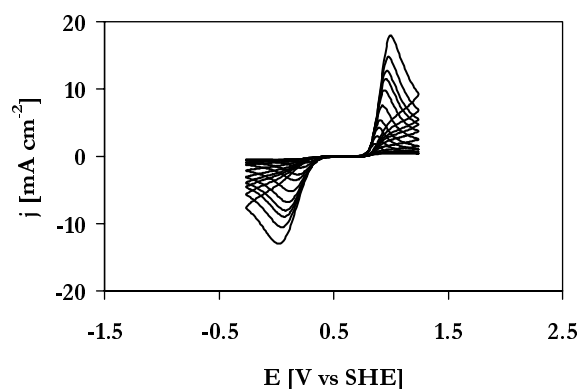


**FIGURE 3.13.A** Cyclic voltammograms of Q/H<sub>2</sub>Q 12.5x10<sup>-3</sup>/ 12.5x0<sup>-3</sup> M in 0.5 M H<sub>2</sub>SO<sub>4</sub> recorded at BDD<sub>ag</sub> electrodes with different scan rates: 5, 10, 20, 50, 100, 200, 300 and 500 mV s<sup>-1</sup>. *T* = 25 °C.

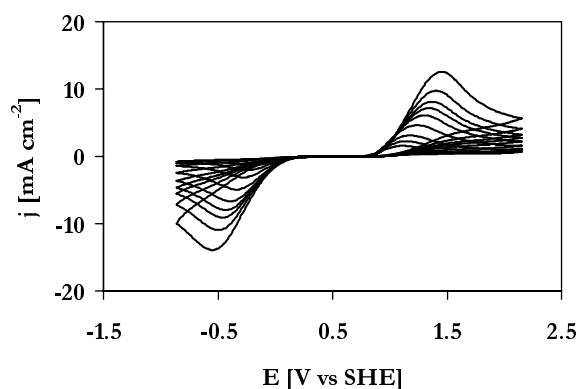


**FIGURE 3.13.B** Cyclic voltammograms of Q/H<sub>2</sub>Q 12.5x10<sup>-3</sup>/ 12.5x0<sup>-3</sup> M in 0.5 M H<sub>2</sub>SO<sub>4</sub> recorded at BDD<sub>mild</sub> electrodes with different scan rates: 5, 10, 20, 50, 100, 200, 300 and 500 mV s<sup>-1</sup>. *T* = 25 °C.

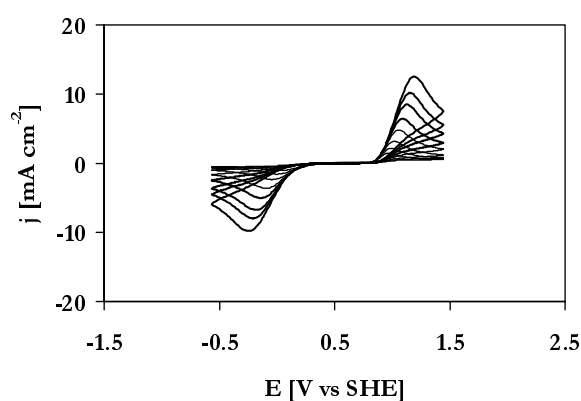


**FIGURE 3.13.C** Cyclic voltammograms of Q/H<sub>2</sub>Q 12.5x10<sup>-3</sup>/ 12.5x0<sup>-3</sup> M in 0.5 M H<sub>2</sub>SO<sub>4</sub> recorded at BDD<sub>severe</sub> electrodes with different scan rates: 5, 10, 20, 50, 100, 200, 300 and 500 mV s<sup>-1</sup>. *T* = 25 °C.

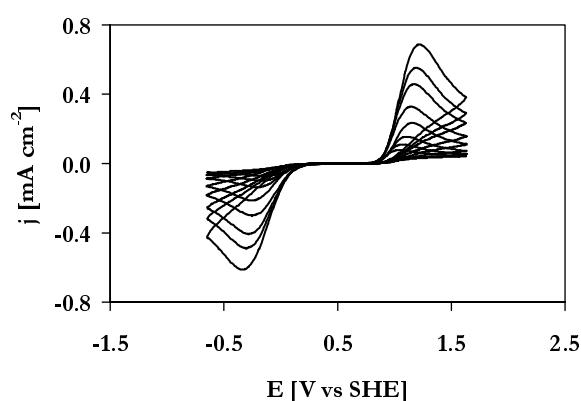


**FIGURE 3.13.D** Cyclic voltammograms of Q/H<sub>2</sub>Q 12.5x10<sup>-3</sup>/ 12.5x0<sup>-3</sup> M in 0.5 M H<sub>2</sub>SO<sub>4</sub> recorded at BDD<sub>AcOH</sub> electrodes with different scan rates: 5, 10, 20, 50, 100, 200, 300 and 500 mV s<sup>-1</sup>. *T* = 25 °C.

The  $\alpha + \beta$  values found for the diamond electrodes were lower than unity on account of the semiconductor character of the boron-doped diamond material. Different values of the rate constant,  $k^0$ , for the oxidation and reduction reaction indicate an asymmetric behaviour of the diamond electrodes. The reaction rate constant values could be compared as all tested electrodes had similar transfer coefficients,  $\alpha_{\text{red}}$  and  $\beta_{\text{ox}}$ . The values of the rate constant decreased with increasing severity of the treatment. The lower response seen at electrodes after a polishing-like

process (BDD<sub>AcOH</sub>) probably is due to the corresponding changes in crystal size and shape, just as found with the ferri/ferrocyanide system.

**TABLE 3.6.** Parameters for the redox system Q/H<sub>2</sub>Q 12.5x10<sup>-3</sup>/ 12.5x0<sup>-3</sup> M in 0.5 M H<sub>2</sub>SO<sub>4</sub> at BDD electrodes after different treatments.

Electrode	$\Delta E_p$	$E^{0'}_{app}$	$\beta_{ox}$	$\beta_{ox}$	$\alpha_{red}$	$\alpha_{red}$	$k^*$	$k^{**}$	$k^0$
	[V]	[V vs SHE]	(1)	(2)	(1)	(2)	[cm/s]	[cm/s]	[cm/s]
BDD <sub>ag</sub>	0.74	0.52	0.5	0.3	0.3	0.3	9.7x10 <sup>-5</sup>	4.1x10 <sup>-5</sup>	7x10 <sup>-5</sup>
BDD <sub>mild</sub>	1.42	0.45	0.2	0.2	0.2	0.2	2.1x10 <sup>-5</sup>	2.6x10 <sup>-5</sup>	2x10 <sup>-5</sup>
BDD <sub>severe</sub>	0.93	0.48	0.3	0.3	0.3	0.2	8.3x10 <sup>-6</sup>	5.1x10 <sup>-5</sup>	6x10 <sup>-5</sup>
BDD <sub>AcOH</sub>	1.18	0.46	0.3	0.3	0.2	0.3	4.2x10 <sup>-7</sup>	2.5x10 <sup>-6</sup>	1x10 <sup>-6</sup>

(1) determined from Eq. 3.2

$k^* = k^0$  determined from the oxidation peak

$k^0 = (k^* + k^{**})/2$

(2) determined from Eq. 3.3

$k^{**} = k^0$  determined from the reduction peak

### *Steady-state polarisation curves*

Steady-state polarisation curves were recorded at different Q/H<sub>2</sub>Q concentrations (Figs. 3.14.A and 3.14.B) in order to calculate the kinetic parameters of the reaction. Because of the straight-line relation seen between current and overpotential, the low-overpotential approximation (Eq. 3.4) was applied to the Butler-Volmer equation for this redox system. The slopes of the polarisation straight lines failed to exhibit the linear increase with organic concentration (Figs. 3.14.A and 3.14.B) expected from the earlier cyclic voltammetry measurements (Figs. 3.12.A and 3.12.B).

The experiments at strongly polarised diamond electrodes were much more difficult. Because of the very low currents, noise was so important that it was impossible to record the electrode's response at these low scan rates (plot not given).

The departures from theory found in these investigations can be attributed to the fact that the experimental equilibrium potential was not constant during the experiments. Fluctuations of  $\pm 0.02$  V before and after experiments were noticed for diamond electrodes. The irreproducible behaviour of the electrodes in repeated

experiments did not allow us to study the effects of concentration on the polarisation curves and calculate the reaction rate constants.

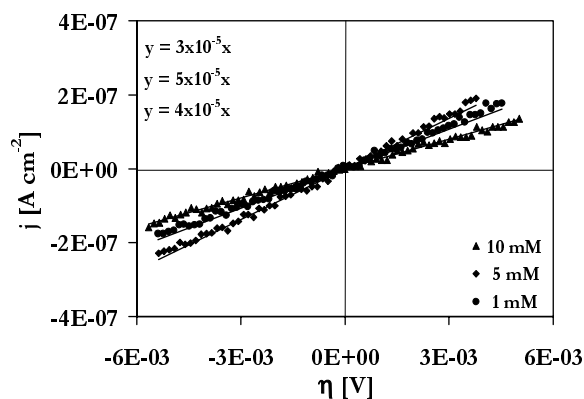


**FIGURE 3.14.A** Polarisation curves of the Q/H<sub>2</sub>Q system recorded at BDD<sub>ag</sub> electrodes and different concentrations. Electrolyte: 0.5 M H<sub>2</sub>SO<sub>4</sub>; scan rate 0.1 mV s<sup>-1</sup>; T = 25 °C.

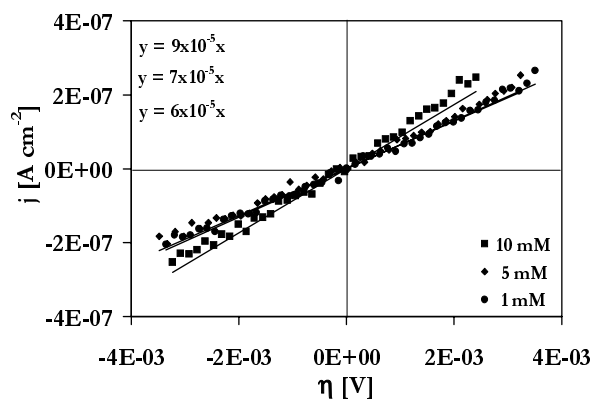


**FIGURE 3.14.B** Polarisation curves of the Q/H<sub>2</sub>Q system recorded at BDD<sub>mild</sub> electrodes and different concentrations. Electrolyte: 0.5 M H<sub>2</sub>SO<sub>4</sub>; scan rate 0.1 mV s<sup>-1</sup>; T = 25 °C.

In an attempt to attain true equilibrium conditions, the immersion potential of a BDD<sub>mild</sub> electrode was measured over a few hours. After more than four hours a constant immersion potential was attained (Fig. 3.15). This observation confirms the very slow reaction and explains the difficulties encountered when working at potentials close to equilibrium conditions.

The currents recorded at these potentials (Figs. 3.14) probably were due to surface charge phenomena rather than to electron transfer involving the redox couple under investigation. This would explain the insensitivity of the polarisation curves to the concentration of the redox couple. The fact that at strongly treated electrodes (BDD<sub>severe</sub>, BDD<sub>AcOH</sub>) exhibiting an extremely reduced surface activity, polarisation measurements (not given) were disturbed by the background noise provides support for this assumption. A similar problem was not noticed in the case of the ferri/ferrocyanide system owing to the higher reversibility of this outer-sphere system.

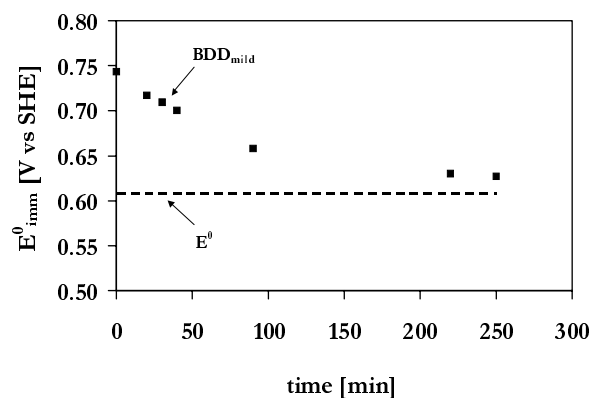


**FIGURE 3.15.** Trend of the immersion potentials measured as a function of time with the redox system Q/H<sub>2</sub>Q 10<sup>-2</sup>/10<sup>-2</sup> M at a BDD<sub>mild</sub> electrode in 0.5 M H<sub>2</sub>SO<sub>4</sub>.  $T = 25$  °C.

## 4. Conclusions

The chemical and electrochemical properties of diamond electrodes were found to be strongly influenced by the surface treatment. A relatively mild polarisation process was sufficient to transform the surface from hydrophobic (BDD<sub>ag</sub>) to hydrophilic (BDD<sub>mild</sub>) without changes in the crystal shape and size. The electrochemical properties were strongly modified, too. The voltammetric charge decreased by one order of magnitude due to the decrease in the concentration of active surface sites. The calculated capacitance decreased as well, which is typical for a surface partly depleted of functional groups (Table 3.7). The irreversibility of redox systems chosen as surface activity probes (ferri/ferrocyanide and 1,4-benzoquinone/hydroquinone) increased significantly between BDD<sub>ag</sub> and BDD<sub>mild</sub>. The  $\Delta E_p$  between the oxidation and reduction peaks doubled after anodic polarisation. The transfer coefficients  $\alpha_{\text{red}}$  and  $\beta_{\text{ox}}$  decreased, and their sum is lower than unity (Tables 3.4 and 3.6). Values of the reaction rate constant,  $k^0$ , also were sensitive to surface oxidation (Table 3.7). Anodic oxidation appears to result in a surface from which impurities were eliminated.

After stronger oxidation processes the electrodes had experienced morphological changes involving both crystal size and crystal shape (BDD<sub>severe</sub> and BDD<sub>AcOH</sub>). The surface became smoother, and the electrochemical activity measured in terms of voltammetric charge strongly decreased. Capacitance values decreased as well, and attained the values typical for single-crystal diamond electrodes. At the BDD<sub>severe</sub> and BDD<sub>AcOH</sub> diamond electrodes, electron transfer

was slower than at BDD<sub>ag</sub> and BDD<sub>mild</sub>, according to the rate constants found for the two redox systems investigated.

**TABLE 3.7.** Summarising the values for voltammetric charge, capacitance and reaction rate constant for the electrodes investigated (Tables 3.2, 3.3, 3.4, 3.6). Geometric surface area = 1 cm<sup>2</sup>.

Electrode	Charge [mC cm <sup>-2</sup> ]	Capacitance [μF cm <sup>-2</sup> ]	k <sup>0</sup> Fe(CN) <sub>6</sub> III/II [cm s <sup>-1</sup> ]	k <sup>0</sup> Q/H <sub>2</sub> Q [cm s <sup>-1</sup> ]
BDD <sub>ag</sub>	1.5	497	4x10 <sup>-4</sup>	7x10 <sup>-5</sup>
BDD <sub>mild</sub>	1.2x10 <sup>-1</sup>	55	8x10 <sup>-5</sup>	2x10 <sup>-5</sup>
BDD <sub>severe</sub>	4.7x10 <sup>-2</sup>	10	9x10 <sup>-5</sup>	6x10 <sup>-5</sup>
BDD <sub>AcOH</sub>	6.3x10 <sup>-3</sup>	2.6	3x10 <sup>-5</sup>	1x10 <sup>-6</sup>

In many studies the electrochemical behaviour of polycrystalline and single-crystal diamond electrodes has been compared [1, 2, 8, 23, 31-33] while emphasising the relation between electrochemical properties, the complexity of crystal structure and crystal face orientation. On diamond deposited by HF-CVD the <111> texture is predominant [34], which is more reactive than <100> because of a higher boron incorporation efficiency [2, Martin, 1999 #6, 16]. Polycrystalline diamonds are more active than single crystal diamond electrodes because of the higher reactivity of grain boundaries [1].

The changes in behaviour resulting from an oxidising treatment can be explained in terms of an initial decrease in the impurity concentration at the diamond surface (BDD<sub>mild</sub>) responsible for slower electron transfer kinetics. More profound oxidation (BDD<sub>AcOH</sub> and BDD<sub>severe</sub>) leads to changes in the diamond morphology (SEM images in Figs. 3.3.C and 3.3.D).

Thus, the strong decrease in electrode activity following anodic treatments is the result of a decrease in charge carrier concentration on the surface, first by elimination of impurities and later by elimination of boron atoms.

The nature of impurities present on the diamond surface is variable and depends on the preparation conditions and on the kind of substrate material used. The  $sp^2$  impurities are most probably responsible for the activity of as-grown diamond electrodes [1, 8]. By analogy with glassy carbon and graphite electrodes [18, 35, 36], the typically aromatic basic structure of non-diamond carbon could be responsible for the high surface activity of BDD<sub>ag</sub> electrodes. It is well known, in fact, that carbon-based electrodes have a six-membered ring structure in which benzoquinone/hydroquinone and carboxyl-like functional groups are present [37] (Fig. 3.16.A). Usually, oxidation and reduction regions are visible in voltammograms recorded on carbon-based electrodes of this kind [18, 35, 36], but both the methods of preparation and the previous history of the material can strongly influence the electrode's response.

Oxidation of these impurities could be responsible for BDD surface changes. Anodic polarisation (BDD<sub>mild</sub>) led to oxidation of the aromatic functional groups and to the elimination of most of the  $sp^2$  carbon from the surface (oxidation to CO<sub>2</sub>). At the same time, the  $sp^2$  carbon still present on the surface was activated [28]; in this case, a pair of peaks is seen (Fig. 3.7.B) which probably are due to a hydroquinone/benzoquinone-like surface system [18, 35, 36]. A lower surface activity after polarisation could be explained in terms of a "cleaner" polycrystalline diamond surface on which only less active aliphatic alcohol, ketone or carboxylic-like groups are present (Fig. 3.16.B). Even stronger anodic polarisation completely changes the surface morphology. The fact that the specific capacitance value for polished electrodes (BDD<sub>AcOH</sub>) corresponds to the capacitance value of <100> single-crystal diamond electrodes [9, 20] confirms the idea that impurities present at the grain boundaries of the crystals are responsible for the electrochemical properties of the diamond electrodes. A clean and polished diamond surface is less active than the surface of as-grown polycrystalline diamond materials.

In the next chapter, the accent will be on the relation between non-diamond ( $sp^2$ ) carbon impurities and the electrochemical activity of diamond electrodes.

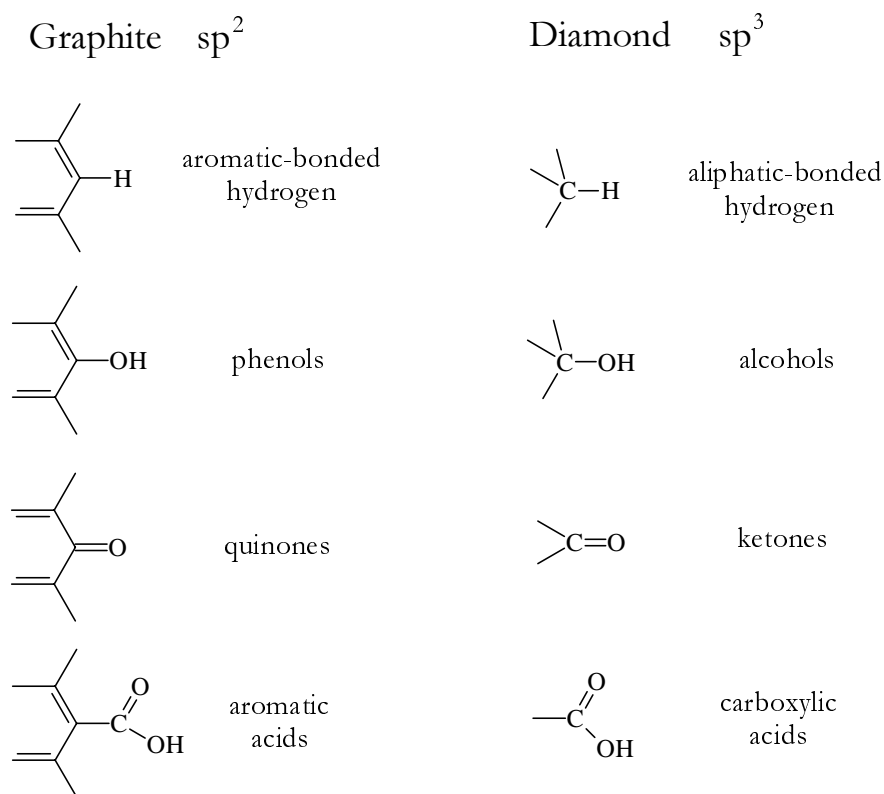


FIGURE 3.16. Surface functional groups on oxidised  $sp^2$  (graphite) and  $sp^3$  (diamond) surfaces.

---

## 5. Acknowledgement

I would like to thank Mr M. Mermoux of CNRS at the National Institute of Technology, Grenoble (F), for recording Raman spectra of the electrodes, and Mrs A. Sahil for the contact angle measurements. I am grateful to Mr L. Ouattara for preparing severely polarised BDD electrodes, and to Mr N. Guignon for performing part of the cyclic voltammetry experiments.



## 6. References

1. H. B. Martin, A. Argoitia, J. C. Angus, and U. Landau, *J. Electrochem. Soc.*, **146** (1999) 2959.
2. T. Kondo, Y. Einaga, B. V. Sarada, T. N. Rao, D. A. Tryk, and A. Fujishima, *J. Electrochem. Soc.*, **149** (2002) E179.
3. K. Hayashi, S. Yamanaka, H. Okushi, and K. Kajimura, *Appl. Phys. Lett.*, **68** (1996) 376.
4. I. Yagi, H. Notsu, T. Kondo, D. A. Tryk, and A. Fujishima, *J. Electroanal. Chem.*, **473** (1999) 173.
5. D. A. Tryk, K. Tsunozaki, T. N. Rao, and A. Fujishima, *Diamond Relat. Mater.*, **10** (2001) 1804.
6. R. J. Zhang, S. T. Lee, and Y. W. Lam, *Diamond Relat. Mater.*, **5** (1996) 1288.
7. C. Lévy-Clément, F. Zenia, N. A. Ndao, and A. Deneuve, *New Diamond Front. Carbon Technol.*, **9** (1999) 189.
8. G. M. Swain, A. B. Anderson, and J. C. Angus, *MRS Bull.*, **23** (1998) 56.
9. M. C. Granger and G. M. Swain, *J. Electrochem. Soc.*, **146** (1999) 4551.
10. H. Notsu, I. Yagi, T. Tatsuma, D. A. Tryk, and A. Fujishima, *J. Electroanal. Chem.*, **492** (2000) 31.
11. H. Notsu, I. Yagi, T. Tatsuma, D. A. Tryk, and A. Fujishima, *Electrochem. Solid-state Lett.*, **2** (1999) 522.
12. T. N. Rao and A. Fujishima, *Diamond Relat. Mater.*, **9** (2000) 384.
13. A. C. Ferrari, *Diamond Relat. Mater.*, **11** (2002) 1053.
14. E. Gheeraert, P. Gonon, and A. Deneuve, *Diamond Relat. Mater.*, **2** (1993) 742.
15. L.-F. Li, D. A. Totir, N. Vinokur, B. Miller, G. Chottiner, E. A. Evans, J. C. Angus, and D. A. Scherson, *J. Electrochem. Soc.*, **145** (1998) L85.
16. K. Ushizawa, K. Watanabe, T. Ando, I. Sakaguchi, M. Nishitani-Gamo, I. Sato, and H. Kanda, *Diamond Relat. Mater.*, **7** (1998) 1719.
17. M. C. Granger, M. Witek, J. Xu, J. Wang, M. Hupert, A. Hanks, M. D. Koppang, J. E. Butler, G. Lucazeau, M. Mermoux, J. W. Strojek, and G. M. Swain, *Anal. Chem.*, **72** (2000) 3793.
18. D. Laser and M. Ariel, *J. Electroanal. Chem.*, **52** (1974) 291.
19. A. J. Bard and L. R. Faulkner, 'Electrochemical methods - Fundamentals and applications', J. Wiley and Sons, Inc., New York, 2001.
20. Y. V. Pleskov, Y. E. Evstefeeva, M. D. Krotova, V. Y. Mishuk, V. A. Laptev, Y. N. Palyanov, and Y. M. Borzdov, *J. Electrochem. Soc.*, **149** (2002) E260.
21. M. N. Latto, D. J. Riley, and P. W. May, *Diamond Relat. Mater.*, **9** (2000) 1181.
22. H. J. Looi, L. Y. S. Pang, A. B. Molloy, F. Jones, J. S. Foord, and R. B. Jackman, *Diamond Relat. Mater.*, **7** (1998) 550.

23. J. v. d. Lagemaat, D. Vanmaeckelbergh, and J. J. Kelly, *J. Electroanal. Chem.*, **475** (1999) 139.
24. A. D. Modestov, Y. E. Evstefeeva, Y. V. Pleskov, V. M. Mazin, V. P. Varnin, and I. G. Teremetskaya, *J. Electroanal. Chem.*, **431** (1997) 211.
25. N. G. Ferreira, L. L. G. Silva, E. J. Corat, and V. J. Trava-Airoldi, *Diamond Relat. Mater.*, **11** (2002) 1523.
26. G. Pastor-Moreno and D. J. Riley, *Electrochem. Commun.*, **4** (2002) 218.
27. R. Ramesham and M. F. Rose, *Diamond Relat. Mater.*, **6** (1997) 17.
28. S. Alehashem, F. Chambers, J. W. Strojek, G. M. Swain, and R. Ramesham, *Anal. Chem.*, **67** (1995) 2812.
29. C. D. Hodgman, 'Handbook of Chemistry and Physics', Chem. Rubber Publ. Co., Cleveland, Ohio, 1944.
30. G. Kokkinidis, *J. Electroanal. Chem.*, **172** (1984) 265.
31. Y. V. Pleskov, Y. E. Evstefeeva, M. D. Krotova, and A. V. Laptev, *Electrochim. Acta*, **44** (1999) 3361.
32. Y. V. Pleskov, Y. E. Evstefeeva, M. D. Krotova, V. V. Elkin, V. M. Mazin, V. Y. Mishuk, V. P. Varnin, and I. G. Teremetskaya, *J. Electroanal. Chem.*, **455** (1998) 139.
33. R. Ramesham, *Sensor and Actuators B*, **50** (1998) 131.
34. D. Gandini, P.-A. Michaud, I. Duo, E. Mahé, W. Haenni, A. Perret, and C. Comninellis, *New Diamond Front. Carbon Technol.*, **9** (1999) 303.
35. R. C. Engstrom and V. A. Strasser, *Anal. Chem.*, **56** (1984) 136.
36. K. F. Blurton, *Electrochim. Acta*, **18** (1973) 869.
37. P. Chen and R. L. McCreery, *Anal. Chem.*, **68** (1996) 3958.

## Results: Graphite deposition on BDD surfaces

The concept of non-diamond ( $sp^2$ ) species as charge transfer mediators on a diamond surface was suggested as an explanation for the electrochemical behaviour of diamond electrodes after surface oxidation treatment. To verify this concept, graphite particles were deposited on mildly polarised diamond electrodes so as to prepare diamond-graphite composite electrodes, and their properties were compared with those of as-grown diamond and carbon electrodes. With increasing graphite loading, the background current as well as the surface capacitance increased. The  $sp^2$  coverage on BDD was estimated by cyclic voltammetry. Charge transfer processes at the electrode surface were studied by steady-state (polarisation) and dynamic (cyclic voltammetry) potential-step methods. Outer-sphere electron transfer processes such as the redox system ferri/ferrocyanide ( $\text{Fe}(\text{CN})_6\text{III/II}$ ) and inner-sphere charge transfer reactions such as 1,4-benzoquinone/hydroquinone ( $\text{Q}/\text{H}_2\text{Q}$ ) were chosen to test the electrochemical properties of the electrodes. These redox systems became more reversible as the graphite loading increased. A strong analogy existed between as-grown diamond electrodes and diamond-graphite composite electrodes. In fact, by depositing graphite particles on diamond after its deactivation by anodic polarisation it was possible to restore the initial properties of the as-grown diamond electrode. A model was proposed which describes the BDD electrode surface as a diamond matrix in which non-diamond ( $sp^2$ ) species are dispersed.

## 1. Introduction

Recently, several research groups (those of Swain [1-5], Fujishima [6-9], Lévy-Clément [10], and Pleskov [11-13]) have made progress toward understanding the factors that can influence the behaviour of diamond electrodes. However, the relationship between the physical, chemical and electronic properties of diamond and the observed electrochemical behaviour is not yet completely understood. The electrochemical properties are influenced by (i) doping type and concentration, (ii) morphological features such as grain boundaries and point defects, (iii) non-diamond impurity content, (iv) crystallographic orientation, and (v) surface group functions (H, O, F, etc.). The combination of important factors and the degree of their influence strongly depend on the electrode reaction mechanism for a particular redox system [14].

In the previous chapter, the concept of  $sp^2$  species as charge transfer promoters on a diamond surface was proposed as an explanation for the electrochemical deactivation of diamond electrodes toward certain redox reactions used as probes after surface oxidation treatment. With the aim of testing this concept, graphite particles were deposited on diamond surfaces, and the electrochemical properties of the diamond-graphite composite electrodes thus obtained were compared with those of as-grown ( $BDD_{ag}$ ) and polarised ( $BDD_{mild}$ ) diamond electrodes and of carbon electrodes.

---

## 2. Experimental

### *Electrode preparation*

Boron-doped diamond electrodes were prepared by hot-filament chemical vapour deposition (HF-CVD) as described in Chapters 2 and 3. As-grown boron-doped diamond electrodes ( $BDD_{ag}$ ) were simply washed once with 2-propanol and twice with Milli-Q water in an ultrasonic bath to clean the surface without changing its hydrophobic properties. BDD electrodes polarised under mild conditions were obtained by 30 minutes of anodic polarisation at  $10 \text{ mA cm}^{-2}$  of as-grown electrodes in  $1 \text{ M H}_2\text{SO}_4$  ( $BDD_{mild}$ ). Graphite particles were deposited on a mildly polarised diamond surface by wiping the diamond sample over a graphite foil (Papyex “N”, Le Carbone S.A., Switzerland). Electrodes were tested with two graphite loadings, a low loading ( $BDD_{-g}$ ) and a high one ( $BDD_{-gh}$ ). The amount of graphite deposited on diamond was estimated from cyclic voltammetry.

### *Morphological characterisation*

The surface morphology was characterised using a JEOL JMS-6300-F scanning electron microscope (SEM). Samples were analysed before and after graphite deposition.

### *Electrochemical measurements*

An electrochemical mounting arrangement (Fig. 3.1 in Chapter 3) was used to accommodate the electrode sample, assure electrical contact, and obtain a geometrically well defined surface area ( $1 \text{ cm}^2$ ). A conventional three-electrode glass cell (0.1 L) was used for voltammetry (Fig. 3.2). The counterelectrode was a platinum spiral. A Hg/Hg<sub>2</sub>SO<sub>4</sub>, K<sub>2</sub>SO<sub>4(sat)</sub> electrode was used as the reference electrode. All values of potential are reported relative to a standard hydrogen electrode (SHE). Fluka Chemie chemicals and Milli-Q water were used to prepare solutions.

Cyclic voltammetry and steady-state polarisation were performed with a computer-controlled Autolab PGstat30. Polarisation curves were recorded at  $0.1 \text{ mV s}^{-1}$  over a 10 mV wide range around the equilibrium potential,  $E^0$ , after conditioning the electrode at the initial potential for 120 seconds.

---

## **3. Results and discussion**

### **3.1. Morphological characterisation**

#### *Scanning electron microscopy (SEM)*

SEM images were taken to characterise the electrode's morphology before (Fig. 4.1.A) and after graphite deposition (Fig. 4.1.B). The diamond surface was almost completely covered by a graphite deposit, but diamond crystals were still visible under the amorphous, discontinuous layer. A complex electrochemical system was investigated in which both graphite and diamond crystals were in contact with the solution (diamond-graphite composite electrodes).

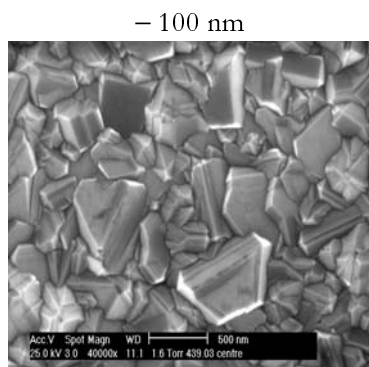


**FIGURE 4.1.A** SEM image of an anodically polarised diamond ( $BDD_{mild}$ ) electrode.

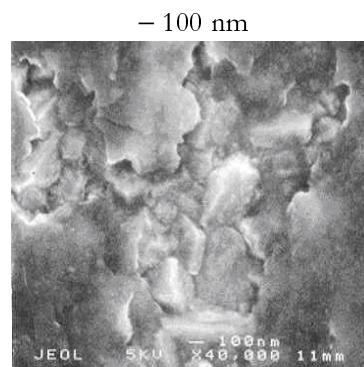


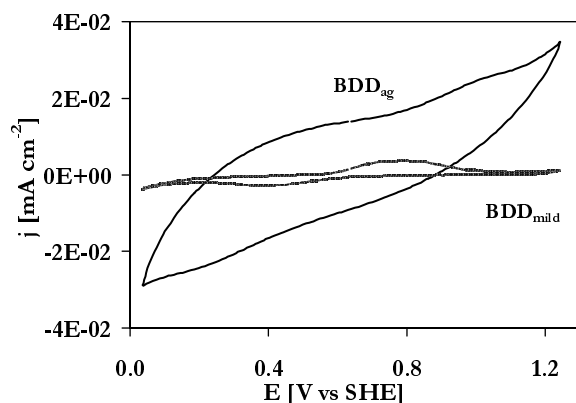
**FIGURE 4.1.B** SEM image of a  $BDD-g_1$  electrode.

### 3.2. Surface redox processes on BDD-graphite surfaces

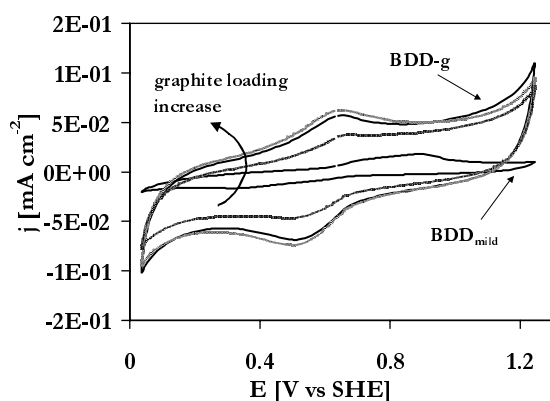
As already seen in the previous chapter, the voltammetric charge due to surface redox processes decreased strongly after mild anodic oxidation. The oxidation of  $sp^2$  carbon on the diamond surface and the resulting elimination of the surface carbon-oxygen functionalities could explain the reduced electroactivity of polarised diamond electrodes ( $BDD_{mild}$ ) in comparison to the as-grown ones ( $BDD_{ag}$ ).

Figure 4.2.A shows the differences in the electrode's response before and after mild anodic oxidation. As previously explained (Chapter 3), the high voltammetric charge of  $BDD_{ag}$  electrodes could be due to a pseudo-capacitance contribution from surface redox couples associated with the  $sp^2$  species present in the diamond matrix. Anodic oxidation eliminated the non-diamond carbon (oxidation to  $CO_2$ ) yielding a cleaner but less electroactive surface (Fig. 4.2.A). Amorphous carbon was reintroduced by wiping the diamond surface over graphite foil (Papyex material) in order to restore the initial properties. Many deposition steps were performed, and the electrode's response was recorded after each step (Fig. 4.2.B).

The voltammetric charge recorded in the voltammograms increased and the surface redox couple, represented by anodic and cathodic peaks in the voltammogram, became more reversible with increasing graphite loading (Fig. 4.2.B). These voltammograms were compared with that obtained for the carbon foil itself (Fig. 4.2.C). The pair of peaks is no longer distinguishable. The voltammetric charge of the carbon electrode is the result of convolution of many peaks due to numerous, more complex surface functionalities [15, 16].



**FIGURE 4.2.A** Cyclic voltammograms recorded at  $BDD_{ag}$  and  $BDD_{mild}$  electrodes in  $0.5\text{ M H}_2\text{SO}_4$ . Scan rate  $0.1\text{ V s}^{-1}$ .  $T = 25\text{ }^\circ\text{C}$ .



**FIGURE 4.2.B** Cyclic voltammograms recorded at a  $BDD_{mild}$  electrode in  $0.5\text{ M H}_2\text{SO}_4$  as a function of increasing graphite loading ( $BDD-g$ ). Scan rate  $0.1\text{ V s}^{-1}$ .  $T = 25\text{ }^\circ\text{C}$ .

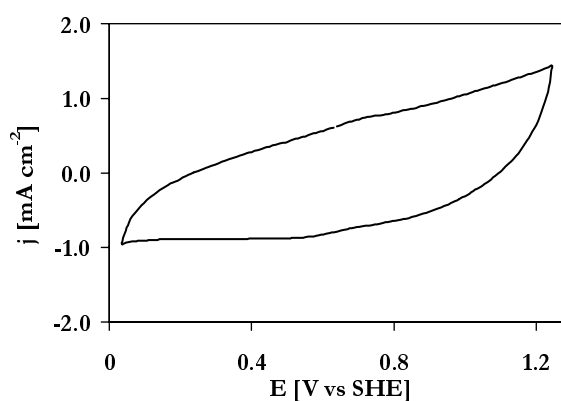


**FIGURE 4.2.C** Cyclic voltammogram recorded at a carbon electrode (Papyex) in  $0.5\text{ M H}_2\text{SO}_4$ . Scan rate  $0.1\text{ V s}^{-1}$ .  $T = 25\text{ }^\circ\text{C}$

The voltammetric charge of the composite electrode was calculated for each loading, and the results were compared with the values obtained for carbon electrodes. In Table 4.1, values for only two graphite loadings on BDD are reported: a low ( $BDD-g_l$  electrodes) and a high ( $BDD-g_h$  electrode) loading. Capacitance values were also calculated (Table 4.1) from cyclic voltammograms for three different values of potential using Equation 4.1:

$$i_c = 2C_{dl}v \quad 4.1$$

**TABLE 4.1.** Voltammetric charge and pseudocapacitance values calculated from cyclic voltammograms, and the average  $sp^2$  coverages for differently treated electrodes. Electrolyte: 0.5 M  $H_2SO_4$ . Scan rate  $0.1 \text{ V s}^{-1}$ .  $T = 25 \text{ }^\circ\text{C}$ .

Electrode	Charge [ $\text{mC cm}^{-2}$ ]	Pseudo-capacitance $C_x$ [ $\mu\text{F cm}^{-2}$ ]			$sp^2$ coverage $\theta$ [%] $C_x/C_{\text{carbon}}$
		0.64 [V vs SHE]	0.8 [V vs SHE]	1.1 [V vs SHE]	
<b>BDD<sub>ag</sub></b>	0.26	157	220	313	3.6
<b>BDD<sub>mild</sub></b>	0.10	61	128	48	1.3
<b>BDD-g<sub>l</sub></b>	0.23	208	151	136	2.6
<b>BDD-g<sub>h</sub></b>	0.52	538	329	306	6.0
<b>carbon</b>	8.16	7040	5662	6517	100

The capacitance values changed with potential because of the presence of surface redox systems active at different potentials (BDD<sub>ag</sub>). After anodic treatment (BDD<sub>mild</sub>), the capacitance values had decreased significantly and became almost potential-independent. The diamond-graphite composite electrodes, BDD-g<sub>l</sub> and BDD-g<sub>h</sub>, to the contrary, exhibited capacitance values similar to those of BDD<sub>ag</sub>.

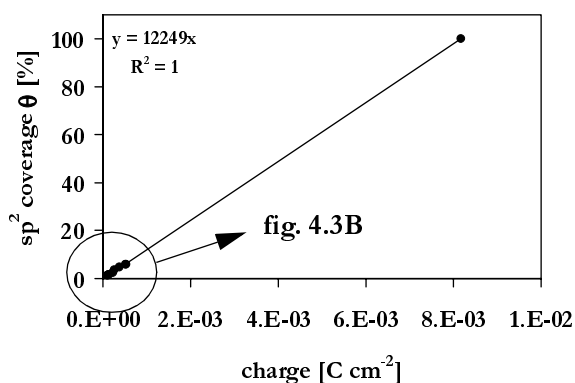


**FIGURE 4.3.A** Calibration curve for  $sp^2$  coverage and voltammetric charge at diamond-graphite composite electrodes. Scan rate:  $0.1 \text{ V s}^{-1}$ .

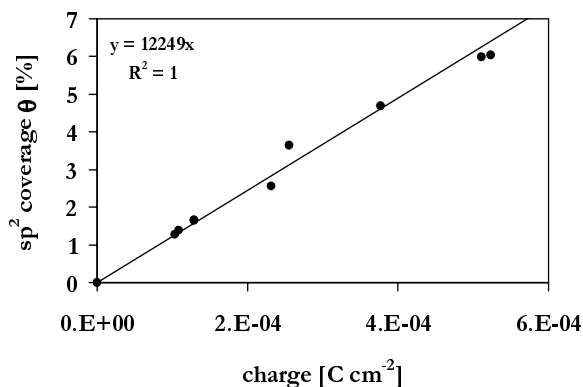


**FIGURE 4.3.B** Calibration curve for  $sp^2$  coverage and voltammetric charge at diamond-graphite composite electrodes. Zoom of Fig. 4.3.A for small  $sp^2$  coverages.

Assuming the carbon (Papyex) electrode to be a compact layer of  $sp^2$  carbon, its capacitance can then be taken as a reference in determining the  $sp^2$  coverage ( $\theta$ )



defined as the BDD surface fraction covered by graphite (Table 4.1). A straight-line relation exists between the  $sp^2$  coverage calculated from capacitance values and the voltammetric charge (Figs. 4.3.A and 4.3.B).

The  $sp^2$ -carbon coverage of a BDD-g surface can be simply calculated from voltammograms and a knowledge of the relation between coverage and voltammetric charge. Using the corresponding calibration curves a  $sp^2$  coverage of 2.6% was estimated for BDD-g<sub>l</sub> electrodes, and a coverage of 6% was calculated for BDD-g<sub>h</sub> electrodes. The  $sp^2$  content of BDD<sub>ag</sub> and BDD<sub>mild</sub> can also be estimated (3.6% and 1.3%, respectively).

### **3.3. Electrochemical behaviour of soluble redox systems at BDD-graphite electrodes**

Two redox reactions were chosen as probes in order to test the activity of the electrodes as a function of graphite coverage. The behaviour of ferri/ferrocyanide (Fe(CN)<sub>6</sub>III/II) and of 1,4-benzoquinone/hydroquinone (Q/H<sub>2</sub>Q) was investigated on BDD electrodes with different graphite loadings. The results were compared with the response of as-grown (BDD<sub>ag</sub>) and polarised (BDD<sub>mild</sub>) diamond electrodes.

**3.3.1. Outer-sphere electron transfer reactions.** On carbon electrodes the ferri/ferrocyanide system exhibits a quasi-reversible behaviour [17] but its kinetics is very sensitive to the electronic properties of the electrode surface [17-19]. Even though it is defined as an outer-sphere electron transfer reaction, the process depends on the chemical composition, oxidation level, and treatment of the electrode surface [20, 21]. Cyclic voltammetry and steady-state polarisation were used to study the influence of the graphite loading on the electron transfer process at diamond-graphite composite electrodes.

#### *Cyclic voltammetry*

Cyclic voltammetry was performed in order to study the behaviour of the ferricyanide/ferrocyanide system and calculate the transfer coefficient,  $\alpha_{\text{red}}$ ,  $\beta_{\text{ox}}$ , and apparent equilibrium potential,  $E^0$ . The voltammetric response of the electrodes is shown in Figures 4.4.A to 4.4.D. The redox system became more irreversible upon polarisation, and the current peak decreased significantly after

oxidation of the electrode surface (BDD<sub>ag</sub> and BDD<sub>mild</sub>). The initial behaviour was restored by graphite deposition (BDD-g<sub>l</sub> with 2.6%  $sp^2$ ).

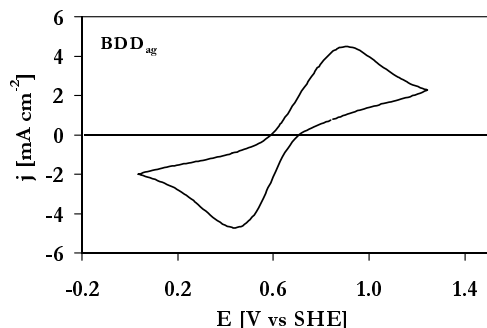


**FIGURE 4.4.A** Cyclic voltammogram for  $\text{Fe}(\text{CN})_6^{\text{III/II}}$   $12.5 \times 10^{-3} / 12.5 \times 10^{-3}$  M in 0.5 M  $\text{H}_2\text{SO}_4$ . Scan rate =  $0.1 \text{ V s}^{-1}$ .  $T = 25 \text{ }^\circ\text{C}$ . BDD<sub>ag</sub> electrodes.

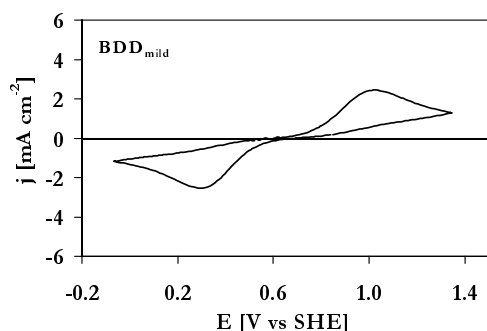


**FIGURE 4.4.B** Cyclic voltammogram for  $\text{Fe}(\text{CN})_6^{\text{III/II}}$   $12.5 \times 10^{-3} / 12.5 \times 10^{-3}$  M in 0.5 M  $\text{H}_2\text{SO}_4$ . Scan rate =  $0.1 \text{ V s}^{-1}$ .  $T = 25 \text{ }^\circ\text{C}$ . BDD<sub>mild</sub> electrodes.

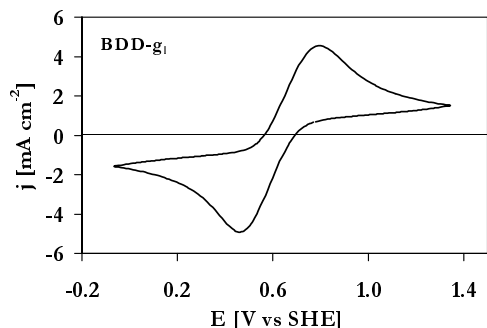


**FIGURE 4.4.C** Cyclic voltammogram for  $\text{Fe}(\text{CN})_6^{\text{III/II}}$   $12.5 \times 10^{-3} / 12.5 \times 10^{-3}$  M in 0.5 M  $\text{H}_2\text{SO}_4$ . Scan rate =  $0.1 \text{ V s}^{-1}$ .  $T = 25 \text{ }^\circ\text{C}$ . BDD-g<sub>l</sub> (2.6%  $sp^2$ ) electrodes.

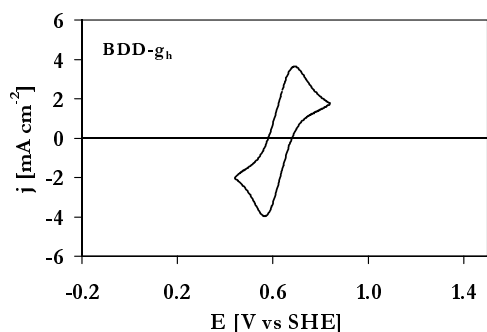


**FIGURE 4.4.D** Cyclic voltammogram for  $\text{Fe}(\text{CN})_6^{\text{III/II}}$   $12.5 \times 10^{-3} / 12.5 \times 10^{-3}$  M in 0.5 M  $\text{H}_2\text{SO}_4$ . Scan rate =  $0.1 \text{ V s}^{-1}$ .  $T = 25 \text{ }^\circ\text{C}$ . BDD-g<sub>h</sub> (6%  $sp^2$ ) electrodes.

The electrode's response was recorded at different scan rates (Figs. 4.5.A to 4.5.C) in order to calculate transfer coefficients. The mathematical treatment known to be valid for metals was applied to all electrodes investigated (Eqs. 2.17, 2.18, 2.19 for irreversible systems). Values of  $D = 7.35 \times 10^{-6} \text{ cm}^2 \text{ s}^{-1}$  and  $6.7 \times 10^{-6} \text{ cm}^2 \text{ s}^{-1}$  were used for the diffusion coefficients of  $\text{Fe}(\text{CN})_6\text{II}$  and  $\text{Fe}(\text{CN})_6\text{III}$ , respectively [22].

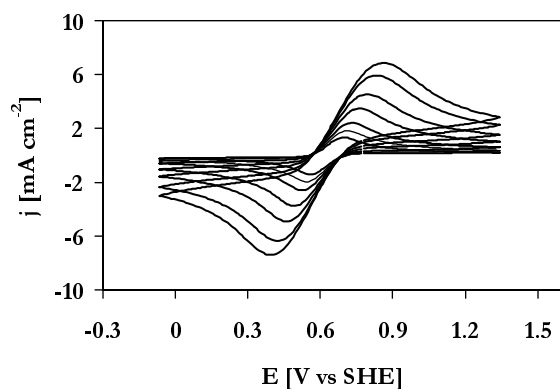


**FIGURE 4.5.A** Cyclic voltammograms for  $\text{Fe}(\text{CN})_6\text{III/II}$   $12.5 \times 10^{-3} / 12.5 \times 10^{-3} \text{ M}$  in  $0.5 \text{ M H}_2\text{SO}_4$  recorded at BDD- $g_1$  electrodes with different scan rates: 0.3; 0.2; 0.1; 0.05; 0.02; 0.01; 0.005  $\text{V s}^{-1}$ .  $T = 25^\circ\text{C}$ .

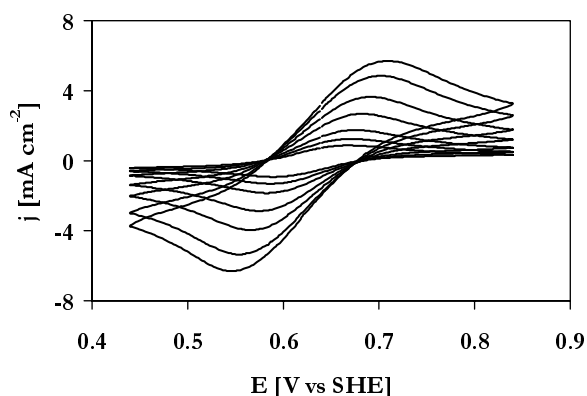


**FIGURE 4.5.B** Cyclic voltammograms for  $\text{Fe}(\text{CN})_6\text{III/II}$   $12.5 \times 10^{-3} / 12.5 \times 10^{-3} \text{ M}$  in  $0.5 \text{ M H}_2\text{SO}_4$  recorded at BDD- $g_h$  electrodes with different scan rates: 0.3; 0.2; 0.1; 0.05; 0.02; 0.01; 0.005  $\text{V s}^{-1}$ .  $T = 25^\circ\text{C}$ .

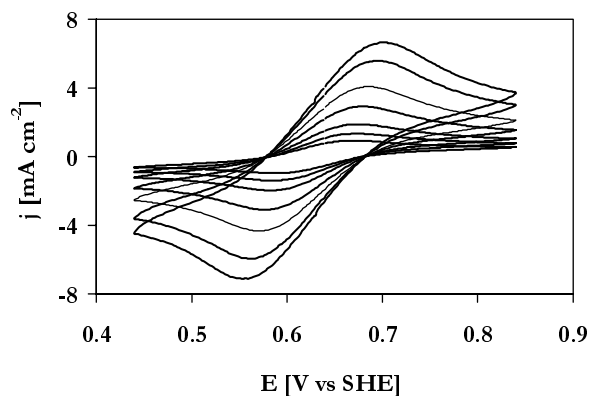


**FIGURE 4.5.C** Cyclic voltammograms for  $\text{Fe}(\text{CN})_6\text{III/II}$   $12.5 \times 10^{-3} / 12.5 \times 10^{-3} \text{ M}$  in  $0.5 \text{ M H}_2\text{SO}_4$  recorded at GC electrodes with different scan rates: 0.3; 0.2; 0.1; 0.05; 0.02; 0.01; 0.005  $\text{V s}^{-1}$ .  $T = 25^\circ\text{C}$

The transfer coefficients ( $\alpha_{\text{red}}$  and  $\beta_{\text{ox}}$ ) were calculated by two different methods: (1) by Equation 4.2, (2) by Equation 4.3. Table 4.2 summarises the parameter values.

$$|E_p - E_{p/2}| = 1.857 \frac{RT}{\alpha F} = 47.7 / \alpha \text{ mV at } 25^\circ\text{C} \quad \text{method (1)} \quad 4.2$$

$$E_p = E^{0'} - \frac{RT}{\alpha F} \left[ 0.78 + \ln \left( \frac{D_O^{1/2}}{k^0} \right) + \ln \left( \frac{\alpha F v}{RT} \right)^{1/2} \right] \quad \text{method (2)} \quad 4.3$$

**TABLE 4.2.** Parameters for the redox system  $\text{Fe}(\text{CN})_6\text{III/II}$  at BDD electrodes calculated from cyclic voltammograms recorded in 0.5 M  $\text{H}_2\text{SO}_4$ .  $T = 25^\circ\text{C}$ . Formal potential  $E^{0'} = 0.72\text{ V vs SHE}$ .

Electrode	$\Delta E_p$	$E^{0'}_{\text{app}}$	$\beta_{\text{ox}}$	$\beta_{\text{ox}}$	$\alpha_{\text{red}}$	$\alpha_{\text{red}}$
	[V]	[V]	(1)	(2)	(1)	(2)
<b>BDD<sub>ag</sub></b>	0.24	0.67	0.3	0.3	0.4	0.3
<b>BDD<sub>mild</sub></b>	0.53	0.66	0.3	0.3	0.3	0.3
<b>BDD-g<sub>l</sub></b>	0.16	0.63	0.3	0.3	0.3	0.3
<b>BDD-g<sub>h</sub></b>	0.08	0.63	0.5	0.5	0.5	0.5
<b>GC</b>	0.07	0.63	0.5	0.5	0.5	0.5

(1) determined from Eq. 4.2

(2) determined from Eq. 4.3

The electrochemical activity of BDD was strongly influenced by the surface treatment. The as-grown diamond (BDD<sub>ag</sub>) had a high activity toward the redox couple, whereas the same electrode after mild anodic polarisation was deactivated (BDD<sub>mild</sub>). The presence of  $sp^2$  carbon deposited on the diamond surface (BDD-g) increased the reaction rate, the irreversibility of the redox couple decreased. The behaviour of the as-grown electrode was completely restored (BDD-g<sub>l</sub>) and further improved (BDD-g<sub>h</sub>) by graphite deposition. A similar trend was found for the  $\alpha$  and  $\beta$  values. The sum  $\alpha_{\text{red}} + \beta_{\text{ox}}$  was lower than unity for diamond with low  $sp^2$  coverage (BDD<sub>ag</sub>, BDD<sub>mild</sub> and BDD-g<sub>l</sub>). For high graphite loadings (BDD-g<sub>h</sub> 6%  $sp^2$ ) and glassy carbon (GC) electrodes,  $\alpha_{\text{red}}$  and  $\beta_{\text{ox}}$  were considered equal to 0.5 because of reversible behaviour of the redox system on these electrodes.

### *Steady-state polarisation curves*

Polarisation of the electrodes was carried out in order to obtain the kinetic parameter,  $k^0$ , of the electrochemical reaction.

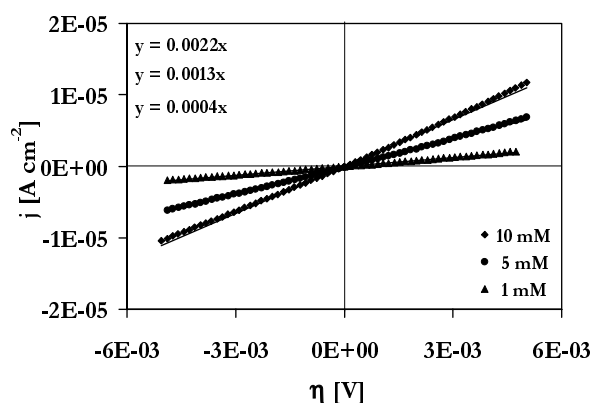


**FIGURE 4.6.A** Polarisation curves of BDD- $g_l$  electrodes in the  $\text{Fe}(\text{CN})_6\text{III/II}$  system at different concentrations. Electrolyte: 0.5 M  $\text{H}_2\text{SO}_4$ ; scan rate 0.1  $\text{mV s}^{-1}$ ;  $T = 25^\circ\text{C}$ .

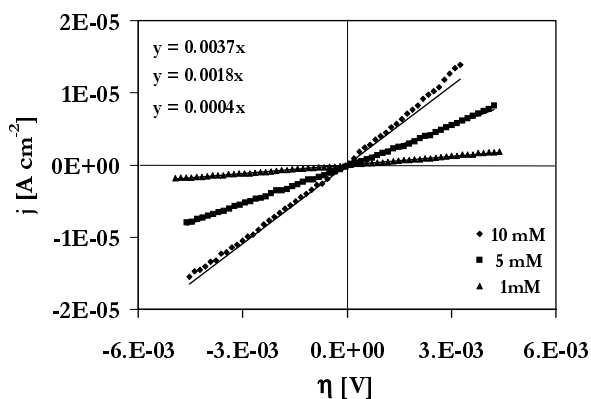


**FIGURE 4.6.B** Polarisation curves of BDD- $g_h$  electrodes in the  $\text{Fe}(\text{CN})_6\text{III/II}$  system at different concentrations. Electrolyte: 0.5 M  $\text{H}_2\text{SO}_4$ ; scan rate 0.1  $\text{mV s}^{-1}$ ;  $T = 25^\circ\text{C}$ .

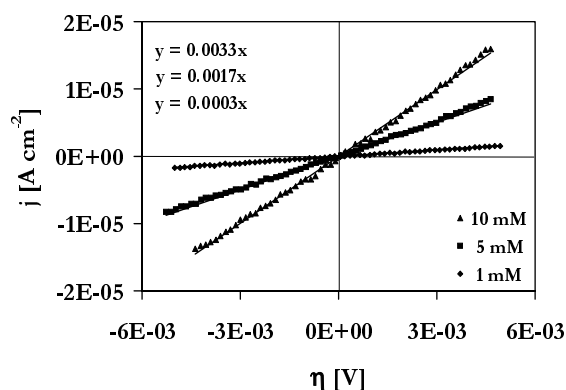


**FIGURE 4.6.C** Polarisation curves of GC electrodes in the  $\text{Fe}(\text{CN})_6\text{III/II}$  system at different concentrations. Electrolyte: 0.5 M  $\text{H}_2\text{SO}_4$ ; scan rate 0.1  $\text{mV s}^{-1}$ ;  $T = 25^\circ\text{C}$ .

The polarisation curves were sensitive to the concentration of the redox couple at all electrodes investigated (Figs. 4.6.A to 4.6.C). The electrode's response decreased upon anodic polarisation, as seen in the previous chapter. The polarisation curves were fitted to straight lines having slopes increasing linearly with the concentration. Using the lower-overpotential approximation ( $\eta < 10$  mV) of the Butler-Volmer equation (Eq. 2.13 of Chapter 2), the exchange current density  $j_0$  and the reaction rate constant  $k^0$  were calculated (Eqs. 4.4 and 4.5).

$$j = j_0 \frac{F}{RT} \eta \quad (n = 1) \quad 4.4$$

$$k^0 = \frac{j_0}{FC} \quad 4.5$$

**TABLE 4.3.** Reaction rate constants of the redox system  $\text{Fe}(\text{CN})_6\text{III/II}$   $12.5 \times 10^{-3} / 12.5 \times 10^{-3}$  M at different electrodes calculated from the results of steady-state polarisation measurements. Electrolyte: 0.5 M  $\text{H}_2\text{SO}_4$ . Scan rate  $0.1 \text{ mV s}^{-1}$ .  $T = 25 \text{ }^\circ\text{C}$ .

Electrode	$k^0$ [ $\text{cm s}^{-1}$ ]
BDD <sub>ag</sub>	$8 \times 10^{-5}$
BDD <sub>mild</sub>	$3 \times 10^{-5}$
BDD-g <sub>l</sub>	$8 \times 10^{-5}$
BDD-g <sub>h</sub>	$1 \times 10^{-4}$
GC	$1 \times 10^{-4}$

In this case, previous experiments by cyclic voltammetry had demonstrated that  $\alpha$  and  $\beta$  have the same value while their sum is a constant smaller than unity (see Eq. 3.8). The relation  $\alpha + \beta = 1$  was still supposed to be valid (see § 1.2.4) so that the Butler-Volmer equation could be used in the low-overpotential approximation ( $\eta < 1 \text{ mV}$ ) (Eq. 4.4).

The redox couple did not seem to be particularly sensitive to an important increase in the  $sp^2$  loading (Tab. 4.3), which is as expected for an outer-sphere redox couple; a similar behaviour was found on diamond ( $sp^3$ ) as well as non-diamond ( $sp^2$ ) carbon.

**3.3.2. Inner-sphere electron transfer reactions.** The behaviour of the inner-sphere benzoquinone/hydroquinone redox couple was investigated at BDD and BDD-graphite electrodes, and should be of interest because of the more complex molecular structure and of its multistep electron and proton transfer mechanism. The results were compared with those obtained on carbon materials.

#### *Cyclic voltammetry*

Cyclic voltammetry was performed on diamond-graphite composite electrodes, the results were compared with those reported in the previous chapter for treated diamond. The reversibility of the redox couple increased with the graphite loading, as shown in Figures 4.7.A to 4.7.D. The peak current was still

lower than in the case of a BDD<sub>ag</sub> electrode, indicating a more highly dispersed surface with  $sp^2$  character for the latter.

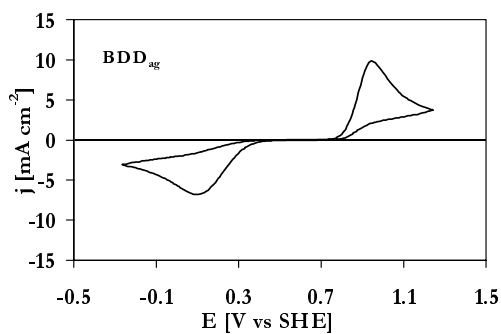


**FIGURE 4.7.A** Cyclic voltammogram for Q/H<sub>2</sub>Q 12.5x10<sup>-3</sup>/ 12.5x10<sup>-3</sup> M in 0.5 M H<sub>2</sub>SO<sub>4</sub>. Scan rate = 0.1 V s<sup>-1</sup>. T = 25 °C. BDD<sub>ag</sub> electrode.

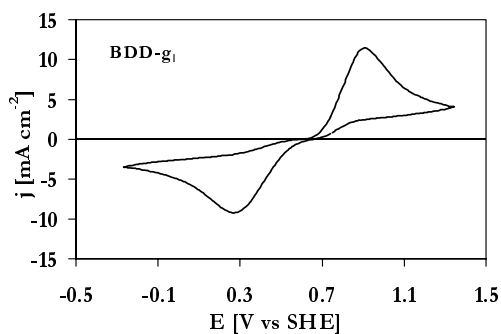


**FIGURE 4.7.B** Cyclic voltammogram for Q/H<sub>2</sub>Q 12.5x10<sup>-3</sup>/ 12.5x10<sup>-3</sup> M in 0.5 M H<sub>2</sub>SO<sub>4</sub>. Scan rate = 0.1 V s<sup>-1</sup>. T = 25 °C. BDD-g<sub>i</sub> electrode.

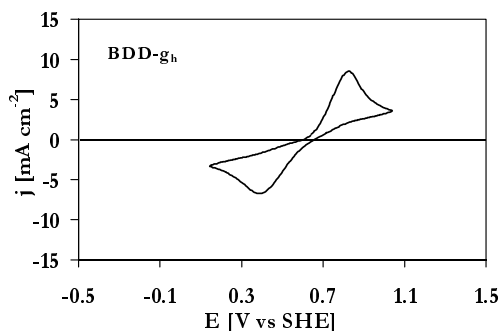


**FIGURE 4.7.C** Cyclic voltammogram for Q/H<sub>2</sub>Q 12.5x10<sup>-3</sup>/ 12.5x10<sup>-3</sup> M in 0.5 M H<sub>2</sub>SO<sub>4</sub>. Scan rate = 0.1 V s<sup>-1</sup>. T = 25 °C. BDD-g<sub>b</sub> electrode.

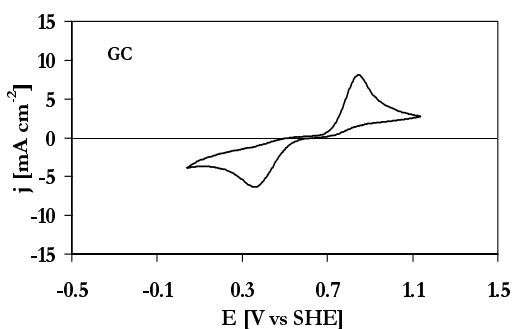


**FIGURE 4.7.D** Cyclic voltammogram for Q/H<sub>2</sub>Q 12.5x10<sup>-3</sup>/ 12.5x10<sup>-3</sup> M in 0.5 M H<sub>2</sub>SO<sub>4</sub>. Scan rate = 0.1 V s<sup>-1</sup>. T = 25 °C. CG electrode.

Measurements were made at several scan rates in order to study the behaviour of the redox system (Figs. 4.8.A to 4.8.D). The reversibility of the system ( $\Delta E_p$  value) and the transfer coefficients,  $\alpha_{\text{red}}$  and  $\beta_{\text{ox}}$ , were calculated from cyclic voltammetry (Eqs. 4.2 and 4.3). One electron was assumed to be transferred in the rate-determining step (r.d.s.) at the electrode surface. Values of  $D = 8.5 \times 10^{-6} \text{ cm}^2 \text{ s}^{-1}$  and  $9.8 \times 10^{-6} \text{ cm}^2 \text{ s}^{-1}$  reported in the literature for the diffusion coefficients of hydroquinone and benzoquinone, respectively [23], were used in the calculations. The results are shown in Table 4.4. Parameter values for  $\text{BDD}_{\text{ag}}$  and  $\text{BDD}_{\text{mild}}$  already reported in the previous chapter are listed for comparison.

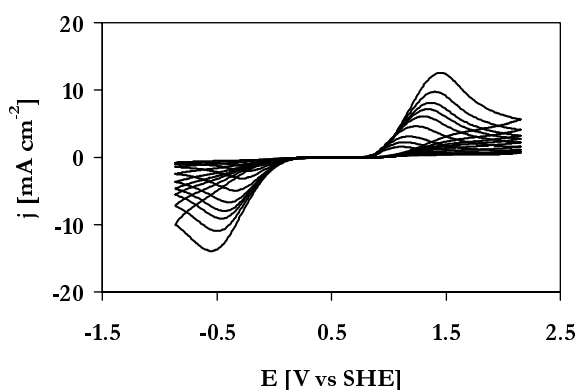


**FIGURE 4.8.A** Cyclic voltammograms for  $\text{Q}/\text{H}_2\text{Q}$   $12.5 \times 10^{-3} / 12.5 \times 10^{-3} \text{ M}$  in  $0.5 \text{ M H}_2\text{SO}_4$  recorded at  $\text{BDD}_{\text{mild}}$  electrodes with different scan rates: 5, 10, 20, 50, 100, 200 and  $300 \text{ mV s}^{-1}$ .  $T = 25 \text{ }^\circ\text{C}$ .

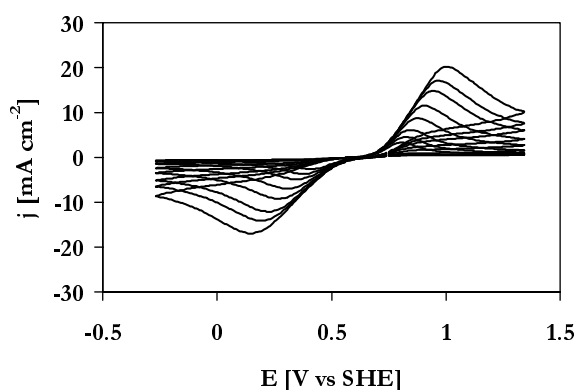


**FIGURE 4.8.B** Cyclic voltammograms for  $\text{Q}/\text{H}_2\text{Q}$   $12.5 \times 10^{-3} / 12.5 \times 10^{-3} \text{ M}$  in  $0.5 \text{ M H}_2\text{SO}_4$  recorded at  $\text{BDD-g}_l$  electrodes with different scan rates: 5, 10, 20, 50, 100, 200 and  $300 \text{ mV s}^{-1}$ .  $T = 25 \text{ }^\circ\text{C}$ .

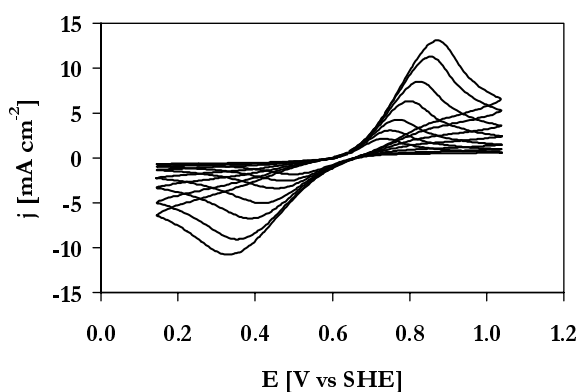


**FIGURE 4.8.C** Cyclic voltammograms for  $\text{Q}/\text{H}_2\text{Q}$   $12.5 \times 10^{-3} / 12.5 \times 10^{-3} \text{ M}$  in  $0.5 \text{ M H}_2\text{SO}_4$  recorded at  $\text{BDD-g}_h$  electrodes with different scan rates: 5, 10, 20, 50, 100, 200 and  $300 \text{ mV s}^{-1}$ .  $T = 25 \text{ }^\circ\text{C}$ .

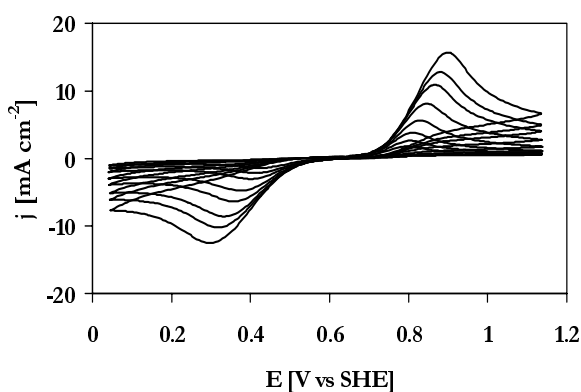


**FIGURE 4.8.D** Cyclic voltammograms for  $\text{Q}/\text{H}_2\text{Q}$   $12.5 \times 10^{-3} / 12.5 \times 10^{-3} \text{ M}$  in  $0.5 \text{ M H}_2\text{SO}_4$  recorded at GC electrodes with different scan rates: 5, 10, 20, 50, 100, 200 and  $300 \text{ mV s}^{-1}$ .  $T = 25 \text{ }^\circ\text{C}$ .



**TABLE 4.4.** Parameters for the redox system Q/H<sub>2</sub>Q 12.5x10<sup>-3</sup>/ 12.5x10<sup>-3</sup> M on BDD electrodes after different treatments. Cyclic voltammetry in 0.5 M H<sub>2</sub>SO<sub>4</sub>. T = 25 °C. Formal potential E<sup>0'</sup> = 0.65 V vs SHE.

Electrode	$\Delta E_p$	$E^{0'}_{app}$	$\beta_{ox}$	$\beta_{ox}$	$\alpha_{red}$	$\alpha_{red}$
	[V]	[V]	(1)	(2)	(1)	(2)
<b>BDD<sub>ag</sub></b>	0.74	0.52	0.5	0.3	0.3	0.3
<b>BDD<sub>mild</sub></b>	1.42	0.45	0.2	0.2	0.2	0.2
<b>BDD-g<sub>l</sub></b>	0.42	0.59	0.3	0.3	0.2	0.2
<b>BDD-g<sub>h</sub></b>	0.23	0.61	0.4	0.4	0.4	0.3
<b>GC</b>	0.37	0.61	0.5	0.4	0.4	0.4

(1) determined from Eq. 4.2

(2) determined from Eq. 4.3

The redox system was irreversible at polarised diamond electrodes, but the reversibility increased with the graphite loading ( $\Delta E_p$  values in Table 4.4). The transfer coefficient increased for both the anodic and the cathodic reaction, and their sum came close to unity (BDD-g<sub>h</sub>).

#### *Steady-state polarisation curves*

Polarisation measurements were performed in order to see how the graphite loading of BDD electrodes would influence the kinetics of the Q/H<sub>2</sub>Q redox process.

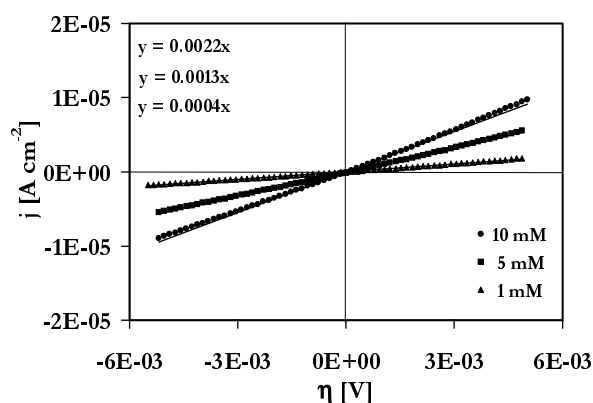


**FIGURE 4.9.A** Polarisation curves of BDD- $g_l$  electrodes in the Q/H<sub>2</sub>Q system at different concentrations. Electrolyte: 1 N H<sub>2</sub>SO<sub>4</sub>; scan rate 0.1 mV s<sup>-1</sup>; T = 25 °C.

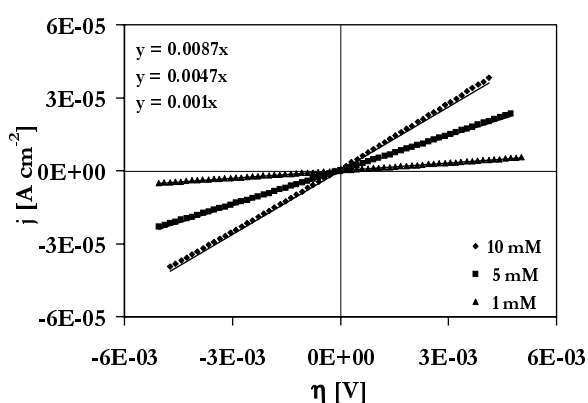


**FIGURE 4.9.B** Polarisation curves of BDD- $g_h$  electrodes in the Q/H<sub>2</sub>Q system at different concentrations. Electrolyte: 1 N H<sub>2</sub>SO<sub>4</sub>; scan rate 0.1 mV s<sup>-1</sup>; T = 25 °C.

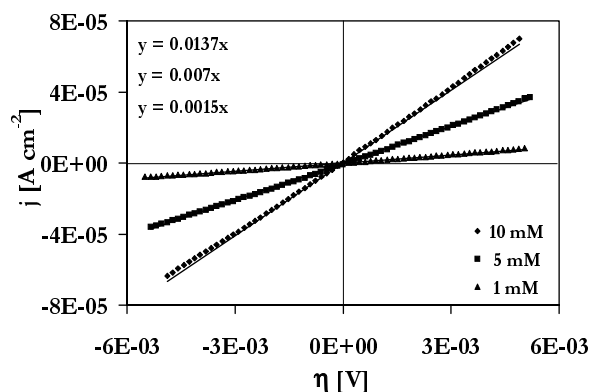


**FIGURE 4.9.C** Polarisation curves of GC electrodes in the Q/H<sub>2</sub>Q system at different concentrations. Electrolyte: 1 N H<sub>2</sub>SO<sub>4</sub>; scan rate 0.1 mV s<sup>-1</sup>; T = 25 °C.

The reaction rate constants were calculated in the low-overpotential approximation (Eqs. 4.4 and 4.5) of the Butler-Volmer equation (Eq. 2.9 of Chapter 2), the results were compared with those obtained at GC electrodes (Figs. 4.9.A and 4.9.B). The table below (Table 4.5) summarises the calculated values.

**TABLE 4.5.** Reaction rate constants calculated for the redox system Q/H<sub>2</sub>Q 12.5x10<sup>-3</sup> / 12.5x10<sup>-3</sup> M at different electrodes from steady-state polarisation measurements. Electrolyte: 0.5 M H<sub>2</sub>SO<sub>4</sub>. Scan rate 0.1 mV s<sup>-1</sup>. *T* = 25 °C.

Electrode	$k^0$ [cm s <sup>-1</sup> ]
BDD-g <sub>l</sub>	8x10 <sup>-5</sup>
BDD-g <sub>h</sub>	2x10 <sup>-4</sup>
GC	4x10 <sup>-4</sup>

Upon graphite deposition on the diamond surface, the reaction rate at the electrode increases up to values typical for carbon materials (GC). As already explained before, a value equal to unity was adopted for the sum of  $\alpha + \beta$ , in order to apply the low-overpotential approximation to the polarisation curves (Eq. 4.4). It is important to notice, however, that the sum of the calculated transfer coefficients was lower than unity for all the electrodes investigated.

### 3.4. Oxygen evolution reaction

The oxygen evolution reaction was also investigated on diamond-graphite composite electrodes. Graphite deposition on diamond decreased the overpotential of oxygen evolution (Fig. 4.10). The voltammetric curves revealed an overpotential decrease of about 1 volt.

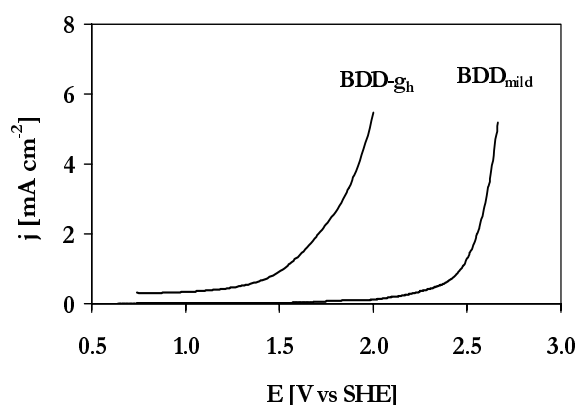


**FIGURE 4.10.** Voltammetric curves recorded at BDD<sub>mild</sub> and BDD-g<sub>h</sub> electrodes in the potential range of electrolyte decomposition. 0.5 M H<sub>2</sub>SO<sub>4</sub>. Scan rate 0.1 V s<sup>-1</sup>. *T* = 25 °C.

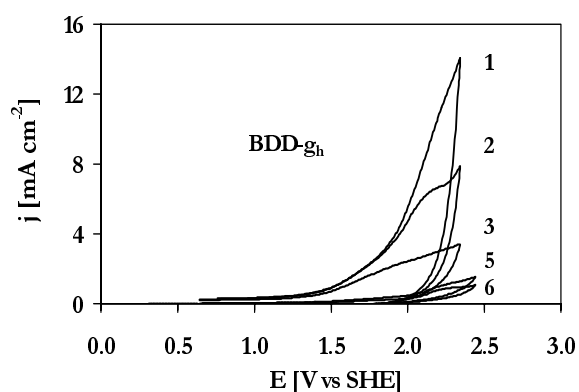


**FIGURE 4.11.** Cyclic voltammograms recorded at BDD-g<sub>h</sub> electrodes in the potential range of electrolyte decomposition. 0.5 M H<sub>2</sub>SO<sub>4</sub>. Scan rate 0.1 V s<sup>-1</sup>. *T* = 25 °C. Consecutive cycles: 1-6.

An activation of the electrode towards the oxygen evolution reaction was obtained. However, the system was not stable under these extreme conditions, and a fast decrease in the electrode's response was observed due to a progressive loss of graphite deposit (Fig. 4.11). In fact, electrochemical decomposition of the electrolyte produced hydroxyl radicals (see Chapter 2) which eliminated  $sp^2$  carbon by a corrosion phenomenon (oxidation to  $CO_2$ ).

---

## 4. Conclusions

Previous research on carbon materials [24] had demonstrated that a ferri/ferrocyanide system was not sensitive to oxide coverage while its kinetics was strongly influenced by the surface properties. On diamond electrodes, surface polarisation strongly decreased the rate of electron transfer [6, 7, 9]. The diamond film behaved like a composite film containing non-diamond carbon species within the diamond matrix [2]. Studies carried out on carbon electrodes showed that the microstructure of the carbon material was an important determinant of electrode reactivity [24]. However, because of the richness of carbon surface chemistry and the variety of existing carbon modifications, the final properties of solid carbon materials were difficult to evaluate, predict, or even reproduce. The irreproducibility of voltammetric experiments often noticed at as-grown diamond electrodes could be due to the presence of  $sp^2$  species that are oxidised during the CV experiment and give rise to a different oxidation level after each voltammetric cycle. The exact location and microstructure of the  $sp^2$  deposits on diamond is not well known as yet. Nevertheless, crystal grain boundaries and surface defects are likely to have a high  $sp^2$  density. On this basis, the deactivation of diamond electrodes by anodic polarisation could be due to the elimination of non-diamond species from the surface, with a consequent decrease in the number of active sites for specific adsorption of the reactant molecules. A nonnegligible amount of non-diamond carbon species on the surface of fresh electrodes ( $BDD_{ag}$ ) could be responsible for the electrocatalytic activity of these fresh BDD electrodes (Table 4.1), in analogy with amorphous carbon electrodes. Graphite and glassy carbon materials are in fact characterised by the presence of a surface quinone/hydroquinone-like system that is responsible for the irreversible pair of peaks seen in the background currents [15, 16]. Anodic polarisation of BDD could cause oxidation of the  $sp^2$  carbon to  $CO_2$ . A decreased surface activity of BDD after polarisation could be explained in terms of a "cleaner" surface on which only 'non-active' polycrystalline diamond was present. Upon graphite deposition on the diamond, the original properties of the  $BDD_{ag}$  electrodes were restored and even improved. This observation confirms the

influence of the  $sp^2$  carbon on BDD activity. The model proposed by Alehashem and others [2] (Fig. 4.12) can be used to represent the effect of the  $sp^2$  species on the electrochemical behaviour of diamond electrodes. BDD itself can be described as a composite electrode consisting of an ‘non-active’ matrix of polycrystalline diamond ( $sp^3$  carbon) in which species ( $sp^2$  carbon) are present. The  $sp^2$  carbon species can be considered as the primary pathway for the charge transfer process, assuming that electron transfer is much more significant at non-diamond than at diamond sites ( $k_{\text{non-diamond}}^0 \gg k_{\text{diamond}}^0$ ). In the potential range of electrolyte stability, the graphite ( $sp^2$ ) present on fresh diamond is quite stable and assures the high activity of electrodes (see also general discussion, Chapter 7).

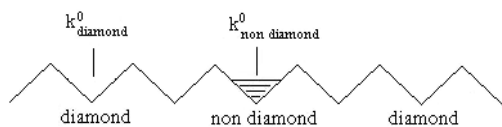


**FIGURE 4.12.** Diagram of diamond electrode structure: non-diamond species in a diamond matrix.  $k_{\text{non-diamond}}^0 \gg k_{\text{diamond}}^0$  [2].

The  $sp^2$  coverage of freshly prepared diamond electrodes decreases upon anodic treatment of the surface by a corrosion effect due to the formation of hydroxyl radicals. Assuming that the  $sp^2$  sites are more active than the  $sp^3$  sites, one can explain the progressive decrease of the current response with the oxidising treatment in terms of  $sp^2$  elimination.

Two potential domains can be distinguished when describing the behaviour of diamond electrodes. In the potential region of electrolyte stability, diamond electrodes exhibit a high activity towards the partial oxidation of organic compounds (oxidation of  $H_2Q$  to  $Q$ ). Since no electrolyte decomposition is involved and the compounds studied do not give rise to electrode fouling, the stability of the electrode's response is assured. In this case BDD behaves like a diamond-graphite composite electrode on which graphite represents the charge-transfer promoter in the system. Cyclic voltammetry can be used to estimate the  $sp^2$  coverage of the BDD surface with higher sensitivity than Raman spectroscopy. When the  $sp^2$  species are eliminated by a surface oxidation process, the electrode's response decreases strongly [25-27]. However, anodised diamond electrodes provide a more stable response, and even after the onset of fouling phenomena the activity can be restored by further anodisation of the surface [28, 29].

In the potential region of electrolyte decomposition, graphite is eliminated from the BDD-graphite composite surface by oxidation to CO<sub>2</sub>. BDD itself behaves as an 'non-active' electrode (see § 2.5). In this case the oxidation of organic compounds is mediated by hydroxyl radicals formed during water discharge. CO<sub>2</sub> and H<sub>2</sub>O are the final products of an oxidation process occurring without any participation of the electrode surface. In the next chapter, the behaviour of 'non-active' diamond in organic oxidation processes occurring in the potential region of water discharge will be described in greater detail.

---

## 5. Acknowledgement

I am thankful to the Interdepartmental Centre of Electronic Microscopy (CIME) at EPFL, Lausanne, and in particular to Mr B. Senior, for SEM measurements. I wish to thank Mr N. Guignon for performing part of the cyclic voltammetry experiments.

---

## 6. References

1. J. K. Zak, J. E. Butler, and G. M. Swain, *Anal. Chem.*, **73** (2001) 908.
2. S. Alehashem, F. Chambers, J. W. Strojek, G. M. Swain, and R. Ramesham, *Anal. Chem.*, **67** (1995) 2812.
3. M. C. Granger and G. M. Swain, *J. Electrochem. Soc.*, **146** (1999) 4551.
4. G. M. Swain, *Anal. Chem.*, **65** (1993) 345.
5. G. M. Swain, A. B. Anderson, and J. C. Angus, *MRS Bull.*, **23** (1998) 56.
6. H. Notsu, I. Yagi, T. Tatsuma, D. A. Tryk, and A. Fujishima, *J. Electroanal. Chem.*, **492** (2000) 31.
7. H. Notsu, I. Yagi, T. Tatsuma, D. A. Tryk, and A. Fujishima, *Electrochem. Solid-state Lett.*, **2** (1999) 522.
8. I. Yagi, H. Notsu, T. Kondo, D. A. Tryk, and A. Fujishima, *J. Electroanal. Chem.*, **473** (1999) 173.
9. D. A. Tryk, K. Tsunozaki, T. N. Rao, and A. Fujishima, *Diamond Relat. Mater.*, **10** (2001) 1804.
10. R. Tenne and C. Lévy-Clément, *Isr. J. Chem.*, **38** (1998) 57.
11. Y. V. Pleskov, Y. E. Evstefeeva, M. D. Krotova, V. V. Elkin, V. M. Mazin, V. Y. Mishuk, V. P. Varnin, and I. G. Teremetskaya, *J. Electroanal. Chem.*, **455** (1998) 139.

12. Y. V. Pleskov, *Russ. Chem. Rev.*, **68** (1999) 381.
13. Y. V. Pleskov, Y. E. Evstefeeva, M. D. Krotova, V. Y. Mishuk, V. A. Laptev, Y. N. Palyanov, and Y. M. Borzdov, *J. Electrochem. Soc.*, **149** (2002) E260.
14. J. Xu, M. G. Granger, J. Wang, Q. Chen, M. A. Witek, M. L. Hupert, A. Hanks, and G. M. Swain, in *Proceedings - Electrochemical Society*, Vol. 99-32 (Diamond Materials), 2000, p. 403.
15. D. Laser and M. Ariel, *J. Electroanal. Chem.*, **52** (1974) 291.
16. K. F. Blurton, *Electrochim. Acta*, **18** (1973) 869.
17. M. R. Deakin, K. J. Stutts, and R. M. Wightman, *J. Electroanal. Chem.*, **182** (1985) 113.
18. W. J. Blaedel and G. W. Schieffer, *J. Electroanal. Chem.*, **80** (1977) 259.
19. R. J. Taylor and A. A. Humffray, *J. Electroanal. Chem.*, **42** (1973) 347.
20. I.-F. Hu, D. H. Karweik, and T. Kuwana, *J. Electroanal. Chem.*, **188** (1985) 59.
21. R. C. Engstrom and V. A. Strasser, *Anal. Chem.*, **56** (1984) 136.
22. C. D. Hodgman, 'Handbook of Chemistry and Physics', Chem. Rubber Publ. Co., Cleveland, Ohio, 1944.
23. G. Kokkinidis, *J. Electroanal. Chem.*, **172** (1984) 265.
24. P. Chen and R. L. McCreery, *Anal. Chem.*, **68** (1996) 3958.
25. T. N. Rao, I. Yagi, T. Miwa, D. A. Tryk, and A. Fujishima, *Anal. Chem.*, **71** (1999) 2506.
26. T. N. Rao, B. V. Sarada, D. A. Tryk, and A. Fujishima, *J. Electroanal. Chem.*, **491** (2000) 175.
27. B. V. Sarada, T. N. Rao, D. A. Tryk, and A. Fujishima, *Anal. Chem.*, **72** (2000) 1632.
28. C. Terashima, T. N. Rao, B. V. Sarada, D. A. Tryk, and A. Fujishima, *Anal. Chem.*, **2** (2002)
29. E. Popa, H. Notsu, T. Miwa, D. A. Tryk, and A. Fujishima, *Electrochem. Solid-state Lett.*, **2** (1999) 45.

## **Results: Electrochemical oxidation of EDTA on BDD. Application to waste water treatment**

---

The electrochemical oxidation of ethylenediaminetetraacetic acid (EDTA) was investigated at boron-doped diamond (BDD) electrodes. Cyclic voltammetry in the potential region of water stability showed that EDTA was oxidised in an irreversible two electron transfer mechanism. No fouling phenomena were noticed on the electrode surface. An oxidation mechanism of EDTA involving intermediates formed during water discharge (hydroxyl radicals) was proposed and the model developed for organic oxidation at 'non-active' anodes was used to predict results for the oxidation of EDTA at BDD electrodes. Preparative electrolyses were performed under current control, mixed control and mass transport control. The very good fit between experimental results and theoretical values confirmed that EDTA oxidation at diamond in the potential region of electrolyte decomposition was a fast reaction involving free electrogenerated hydroxyl radical intermediates formed at the anode during water discharge.



## 1. Introduction

Recent research has demonstrated that electrochemistry is an attractive alternative to traditional methods for waste water treatment [1-3]. Several anodes have so far been tested in the electrochemical oxidation of organic model compounds. It had already been found that electrochemical oxidation of most organics in aqueous media only occurs at high potentials and with the concomitant evolution of molecular oxygen, and without any loss in electrode activity [2, 4-6]. It had also been demonstrated that the nature of the electrode material strongly influences both the selectivity and the efficiency of the process [5, 7-9]. A comprehensive model for anodic oxidation of organics in acidic media including the competition with oxygen evolution has been proposed in order to interpret these observations [5, 7-9]. The model allows two different cases to be distinguished, viz., 'active' and 'non-active' electrodes (see § 2.5 of Chapter 2).

Because of its high chemical and electrochemical stability and large potential window, diamond is a promising material for waste water treatment applications [10-13]. Because of its inert character and weak adsorption properties, boron-doped diamond exhibits the typical behaviour of a 'non-active' electrode. In fact, at high overpotentials, which is the region of electrolyte decomposition, electrogenerated hydroxyl radicals can oxidise the organic compounds to CO<sub>2</sub> and water with a very high current efficiency. The formation of free hydroxyl radicals on BDD in the potential region of water discharge was recently demonstrated {[14] by spin trapping using electron spin resonance (ESR).

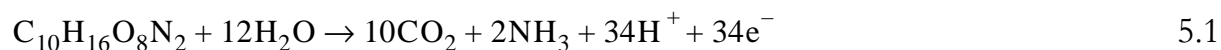
Ethylenediaminetetraacetic acid (EDTA) is the chelating agent most often employed in industrial and commercial applications. It is used to complex metal ions in electroplating and paper processes, leather manufacture and textile finishing. It is also used in consumer products such as shampoos, and to protect food from spoilage. While EDTA itself does not pose significant problems to the environment, its ability of complexing metals has an adverse effect on metal removal in waste water treatment plants. EDTA increases the mobility of metals in aquatic systems, but EDTA complexation also reduces the toxicity of pollutant metals to aquatic organisms. Several chromatographic techniques have been developed to detect EDTA-metal complexes in environmental systems. Few studies have been performed, to the contrary, to investigate the electrochemical oxidation of EDTA and the simultaneous recovery of metals by reduction [15-17].

In the present work the electrochemical oxidation of EDTA was investigated at BDD anodes, both at the potentials of electrolyte stability and at those of

electrolyte decomposition. The experimental results have been compared with the theoretical model for organic oxidation at ‘non-active’ anodes [18].

### 1.1. Theoretical model for oxidation of EDTA at BDD electrodes

The theoretical model has been developed to predict the current efficiency of the electrochemical oxidation of organic compounds in a batch recirculation system under galvanostatic conditions. It is assumed in this model, which here is applied to EDTA oxidation (Eq. 5.1), that the rate of electrochemical combustion of the organic substance is a fast reaction controlled by mass transport of the organic toward the anode (see Chapter 2).



The limiting current density,  $j_{\text{lim}}$ , of the reaction can be calculated as follows (Eq. 5.2):

$$j_{\text{lim}}(t) = 34 F k_m \left[ \text{C}_{10}\text{H}_{16}\text{O}_8\text{N}_2 \right]_{(t)} \quad 5.2$$

where  $k_m$  is the average mass transfer coefficient in the reactor. Since the overall reaction of complete EDTA oxidation to  $\text{CO}_2$  and water can be written as follows (Eq. 5.3):



the limiting current density can be related to the COD of the solution during the reaction (Eq. 5.4):

$$j_{\text{lim}}(t) = 4 F k_m \text{COD}(t) \quad 5.4$$

Depending on the value of applied current density relative to the limiting current density, two different operating regimes have been identified:

- $j_{\text{appl}} < j_{\text{lim}}$ : electrolysis proceeds under current control, the current efficiency is 100%, and the COD decreases linearly with the charge consumed.
- $j_{\text{appl}} > j_{\text{lim}}$ : electrolysis proceeds under mass-transport control, side reactions which take place at the anode (oxygen evolution, peroxodisulphate formation, etc.) depress the ICE to values distinctly below 100 %. The COD removal follows an exponential decay curve.

Table 5.1 briefly summarises the equations of the theoretical model which hold under current and mass-transport control (see § 2.5 of Chapter 2):

**TABLE 5.1.** Equations of the theoretical model which predict the current efficiency,  $\eta$ , and COD as functions of time in the electrochemical oxidation of organic compounds at BDD electrodes.

Work limitations	$\eta$	COD
$j_{\text{appl}} < j_{\text{lim}}$ current control	$ICE = 1$	$COD = COD^0 \left( 1 - \alpha \frac{Ak_m t}{V_R} \right)$
$j_{\text{appl}} > j_{\text{lim}}$ mass transport control	$ICE = \exp \left( -\frac{Ak_m t}{V_R} + \frac{1 - \alpha}{\alpha} \right)$	$COD = \alpha COD^0 \left( -\frac{Ak_m t}{V_R} + \frac{1 - \alpha}{\alpha} \right)$

It is assumed in the model that EDTA combustion is a fast process at diamond. This implies that electrogenerated hydroxyl radicals are extremely active intermediates able to react with the organic compound in a fast chemical reaction. This high activity is due to the free state of these intermediates on BDD. The high overpotential of water discharge on diamond allows extremely active free hydroxyl radicals to be electrogenerated which then undergo a fast reaction with EDTA molecules in the solution layer close to the anode surface. These free radicals have recently been trapped by spin trapping and identified by electron spin resonance (ESR) [14].

## 2. Experimental

### *Electrode preparation*

Boron-doped diamond electrodes were prepared by hot-filament chemical vapour deposition (HF-CVD) using the procedure explained in Chapter 2 and 3. The process gas was a mixture of 1% CH<sub>4</sub> in H<sub>2</sub> containing trimethylboron as a boron source. A gas flow of 5 dm<sup>3</sup> min<sup>-1</sup> was supplied into the chamber where a tantalum filament was heated to 2440-2560 °C while a pressure of 5000 to 10 000 Pa was maintained. Film growth occurred at a rate of 0.24 μm h<sup>-1</sup>, and polycrystalline films were grown to a thickness of 1 μm. The boron/carbon ratio in the diamond films was about 4500 to 5500 ppm, corresponding to a concentration of 10<sup>20</sup> to

$10^{21}$  boron atoms  $\text{cm}^{-3}$  (the semiconductor-metal transition occurs at  $2 \times 10^{20} \text{ cm}^{-3}$ ). The electrical resistivity,  $\rho$ , was 10-20  $\text{m}\Omega \text{ cm}$ . These diamond electrodes were anodised at  $10 \text{ mA cm}^{-2}$  in 1 M  $\text{H}_2\text{SO}_4$  in order to remove  $sp^2$  carbon from the surface.

### *Electrochemical measurements*

Cyclic voltammetry was performed with a computer-controlled Autolab PGstat30. A conventional three-electrode glass cell (0.1 L) was used for voltammetry. A polarised diamond electrode ( $\text{BDD}_{\text{mild}}$ ) was used as the working electrode. The counterelectrode was a platinum spiral. A  $\text{Hg}/\text{Hg}_2\text{SO}_4$ ,  $\text{K}_2\text{SO}_{4,\text{sat}}$  electrode was used as the reference electrode. All values of potential are reported relative to a standard hydrogen electrode (SHE). The supporting electrolyte was 1 M  $\text{NaClO}_4$  to which concentrate solutions of  $\text{HClO}_4$  or  $\text{NaOH}$  were added in order to adjust the pH to values between 1 and 10. Fluka Chemie chemicals and Milli-Q water were used to prepare the solutions.

### *Bulk electrolysis*

Bulk electrolyses were performed using the complete setup shown in Figure 5.1.A. The solution was introduced into a thermostatted glass tank (1) and circulated through the electrochemical flow-through cell (2) using an Iwaki, Model MD 40R. magnetic pump (4). The flow rate of the solution in the system was  $67 \text{ L h}^{-1}$ . The galvanostatic conditions were obtained by a current supply (3).

In Figure 5.1.B, details of the electrochemical batch reactor are shown. Cathode (zirconium) and anode (BDD) were arranged in the cell (3 and 4 in Fig. 5.1.B) at a mutual distance of 1 cm, and parallel to the flow direction (from 2 to 1). A mass transfer coefficient of  $2 \times 10^{-5} \text{ m s}^{-1}$  was calculated using the ferri/ferro redox couple as a probe. The electrodes (6 and 7) were contacted from the rear. Fluka Chemie chemicals and Milli-Q water were used to prepare the solutions. Chemical oxygen demand (COD) was measured by UV-visible spectrophotometry using HACH chemicals. Total organic carbon (TOC) was measured by a TOC-5050 Shimadzu analyser.

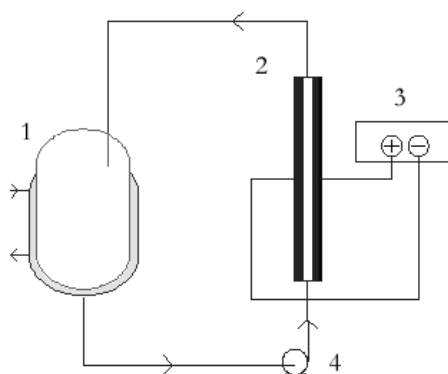


**FIGURE 5.1.A** Electrochemical setup: (1) thermostatted glass tank, (2) electrochemical flow-through cell, (3) current supply, (4) magnetic pump.

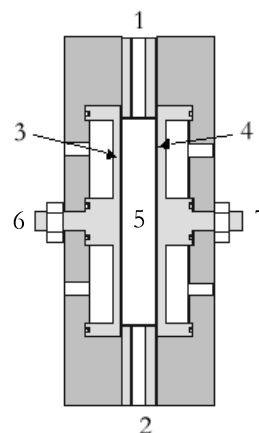


**FIGURE 5.1.B** Electrochemical flow-through cell: (1) and (2) outlet and inlet of the solution, (3) anode, (4) cathode, (5) reactor compartment, (6) and (7) electrical contacts.

The instantaneous current efficiency (ICE) for the anodic oxidation of EDTA has been calculated from the values of COD using the following relation:

$$ICE = 4FV \frac{[(COD)_t - (COD)_{t+\Delta t}]}{I\Delta t} \quad 5.5$$

where  $(COD)_t$  and  $(COD)_{t+\Delta t}$  are the chemical oxygen demand values ( $\text{mol O}_2 \text{ m}^{-3}$ ) at times  $t$  and  $t+\Delta t$ , respectively,  $I$  is the current (A),  $F$  is the Faraday constant ( $\text{C mol}^{-1}$ ) and  $V$  is the volume of electrolyte ( $\text{m}^3$ ).

Formaldehyde was detected using a spot test that was appropriately modified in order to quantify the product concentration [16]. A 0.2-mL solution sample containing formaldehyde was given into a 50-mL flask to which 3 mL of concentrated  $\text{H}_2\text{SO}_4$  and 1 mL of 10% chromotropic acid were added. The sample was heated for 10 min in a water bath to 60 °C. The sample was then diluted to 50 mL and analysed using a UV-vis spectrophotometer. The formaldehyde peak was observed at 580 nm. The concentrations were calculated via a calibration curve constructed with standard solutions.

### 3. Results and discussion

The electrochemical behaviour of EDTA was tested by cyclic voltammetry at BDD electrodes. The electrochemical oxidation of EDTA was investigated in the potential region of electrolyte stability as well as in the presence of electrolyte decomposition. The theoretical model for EDTA oxidation at a 'non-active' BDD electrode was used to predict COD removal and current efficiency in the process.

#### 3.1. Cyclic voltammetry

BDD electrodes were investigated by cyclic voltammetry in the presence of EDTA in aqueous  $\text{NaClO}_4$  solutions at different pH values. The pH value was adjusted by adding aqueous  $\text{NaOH}$  or  $\text{HClO}_4$  solutions to the supporting electrolyte,  $\text{NaClO}_4$ . Figure 5.2 shows the cyclic voltammograms recorded at different pH values. In experiments at pH 1 through pH 4, well defined peaks due to EDTA oxidation at the electrode surface were visible. The oxidation process was irreversible (no reverse peak was recorded) and took place at potentials below 2 V *vs* SHE, *i.e.*, in the potential region of electrolyte stability. At higher values of pH the electrode's response split up into two peaks (curves not reported), which were both attributed to EDTA oxidation. The fact that two peaks appeared at higher pH values was probably related to the various equilibria of hydrogen with EDTA [19]. An acidic medium was preferred for studying the electrochemical oxidation of EDTA at diamond.

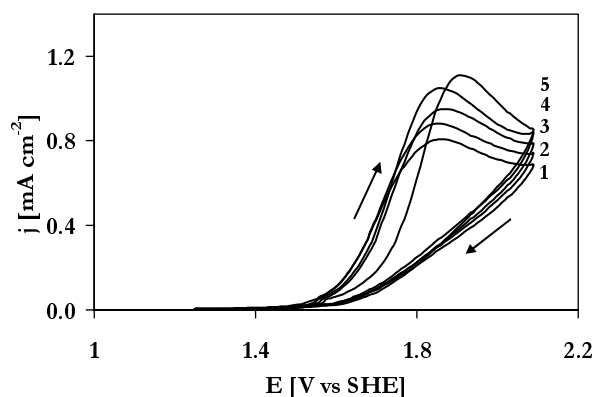


**FIGURE 5.2.** Cyclic voltammetry of  $10^{-3}$  M EDTA in 1 M  $\text{NaClO}_4$  at different pH: 1) 1; 2) 1.5; 3) 2; 4) 2.5; 5) 4. Scan rate  $0.1 \text{ V s}^{-1}$ .  $T = 25$  °C.

The dependence of the current peaks on scan rate was investigated at a fixed EDTA concentration and pH. Figure 5.3 shows the linear relation found between the peak currents and the square root of scan rate, which is typical for a diffusion-controlled process. A value of  $D = 3.6 \times 10^{-6} \text{ cm}^2 \text{ s}^{-1}$  was calculated for the diffusion coefficient using the relation 5.6 [20]:

$$i_p = (2.99 \times 10^5) \alpha^{1/2} A C^* D_o^{1/2} v^{1/2} \quad 5.6$$

where  $A = 1 \text{ cm}^2$ ,  $C = 1 \text{ mM}$  and  $\alpha = 0.5$ .

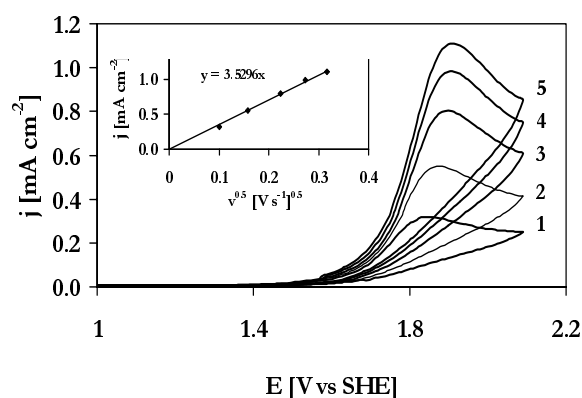


**FIGURE 5.3.** Cyclic voltammetry of 1 mM EDTA in 1 M  $\text{NaClO}_4$  recorded at  $\text{pH} = 2$  with different scan rates ( $\text{mV s}^{-1}$ ): 1) 10; 2) 25; 3) 50; 4) 75; 5) 100.  $T = 25 \text{ }^\circ\text{C}$ .

The increase of the peak currents with increasing EDTA concentration (Fig. 5.4) indicated that EDTA oxidation was responsible for the electrode's response. The linear relation between these currents and the concentration and the absence of fouling processes at the electrode surface suggested that it should be possible to follow the EDTA concentration in solution by cyclic voltammetry during the electrolysis process. A value of  $D = 3.2 \times 10^{-4} \text{ cm}^2 \text{ s}^{-1}$  was calculated for the diffusion coefficient from the figure 5.4 using the relation 5.6[20].

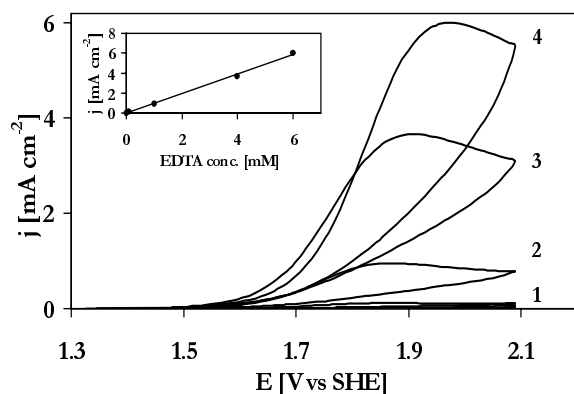


**FIGURE 5.4.** Cyclic voltammetry of EDTA in 1 M  $\text{NaClO}_4$  at  $\text{pH} = 2$  for different EDTA conc. (mM): 1) 0.1; 2) 1; 3) 4; 4) 6.  $\text{pH} = 2$ . Scan rate  $0.1 \text{ V s}^{-1}$ .  $T = 25 \text{ }^\circ\text{C}$ .

A possible mechanism had been already proposed for the oxidation of EDTA at Pt anodes[17]. A sequence *E-C-E* (Electrochemical - Chemical - Electrochemical) was proposed (Fig. 5.5) in which a first electron transfer step was followed by a chemical step in which a proton was eliminated. Then another electron transfer step took place leading to two possible molecular rearrangements. Thus, the electroactivity of EDTA at BDD electrodes in the potential region of electrolyte stability can be explained by an overall two-electron transfer mechanism (Fig. 5.5).

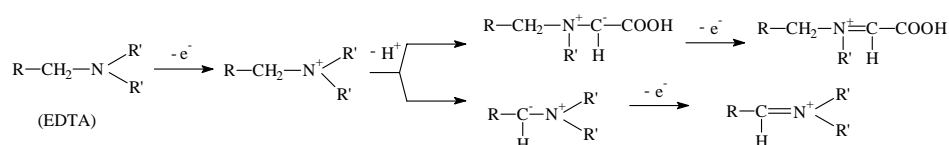


**FIGURE 5.5.** Reaction scheme for the electrooxidation of EDTA in the potential region of electrolyte stability. R = -CH<sub>2</sub>N(CH<sub>2</sub>COOH)<sub>2</sub>; R' = -CH<sub>2</sub>COOH. [17].

The behaviour of EDTA at diamond was also investigated in the potential region of electrolyte decomposition. Figure 5.6 shows typical voltammograms obtained in the potential region of electrolyte decomposition. The presence of EDTA caused a decrease in overpotential. This observation may indicate that EDTA oxidation involved intermediates formed during water discharge. Tafel plots (the inset in Fig. 5.6) were recorded for different EDTA concentrations. The Tafel slopes increased from 114 to 200 mV dec<sup>-1</sup> as the EDTA concentration rose from 0 to 4 x 10<sup>-3</sup> M. EDTA influenced the kinetics of O<sub>2</sub> evolution by reacting with intermediates involved in oxygen evolution.

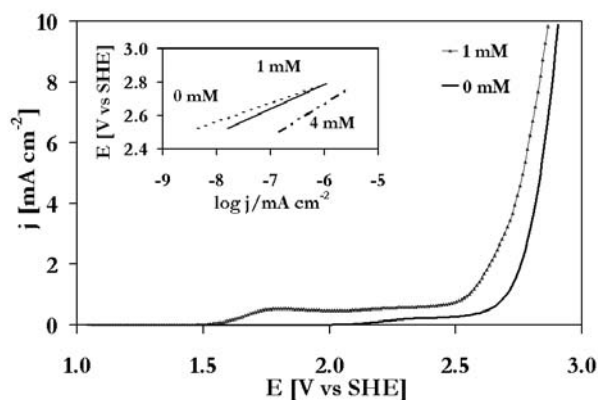


**FIGURE 5.6.** Steady-state polarisation curves of a BDD electrode in 1 M NaClO<sub>4</sub> recorded at different EDTA concentration (mM): 1) 0; 2) 1; 3) 4. pH = 2. Scan rate 0.1 mV s<sup>-1</sup>. T = 25 °C. Inset: tafel plots.



## 3.2. Bulk electrolysis

The electrochemical oxidation of EDTA at diamond anodes was carried out in a batch reactor (Figs. 5.1.A and 5.1.B). The values of TOC (total organic carbon), COD (chemical oxygen demand), and EDTA concentration were followed during the experiments. The values were normalized to the initial values. The experimental conditions were chosen so as to investigate the oxidation process under 1) current limitation, 2) mixed current-mass transport control and 3) mass transport control, in order to be able to compare the experimental results with the theoretical model developed by Ch. Comninellis and coworkers (Table 5.1) [18]. Figure 5.7 shows the COD values as functions of time during electrolysis in the three cases investigated. The experimental data (points) have been compared with theoretical values from the model (solid lines). The COD values exhibit a linear decrease with time (curve 1 in Fig. 5.7) under conditions of current control (at low current densities) corresponding to an instantaneous current efficiency (ICE) of 100% (curve 1 in Fig. 5.8). In the mixed regime (curve 2 in Fig 5.7), the COD values decrease linearly with time in the initial part of the experiment (current regime). After a critical time, the COD decrease changes to an exponential time dependence typical of mass transport control (see § 2.5 of Chapter 2). The corresponding ICE values also exhibit an exponential decrease during the experiment (curve 2 in Fig. 5.8). In the third case, *i.e.*, that of mass-transport control throughout the experiment, both COD and the ICE values decrease exponentially with the time. The TOC-time curves (Fig. 5.9) reveal that total organic carbon removal is slower than EDTA oxidation in all cases investigated (*e.g.*, 20% TOC removal for a COD decrease of 50% in case 1 under current control). This is due to the presence of oxidation intermediates produced in the region under current control. In the mass-transport regime (curve 3 in Fig. 5.9), the gap between TOC and COD as functions of time is not so important: in this case the high current density sustains to a fast reaction, and few organic intermediates accumulate (formation of large amount of hydroxyl radicals relative to organics close to the anode surface).

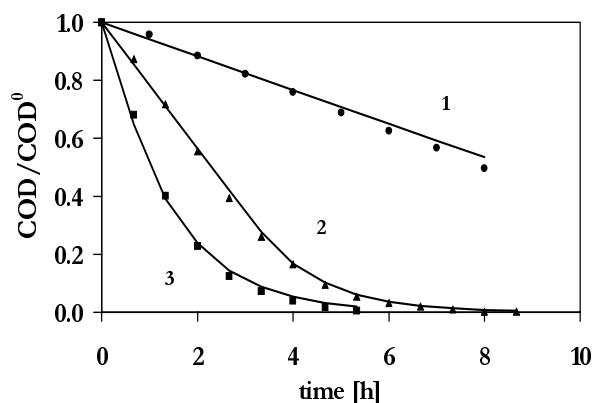


**FIGURE 5.7.** Electrochemical oxidation of a solution of EDTA in 1 M NaClO<sub>4</sub> (pH = 2) at BDD anodes at different current densities  $j$ : 1) current control (5 mA cm<sup>-2</sup>), 2) mixed control (20 mA cm<sup>-2</sup>), 3) mass-transfer control (50 mA cm<sup>-2</sup>).  $T = 25$  °C. Comparison between experimental data (points) and the theoretical model (solid lines). Initial COD<sup>0</sup> = 2330 ppm.

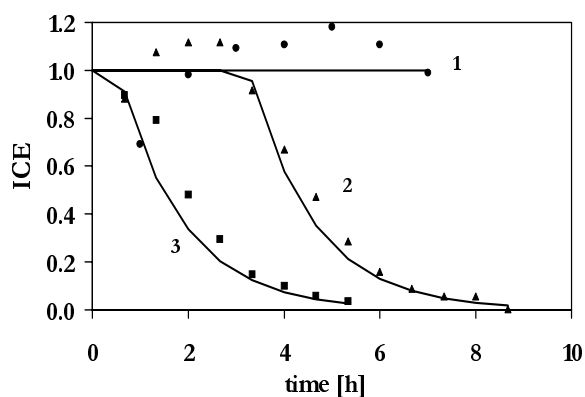


**FIGURE 5.8.** Electrochemical oxidation of a solution of EDTA in 1 M NaClO<sub>4</sub> (pH = 2) at BDD anodes at different current densities  $j$ : 1) current control (5 mA cm<sup>-2</sup>), 2) mixed control (20 mA cm<sup>-2</sup>), 3) mass-transfer control (50 mA cm<sup>-2</sup>).  $T = 25$  °C. Comparison between experimental data (points) and the theoretical model (solid lines). Initial COD<sup>0</sup> = 2330 ppm

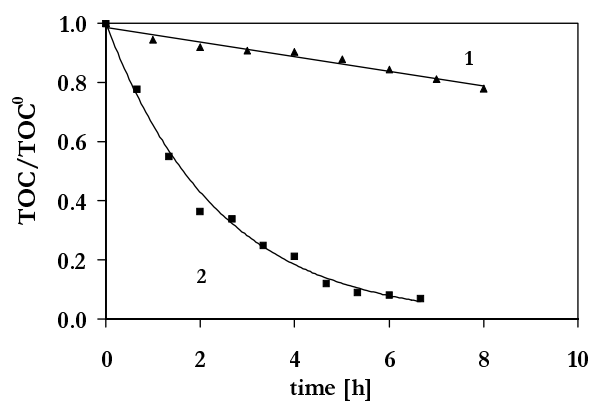


**FIGURE 5.9.** Electrochemical oxidation of a solution of EDTA in 1 M NaClO<sub>4</sub> (pH = 2) at BDD anodes at different current densities  $j$ : 1) current control (5 mA cm<sup>-2</sup>), 2) mass-transfer control (50 mA cm<sup>-2</sup>).  $T = 25$  °C. Initial TOC<sup>0</sup> = 2723 ppm.

A study of the reaction intermediates was carried out to identify the possible mechanism of EDTA oxidation at diamond. The decrease of EDTA concentration during the experiment was followed by cyclic voltammetry of the BDD in the solution being electrolysed. Formaldehyde was one of the intermediates detected. Its concentration increased rapidly, already during the first hour of the experiment (Fig. 5.10), while EDTA was oxidised. Both compounds were oxidised at the diamond anode when their concentrations were comparable.

HPLC performed on samples withdrawn from the solution confirmed the presence of formaldehyde and signalled the presence of further intermediates initially formed and then oxidised during the experiments (not given).

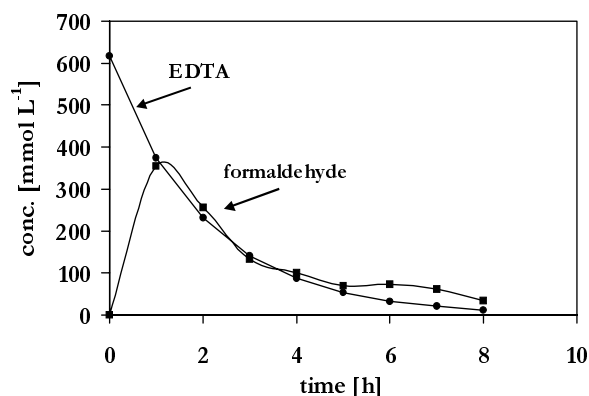


**FIGURE 5.10.** Concentrations of EDTA and formaldehyde as functions of electrolysis time. Current control regime. Initial conditions as in Figures 5.7 to 5.9.

In harmony with our preliminary results concerning the identification of intermediates, a mechanism involving hydroxyl radicals formation can be proposed (Fig. 5.11). According to the mechanism, the initial step of the reaction is the formation of hydroxyl radicals from water decomposition (reaction a in Fig. 5.11). Hydroxyl radicals, formed in the reaction a, are involved in hydrogen abstraction from EDTA (see reaction 2.32 of Chapter 2) as is shown in details by reaction b in Fig. 5.11. The reaction b is thought to form carboxyl free radicals, which lead to decarboxylation (reaction c in Fig. 5.11). Radicals could be involved in an homogeneous reaction (reaction d in Fig. 5.11) to form the group N-CH<sub>2</sub>OH. This unstable group produces formaldehyde (reaction e in Fig. 5.11).

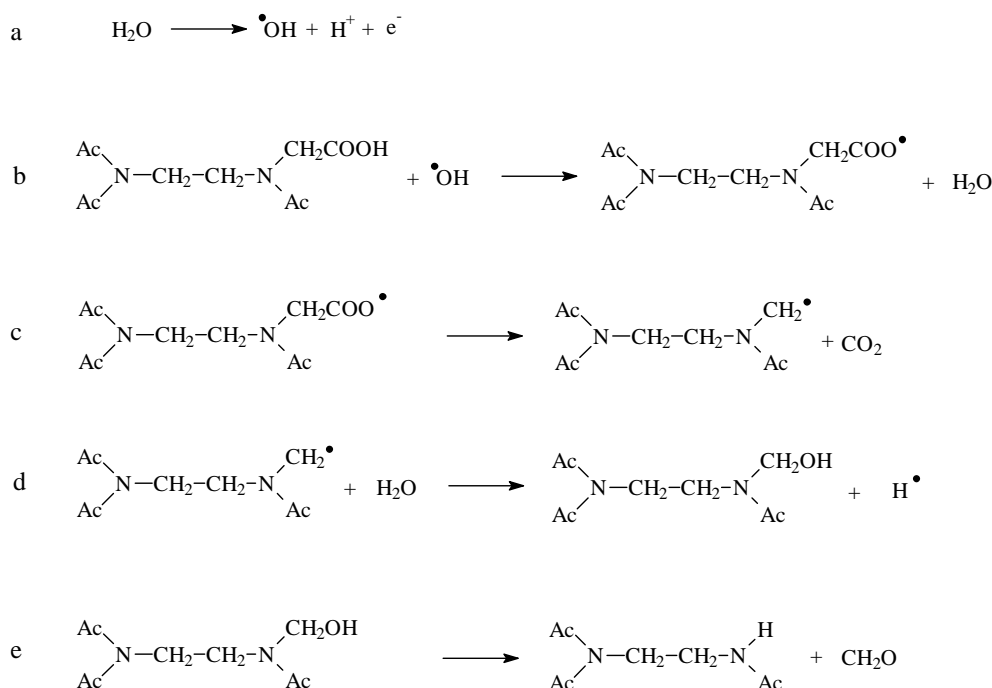


**FIGURE 5.11.** Scheme of the decarboxylation step of EDTA. a) decomposition of water, b) formation of the carboxyl radical, c) production of  $\text{CO}_2$ , d) formation of alcohol, e) formation of formaldehyde.  $\text{Ac} = \text{CH}_2\text{COOH}$ .

Dioxygen very probably also participates in the combustion of organics according to the following reaction scheme:



where  $\text{R}^\bullet$ ,  $\text{ROO}^\bullet$ ,  $\text{R}'^\bullet$ , are the organic radicals. Since the organic hydroperoxides are relatively unstable, decomposition of such intermediates often leads to molecular breakdown and formation of subsequent intermediates with lower carbon numbers. These scission reactions continue rapidly until the organic substance has been completely transformed to  $\text{CO}_2$  and  $\text{H}_2\text{O}$ .

Each decarboxylation reaction involving hydroxyl radicals (Fig. 5.11) is a separate chemical reaction that gives a product capable of further similar reactions as long as acetate groups are available. The result is a complete decarboxylation of

EDTA to form ethylenediamine (EDA) accompanied by formation of formaldehyde (Fig. 5.12).

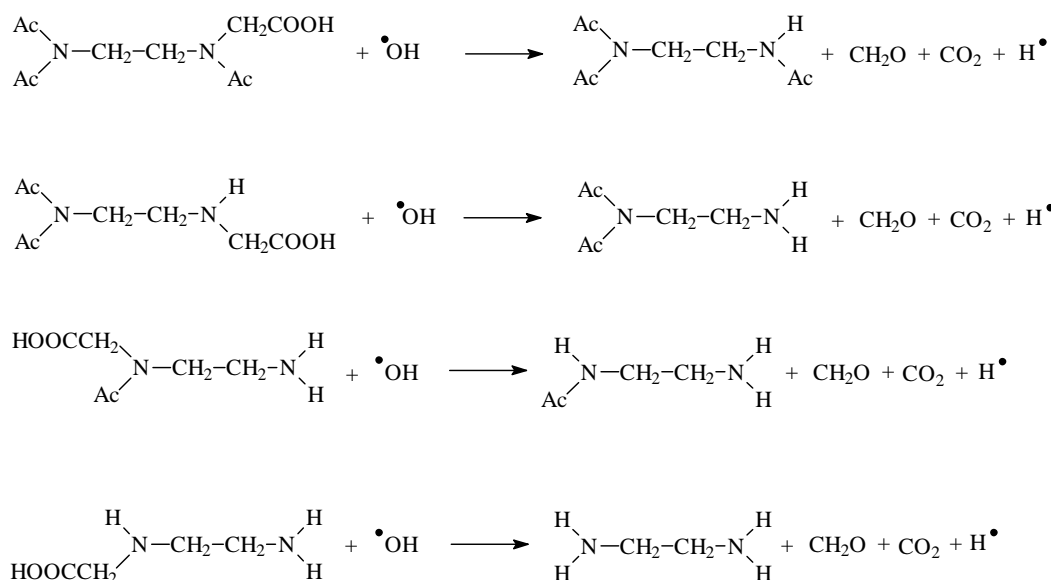


**FIGURE 5.12.** Scheme of the four-step decarboxylation of EDTA by reaction with hydroxyl radicals formed from water discharge. Ac = CH<sub>2</sub>COOH. The mechanism of each decarboxylation step is explained in details in Fig. 5.11

The scheme in Figure 5.13, proposed by Pakalapati *et al* [16] for the oxidation of EDTA at platinum electrodes, shows the possible reaction pathway for the complete oxidation of EDTA to CO<sub>2</sub> at BDD electrodes. The oxidation of EDA goes further until combustion to CO<sub>2</sub> and water by formation of intermediates as such glyoxal and oxalic acid. The oxidation of formaldehyde leads to the formation of formic acid. Closer HPLC studies aimed at confirming the presence of supposed intermediates are actually in progress.

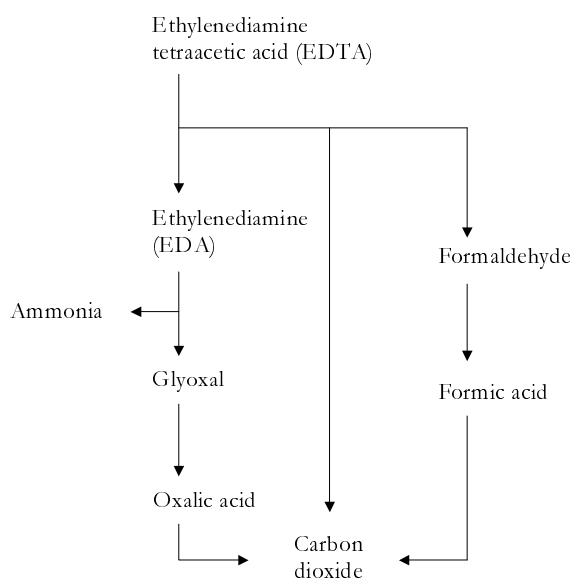


**FIGURE 5.13.** Possible reaction pathway for the complete oxidation of EDTA at Pt [16].

## 4. Conclusions

The partial electrochemical oxidation of EDTA at boron-doped diamond electrodes was investigated in the potential region of electrolyte stability. No fouling phenomena were detected during the experiments. An overall two-electron transfer mechanism was proposed for the partial direct electrochemical oxidation of EDTA at diamond.

Complete combustion of EDTA was performed at diamond electrodes in the potential region of electrolyte decomposition, and found to occur with very high current efficiency. The theoretical model developed for the oxidation of organics at 'non-active' anodes correctly predicted the experimental results in terms of COD removal and instantaneous current efficiency (ICE). The EDTA was oxidised at diamond through an indirect reaction involving electrogenerated free hydroxyl radicals formed at the anode during water discharge.

A preliminary identification and quantification of formaldehyde as an intermediate in EDTA oxidation was performed. HPLC studies for the identification of other intermediates are actually in progress. First results of these studies appear to confirm the mechanism proposed for EDTA oxidation at BDD electrodes.

Since water discharge was not involved, only a partial oxidation of organics was possible at diamond in the region of electrolyte stability. In the potential region of water discharge, to the contrary, complete combustion of organics occurred at diamond. It had already been shown that the activity of diamond-graphite composite electrodes (BDD<sub>ag</sub> and BDD-g, see Chapters 3 and 4) towards the partial oxidation of organics was much higher than that of polarized diamond. However, diamond-graphite electrodes could only be tested in the potential region of water stability, where  $sp^2$  impurities have not yet been removed from the surface. Another material will have to be used to modify the electrochemical properties of diamond and obtain an 'active' diamond electrode that is stable under water discharge conditions. IrO<sub>2</sub> was chosen because of its well-known stability. Up to now, this material had been deposited on titanium-base metal so as to obtain dimensionally stable anodes (DSA). In the next chapter, results will be presented concerning the deposition of IrO<sub>2</sub> nanoparticles on a diamond substrate. This diamond-IrO<sub>2</sub> composite electrode has been tested in the potential region of water stability and in the potential region of water discharge.

---

## 5. Acknowledgment

I am very thankful to the CSEM for providing boron-doped diamond electrodes.

I would like to thank the laboratory of Applied Chemistry of the University of Tokyo, Japan for collaborating with me in the set-up of the electrochemical system. I would like to thank in particular Mrs. Ivandini for helping me in the experimental part of the work, Dr. Sarada and Prof. Rao for very helpful discussion.

Thank you to Mr. Ouattara for the analytical investigation.

---

## 6. References

1. C. Comninellis and C. Pulgarin, *J. Appl. Electrochem.*, **23** (1993) 108.
  2. C. Comninellis and E. Plattner, *Chimia*, **42** (1988) 250.
  3. C. Comninellis and C. Pulgarin, *J. Appl. Electrochem.*, **21** (1991) 703.
  4. C. Comninellis and A. Nerini, *J. Appl. Electrochem.*, **25** (1995) 23.
  5. C. Comninellis and A. D. Battisti, *J. Chim. Phys.*, **93** (1996) 673.
-

6. N. B. Tahar and A. Savall, *J. Electrochem. Soc.*, **145** (1998) 3427.
7. C. Comninellis, *Electrochim. Acta*, **39** (1994) 1857.
8. G. Fóti, D. Gandini, and C. Comninellis, *Current Topics in Electrochem.*, **5** (1997) 71.
9. O. Simond, V. Shaller, and C. Comninellis, *Electrochim. Acta*, **42** (1997) 2009.
10. M. C. Granger and G. M. Swain, *J. Electrochem. Soc.*, **146** (1999) 4551.
11. Y. V. Pleskov, Y. E. Evstefeeva, M. D. Krotova, and A. V. Laptev, *Electrochim. Acta*, **44** (1999) 3361.
12. G. M. Swain, A. B. Anderson, and J. C. Angus, *MRS Bull.*, **23** (1998) 56.
13. J. Xu and G. M. Swain, *Anal. Chem.*, **70** (1998) 1502.
14. B. Marselli, J. Garcia-Gomez, P.-A. Michaud, M. A. Rodrigo, and C. Comninellis, *J. Electrochem. Soc.*, **150** (2003) D79.
15. J. W. Johnson, H. W. Jiang, S. B. Hanna, and W. J. James, *J. Electrochem. Soc.*, (1972) 574.
16. S. N. R. Pakalapati, B. N. Popov, and R.E.White, *J. Electrochem. Soc.*, **143** (1996) 1636.
17. K. Kusakabe, H. Nishida, S. Morooka, and Y. Kato, *J. Appl. Electrochem.*, **16** (1986) 121.
18. M. Panizza, P.-A. Michaud, G. Cerisola, and C. Comninellis, *J. Electroanal. Chem.*, **507** (2001) 206.
19. G. Anderegg, *Helv. Chim. Acta*, **50** (1967) 2333.
20. A. J. Bard and L. R. Faulkner, 'Electrochemical methods - Fundamentals and applications', J. Wiley and Sons, Inc., New York, 2001.



---

## Results: Iridium dioxide-modified BDD electrodes

---

Nanoparticles of IrO<sub>2</sub> were deposited by thermal decomposition on boron-doped diamond electrodes in order to improve and better understand their electrocatalytic activity toward redox processes and the oxygen evolution reaction. Electrodes with different IrO<sub>2</sub> loadings were prepared and their electrochemical properties tested. The morphology of the samples was investigated by scanning and transmission electron microscopy. It was noticed that with increasing IrO<sub>2</sub> loading the nanoparticle deposit starts forming clusters. Cyclic voltammetry, steady-state polarisation and impedance measurements were applied to calculate kinetic parameters for outer-sphere (Fe(CN)<sub>6</sub>III/II) and inner-sphere (Q/H<sub>2</sub>Q) charge transfer processes. Increasing values of capacitance of the electrodes constitute evidence for the improved activity of diamond electrodes surface-modified by nanoparticle deposition. The reaction rate constants of redox processes increased by several orders of magnitude, the overpotential of the oxygen evolution reaction decreased by about one volt. The IrO<sub>2</sub> deposition completely altered the electrochemical properties of diamond from an ‘*non-active*’ to an ‘*active*’ material. The high electrocatalytic activity of BDD-IrO<sub>2</sub> electrodes toward the OER was also confirmed in an indirect way by the observation that the oxidation of organic substances and the production of peroxodisulphate are inhibited. The high degree of dispersion of the IrO<sub>2</sub> particles led to a high electrocatalytic activity, even at extremely low IrO<sub>2</sub> loadings. A structural model was proposed for the surface-modified diamond structure.

## 1. Introduction

The field of diamond surface modification has been rather active during the last few years because of growing interest in the solid/liquid interface at diamond electrodes. Particular attention has been given to the deposition of catalyst nanoparticles on diamond surfaces, the aim being that of combining the improved catalytic properties of highly dispersed catalyst particles with the extremely high corrosion resistance of diamond. Several metals and oxide materials have been chosen, and many deposition techniques have already been tested.

Metals such as platinum, silver and lead [1-3] or transition metal oxides such as ruthenium, iridium and lead dioxide [4, 5] have been deposited on diamond, and the resulting physical and electrochemical properties have been investigated. The catalytic activity of diamond was greatly improved by metal particle deposition, and these new composite materials have been used in electroanalytical applications. The aspects most thoroughly investigated have been the particle size and distribution and the stability of the deposits under a number of different working conditions.

Many deposition techniques have been tested in an effort to improve particle adherence and dispersion. Spontaneous deposition by immersion [2, 5], electrochemical deposition [6], thermal decomposition [4, 7], and the incorporation of metal particles by codeposition during diamond film growth [1] are some of the methods most often investigated.

The choice of the material being deposited depends on the intended application of the electrode (sensitivity and selectivity in electroanalysis, electrocatalytic activity toward redox reactions such as chlorine, hydrogen or oxygen evolution) and its required stability under harsh working conditions. The deposition technique should be simple and yield good dispersion of the particles on the substrate surface.

The actual trends in applied electrocatalytic research can be summarised by the following points [8]:

- improvement of the electrocatalytic activity for wanted reactions
- depression of the electrocatalytic activity for unwanted reactions
- stabilisation of electrode materials
- replacement of materials containing precious metals with cheaper materials based on nonprecious metals
- finding substitutes for polluting materials.

Furthermore, the electrode material should have a high surface area and high electrical conductivity in order to be of technological interest.

The support (substrate) properties must also be taken into account, because they may limit the range of the working conditions and are responsible for adherence of the catalyst layer. Moreover, the reactivity of the support materials may influence the charge-transfer and nucleation processes occurring during metal deposition.

In the present work, the thermal decomposition technique was selected for the deposition of iridium dioxide on diamond. IrO<sub>2</sub> has a remarkable stability toward chemical and electrochemical attack, a metallike conductivity and an appreciable catalytic (and electrocatalytic) activity [9]. This transition metal oxide is particularly electroactive in the chlorine, oxygen, and hydrogen evolution reactions, which occur at BDD-IrO<sub>2</sub> electrodes at a rather low overvoltage.

The thermal decomposition of appropriate precursors that have been dissolved in suitable solvents and spread on a metallic support [10-12] is the procedure most often applied to prepare iridium dioxide electrodes. The nature of the precursor and the decomposition temperature must be controlled during the procedure, because they will affect the particle size, nonstoichiometry, and morphology of the oxide layer [12, Trasatti, 1991 #82].

Because of its extremely high stability even under very harsh chemical and electrochemical conditions and because of its inertness over a wide range of potentials, diamond is a perfect substrate material.

With the aim of gaining a better understanding of the relation between the electrochemical properties of diamond and its surface structure, and in harmony with current research trends, iridium dioxide nanoparticles were deposited on diamond surfaces to different levels of loading [4]. The morphological and electrochemical properties were investigated and compared with those of bare boron-doped diamond electrodes [7].

## 2. Experimental

### *Electrode preparation*

Boron-doped diamond electrodes were prepared by hot-filament chemical vapour deposition (HF-CVD) using the procedure explained in Chapters 2 and 3. IrO<sub>2</sub> particles were deposited on BDD surfaces by thermal decomposition. The hydrophobic surface of an as-grown diamond sample (BDD<sub>ag</sub>) was treated for 30 minutes by anodic oxidation at 10 mA cm<sup>-2</sup> in 1 M H<sub>2</sub>SO<sub>4</sub> (BDD<sub>mild</sub>) in order to obtain a hydrophilic substrate for IrO<sub>2</sub> deposition. Solutions of H<sub>2</sub>IrCl<sub>6</sub>.aq in 2-propanol were prepared with different concentrations of the precursor acid so as to deposit different amounts of IrO<sub>2</sub>. Five μl of the solution were placed on the BDD surface (geometric area of 1 cm<sup>2</sup>) for a single deposition step. After solvent evaporation at 80 °C, calcination was performed at a selected target temperature. Temperatures of 350 and 450 °C were used to oxidise the precursor acid to IrO<sub>2</sub>. A value of 10<sup>15</sup> molecules IrO<sub>2</sub> cm<sup>-2</sup> was defined as the loading corresponding to Γ = 1. The IrO<sub>2</sub> loadings investigated were equivalent to values of Γ in the range from 0.06 to 30.

### *Morphological characterisation*

The surface morphology was characterised using a JEOL JMS-6300-F scanning electron microscope (SEM). Samples of BDD and BDD-IrO<sub>2</sub> were analysed without any pretreatment. Only a rather high IrO<sub>2</sub> loading was analysed because of the instrument's power limitation. A Philips EM 430 ST tunnelling electron microscope (TEM) was used to study very low IrO<sub>2</sub> loadings on BDD surfaces. Again, only as-prepared samples of BDD and BDD-IrO<sub>2</sub> were analysed by TEM. The cleaved-edge technique was used to prepare samples for the TEM investigations [13]. Crystals were cleaved in correspondence with weakly bonded planes so as to obtain atomically smooth surfaces. Wedge-shape samples were placed on a copper support and observed by a beam parallel to the {100} direction. In this way the BDD crystal's profile could be observed and a very thin portion of the crystal's surface was investigated. Microanalysis of the samples was performed by energy-dispersive spectroscopy (EDS) in order to obtain the chemical composition of the surface. The elemental analysis (XPS) was performed with a Kratos (AXIS ULTRA) analyser in order to identify the oxidation state of Ir in the particles deposited. A total area of 700 x 300 μm was analysed over a thickness of 50 ÷ 100 angstroms using a 15 kV Al-mono as the (monochromatic) x-ray source. Only as-prepared samples were analysed.

*Electrochemical characterisation*

An electrochemical arrangement (Fig. 3.1 in Chapter 3) was used to accommodate the electrode sample, assure electrical contact, and obtain a geometrically well defined surface area ( $1 \text{ cm}^2$ ). A conventional three-electrode glass cell (0.1 L) was used for voltammetry (Fig. 3.2). The counterelectrode was a platinum spiral. A  $\text{Hg}/\text{Hg}_2\text{SO}_4, \text{K}_2\text{SO}_{4(\text{sat})}$  electrode was used as the reference electrode. All values of potential are reported relative to a standard hydrogen electrode (SHE). Fluka Chemie chemicals and Milli-Q water were used to prepare solutions.

Cyclic voltammetry and steady-state polarisation were performed with a computer-controlled Autolab PGstat30. Polarisation curves were recorded at  $0.1 \text{ mV s}^{-1}$  over a 10 mV wide range around the equilibrium potential,  $E^{0'}$ , after conditioning the electrode at the initial potential for 120 seconds.

Impedance measurements were performed while using a computer-controlled Autolab PGstat30. A frequency range between 0.1 Hz and 50 kHz was chosen for the measurements. An overpotential of  $\Delta E = \pm 5 \text{ mV}$  was applied when investigating the redox couples.

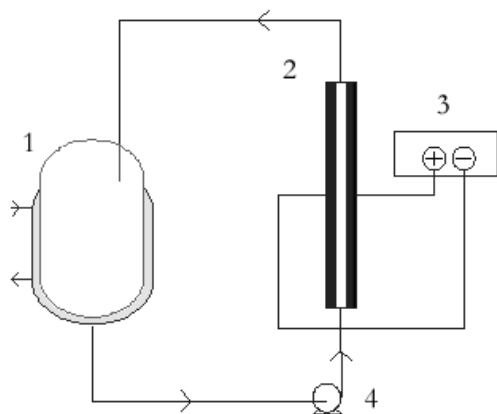


**FIGURE 6.1.A** Electrochemical setup: (1) thermostatted glass tank, (2) electrochemical flow-through cell, (3) current supply, (4) magnetic pump.

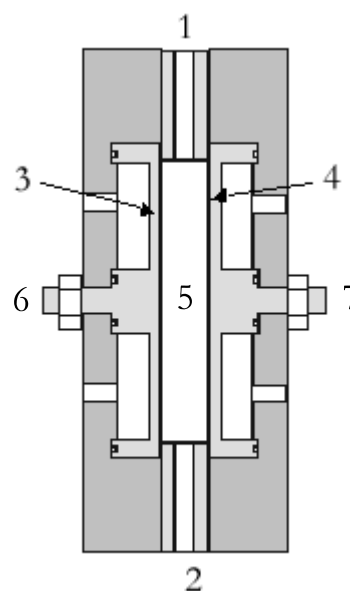


**FIGURE 6.1.B** Electrochemical flow-through cell: (1) and (2) outlet and inlet of the solution, (3) anode, (4) cathode, (5) reactor compartment, (6) and (7) electrical contacts.

Preparative electrolyses were performed using the complete setup shown in Figure 6.1.A. The solution was introduced into a thermostatted glass tank (1) and circulated through the electrochemical flow-through cell (2) using an Iwaki Model MD 40R. magnetic pump (4). The flow rate of the solution in the system was  $67 \text{ L h}^{-1}$ . The galvanostatic conditions were obtained by a current supply (3).

In Figure 6.1.B, details of the electrochemical batch reactor are shown. Cathode (zirconium) and anode (3 and 4 in Fig. 6.1.B) were arranged in the cell at a mutual distance of 1 cm, and parallel to the flow direction (from 2 to 1). A mass transfer coefficient of  $2 \times 10^{-5} \text{ m s}^{-1}$  was calculated for the reactor compartment (5) using the ferri/ferro redox couple as a probe. The electrodes (6 and 7) were contacted from the rear. Fluka Chemie chemicals and Milli-Q water were used to prepare the solutions. Chemical oxygen demand (COD) was measured by UV-visible spectrophotometry using HACH chemicals. Total organic carbon (TOC) was measured with a TOC-5050 Shimadzu analyser.

---

### 3. Results and discussion

Electrodes with different  $\text{IrO}_2$  loadings,  $\Gamma$ , were prepared ( $\text{BDD-IrO}_2$ ) and their morphological and electrochemical properties tested. The morphology of the samples was investigated by scanning and transmission electron microscopy. Cyclic voltammetry, steady-state polarisation and impedance measurements were applied to calculate kinetic parameters for outer-sphere ( $\text{Fe(CN)}_6^{\text{III/II}}$ ) and inner-sphere ( $\text{Q/H}_2\text{Q}$ ) charge transfer processes.

#### 3.1. Morphological characterisation

Only the  $\text{BDD-IrO}_2$  samples prepared at  $450 \text{ }^\circ\text{C}$  were investigated by SEM and TEM in order to determine the size and distribution of  $\text{IrO}_2$  particles on the diamond surface.

##### *Scanning electron microscopy (SEM)*

SEM images were recorded for  $\text{BDD}_{\text{ag}}$  (Fig. 6.2.A) and for a  $\text{BDD-IrO}_2$  sample with a loading of  $\Gamma = 13$  (Fig. 6.2.B). The  $\text{IrO}_2$  loading was found to be organised in the form of discrete particles on the diamond surface, rather than as a more or less continuous film.

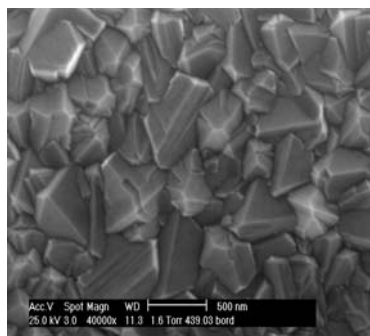


**FIGURE 6.2.A** SEM images of a BDD<sub>ag</sub> electrode.

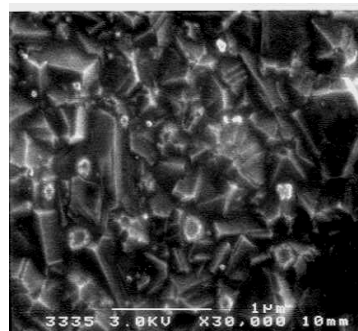


**FIGURE 6.2.B** SEM image of a BDD electrode with an IrO<sub>2</sub> loading of  $\Gamma = 13$ . Deposition temperature: 450 °C.

The distribution of the visible IrO<sub>2</sub> particles was quite homogeneous over the region investigated. IrO<sub>2</sub> particles were mainly located at grain boundaries of the BDD crystals. The average particle size was lower than 200 nm. At lower IrO<sub>2</sub> loadings, the particles deposited could not be seen in the SEM. In this case a transmission electron microscope was used for further investigations.

#### *Transmission electron microscopy (TEM)*

TEM images were recorded in order to examine electrodes with low IrO<sub>2</sub> loadings ( $\Gamma = 6.4$  and 0.6) having a very small size of the IrO<sub>2</sub> particles deposited. In the case of  $\Gamma = 0.6$  (Fig. 6.3.A), isolated particles had a size of about 2-3 nm and were concentrated in the grain boundaries of the diamond crystals. On the sample with a 10 times higher loading ( $\Gamma = 6.4$ , Fig. 6.3.B) the IrO<sub>2</sub> particles were larger (10 nm), and their concentration in the grain boundaries of the diamond crystals was significantly higher.

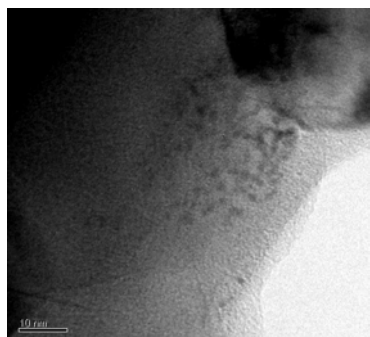


**FIGURE 6.3.A** TEM image of a BDD-IrO<sub>2</sub> electrode with  $\Gamma = 0.64$ .

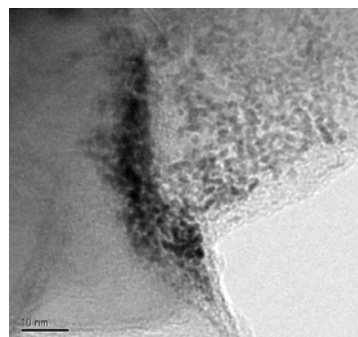


**FIGURE 6.3.B** TEM image of a BDD-IrO<sub>2</sub> electrode with  $\Gamma = 6.4$ .

Microanalysis by EDS (energy-dispersive spectrometry) performed for an electrode with  $\Gamma = 6.4$  demonstrated that the nanoparticles investigated contained Ir (Fig. 6.4). The peaks of carbon and silicon were extremely high, as predicted, but the Ir response was distinct. Peaks related to copper were due to the metallic sample support inside the microscope. These measurements were made in a region of high particle concentration (Fig. 6.3.B).

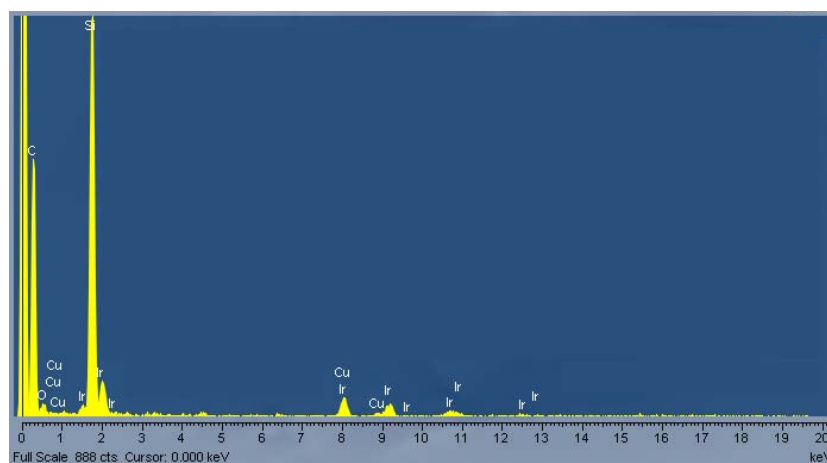
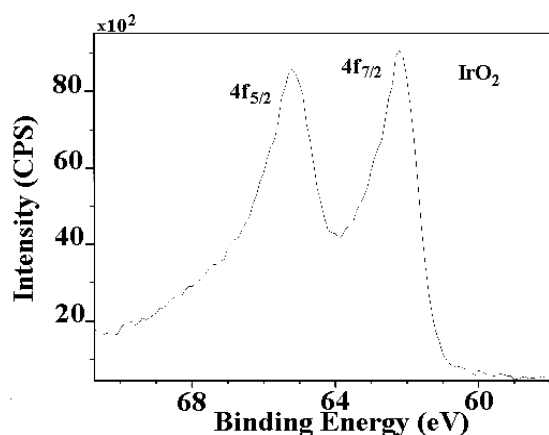


FIGURE 6.4. DS analysis of a BDD-IrO<sub>2</sub> ( $\Gamma = 6.4$ ) electrode.

### *X-ray photoelectron spectroscopy (XPS)*

XPS measurements were made on BDD-IrO<sub>2</sub> with a loading of  $\Gamma = 6.4$  in order to verify the oxidation state of Ir in the particles deposited (Fig. 6.5). A comparison with Ir spectra in published tables [14] confirmed the absence of metallic Ir from the deposits (Fig. 6.6). The 4f<sub>7/2</sub> peak appeared at 62 eV, which corresponds to the oxidation state of Ir in IrO<sub>2</sub> (Table 6.1). On the surface element investigated (84  $\mu^2$ ), a total Ir concentration of 2% was found. These results suggest that the particles tend to concentrate in particular regions of the surface, probably in the grain boundaries of the diamond crystals (see SEM image in Fig. 6.3.B).





**FIGURE 6.5.** XPS results for a BDD-IrO<sub>2</sub> electrode with  $\Gamma = 6.4$ . Decomposition temperature: 450 °C.

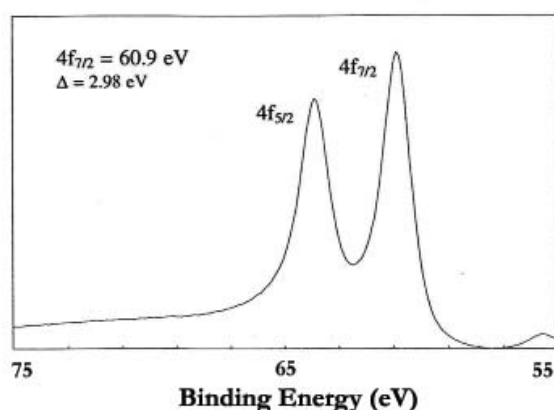


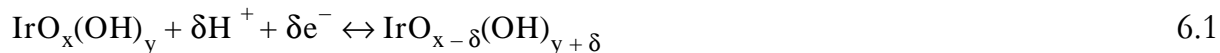
**FIGURE 6.6.** XP spectrum for elemental Ir in tables [14].

**TABLE 6.1.** Binding energies of Ir4f<sub>7/2</sub> in different oxidation states [14].

Compound Type	4f <sub>7/2</sub> Binding Energy (eV)			
	60	61	62	63
Ir		■		
IrCl <sub>3</sub>				■
IrO <sub>2</sub>			■	

### 3.2. Surface redox processes on BDD-IrO<sub>2</sub> surfaces

The most informative *in situ* characterisation of oxide electrodes can be performed by cyclic voltammetry in solutions of an inert electrolyte over a range of potentials where the solvent is not electrochemically decomposed. The voltammetric curves provide an electrochemical spectrum of electrode surface transitions occurring during the potential scan. It is known that such surface changes only occur on the active surface sites of thermally prepared oxides [8, 15, 16]. Thus, the voltammetric charge ( $q^*$ ) could serve as a measure of the number of sites able to exchange electrons with solution species (Eq. 6.1).



Nevertheless, a precise conversion of charge into surface area is difficult, because the nature of the surface reactions is not well known. Also, it is found experimentally that the voltammetric charge depends on the potential scan rate. It had already been shown [17] that the scan rate dependence of charge is due to the existence of less accessible surface regions which are progressively excluded as the scan rate increases.

In the case of DSA-type  $\text{IrO}_2$  electrodes with Ti as a substrate, good spectra of the surface transitions could not be obtained because of “segregation” phenomena of  $\text{TiO}_x$  at the electrode surface [18]. Because of the inert nature of the boron-doped diamond material, this problem was not present in the case of BDD- $\text{IrO}_2$  electrodes. Therefore, voltammetry was performed in order to find the relation between the ‘inner’ and ‘outer surface’ [17]. The true surface area and roughness factor of the  $\text{IrO}_2$  particles were calculated by comparing voltammetric data with the results of morphological characterisation by spectroscopic methods.

#### *The active surface area*

Cyclic voltammetry was performed at all samples prepared at 350 and 450 °C. For each  $\text{IrO}_2$  loading, the influence of the scan rate was investigated. For the purposes of studying the electrocatalytic activity of the electrodes, a small potential range was chosen so as to avoid the anodic and cathodic decomposition of the supporting electrolyte. Figure 6.7.A shows the response of a BDD- $\text{IrO}_2$  ( $\Gamma = 6.4$ , prepared at 450 °C) recorded as a cyclic voltammogram at  $2 \text{ V s}^{-1}$  (curve 2), in comparison with the background current of a bare BDD electrode (curve 1). The high capacitive currents of a BDD- $\text{IrO}_2$  electrode (curve 2 in Fig. 6.7.A) are related to oxidation state changes of the  $\text{IrO}_2$  surface during the potential scan. Two pairs of peaks seen at 0.4 and 0.95 V could be related to the surface redox couples  $\text{Ir(III)/Ir(II)}$  and  $\text{Ir(IV)/Ir(III)}$ , respectively [19, 20]. The broadness of the peaks probably is due to different degrees of hydration of the oxide lattice [21]. The very low currents recorded at a BDD electrode (curve 1 in Fig. 6.7.A) probably are due to a different mechanism involving surface changes occurring during the potential scan (see Chapter 3). The voltammetric charge ( $q^*$ ), which is proportional to the number of protons exchanged between the surface and the solution, and thus to the number of active surface sites [8], was calculated by integrating the voltammetric curves. Figure 6.7.B shows that the voltammetric charge increases linearly with the  $\text{IrO}_2$  loading. The values of charge were calculated from curves recorded with scan rates

higher than  $0.1 \text{ V s}^{-1}$ , because starting from this value the charge was no longer a function of the scan rate itself, as will be explained later (Figs. 6.8.A and 6.8.B).

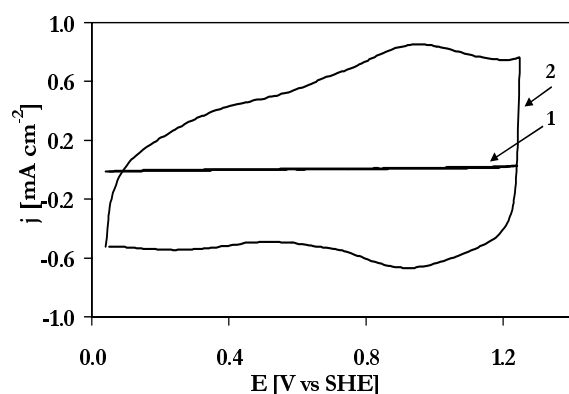


**FIGURE 6.7.A** Cyclic voltammograms: (1) BDD electrode, (2) BDD-IrO<sub>2</sub> electrode with  $\Gamma = 6.4$  prepared at 450 °C. Electrolyte: 0.5 M H<sub>2</sub>SO<sub>4</sub>; scan rate 2 V s<sup>-1</sup>.  $T = 25$  °C.  $\Gamma = 1$  corresponds to  $10^{15}$  molecules IrO<sub>2</sub> cm<sup>-2</sup>.

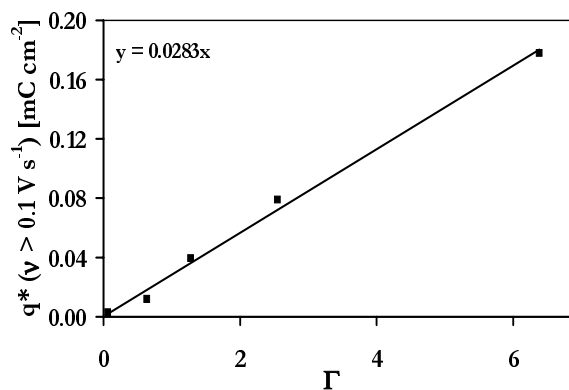


**FIGURE 6.7.B** Voltammetric charge  $q^*$  as a function of IrO<sub>2</sub> loading on BDD electrodes. Preparation temperature 450 °C. Scan rate 0.1 V s<sup>-1</sup>.

Figures 6.8.A and 6.8.B show the decrease of capacitive charge occurring with increasing scan rate for each of the IrO<sub>2</sub> loadings obtained at the two decomposition temperatures (350 °C and 450 °C). These results confirm the porosity of the particles deposited, and thus the presence of surface sites less exposed to the solution which can only be active at very low potential scan rates. From this experimental evidence, a distinction between an *inner* (less accessible) and an *outer* (more accessible) active surface was proposed [17]. For scan rates higher than  $0.1 \text{ V s}^{-1}$ , the capacitive charge  $q_s^*$  was almost constant and proportional to the outer surface area ( $A_o$ ) of the particles. At lower scan rates, diffusion of solution species into the particle pores led to an increase in total active surface area now including the external as well as the internal one. It was assumed that the charge corresponding to a scan rate of  $0.02 \text{ V s}^{-1}$  ( $q_t^*$ ) represented the *total* active surface area ( $A_t$ ) exposed to the solution. A total active charge and a corresponding total active surface area can be defined as follows:

$$q_t^* = q_s^* + q_i^* \quad 6.2$$

$$A_t = A_o + A_i \quad 6.3$$

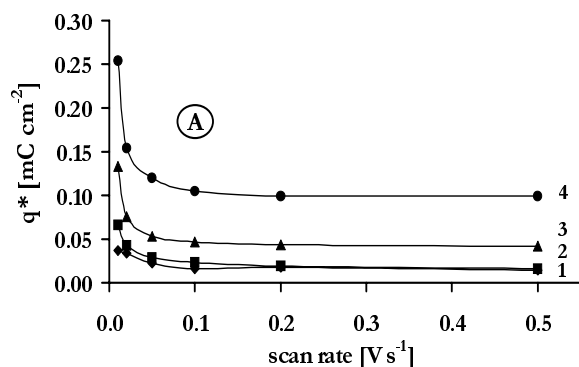


**FIGURE 6.8.A** Voltammetric charge calculated for different  $\text{IrO}_2$  loadings as a function of potential scan rate. Values of  $\Gamma$ : (1) 0.64, (2) 1.3, (3) 2.5, (4) 6.4. (A) BDD- $\text{IrO}_2$  electrodes prepared at 350 °C.  $\Gamma = 1$  corresponds to  $10^{15}$  molecules  $\text{IrO}_2 \text{ cm}^{-2}$ .

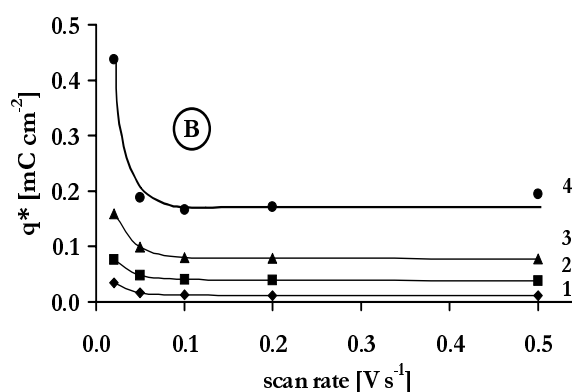


**FIGURE 6.8.B** Voltammetric charge calculated for different  $\text{IrO}_2$  loadings as a function of potential scan rate. Values of  $\Gamma$ : (1) 0.64, (2) 1.3, (3) 2.5, (4) 6.4. (B) BDD- $\text{IrO}_2$  electrodes prepared at 450 °C.

Assuming that all oxide surface sites were involved in the charging process, a theoretical charge  $q_{\text{th}}^*$  was calculated with Faraday's law. Assuming further that only the redox system  $\text{Ir(IV)}/\text{Ir(II)}$  was involved in the surface state transitions (two electrons exchanged), a theoretical charge of  $q_{\text{th}} = 3.2 \times 10^{-16}$  mC per molecule of  $\text{IrO}_2$  was calculated. For each loading  $\Gamma$ , a dispersion efficiency  $\gamma$  was defined as the ratio between the external charge  $q^*$  ( $v > 0.1$  V) and the theoretical charge  $q_{\text{th}}^*$  ( $q_{\text{th}}^* = q_{\text{th}} \times \Gamma$ ):

$$\gamma = \frac{q^*(v \geq 0.1 \text{ V s}^{-1})}{q_{\text{th}}^*} \quad 6.4$$

Figure 6.9 shows the dispersion efficiencies as functions of loadings  $\Gamma$  for the BDD- $\text{IrO}_2$  electrodes prepared at 350 and 450 °C. As expected, the dispersion efficiency increased with decreasing  $\text{IrO}_2$  loading on the BDD surface. With particles of smaller size, a larger number of  $\text{IrO}_2$  sites was exposed to the solution and contributed to the outer active surface area. For loadings higher than  $\Gamma = 1$  (equivalent to an  $\text{IrO}_2$  monolayer), the external active surface area increased linearly with the theoretical one, thus the dispersion efficiency was almost constant. For low loadings, the inner surface area remained quite small, and increased significantly only at higher loadings. This can be attributed to the increase of the pore surface area with 3D growth of the particles. For  $\text{IrO}_2$  prepared at 350 °C the dispersion efficiency was lower than for  $\text{IrO}_2$  prepared at 450 °C, probably because of

incomplete decomposition of the precursor [16]. For  $1 \leq \Gamma \leq 6$  the particle size of  $\text{IrO}_2$  remained almost constant.

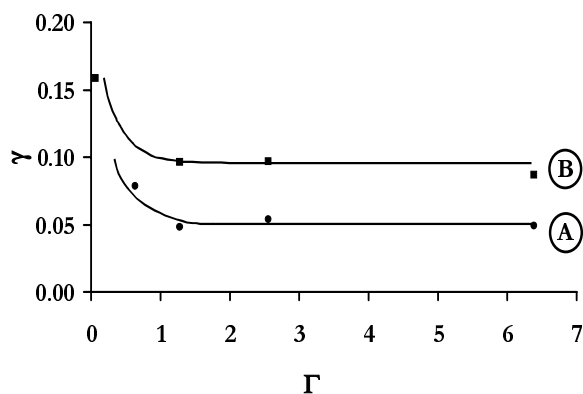


**FIGURE 6.9.** Dispersion efficiencies (Eq. 6.4) as a function of the  $\text{IrO}_2$  loading on diamond electrodes prepared at (A) 350 °C and (B) 450 °C.

Electrodes prepared at 450 °C exhibited a higher active surface area and dispersion efficiency than those prepared at 350 °C but having the same  $\text{IrO}_2$  loading,  $\Gamma$ . For this reason, only BDD- $\text{IrO}_2$  electrodes prepared at 450 °C have been the subject of further investigations.

In an effort to confirm the above results, a different approach was used for calculations. The inner and outer active surface areas were calculated from phenomenological equations proposed by S. Ardizzone et al. [17]. These authors obtained an expression for the *outer* surface area from the charge density ( $q_s^*$ ) at infinitely high potential scan rate  $v \rightarrow \infty$ , and for the *total* surface area from the charge density ( $q_t^*$ ) at a scan rate  $v \rightarrow 0$ . They correlated the experimental data by two linear functions (Eqs. 6.5 and 6.6) in order to obtain values for the outer and total surface area.

$$q^* = q_s^* + \text{const} \frac{1}{\sqrt{v}} \quad 6.5$$

$$\frac{1}{q^*} = \frac{1}{q_t^*} + \text{const}' \sqrt{v} \quad 6.6$$

The values obtained with these two methods are compared in the following table. There is very good agreement between the values, particularly for lower loadings.

**TABLE 6.2.** Total active charge calculated from CV with two methods: (1) from voltammetric charge; (2) with the “phenomenological” equations of Ardizzone and al. BDD-IrO<sub>2</sub> electrodes prepared at 450 °C.  $\Gamma = 1$  corresponds to  $10^{15}$  molecules IrO<sub>2</sub> cm<sup>-2</sup>.

loading $\Gamma$	$q_t^*$ [mC cm <sup>-2</sup> ] (1)	$q_t^*$ [mC cm <sup>-2</sup> ] (2)
6.4	0.437	0.268
2.6	0.160	0.137
1.3	0.076	0.067
0.64	0.034	0.024
0.06	0.010	0.013

The capacitance was also calculated from the total anodic and cathodic currents as functions of the scan rate for each IrO<sub>2</sub> loading (Eq. 6.7). The values obtained are reported in the following table (Table 6.3).

$$i_c = 2C_{dl} v \quad 6.7$$

**TABLE 6.3.** Capacitance values ( $E = 0.64$  V vs SHE, scan rate = 20 mV s<sup>-1</sup>) of BDD electrodes with different IrO<sub>2</sub> loadings.  $\Gamma = 1$  corresponds to  $10^{15}$  molecules IrO<sub>2</sub> cm<sup>-2</sup>.

Electrodes	capacitance [ $\mu$ F cm <sup>-2</sup> ]
BDD <sub>mild</sub>	16
BDD-IrO <sub>2</sub> ( $\Gamma = 0.64$ )	4 000
BDD-IrO <sub>2</sub> ( $\Gamma = 1.3$ )	18 000
BDD-IrO <sub>2</sub> ( $\Gamma = 2.6$ )	28 000
BDD-IrO <sub>2</sub> ( $\Gamma = 6.4$ )	80 000

The very considerable increase of capacitance with increasing IrO<sub>2</sub> loading was evidence for the high activity of the IrO<sub>2</sub> surface sites. A pseudocapacitance could in fact be defined for BDD-IrO<sub>2</sub> electrodes which includes the double-layer

capacitance typical of a BDD<sub>mild</sub> electrode and a capacitance due to the redox transitions of surface redox couples.

*True surface area and roughness factor of IrO<sub>2</sub> on BDD*

From the size and distribution density of the IrO<sub>2</sub> particles (SEM image in Figure 6.2.B), the true surface area and roughness factor of IrO<sub>2</sub> were estimated for a loading of  $\Gamma = 13$ . A spherical geometry with an average radius of 0.7  $\mu\text{m}$  and an external spherical surface area of 6.2  $\mu\text{m}^2$  was chosen to describe the shape of the IrO<sub>2</sub> particles on the BDD. Assuming the particle distribution to be homogeneous on all samples, calculations made for the surface fragment investigated (of 9.9  $\mu\text{m}^2$ ) were extended to the full deposit surface (1  $\text{cm}^2$ ). For  $\Gamma = 13$ , a true surface area of 9.4  $\text{cm}^2$  was calculated for the geometric surface area of 1  $\text{cm}^2$  (and hence a roughness factor of 9 - 10). Similar considerations were extended to all values of  $\Gamma$  investigated. According to the arguments concerning the active surface area presented in the previous paragraph (Fig. 6.7.B), the true active surface area was taken to increase linearly with the IrO<sub>2</sub> loading. Table 6.4 lists the results obtained.

**TABLE 6.4.** Roughness factors for different IrO<sub>2</sub> loadings. BDD-IrO<sub>2</sub> samples prepared at 450 °C. Geometric surface area 1  $\text{cm}^2$ .

Loading $\Gamma$	Roughness factor
6.4	4
2.6	2
1.3	1
0.6	0.3

The true surface area was four times larger than the geometric one in the case of  $\Gamma = 6.4$ . In this case the true surface areas of diamond and IrO<sub>2</sub> were comparable. For lower loadings the true surface areas decreased by more than a factor of ten.

### 3.3. Electrochemical behaviour of soluble redox systems at BDD-IrO<sub>2</sub> electrodes

The influence of IrO<sub>2</sub> on the properties of diamond was tested in the presence of the ferri/ferrocyanide and 1,4-benzoquinone/hydroquinone redox systems. Calculations of the apparent equilibrium potential,  $E_{\text{app}}^{0'}$ , and of kinetic parameters

of the reactions were performed for all electrodes investigated. Cyclic voltammetry was performed to study the reversibility of the system. Impedance measurements provided values of the kinetic reaction parameters.

**3.3.1. Outer-sphere electron transfer reactions.** The outer-sphere redox couple ferri/ferrocyanide had already been used as a redox probe in previous chapters. Cyclic voltammetry as well as impedance measurements were performed to calculate the kinetic parameters. The results were compared with those obtained for bare BDD and for Ti-IrO<sub>2</sub> electrodes.

#### *Cyclic voltammetry*

Cyclic voltammetry was performed for all the IrO<sub>2</sub> loadings on the BDD surface. The following figures summarise the trends of reversibility as functions of catalyst loading. The outer-sphere redox system had exhibited an irreversible behaviour at diamond electrodes (Fig. 6.10.A), as already seen in Chapter 3, however, the reversibility increased with increasing IrO<sub>2</sub> loading (Figs. 6.10.B and 6.10.C). Increasing height of the current peaks is indicative of the extremely high electrocatalytic activity of the well dispersed IrO<sub>2</sub> nanoparticles, even at very small loadings (Fig. 6.10.B).

The kinetic parameters were calculated by investigating the electrode's response as a function of scan rate. The potential difference between the anodic and cathodic peak,  $\Delta E_p$ , and the transfer coefficients  $\alpha_{\text{red}}$  and  $\beta_{\text{ox}}$  as well as the reaction rate constants,  $k^0$ , were calculated for all electrodes, and the results are shown in Table 6.5. The mathematical treatment that is valid for metal electrodes was used (see Chapter 2).



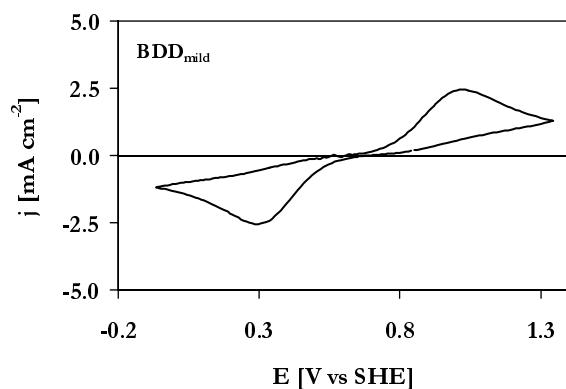


**FIGURE 6.10.A** Cyclic voltammogram recorded at a BDD<sub>mild</sub> electrode in 0.5 M H<sub>2</sub>SO<sub>4</sub> containing Fe(CN)<sub>6</sub> III/II 12.5 x 10<sup>-3</sup>/12.5 x 10<sup>-3</sup> M. Scan rate 0.1 V s<sup>-1</sup>. Geometric surface area: 1 cm<sup>2</sup>.

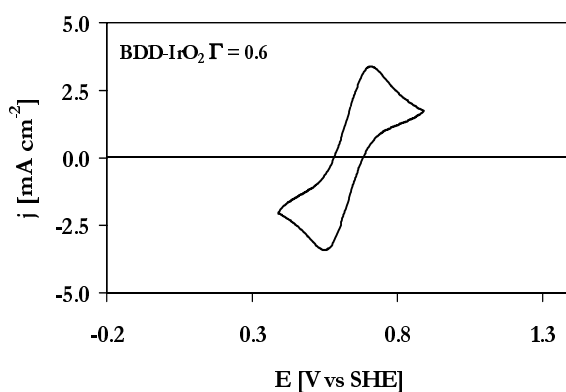


**FIGURE 6.10.B** Cyclic voltammogram recorded at a BDD-IrO<sub>2</sub> electrode with  $\Gamma = 0.6$  in 0.5 M H<sub>2</sub>SO<sub>4</sub> containing Fe(CN)<sub>6</sub> III/II 12.5 x 10<sup>-3</sup>/12.5 x 10<sup>-3</sup> M. Scan rate 0.1 V s<sup>-1</sup>. Geometric surface area: 1 cm<sup>2</sup>.  $\Gamma = 1$  corresponds to 10<sup>15</sup> molecules IrO<sub>2</sub> cm<sup>-2</sup>.

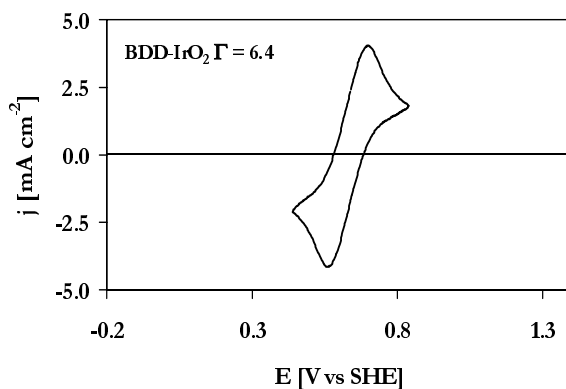


**FIGURE 6.10.C** Cyclic voltammogram recorded at a BDD-IrO<sub>2</sub> electrode with  $\Gamma = 6.4$  in 0.5 M H<sub>2</sub>SO<sub>4</sub> containing Fe(CN)<sub>6</sub> III/II 12.5 x 10<sup>-3</sup>/12.5 x 10<sup>-3</sup> M. Scan rate 0.1 V s<sup>-1</sup>. Geometric surface area: 1 cm<sup>2</sup>.  $\Gamma = 1$  corresponds to 10<sup>15</sup> molecules IrO<sub>2</sub> cm<sup>-2</sup>.

**TABLE 6.5.** Parameter values of the redox system  $\text{Fe}(\text{CN})_6$  III/II  $12.5 \times 10^{-3}/12.5 \times 10^{-3}$  M in 0.5 M  $\text{H}_2\text{SO}_4$  at BDD electrodes with different  $\text{IrO}_2$  loadings  $\Gamma$ . Formal potential  $E^0 = 0.72$  V vs SHE.

Electrode	$\Delta E_p$ [V]	$E^{0'}_{\text{app}}$ [V vs SHE]	$\beta_{\text{ox}}$ (*)	$\alpha_{\text{red}}$ (*)	$k^*$ [cm s <sup>-1</sup> ]	$k^{**}$ [cm s <sup>-1</sup> ]	$k^0$ [cm s <sup>-1</sup> ]
<b>BDD<sub>mild</sub></b>	0.53	0.7	0.3	0.3	$1 \times 10^{-4}$	$6 \times 10^{-5}$	$8 \times 10^{-5}$
<b>BDD-IrO<sub>2</sub></b> ( $\Gamma = 0.6$ )	0.10	0.5	0.5	0.5	$2 \times 10^{-3}$	$2 \times 10^{-3}$	$2 \times 10^{-3}$
<b>BDD-IrO<sub>2</sub></b> ( $\Gamma = 6.4$ )	0.09	0.6	0.5	0.5	$3 \times 10^{-3}$	$3 \times 10^{-3}$	$3 \times 10^{-3}$

(\*) determined with the Eq. 6.8.

 $k^* = k^0$  determined from the oxidation peak $k^0 = (k^* + k^{**})/2$  $k^{**} = k^0$  determined from the reduction peak

The sum of the transfer coefficients,  $\alpha$  and  $\beta$ , was lower than unity for diamond electrodes but increased after  $\text{IrO}_2$  deposition. Values of  $\alpha + \beta < 1$  indicate that the electron transfer process was hindered on the diamond surface (BDD<sub>mild</sub>), while  $\text{IrO}_2$  promoted the charge transfer through the electrode/electrolyte interface. The equation 6.8 was used to calculate values of the reaction rate constant,  $k^0$ .

$$E_p = E^0 + \frac{RT}{\alpha n F} \left( 0.78 - \ln k^0 + \ln \sqrt{D^0 \frac{\alpha n F}{RT}} \right) - \frac{RT}{2\alpha F} \ln v \quad 6.8$$

The very considerable increase of the reaction rate constant confirms the kinetic enhancement caused by  $\text{IrO}_2$  deposition.

### *Impedance measurements*

Impedance measurements were performed in order to investigate the elementary phenomena seen at the electrochemical interfaces (diffusion, chemical and electrochemical reactions) of BDD and BDD-IrO<sub>2</sub> in the presence of the ferri/ferrocyanide outer-sphere redox system.

The behaviour of a BDD electrode could be represented by the electrical equivalent circuit shown in Figure 6.11. The solution resistance  $R_s$  is in series with a more complex system due to the electrode's behaviour toward the redox system. A

resistance  $R_{ct}$  and a capacitance  $C_{dl}$  represent the two simultaneous phenomena taking place during electrode polarisation: the electron-transfer process and the double-layer charging, respectively. The impedance term,  $Z_W$ , which is the well-known Warburg impedance, could be neglected at high frequencies, because the process was kinetically controlled (Fig. 6.11).

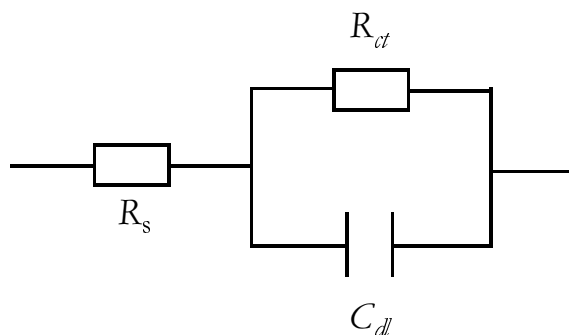


**FIGURE 6.11.** Circuit simulating a BDD<sub>mild</sub> electrode in an equimolar solution of Fe(CN)<sub>6</sub> III/II  $2.5 \times 10^{-3} / 2.5 \times 10^{-3}$  M in 0.5 M H<sub>2</sub>SO<sub>4</sub>. High-frequency range.

When analysing the results obtained at high frequencies with the simple circuit, a mathematical treatment (see Chapter 2) was made in terms of admittance,  $Y$ , instead of impedance values,  $Z$  [22]. Prior to calculations the solution resistance,  $R_s = 8 \Omega$ , was subtracted from the measured impedance,  $Z_{meas}$ , in order to only retain the term related to the electrode,  $Z_{el}$  (Eq. 6.9):

$$Z_{el} = Z_{meas} - R_s = \frac{R_{ct}}{1 + i\omega R_{ct} C_{dl}} \quad 6.9$$

where  $C_{dl}$  is the capacitance of the double layer. The electrode admittance,  $Y_{el}$ , as the inverse of electrode impedance,  $Z_{el}$ , was expressed by Equation 6.10:

$$Y_{el} = \frac{1}{R_{ct}} + i\omega C_{dl} = Re(Y) + iIm(Y) \quad 6.10$$

When plotting the real part of admittance,  $Re(Y)$ , as a function of  $\log(\omega)$ , one can find the inverse of electrode resistance as the intercept. When plotting the imaginary part of impedance divided by  $\omega$ , one finds the double-layer capacity of the electrode as an intercept. Neither the resistance nor the capacitance of the electrodes was a function of frequency, and the circuit parameters could be calculated. A similar analysis was performed for BDD-IrO<sub>2</sub> electrodes. The values obtained are listed in Table 6.6.

At diamond electrodes, the charge-transfer resistance was higher than at BDD-IrO<sub>2</sub> electrodes; this had already been noticed during cyclic voltammetry. Resistance values calculated for the IrO<sub>2</sub> electrodes were in agreement with values obtained by Boodts and co-workers [15, 16], who had studied continuous ceramic films. The effect of IrO<sub>2</sub> deposition was that of a strong decrease in the resistance to charge transfer between active sites and the redox system dissolved in the solution (Table 6.6).

Upon IrO<sub>2</sub> deposition, the double-layer capacitance increased by several orders of magnitude (Table 6.6), *viz.*, from 10 for BDD to 10 000 μF cm<sup>-2</sup> for BDD-IrO<sub>2</sub> ( $\Gamma = 6.4$ ). The increase in double-layer capacitance is due to a pseudocapacitance contribution made by surface redox transitions occurring when an IrO<sub>2</sub> deposit is present. The values obtained are in harmony with the results of Boodts and co-workers [16].

**TABLE 6.6.** Charge-transfer resistance and double-layer capacitance values calculated from the results of impedance measurements at BDD and BDD-IrO<sub>2</sub> electrodes in 0.5 M H<sub>2</sub>SO<sub>4</sub> containing Fe(CN)<sub>6</sub> III/II 2.5 x 10<sup>-3</sup> M / 2.5 x 10<sup>-3</sup> M.  $\Gamma = 1$  corresponds to 10<sup>15</sup> molecules IrO<sub>2</sub> cm<sup>-2</sup>.

Electrodes	R <sub>ct</sub> [Ω]	C <sub>dl</sub> [μF cm <sup>-2</sup> ]
BDD <sub>mild</sub>	256	10
BDD-IrO <sub>2</sub> Γ = 6.4	111	1 000

**3.3.2. Inner-sphere electron transfer reactions.** The inner-sphere 1,4 benzoquinone/hydroquinone system was active on BDD electrodes in the potential region of supporting electrolyte stability. Its activity in the case of Ti-IrO<sub>2</sub> continuous-film electrodes was already tested in previous work [23]. Investigations were performed by cyclic voltammetry and impedance spectroscopy in order to see the influence of the IrO<sub>2</sub> catalyst loading on the behaviour of the redox system.

#### *Cyclic voltammetry*

The kinetic parameters of the 1,4 benzoquinone/hydroquinone system were calculated from the results of cyclic voltammetry for all IrO<sub>2</sub> loadings ( $\Gamma = 0.6; 6.4$ ;

30), and the results were compared with those obtained on bare BDD and on Ti-IrO<sub>2</sub> thin-film electrodes.

The trends of reversibility of the system as a function of the IrO<sub>2</sub> loading are shown in Figures 6.12.A to 6.12.E. The redox couple was irreversible at polarised diamond electrodes (BDD<sub>mild</sub>), but increasing reversibility was found at BDD with increasing IrO<sub>2</sub> loadings. The current peak increased as well, indicating an increase in active surface area.

The cyclic voltammogram of Ti-IrO<sub>2</sub> (Fig. 6.12.E) suggests a quasi-reversible behaviour of the couple, but the background currents are much more important.

The kinetic parameters were calculated in accordance with the mathematical treatment reserved for metallic electrodes [24]. In case of a Ti-IrO<sub>2</sub> electrode, the reaction rate constant was calculated with the equation 2.24, using value in table 2.1 (see Chapter 2) for a quasi-reversible system. Table 6.7 summarises results for several electrodes. The reaction rate constants,  $k^0$ , increased by two orders of magnitude between bare diamond and BDD-IrO<sub>2</sub> ( $\Gamma = 6.4$ ). At the highest IrO<sub>2</sub> loading investigated ( $\Gamma = 30$ ), the behaviour approached that of continuous films on titanium. The transfer coefficient increased as well, reaching values typical for metal-based electrodes.

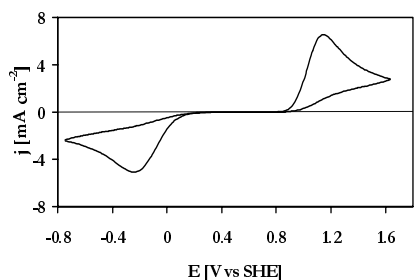


**FIGURE 6.12.A** Cyclic voltammogram recorded at a BDD<sub>mild</sub> electrode in 0.5 M H<sub>2</sub>SO<sub>4</sub> with Q/H<sub>2</sub>Q 12.5 x 10<sup>-3</sup>/12.5 x 10<sup>-3</sup> M. Scan rate 0.1 V s<sup>-1</sup>. Geometric surface area: 1 cm<sup>2</sup>.

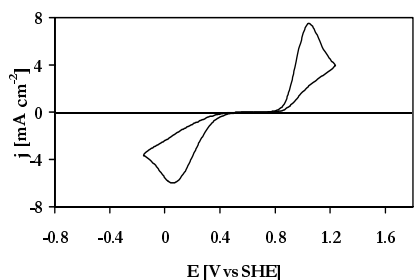


**FIGURE 6.12.B** Cyclic voltammogram recorded at a BDD-IrO<sub>2</sub> electrode ( $\Gamma = 0.64$ ) in 0.5 M H<sub>2</sub>SO<sub>4</sub> with Q/H<sub>2</sub>Q 12.5 x 10<sup>-3</sup>/12.5 x 10<sup>-3</sup> M. Scan rate 0.1 V s<sup>-1</sup>. Geometric surface area: 1 cm<sup>2</sup>.  $\Gamma = 1$  corresponds to 10<sup>15</sup> molecules IrO<sub>2</sub> cm<sup>-2</sup>.

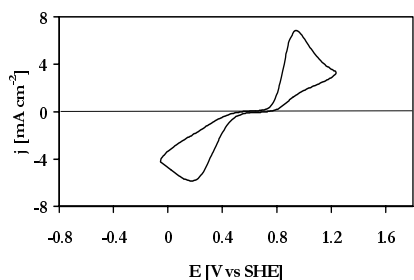


**FIGURE 6.12.C** Cyclic voltammogram recorded at a BDD-IrO<sub>2</sub> electrode ( $\Gamma = 6.4$ ) in 0.5 M H<sub>2</sub>SO<sub>4</sub> with Q/H<sub>2</sub>Q 12.5 x 10<sup>-3</sup>/12.5 x 10<sup>-3</sup> M. Scan rate 0.1 V s<sup>-1</sup>. Geometric surface area: 1 cm<sup>2</sup>.  $\Gamma = 1$  corresponds to 10<sup>15</sup> molecules IrO<sub>2</sub> cm<sup>-2</sup>.

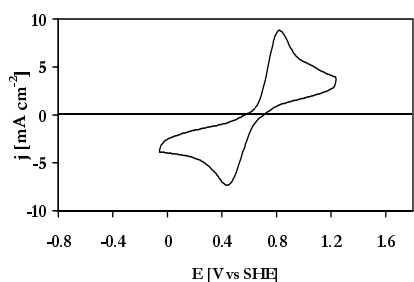


**FIGURE 6.12.D** Cyclic voltammogram recorded at a BDD-IrO<sub>2</sub> electrode ( $\Gamma = 30$ ) in 0.5 M H<sub>2</sub>SO<sub>4</sub> with Q/H<sub>2</sub>Q 12.5 x 10<sup>-3</sup>/12.5 x 10<sup>-3</sup> M. Scan rate 0.1 V s<sup>-1</sup>. Geometric surface area: 1 cm<sup>2</sup>.  $\Gamma = 1$  corresponds to 10<sup>15</sup> molecules IrO<sub>2</sub> cm<sup>-2</sup>.

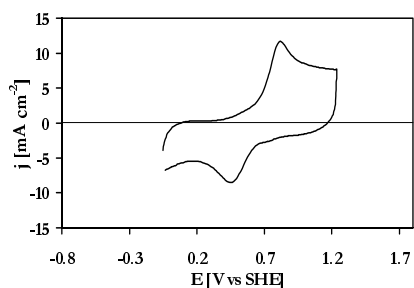


**FIGURE 6.12.E** Cyclic voltammogram recorded at a Ti-IrO<sub>2</sub> thin-film electrode in 0.5 M H<sub>2</sub>SO<sub>4</sub> with Q/H<sub>2</sub>Q 12.5 x 10<sup>-3</sup>/12.5 x 10<sup>-3</sup> M. Scan rate 0.1 V s<sup>-1</sup>. Geometric surface area: 1 cm<sup>2</sup>.

**TABLE 6.7.** Kinetic parameters for the redox couple Q/H<sub>2</sub>Q 12.5 x 10<sup>-3</sup>/12.5 x 10<sup>-3</sup> M in 0.5 M H<sub>2</sub>SO<sub>4</sub> at diamond electrodes with different IrO<sub>2</sub> loadings. Formal potential  $E^0 = 0.65$  V *vs* SHE.  $\Gamma = 1$  corresponds to 10<sup>15</sup> molecules IrO<sub>2</sub> cm<sup>-2</sup>.

Electrodes	$\Delta E_p$ [V]	$E^{0'}_{app}$ [V vs SHE]	$\beta_{ox}$ (2)	$\alpha_{red}$ (2)	$k^*$ [cm s <sup>-1</sup> ]	$k^{**}$ [cm s <sup>-1</sup> ]	$k^0$ [cm s <sup>-1</sup> ]
<b>BDD<sub>mild</sub></b>	1.42	0.5	0.2	0.2	2x10 <sup>-5</sup>	2x10 <sup>-5</sup>	2x10 <sup>-5</sup>
<b>BDD-IrO<sub>2</sub></b> ( $\Gamma = 0.6$ )	0.57	0.6	0.5	0.5	6x10 <sup>-6</sup>	5x10 <sup>-6</sup>	6x10 <sup>-6</sup>
<b>BDD-IrO<sub>2</sub></b> ( $\Gamma = 6.4$ )	0.45	0.6	0.5	0.5	3x10 <sup>-5</sup>	2x10 <sup>-5</sup>	3x10 <sup>-5</sup>
<b>BDD-IrO<sub>2</sub></b> ( $\Gamma = 30$ )	0.25	0.6	0.5	0.5	1x10 <sup>-4</sup>	2x10 <sup>-4</sup>	2x10 <sup>-4</sup>
<b>Ti-IrO<sub>2</sub></b>	0.19	0.5	0.5	0.5	-	-	4.4x10 <sup>-4</sup>

(2) determined with the Eq. 6.8.

$k^* = k^0$  determined from the oxidation peak

$k^0 = (k^* + k^{**})/2$

$k^{**} = k^0$  determined from the reduction peak

As already noticed for the ferri/ferrocyanide system (as an outer-sphere reaction), a resistance to charge transfer at the electrode/electrolyte interface seemed to be the cause of irreversibility of the redox reactions on diamond. The fact that IrO<sub>2</sub> deposition improved the reaction kinetics in the cases investigated, demonstrates that this resistance was not related to the resistivity of the diamond film but to the lack of active surface sites at the electrode/electrolyte interface (see the general discussion, Chapter 7).

### *Impedance measurements*

The double-layer capacitance of the electrodes,  $C_{dl}$ , and the reaction rate constants,  $R_{ct}$ , were calculated from the results of impedance measurements performed at BDD and BDD-IrO<sub>2</sub> in the presence of equimolar solutions of the

inner-sphere Q/H<sub>2</sub>Q redox couple. The circle obtained as a Nyquist plot suggests that the following circuit model can be adopted (Fig. 6.13):

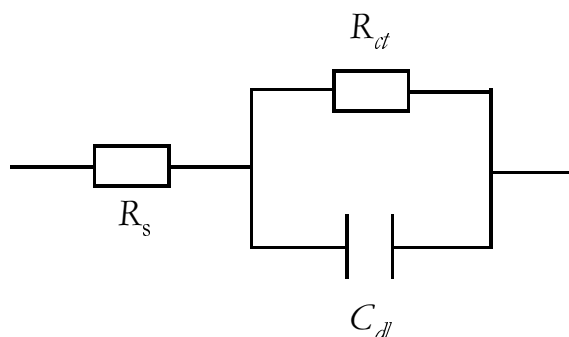


**FIGURE 6.13.** Circuit simulating a BDD<sub>mild</sub> electrode in an equimolar solution of Q/H<sub>2</sub>Q.

Via the mathematical treatment used for the Fe(CN)<sub>6</sub>III/II system (Eqs. 6.9 and 6.10), the BDD parameters were calculated for several values of potential (Figs. 6.14.A and 6.14.B).

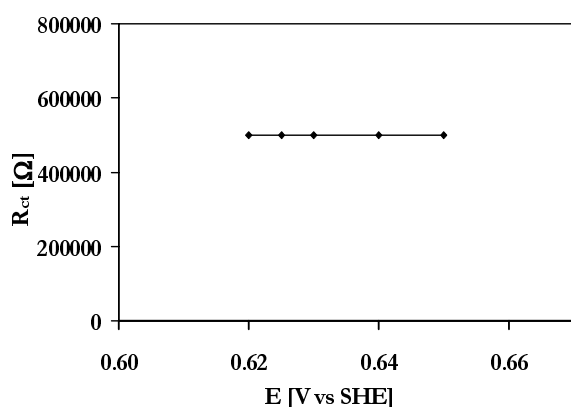


**FIGURE 6.14.A** Charge-transfer resistance values  $R_{ct}$  calculated around the value of  $E^0_{app}$  for the Q/H<sub>2</sub>Q redox system  $2.5 \times 10^{-3} / 2.5 \times 10^{-3}$  M in 0.5 M H<sub>2</sub>SO<sub>4</sub> at a BDD<sub>mild</sub> electrode.

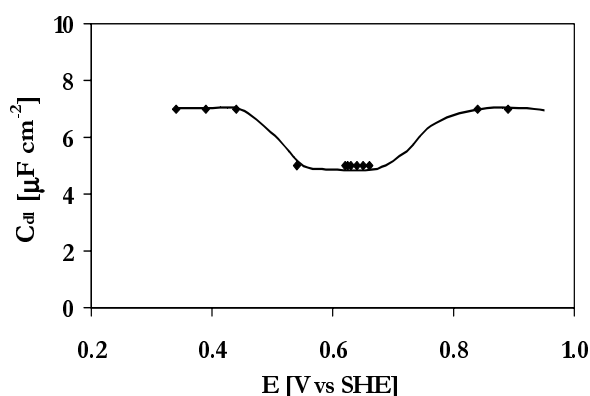


**FIGURE 6.14.B** Double-layer capacitance values  $C_{dl}$  of a BDD<sub>mild</sub> electrode in the Q/H<sub>2</sub>Q redox system  $2.5 \times 10^{-3} / 2.5 \times 10^{-3}$  M in 0.5 M H<sub>2</sub>SO<sub>4</sub>.

The charge-transfer resistance  $R_{ct}$  was very high (50 000 Ω) at potentials close to the equilibrium potential of the reaction. The capacitance value,  $C_{dl}$ , of 5 μF cm<sup>-2</sup> did not change significantly with potential. These results confirm what had been found by cyclic voltammetry and impedance measurements with the Fe(CN)<sub>6</sub>III/II redox couple. The charge-transfer process is hindered at the diamond electrode, and



high overpotentials are required for the reaction; a pure double-layer capacitance indicates that redox functionalities are not present on the diamond surface.

These results were compared with those obtained at BDD-IrO<sub>2</sub> electrodes for two IrO<sub>2</sub> loadings (Figs.6.15.A to 6.15.D).

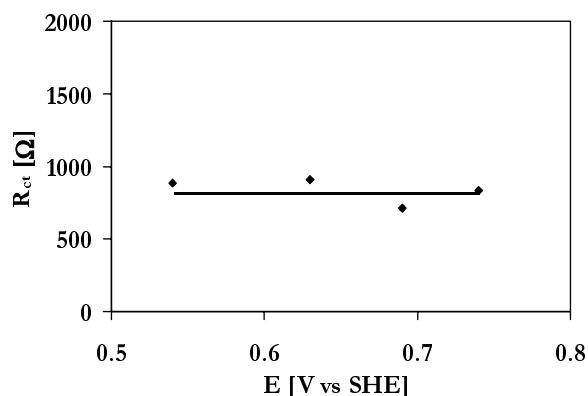


**FIGURE 6.15.A** Charge-transfer resistance values  $R_{ct}$  calculated around the value of  $E^{0'}_{app}$  for the Q/H<sub>2</sub>Q redox system  $2.5 \times 10^{-3} / 2.5 \times 10^{-3}$  M in 0.5 M H<sub>2</sub>SO<sub>4</sub> at a BDD-IrO<sub>2</sub> electrode ( $\Gamma = 0.64$ ).

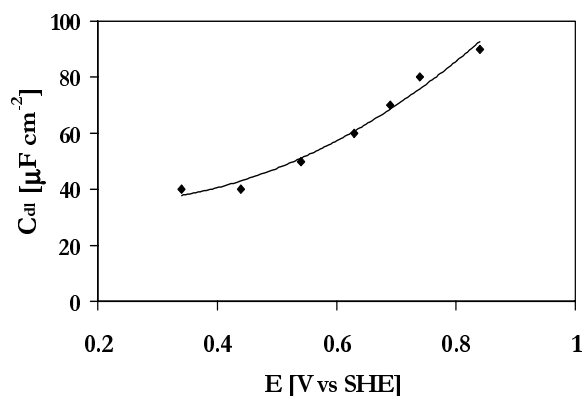


**FIGURE 6.15.B** Double-layer capacitance values  $C_{dl}$  of a BDD-IrO<sub>2</sub> electrode ( $\Gamma = 0.64$ ) in the Q/H<sub>2</sub>Q redox system  $2.5 \times 10^{-3} / 2.5 \times 10^{-3}$  M in 0.5 M H<sub>2</sub>SO<sub>4</sub>.  $\Gamma = 1$  corresponds to  $10^{15}$  molecules IrO<sub>2</sub> cm<sup>-2</sup>.

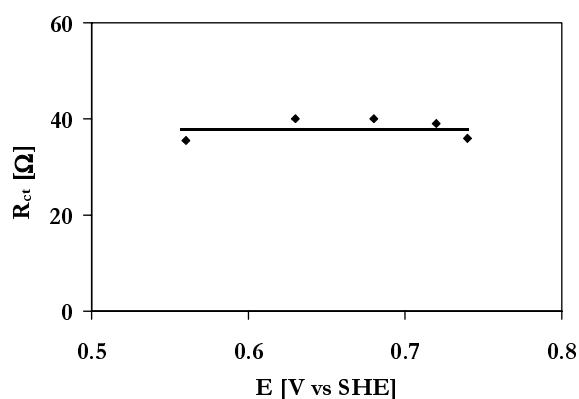


**FIGURE 6.15.C** Charge-transfer resistance values  $R_{ct}$  calculated around the value of  $E^{0'}_{app}$  for the Q/H<sub>2</sub>Q redox system  $2.5 \times 10^{-3} / 2.5 \times 10^{-3}$  M in 0.5 M H<sub>2</sub>SO<sub>4</sub> at a BDD-IrO<sub>2</sub> electrode ( $\Gamma = 6.4$ ).

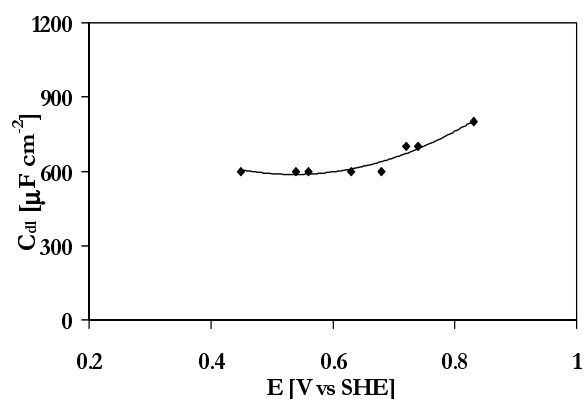


**FIGURE 6.15.D** Double-layer capacitance values  $C_{dl}$  of a BDD-IrO<sub>2</sub> electrode ( $\Gamma = 6.4$ ) in the Q/H<sub>2</sub>Q redox system  $2.5 \times 10^{-3} / 2.5 \times 10^{-3}$  M in 0.5 M H<sub>2</sub>SO<sub>4</sub>.  $\Gamma = 1$  corresponds to  $10^{15}$  molecules IrO<sub>2</sub> cm<sup>-2</sup>.

At low IrO<sub>2</sub> loadings already ( $\Gamma = 0.64$ ) the charge-transfer resistance determined at  $E^{0'}_{app}$  decreased (Fig. 6.15.A) relative to that found at bare diamond

(Fig. 6.14.A). The double-layer capacitance increased (Fig. 6.15.B) over that found at bare BDD because of the pseudocapacitance contribution from the surface redox couples present on IrO<sub>2</sub> deposits [15, 16]. The electron-transfer resistance decreased with increasing IrO<sub>2</sub> loading ( $\Gamma = 6.4$  in Fig. 6.15.C). The capacitance values (Fig. 6.15.D) are in agreement with those found for the ferri/ferrocyanide system, confirming the contribution of pseudocapacitance.

Using the Butler-Volmer equation as written for low applied overpotentials:

$$j = j_0 \frac{zF}{RT} \eta \quad 6.11$$

and remembering that the charge-transfer resistance can be expressed as:

$$R_{ct} = \frac{\eta}{j} = \frac{RT}{zFj_0} \quad 6.12$$

it was possible to calculate the exchange current density,  $j_0$ , at the equilibrium potential. Values calculated as a function of the IrO<sub>2</sub> loading are reported in the following Table 6.8.

**TABLE 6.8.** Kinetic parameters of the Q/H<sub>2</sub>Q  $2.5 \times 10^{-3}/2.5 \times 10^{-3}$  M system in 0.5 M H<sub>2</sub>SO<sub>4</sub> at BDD electrodes with different IrO<sub>2</sub> loadings.  $\Gamma = 1$  corresponds to  $10^{15}$  molecules IrO<sub>2</sub> cm<sup>-2</sup>.

electrode	$j_0$ [A cm <sup>-2</sup> ]	$k^0$ [cm s <sup>-1</sup> ]
BDD <sub>mild</sub>	$1.5 \times 10^{-7}$	$3 \times 10^{-7}$
BDD-IrO <sub>2</sub> $\Gamma = 0.64$	$2.8 \times 10^{-5}$	$6 \times 10^{-5}$
BDD-IrO <sub>2</sub> $\Gamma = 6.4$	$6.4 \times 10^{-4}$	$1 \times 10^{-3}$

The trend observed for the reaction rate constants deduced from impedance measurements was in agreement with that following from cyclic voltammetry, indicating that the equivalent-circuit model for BDD-IrO<sub>2</sub> electrodes was valid. The redox reaction is assumed to be associated simultaneously with the diamond matrix and with the IrO<sub>2</sub> deposit. The overall reaction occurring at the BDD and IrO<sub>2</sub> systems can then be described by two circuits in parallel (Fig. 6.16).

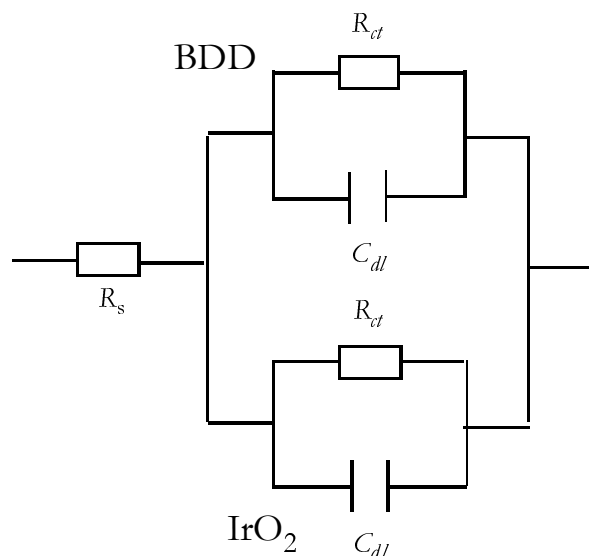


**FIGURE 6.16.** Theoretical circuit for a BDD-IrO<sub>2</sub> electrode in a redox system solution. BDD system and IrO<sub>2</sub> system represented by two circuits in parallel.

Since the charge-transfer resistance on diamond is extremely high, and the capacitance very small, the diamond system can be neglected entirely. In fact, the presence of BDD can be neglected (Figs. 6.11 and 6.13) in the circuit model given in Fig. 6.16. The reactions take place on active IrO<sub>2</sub> sites, and the BDD merely acts as an inert substrate (see General discussion, Chapter 7).

### 3.4. Oxygen evolution reaction (an inner-sphere reaction)

DSA-type IrO<sub>2</sub> electrodes (DSA-O<sub>2</sub>) are widely employed as anodes in galvanic processes and electrowinning because of their high electrochemical stability under the conditions of anodic oxygen evolution [10]. Diamond electrodes exhibit a very high stability under the conditions of oxygen evolution, but because of the high overvoltage for this reaction, the electrode is not a suitable material for such applications.

The effects produced by IrO<sub>2</sub> deposition on diamond in the oxygen evolution reaction (OER) were investigated by cyclic voltammetry and steady-state polarisation, and the results are described in the following paragraphs.

### Cyclic voltammetry

Cyclic voltammetry was performed in the potential region of electrolyte decomposition to study the oxygen evolution reaction (OER) at BDD and BDD-IrO<sub>2</sub> electrodes. At bare diamond electrodes the process took place at very high overpotentials (Fig. 6.17 (A)). Following the deposition of IrO<sub>2</sub> ( $\Gamma = 6.4$ ) the onset potential shifted to less positive values (Fig. 6.17 (B)). A potential shift of almost 1 V was noticed between BDD and BDD-IrO<sub>2</sub> electrodes.

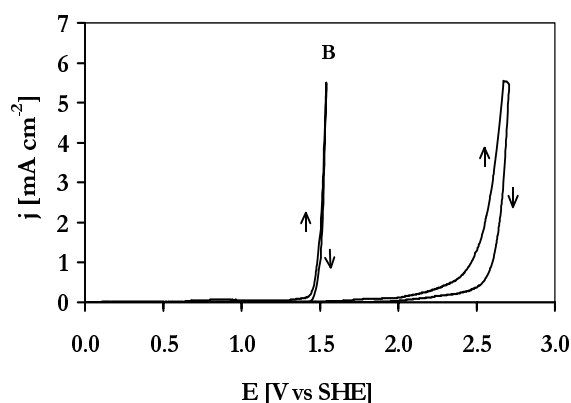


**FIGURE 6.17.** Cyclic voltammograms recorded at (A) BDD and (B) BDD-IrO<sub>2</sub> ( $\Gamma = 6.4$ ) electrodes in 0.5 M H<sub>2</sub>SO<sub>4</sub>. Scan rate: 0.1 V s<sup>-1</sup>. Geometric surface area 1 cm<sup>2</sup>.  $\Gamma = 1$  corresponds to 10<sup>15</sup> molecules IrO<sub>2</sub> cm<sup>-2</sup>.

At BDD-IrO<sub>2</sub> in 0.5 M H<sub>2</sub>SO<sub>4</sub>, oxygen evolution took place at 1.45 V *vs* SHE, close to the equilibrium potential of the redox system Ir(VI)/Ir(IV) (1.35 V *vs* SHE). The current increased sharply at the OER potential, indicating a high electrocatalytic activity of BDD-IrO<sub>2</sub> electrodes. Similar results were obtained in 1 M HClO<sub>4</sub>.

### Steady-state polarisation curves

Steady-state polarisation curves were recorded at BDD electrodes having different IrO<sub>2</sub> loadings. Figure 6.18.A shows that the oxygen evolution reaction shifted to less positive overpotentials with increasing IrO<sub>2</sub> loading. It is reasonable to suppose at this stage that only the IrO<sub>2</sub> particles on BDD are active in the oxygen evolution reaction. The true surface area of the IrO<sub>2</sub> deposits must then be considered. The values of current plotted in Fig. 6.18.A were normalized so as to suppress the roughness factor effects of IrO<sub>2</sub>, and are replotted in Figure 6.18.B. The new curves are found to coincide, and oxygen evolution started at 1.45 V with all IrO<sub>2</sub> loadings.

The mechanism of the reaction can be summarised as follows. For IrO<sub>2</sub> electrodes, the sequence of steps must be considered in which the two electrochemical steps of water discharge (a) and surface oxide formation (c) are followed by the chemical step (d) of oxygen evolution. At BDD, the mechanism can

be represented in terms of the electrochemical steps (a) and (b) in which oxygen is obtained by the combination of hydroxyl radicals.

- a.  $\text{H}_2\text{O} + \text{S} \rightarrow \text{S-OH}^* + \text{H}^+ + \text{e}^-$
- b.  $\text{S-OH}^* + \text{S-OH}^* \rightarrow 2\text{S} + \text{O}_2 + 2\text{H}^+ + 2\text{e}^-$
- c.  $\text{S-OH}^* \rightarrow \text{S-O} + \text{H}^+ + \text{e}^-$
- d.  $\text{S-O} + \text{S-O} \rightarrow 2\text{S} + \text{O}_2$

Tafel plots were obtained for the OER (Figs. 6.18.C and 6.18.D). For BDD electrodes, the Tafel slope (see Chapter 2) was around  $0.14 \text{ V dec}^{-1}$ , implying that the rate-determining step of the reaction on diamond was water discharge to hydroxyl radicals ( $b = 0.12 \text{ V dec}^{-1}$ ), *i.e.*, the step (a).  $\text{IrO}_2$  deposition strongly changed the electrode's behaviour, the Tafel slopes now varied between  $0.04$  and  $0.06 \text{ V dec}^{-1}$ , depending on the  $\Gamma$  value. After normalising to the true surface areas, all curves for BDD- $\text{IrO}_2$  electrodes were superimposed, and an average value of  $0.05 \text{ V dec}^{-1}$  was calculated for the slope. This value is closer to the value of  $0.03 \text{ V dec}^{-1}$  that is typical for a rate-determining step (c).

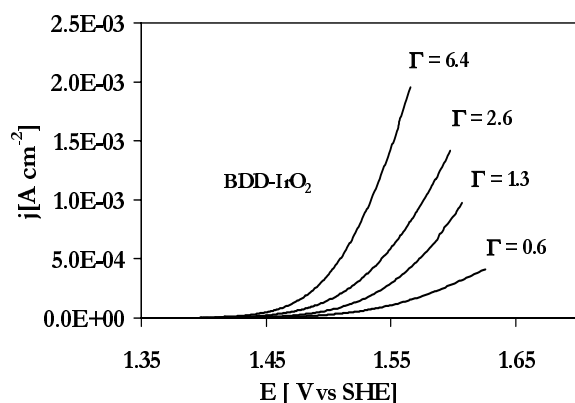


**FIGURE 6.18.A** Polarisation curves of BDD- $\text{IrO}_2$  electrodes with different loadings  $\Gamma$  recorded in  $0.5 \text{ M H}_2\text{SO}_4$ . Geometric surface area  $1 \text{ cm}^2$ , scan rate  $0.1 \text{ mV s}^{-1}$ .  $\Gamma = 1$  corresponds to  $10^{15}$  molecules  $\text{IrO}_2 \text{ cm}^{-2}$ .

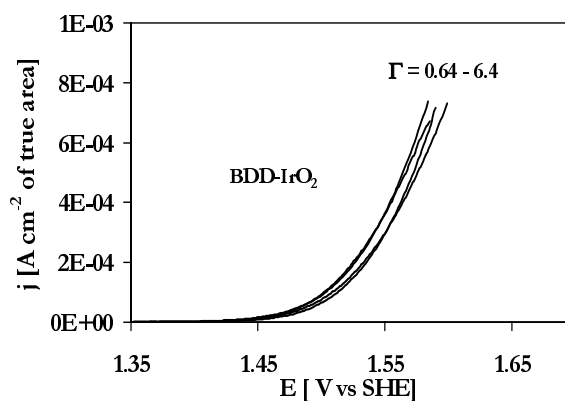


**FIGURE 6.18.B** Polarisation curves of BDD- $\text{IrO}_2$  electrodes with different loadings  $\Gamma$  recorded in  $0.5 \text{ M H}_2\text{SO}_4$ . Curves normalised to the deposit's true surface areas as listed in Table 6.4, scan rate  $0.1 \text{ mV s}^{-1}$ .  $\Gamma = 1$  corresponds to  $10^{15}$  molecules  $\text{IrO}_2 \text{ cm}^{-2}$ .

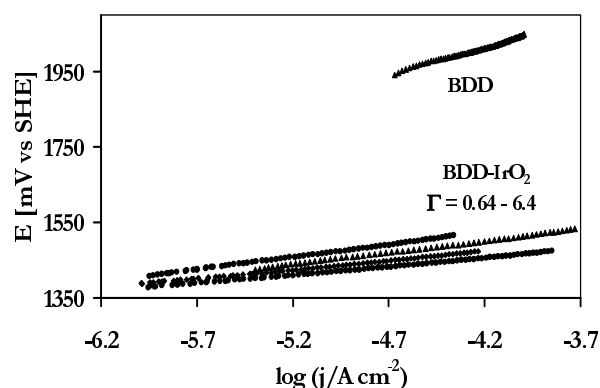


**FIGURE 6.18.C** Tafel plots for BDD electrodes with different loadings  $\Gamma$  from polarisation curves recorded in 0.5 M  $\text{H}_2\text{SO}_4$ . Geometric surface area  $1 \text{ cm}^2$ , scan rate  $0.1 \text{ mV s}^{-1}$ .  $\Gamma = 1$  corresponds to  $10^{15}$  molecules  $\text{IrO}_2 \text{ cm}^{-2}$ .

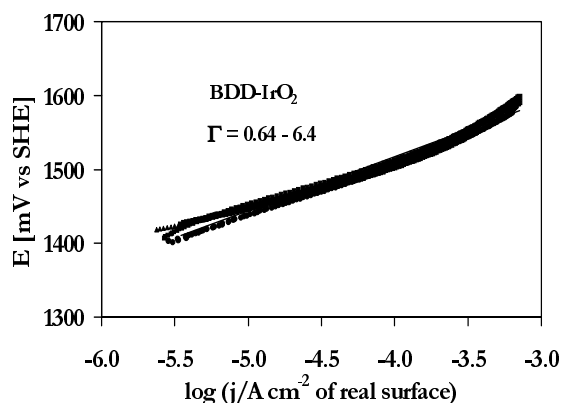


**FIGURE 6.18.D** Tafel plots for BDD electrodes with different loadings  $\Gamma$  from polarisation curves recorded in 0.5 M  $\text{H}_2\text{SO}_4$ . Currents normalised to the deposit's true surface areas as listed in Table 6.4, scan rate  $0.1 \text{ mV s}^{-1}$ .  $\Gamma = 1$  corresponds to  $10^{15}$  molecules  $\text{IrO}_2 \text{ cm}^{-2}$ .

The behaviour of the BDD- $\text{IrO}_2$  electrodes can be interpreted entirely as that of  $\text{IrO}_2$  continuous-film electrodes. Diamond merely acts as an inert substrate on which the catalytic activity of deposited  $\text{IrO}_2$  particles can be investigated without any interference. Differences in the behaviour of electrodes having different  $\text{IrO}_2$  loadings probably are due, chiefly to different active surface areas. In terms of results normalised to the  $\text{IrO}_2$  loading, all electrodes exhibited similar electrocatalytic properties. However, it was of particular interest to notice that even extremely low  $\text{IrO}_2$  loadings on a diamond substrate exhibit the electrode properties of  $\text{IrO}_2$  continuous-film electrodes. The well dispersed  $\text{IrO}_2$  nanoparticles assured a high electrocatalytic activity of the electrodes.

With the phenomenological model that had been suggested previously for the OER on  $\text{IrO}_2$  continuous-film electrodes [25], the oxygen evolution pathway can also be described at BDD- $\text{IrO}_2$  and at BDD electrodes (Fig. 6.19). According to this model, electrodes are classified as *active* and *non-active*. The former (including  $\text{IrO}_2$  and other metal oxides) participate in the oxygen evolution reaction (Fig. 6.19, path c) through a change in oxidation state of the electrode material which thus incorporates the oxygen atom generated by water discharge (step a). Returning from the higher oxidation state to the most stable oxidation state (step d), electrode sites then liberate oxygen atoms which combine to oxygen. *Non-active* electrodes (such as BDD) do not participate directly in the oxygen evolution process. Oxygen generated by water decomposition is physically absorbed on the electrode surface in the form

of hydroxyl radicals, which then react and combine to be liberated as molecular oxygen.

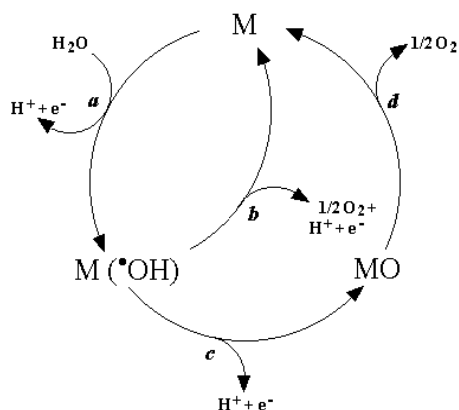


**FIGURE 6.19.** Scheme of the oxygen evolution reaction at ‘active’ (BDD-IrO<sub>2</sub>) and ‘non-active’ (BDD) electrode materials. (a) Water decomposition step; (b) oxygen evolution reaction on ‘non-active’ electrodes via physically adsorbed hydroxyl radicals; (c) chemical adsorption of oxygen on ‘active’ electrodes (formation of IrO<sub>3</sub>); (d) oxygen evolution reaction at active (BDD-IrO<sub>2</sub>) electrodes.

Thus, by depositing IrO<sub>2</sub> nanoparticles on the diamond surface, the character of BDD is changed from that of an *non-active* to that of an *active* electrode material.

### 3.5. Peroxodisulphate production (an inner-sphere reaction)

Peroxodisulphuric acid and its salts are among the strongest known oxidising agents ( $E^0 = 2.01$  V vs SHE). The two most important applications are in the etching of printed circuits and in acrylonitrile polymerisation [26]. Other applications are in waste water treatment, dye oxidation, and fibre bleaching. Peroxodisulphuric acid is also an important intermediate in the electrochemical production of hydrogen peroxide. It can be synthesised by electrolysis of H<sub>2</sub>SO<sub>4</sub> at platinum anodes [27]. In this process an electrolyte recycling step occurs which requires a prior purification step because of corrosion of the platinum anodes during peroxodisulphate formation. The efficiency of this oxidation reaction strongly depends on the anode material; a high oxygen overvoltage is in fact required to minimise oxygen evolution as a side reaction.

Because of its very high stability and high overpotential for oxygen evolution, boron-doped diamond was recently used for peroxodisulphate production, and found to yield a very high current efficiency [28, 29].

As a tool for understanding the effects of IrO<sub>2</sub> deposition on diamond, electrodes with IrO<sub>2</sub> deposits were tested in peroxodisulphate production, and the results were compared with those obtained on bare diamond under the same

working conditions. Electrolyses were carried out, both with diamond and with BDD-IrO<sub>2</sub> electrodes as an anode material, and peroxodisulphate formation was followed by titration methods [29]. By the deposition of IrO<sub>2</sub> nanoparticles on boron-doped diamond, the electrocatalytic activity of the electrodes for peroxodisulphate production is altered to such an extent that the reaction is completely suppressed (Fig. 6.20).

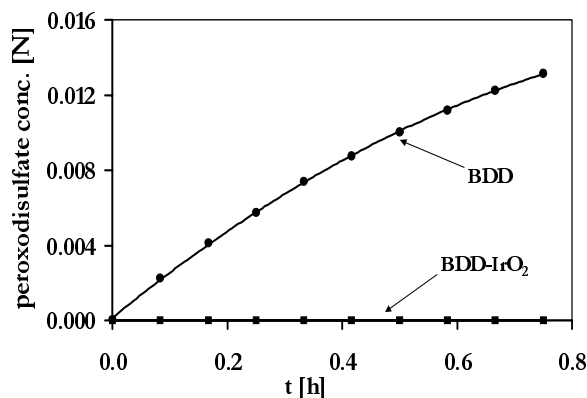


**FIGURE 6.20.** Formation of peroxodisulphate at BDD and BDD-IrO<sub>2</sub> ( $\Gamma = 6.4$ ) electrodes. 1M H<sub>2</sub>SO<sub>4</sub>, 10 mA cm<sup>-2</sup>.  $T = 30$  °C.  $\Gamma = 1$  corresponds to  $10^{15}$  molecules IrO<sub>2</sub> cm<sup>-2</sup>.

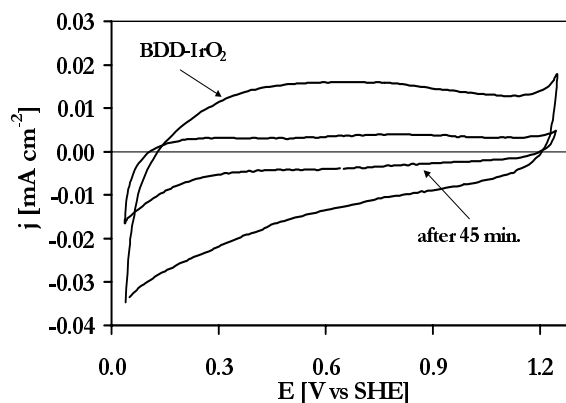


**FIGURE 6.21.** Cyclic voltammetry of BDD-IrO<sub>2</sub> ( $\Gamma = 6.4$ ) electrodes before and after preparative electrolysis (Fig. 6.20).  $\Gamma = 1$  corresponds to  $10^{15}$  molecules IrO<sub>2</sub> cm<sup>-2</sup>.

Deposition of IrO<sub>2</sub> on BDD reduced the overvoltage for the OER (page 149), by increasing the electrocatalytic activity of the electrodes towards the reaction. The oxygen evolution reaction thus became the main process at modified electrodes, suppressing peroxodisulphate formation. After 45 minutes of electrolysis, 80% of the initial IrO<sub>2</sub> loading had disappeared from the diamond surface, as shown by the response of this electrode seen by cyclic voltammetry (Fig. 6.21). Electrolysis was then continued for two more days but no peroxodisulphate could be detected. An increase in the electrode's working potential during the experiments (not illustrated in the figures) indicated a progressive depletion of IrO<sub>2</sub> catalyst on the diamond surface, but no qualitative change in the electrode's behaviour was noticed. The catalytic activity of IrO<sub>2</sub> on diamond was so strong that peroxodisulphate formation was suppressed even by an extremely low residual IrO<sub>2</sub> loading. The mechanism previously proposed for peroxodisulphuric acid formation [29], which involves the formation of hydroxyl radicals and their further reaction with HSO<sub>4</sub><sup>-</sup>, cannot be valid in the case of BDD-IrO<sub>2</sub> electrodes. Here the hydroxyl radicals produced by water discharge are chemically adsorbed, and lead to the formation of IrO<sub>3</sub> (Fig. 6.19). Thus, their reactivity toward the hydrogen sulphate ions is extremely low, and oxygen evolution occurs instead.



### 3.6. Oxidation of organic compounds (an inner-sphere reaction)

Because of its high chemical and electrochemical stability, boron-doped diamond had been investigated as an electrode for the oxidation of organic substances. A wide range of organic compounds have already been tested [30 and references therein], and the powerful electrochemical properties of diamond were confirmed. Diamond behaves like a non-active electrode: it does not participate directly in the oxidation reaction but produces extremely active hydroxyl radicals by water decomposition which then act as oxidants. A very high overpotential is needed ( $\cong 2.3$  V *vs* SHE) to decompose water and thus produce hydroxyl radicals. While oxygen evolution is a slow reaction on diamond, the oxidation of organic compounds can occur with a very high current efficiency under these extreme working conditions. As a corollary, however, the required high overvoltage leads to high energy consumption. With the aim of reducing the overvoltage for the oxidation of organic substances, IrO<sub>2</sub> nanoparticles were deposited on a diamond surface. The oxidation of 2-propanol, formic acid, and oxalic acid was investigated, both on BDD and on BDD-IrO<sub>2</sub> ( $\Gamma = 6.4$ ) electrodes, these substances serving as models for alcohol and carboxylic acid compounds, respectively.

#### *Polarisation curves*

The organic compounds investigated were not electroactive at BDD and BDD-IrO<sub>2</sub> electrodes in the potential region of electrolyte stability. Their oxidation reaction occurred, both at BDD and at BDD-IrO<sub>2</sub> electrodes, in the potential region of water decomposition. As seen above, the overpotential of water discharge on diamond decreased by about 1 volt upon IrO<sub>2</sub> deposition. A similar behaviour was found in the organic oxidation processes (Figs. 6.22.A to 6.22.F). The BDD-IrO<sub>2</sub> electrodes were more electroactive than bare BDD toward the oxidation of organic substances.

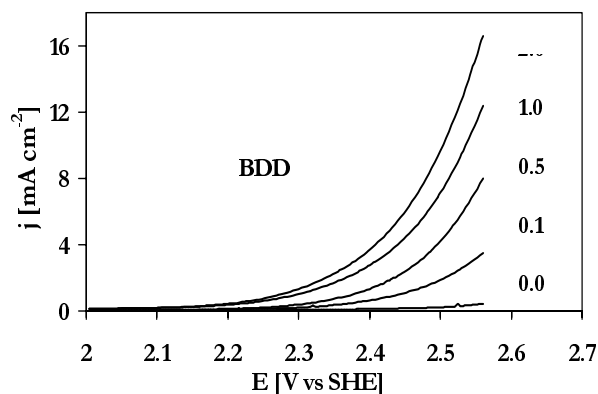


**FIGURE 6.22.A** Polarisation curves recorded at a BDD electrode in 0.5 M  $\text{H}_2\text{SO}_4$  containing 2-propanol in different concentrations (M). Scan rate:  $0.02 \text{ V s}^{-1}$ .

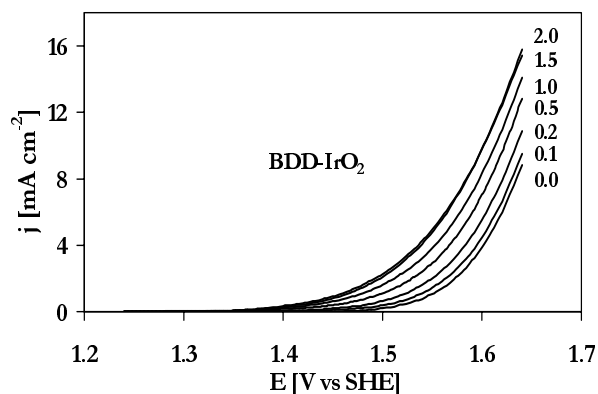


**FIGURE 6.22.B** Polarisation curves recorded at a BDD- $\text{IrO}_2$  electrode ( $\Gamma = 6.4$ ) in 0.5 M  $\text{H}_2\text{SO}_4$  containing 2-propanol in different concentrations (M). Scan rate:  $0.02 \text{ V s}^{-1}$ .  $\Gamma = 1$  corresponds to  $10^{15}$  molecules  $\text{IrO}_2 \text{ cm}^{-2}$ .

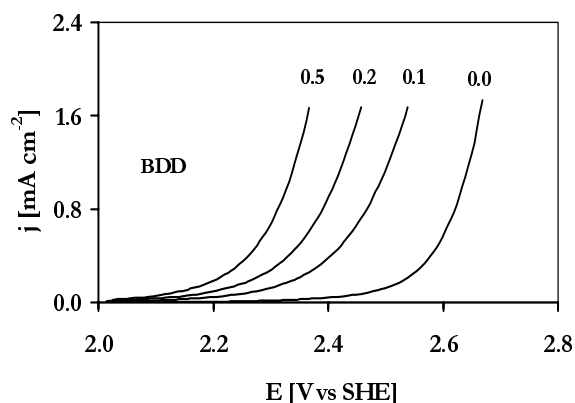


**FIGURE 6.22.C** Polarisation curves recorded at a bare BDD electrode in 0.5 M  $\text{H}_2\text{SO}_4$  containing oxalic acid in different concentrations (M). Scan rate:  $0.02 \text{ V s}^{-1}$ .

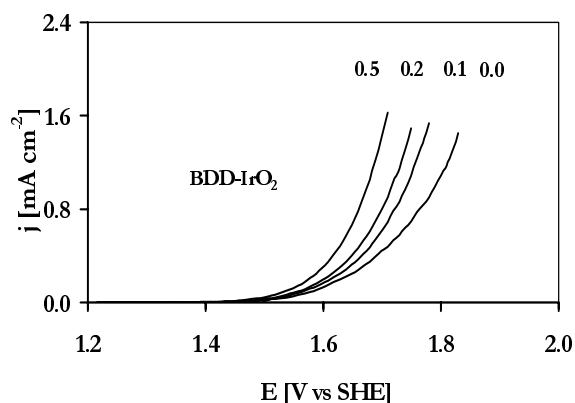


**FIGURE 6.22.D** Polarisation curves recorded at a BDD- $\text{IrO}_2$  electrode ( $\Gamma = 6.4$ ) in 0.5 M  $\text{H}_2\text{SO}_4$  containing oxalic acid in different concentrations (M). Scan rate:  $0.02 \text{ V s}^{-1}$ .  $\Gamma = 1$  corresponds to  $10^{15}$  molecules  $\text{IrO}_2 \text{ cm}^{-2}$ .

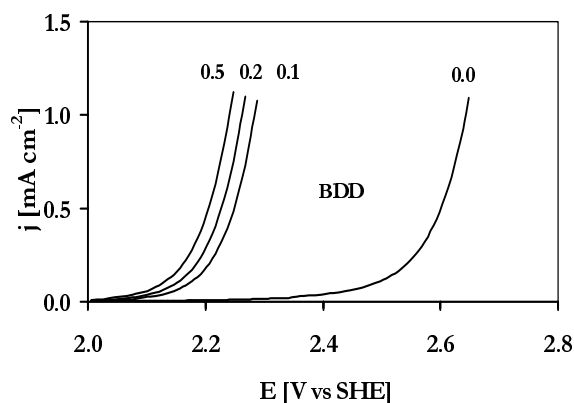


**FIGURE 6.22.E** Polarisation curves recorded at a bare BDD electrode in 0.5 M  $\text{H}_2\text{SO}_4$  containing formic acid in different concentrations (M). Scan rate:  $0.02 \text{ V s}^{-1}$ .

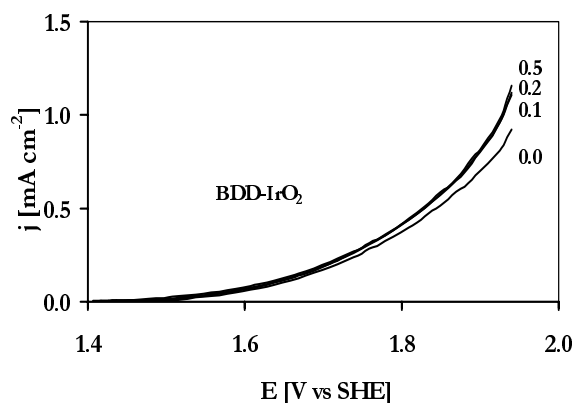


**FIGURE 6.22.F** Polarisation curves recorded at a BDD- $\text{IrO}_2$  ( $\Gamma = 6.4$ ) in 0.5 M  $\text{H}_2\text{SO}_4$  containing formic acid in different concentrations (M). Scan rate:  $0.02 \text{ V s}^{-1}$ .  $\Gamma = 1$  corresponds to  $10^{15}$  molecules  $\text{IrO}_2 \text{ cm}^{-2}$ .

In Figures 6.23.A to 6.23.C, the potential shifts  $\Delta E$  are plotted as functions of the concentration of organic substance for bare and surface-modified diamond. Such a shift of the anode potential toward less positive values occurring in the presence of organic compounds was found, both at BDD and at BDD- $\text{IrO}_2$  electrodes. Bare diamond was found to be more sensitive in this respect: for a given concentration of 1-propanol, oxalic acid, or formic acid, the potential shifts were more important on diamond than on BDD- $\text{IrO}_2$ . This potential shift indicates that intermediates formed during water decomposition are involved in the organic oxidation process. The fact that the shift is more important on diamond electrodes can be explained in terms of a higher reactivity of the intermediates formed on diamond.

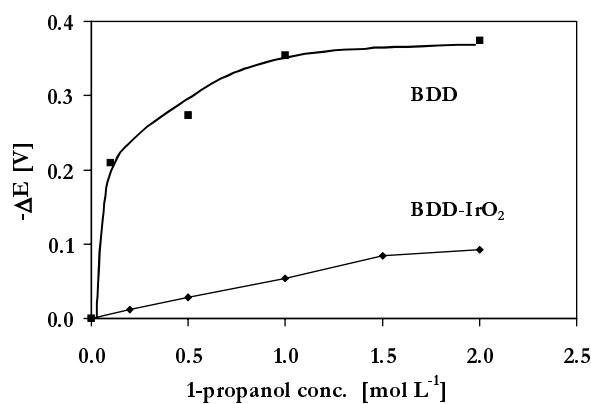


**FIGURE 6.23.A** The shifts of anode potential toward less positive values as functions of 1-propanol concentration, observed at BDD and BDD- $\text{IrO}_2$  ( $\Gamma = 6.4$ ) electrodes. Values calculated from Figs. 6.22.A and 6.22.B at  $1 \text{ mA cm}^{-2}$ .  $\Gamma = 1$  corresponds to  $10^{15}$  molecules  $\text{IrO}_2 \text{ cm}^{-2}$ .

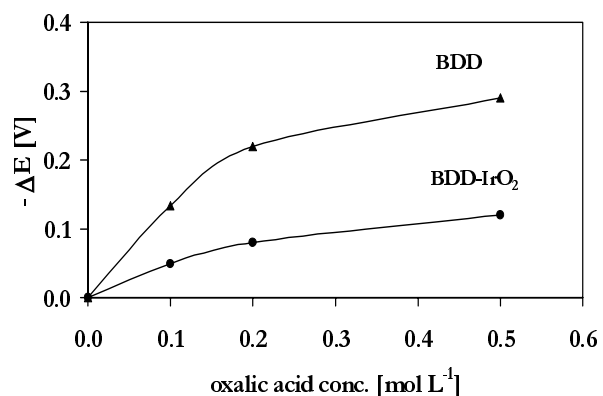


**FIGURE 6.23.B** The shifts of anode potential toward less positive values as functions of oxalic acid concentration, observed at BDD and BDD-IrO<sub>2</sub> ( $\Gamma = 6.4$ ) electrodes. Values calculated from Figs. 6.22.C and 6.22.D at 1 mA cm<sup>-2</sup>.  $\Gamma = 1$  corresponds to 10<sup>15</sup> molecules IrO<sub>2</sub> cm<sup>-2</sup>.

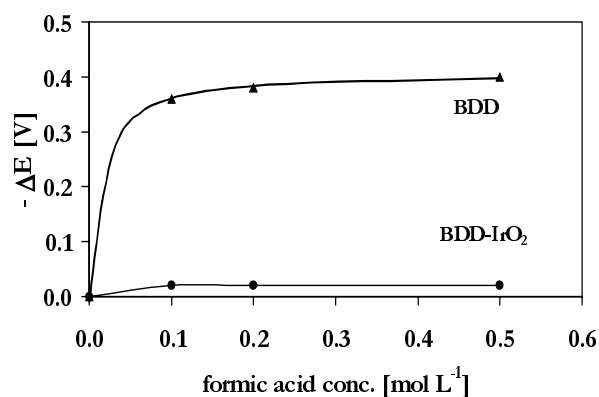


**FIGURE 6.23.C** The shifts of anode potential toward less positive values as functions of formic acid concentration, observed at BDD and BDD-IrO<sub>2</sub> ( $\Gamma = 6.4$ ) electrodes. Values calculated from Figs. 6.22.E and 6.22.F at 1 mA cm<sup>-2</sup>.  $\Gamma = 1$  corresponds to 10<sup>15</sup> molecules IrO<sub>2</sub> cm<sup>-2</sup>.

### *Bulk electrolysis*

For a more thorough understanding of the electrocatalytic activity of electrodes towards organic oxidation processes, the electrolysis of oxalic acid was followed by analytical methods at BDD and BDD-IrO<sub>2</sub> under the same working conditions (Fig. 6.24). Total organic carbon (TOC) and chemical oxygen demand (COD) were measured in order to follow the organic concentration in solution during electrolysis. The oxidation of oxalic acid (Fig. 6.24) was extremely fast on diamond electrodes and occurred with a very high current efficiency until complete consumption of the organic substance. The COD and TOC values recorded as functions of time confirmed the complete combustion of oxalic acid (curves not reported). At BDD-IrO<sub>2</sub> electrodes under the same conditions, the reaction was so slow that a mere 20% of the oxalic acid initially present had been oxidised after 20 hours of electrolysis (Fig. 6.24).

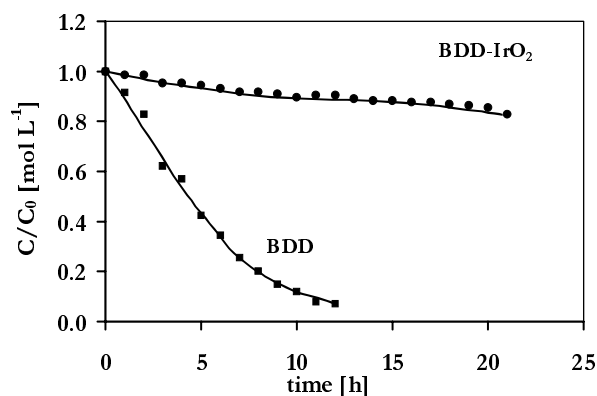


**FIGURE 6.24.** Electrochemical oxidation of oxalic acid (0.17 M) in 1 M HClO<sub>4</sub> at BDD and BDD-IrO<sub>2</sub> ( $\Gamma = 6.4$ ) electrodes.  $j = 10 \text{ mA cm}^{-2}$ ,  $T = 30^\circ\text{C}$ .  $\Gamma = 1$  corresponds to  $10^{15}$  molecules IrO<sub>2</sub> cm<sup>-2</sup>.

The phenomenological model of Fig. 6.25 can explain the general behaviour of the electrodes toward organic oxidation. In the case of *non-active* electrodes such as diamond, hydroxyl radicals are formed as intermediates of water decomposition (a) and undergo weak physical adsorption on the electrode surface. Their high reactivity leads to a high current efficiency of the organic oxidation reaction (b), while the OER remains a side reaction in the process (c). The strong chemical bond formed between the hydroxyl radicals and the active sites of *active* electrodes such as IrO<sub>2</sub> (formation of IrO<sub>3</sub>) makes these intermediates less reactive toward the organic substance (e). The main process then is oxygen evolution (f), while the electrochemical oxidation of the organic compounds takes place with a rather low current efficiency.

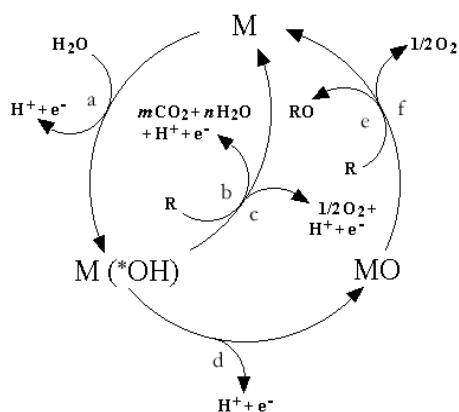


**FIGURE 6.25.** Phenomenological model for the anodic oxidation of organic compounds with simultaneous oxygen evolution at BDD anodes (reactions a, b and c) and at BDD-IrO<sub>2</sub> anodes (reactions a, d, e and f). (a) Water discharge to hydroxyl radicals, OH\*; (b) combustion of the organic compound, R, *via* hydroxyl radicals; (c) oxygen evolution by electrochemical oxidation of hydroxyl radicals; (d) formation of the higher metal oxide, MO; (e) partial (selective) oxidation of the organic compound; (f) oxygen evolution by chemical decomposition of the higher metal oxide.

### 3.7. Stability of BDD-IrO<sub>2</sub> electrodes

The electrochemical stability of a BDD-IrO<sub>2</sub> ( $\Gamma = 6.4$ ) electrode has been investigated. The electrode was subjected in two-day experiments at 30 °C to different current densities from 0.01 to 0.5 and 1 A cm<sup>-2</sup> in 1 M H<sub>2</sub>SO<sub>4</sub>. The working electrode potentials were recorded during this stability test. At the lowest current density, the stability of the electrodes was quite good (Fig. 6.26.A): the potential increased during the first few hours from an initial value of 1.7 V to 2.3 V *vs* SHE, but then it was stable during the remainder of the experiment. IrO<sub>2</sub> was deposited, both on an as-grown diamond surface (BDD<sub>ag</sub>) and on a mildly anodised diamond (BDD<sub>mild</sub>) (see Chapter 3), and the stability of these two electrodes was examined for comparison under the same conditions (Fig. 6.26.A). The IrO<sub>2</sub> deposit was initially more stable on the mildly polarised BDD surface than on as-grown diamond, but beyond the first few hours almost no differences remained. Cyclic voltammetry was performed in order to calculate the amount of IrO<sub>2</sub> remaining on the electrode after the stability tests (Figs. 6.26.B and 6.26.C). Only 6% of the initial IrO<sub>2</sub> loading was still present on the diamond surface.

The stability of IrO<sub>2</sub> was also tested under practical working conditions at 1 A cm<sup>-2</sup> over a period of 72 hours. The electrode's potential slowly increased, indicating a progressive IrO<sub>2</sub> loss. XPS measurement (not illustrated) were made on the sample after this period in order to identify the Ir compound still present on the surface. A shift of the 4f<sub>7/2</sub> peak from 62 eV to 63 V indicated that the properties of the Ir deposit had changed. Probably this was due to a reorganization of crystal structure of Ir or to the formation of a C-Ir compound.

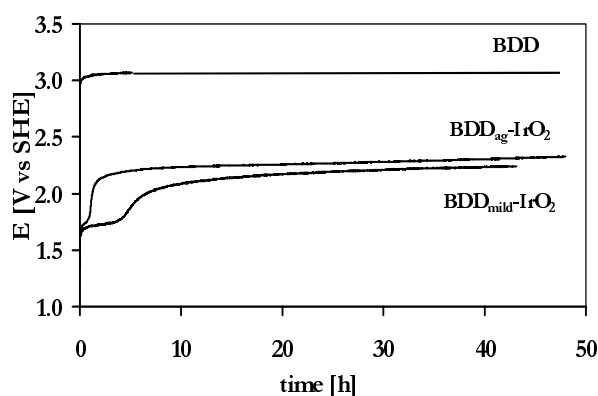


**FIGURE 6.26.A** Electrode potentials recorded as functions of time at BDD and BDD-IrO<sub>2</sub> ( $\Gamma = 6.4$ ) electrodes during a short life test in 1 M H<sub>2</sub>SO<sub>4</sub>.  $j = 0.01$  A cm<sup>-2</sup>.  $T = 30$  °C.  $\Gamma = 1$  corresponds to  $10^{15}$  molecules IrO<sub>2</sub> cm<sup>-2</sup>.

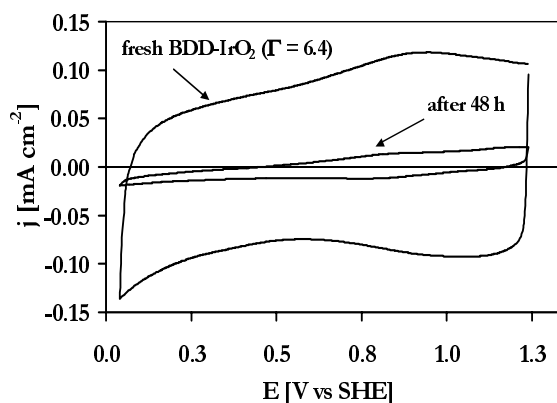


**FIGURE 6.26.B** Cyclic voltammograms recorded at BDD-IrO<sub>2</sub> ( $\Gamma = 6.4$ ) electrodes before and after the life test. Scan rate  $0.1$  V s<sup>-1</sup>. Conditions as in Fig. 6.26.A.  $\Gamma = 1$  corresponds to  $10^{15}$  molecules IrO<sub>2</sub> cm<sup>-2</sup>.

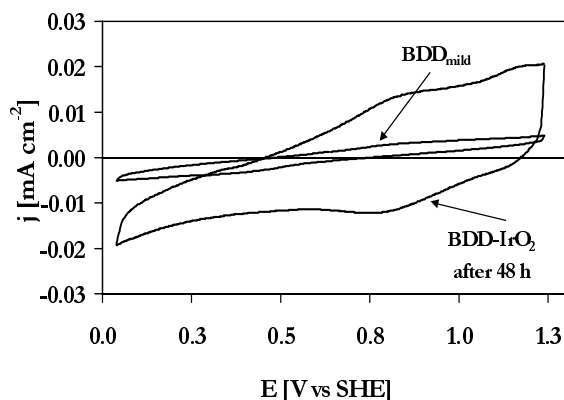


**FIGURE 6.26.C** Cyclic voltammograms recorded at BDD-IrO<sub>2</sub> ( $\Gamma = 6.4$ ) electrodes after the life test. Scan rate  $0.1$  V s<sup>-1</sup>.  $\Gamma = 1$  corresponds to  $10^{15}$  molecules IrO<sub>2</sub> cm<sup>-2</sup>.

## 4. Conclusions

The surface activity of BDD electrodes was increased by the deposition of IrO<sub>2</sub> nanoparticles on the diamond surface. Cyclic voltammetry provided an electrochemical spectrum of the surface redox transitions due to the redox couples Ir(III)/(II) and Ir(IV)/Ir(III) being electroactive at different values of potential. The voltammetric charge and the surface capacitance calculated from the results of cyclic voltammetry provide a measure of active surface area of the electrodes, which depends on the IrO<sub>2</sub> loading.

The electrochemical behaviour of the electrodes was tested in the presence of outer-sphere and inner-sphere redox couples ( $\text{Fe}(\text{CN})_6^{\text{III/II}}$  and  $\text{Q}/\text{H}_2\text{Q}$ , respectively). The electrocatalytic activity towards redox reactions was increased by the deposition of  $\text{IrO}_2$  nanoparticles on the diamond surface. The effect was similar to that noticed for freshly prepared diamond electrodes and for graphite-modified BDD electrodes. After deposition of the  $\text{IrO}_2$  particles, the resistance to charge transfer decreased by several orders of magnitude, and the reaction rate constants for the redox processes decreased as well. The electrocatalytic activity of the electrodes towards the oxygen evolution reaction was also increased by the deposition of  $\text{IrO}_2$ . The overpotential decreased by about 1 volt, even at very low  $\text{IrO}_2$  loadings on diamond. The behaviour of the BDD- $\text{IrO}_2$  electrodes came close to that of  $\text{IrO}_2$  continuous films on Ti (DSA electrodes).

The activity of the electrodes was also tested in peroxodisulphate production and in the oxidation of organic substances. According to the phenomenological model proposed for the oxidation of organic compounds and simultaneous oxygen evolution (Fig. 6.25), BDD- $\text{IrO}_2$  electrodes can be classified as an ‘active’ anode material, while bare BDD electrodes behave as ‘non-active’ electrodes. The strong interaction between the electrode material and the hydroxyl radicals formed during water discharge leads to formation of a higher oxide,  $\text{IrO}_3$ . The organic oxidation process on BDD- $\text{IrO}_2$  electrodes is mediated by the surface redox system  $\text{IrO}_3/\text{IrO}_2$  (see Fig. 2.2 of Chapter 2). This surface redox system, however, is less active than the free hydroxyl radicals produced at diamond under the same conditions. This explains the lower current efficiency of the organic oxidation process relative to bare BDD electrodes and the total suppression of peroxodisulphate production. The catalytic activity of  $\text{IrO}_2$  completely masked that of diamond, as if reactions could only take place on  $\text{IrO}_2$  sites; this was actually demonstrated by impedance measurements.

A simple model could explain the behaviour of modified diamond electrodes. Surface-modified diamond electrodes can be visualised as a diamond matrix in which particles are deposited more or less homogeneously (Fig. 6.27). The reaction takes place on diamond as well as on the active sites offered by the deposited  $\text{IrO}_2$  particles. A distinct reaction rate constant can be associated with both processes, however, the reaction is faster on the deposited  $\text{IrO}_2$  nanoparticles than on diamond (Eq. 6.13).

$$k_{\text{IrO}_2}^0 \gg k_{\text{diamond}}^0 \quad 6.13$$



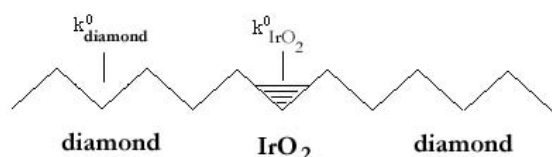


**FIGURE 6.27.** Diagram of the modified diamond electrode structure: deposited particles in a diamond matrix.  $k^0_{\text{IrO}_2} \gg k^0_{\text{diamond}}$ .

The electrocatalytic activity sustaining the electron-transfer reactions at the electrode/electrolyte interface is improved by the IrO<sub>2</sub> deposited. The diamond acts in these cases, merely as an inert substrate on which the deposited IrO<sub>2</sub> particles alone are electroactive. The effect is so strong that even with very small amounts deposited, the activity of BDD is completely masked, and the electrode's behaviour can be attributed solely to the properties of the deposited IrO<sub>2</sub>. The high degree of dispersion of the deposited IrO<sub>2</sub> particles, however, leads to a higher electrocatalytic activity than would be found on continuous-film deposits of the same material.

The stability of the IrO<sub>2</sub> particles on diamond under the conditions of oxygen evolution is quite low. A continuing loss of IrO<sub>2</sub> deposit was recorded in terms of a continuing increase in electrode potential. However, a complete elimination of IrO<sub>2</sub> was not seen after 72 hours. The formation of a C-Ir compound, or a reorganisation of the Ir crystal structure, may explain the high stability of very low amounts of IrO<sub>2</sub> on diamond.

---

## 5. Acknowledgment

I am thankful to the Interdepartmental Centre of Electronic Microscopy at EPFL (CIME), Lausanne, for the morphological characterisation of electrode surfaces. I would like to thank in particular Mrs D. Laube for TEM measurements, Mr B. Senior for SEM analyses, and Prof. P. Buffat for very useful discussions. I would like to thank Mr N. Xanthopoulos for XPS measurements and Prof. H. J. Mathieu (Laboratory of Metallurgical Chemistry, Material Department at EPFL, Lausanne) for discussions and precious advice. I would like to thank Dr S. Ferro for supplying precious details concerning the mathematical treatment of the results of impedance measurements. I am grateful to Mr D. Bachelin for performing part of the voltammetric experiments.

## 6. References

1. J. Wang, G. M. Swain, T. Tachibana, and K. Kobashi, *Electrochem. Solid-state Lett.*, **3** (2000) 286.
2. J.-S. Gao, T. Arunagiri, J.-J. Chen, P. Goodwill, and O. Chyan, *Chem. Mater.*, **12** (2000) 3495.
3. K. Honda, M. Yoshimura, T. N. Rao, D. A. Tryk, A. Fujishima, K. Yasui, Y. Sakamoto, K. Nishio, and H. Masuda, *J. Electroanal. Chem.*, **514** (2001) 35.
4. I. Duo, P.-A. Michaud, W. Haenni, A. Perret, and C. Comninellis, *Electrochem. Solid-state Lett.*, **3** (2000) 325.
5. K. McKenzie and F. Marken, *Electrochem. Solid-state Lett.*, **5** (2002) E47.
6. N. Vinokur, B. Miller, Y. Avyigal, and R. Kalish, *J. Electrochem. Soc.*, **146** (1999) 125.
7. I. Duo, S. Ferro, A. D. Battisti, and C. Comninellis, in *Catalysis at nanoparticles surfaces* (A. Wieckowski, E. R. Savinova, and C. G. Vayenas, eds.), Marcel Dekker Inc., New York, in press.
8. S. Trasatti, *Electrochim. Acta*, **36** (1991) 225.
9. S. Trasatti, in *Interfacial Electrochemistry* (A. Wieckowski, ed.), Marcel Dekker, Inc., New York, 1999, p. 769.
10. J. Rolewicz, C. Comninellis, E. Plattner, and J. Hinden, *Electrochim. Acta*, **33** (1988) 573.
11. S. Trasatti and G. Lodi, 'Electrodes of conductive metallic oxides', Elsevier Sci. Publ. Co, Amsterdam, 1980.
12. C. Comninellis and G. P. Vercesi, *J. Appl. Electrochem.*, **21** (1991) 136.
13. J.-M. Bonard and J.-D. Ganière, *Ultramicroscopy*, **62** (1995) 249.
14. C. Wagner, W. Riggs, L. Davis, and J. Moulder, 'Handbook of x-ray photoelectron spectroscopy', Perkin Elmer Corporation, Physical Electronics Division, Eden Prairie, Minnesota, 1979.
15. S. H. Glarum and J. H. Marshall, *J. Electrochem. Soc.*, **127** (1980) 1467.
16. L. A. d. Silva, V. A. Alves, M. A. P. d. Silva, S. Trasatti, and J. F. C. Boodts, *Electrochim. Acta*, **42** (1997) 271.
17. S. Ardizzone, G. Fregonara, and S. Trasatti, *Electrochimica Acta*, **35** (1990) 263.
18. A. D. Battisti, G. Lodi, L. Nanni, G. Battaglin, and A. Benetti, *Can. J. Chem.*, **75** (1997) 1759.
19. L. D. Burke and D. P. Whelan, *J. Electroanal. Chem.*, **162** (1984) 121.
20. L. D. Burke and D. P. Whelan, *J. Electroanal. Chem.*, **124** (1981) 333.
21. S. Ardizzone, A. Carugati, and S. Trasatti, *J. Electroanal. Chem.*, **126** (1981) 287.
22. L. Mészáros, B. Lengyel, T. Garai, and G. Trabanelli, *Acta Chim. Hung.*, **127** (1990) 113.

23. G. Fóti, D. Gandini, and C. Comninellis, *Current Topics in Electrochem.*, **5** (1997) 71.
24. A. J. Bard and L. R. Faulkner, 'Electrochemical methods - Fundamentals and applications', J. Wiley and Sons, Inc., New York, 2001.
25. G. Fóti, D. Gandini, Ch. Comninellis, A. Perret, and W. Haenni, *Electrochem. Solid-state Lett.*, **2** (1999) 228.
26. H. Wendt and G. Kreysa, in *Electrochemical Engineering*, Springer, Berlin, 1998, p. 314.
27. B. Elvers, S. Hawkins, and G. Schulz, 'Ullmann's Encyclopedia of Industrial Chemistry', Weinheim, 1991.
28. P.-A. Michaud, C. Comninellis, W. Haenni, A. Perret, and M. Fryda, in *International Patent*, 2001.
29. P.-A. Michaud, E. Mahé, W. Haenni, A. Perret, and C. Comninellis, *Electrochem. Solid-state Lett.*, **3** (2000)
30. P.-A. Michaud, 'Comportement anodique du diamant synthétique dopé au bore', Thesis No 2595, EPFL, Lausanne (2002)

The electrochemical properties of diamond electrodes vary considerably with the working conditions prevailing during deposition of the diamond film on the substrate and with subsequent treatment of the surface. From an electrochemical point of view, the preparation and treatment of the diamond films will affect the stability of the electrode's response, the values of the background currents, the width of the potential window between hydrogen and oxygen evolution, the reversibility of redox reactions at diamond, and the current efficiency during the oxidation of organic compounds. The current lack of a standard procedure for the preparation and treatment of diamond films is responsible for the wide range of variation of diamond quality and properties reported in the literature. The conflicting conclusions as to effects of surface treatments by etching, oxygen plasma, and electrochemical oxidation further contribute to the confusion and make it even more difficult to compare results from different laboratories. In this chapter the most important literature results concerning the electrochemical properties of diamond are presented, then the results obtained in our laboratory for the properties of diamond after treatment of the surface by anodic oxidation, deposition and subsequent elimination of graphite, and deposition of IrO<sub>2</sub> particles are summarised and compared with those of other research groups. A phenomenological model is proposed to explain the results observed.

Critical review of the results available from different laboratories, including our own, has shown that it is more specifically the presence of non-diamond carbon ( $sp^2$ ), the nature of particular surface terminations, and the size and faces of the crystals in the diamond film, which will influence the film quality of boron-doped diamond electrodes (BDD) and their electrochemical properties. A wide variety of parameters can be adjusted during preparation of the diamond films in order to obtain films with particular physical, chemical and electrochemical properties. The configuration of the reactor, the gas composition, growth rate and time, and the cool-down procedure are some of the conditions that can be varied to modify diamond quality. The diamond properties can also be modified after film growth, by oxidising the surface (electrochemical or plasma oxidation), by etching, and by deposition or incorporation of other materials on/into the diamond surface. This freedom in experimental design is, of course, a positive aspect in fundamental investigations of materials properties. However, as a corollary, it also leads to large differences in the results obtained and to considerable difficulties in interpretation of the phenomena investigated. It is the aim of the present work to clarify some aspects of the electrochemical activity of boron-doped diamond electrodes in the light of the results obtained in our and other laboratories.

---

## 1. Boron-doped diamond electrodes

### 1.1. Literature results

The boron level determines the electrical conductivity of the electrodes. At doping levels above  $10^{17}$ - $10^{18}$  boron atoms  $\text{cm}^{-3}$ , diamond is a *p*-type semiconductor material [1]. Above  $10^{21}$  boron atoms  $\text{cm}^{-3}$ , diamond electrodes have a metallic conductivity, their resistivity being around  $10 \text{ m}\Omega \text{ cm}$ . Most of the surface treatment processes that serve to modify the diamond's electrochemical activity do not involve the boron level in the lattice. The electrochemical behaviour of diamond appears to be due to interface phenomena, rather than to the bulk properties of the material, so long as the doping level is sufficiently high.

The boron-doped films are polycrystalline diamond, but in addition, the presence of non-diamond amorphous carbon ( $sp^2$ ) has been demonstrated [2, 3]. From a materials standpoint, such carbon constitutes an impurity detracting from the quality of the diamond synthesised. Using Raman spectrometry one can distinguish between high-quality and low-quality diamond. A high-quality film has a well developed  $1332 \text{ cm}^{-1}$  line and a negligible non-diamond carbon signal in the

1550-1600  $\text{cm}^{-1}$  range, whereas low-quality films have a significant peak in this range that is attributed to the non-diamond carbon [3-5]. One consequence of the presence of  $sp^2$  carbon is a higher surface activity of the material. Voltammetry of high-quality diamond shows a featureless, low-background response with no evidence of redox surface functionalities [6]. Low-quality diamond films yield a high voltammetric charge in the potential region of water stability. The overpotentials of oxygen and hydrogen evolution also are sensitive to the quality of the diamond film. Figures 7.1.A and B show cyclic voltammograms recorded at diamond electrodes with a high-quality (curve A) and a low-quality (curve B) film [1]. The width of the low-current potential window between hydrogen and oxygen evolution decreases with increasing incorporation of non-diamond carbon into the diamond film [1].

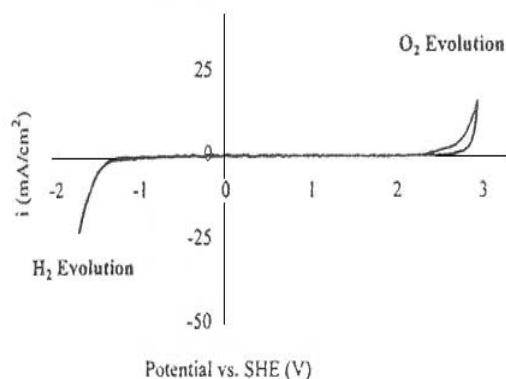


**FIGURE 7.1.A** Cyclic voltammogram recorded at a boron-doped diamond electrode with a high-quality film in 0.5 M  $\text{H}_2\text{SO}_4$  [1].

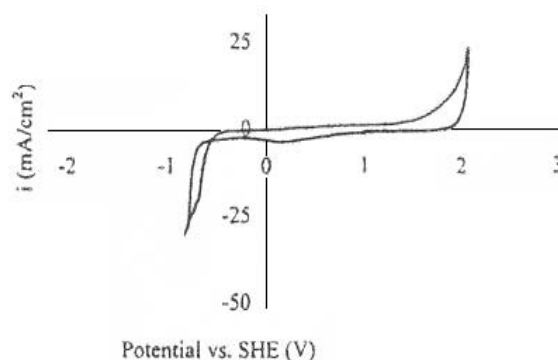


**FIGURE 7.1.B** Cyclic voltammogram recorded at a boron-doped diamond electrode with a low-quality film in 0.5 M  $\text{H}_2\text{SO}_4$  [1].

The progressive elimination of  $sp^2$  species from the diamond surface which occurs during oxygen evolution leads to a deactivation of the electrode attended by a progressive increase in the overpotentials of oxygen and hydrogen evolution. This oxidising treatment of the surface leads to a more reproducible behaviour of the diamond material while the electrochemical properties of the electrodes are thoroughly changed. The most widely accepted theories attribute these changes in surface properties to two factors. One is the introduction of oxygen functions on the diamond surface [7, 8]. XPS signals due to C-O bonds were recorded, and a direct oxidation of diamond sites was proposed. Other authors have affirmed that by oxidising treatment of the diamond surface,  $sp^2$  carbon is oxidised to  $\text{CO}_2$  and thus eliminated from the surface [1, 2]. Probably, both of these mechanisms are

involved during anodic polarisation of the diamond surface. The influence that each of them will have on the electrochemical properties of diamond will largely depend on the nature of the redox couple investigated. After anodic treatment of the surface, for instance, diamond exhibits a selectivity towards the oxidation of dopamine that is higher than that towards the oxidation of ascorbic acid [9]. After oxidation of the diamond surface, the reversibility of positively charged redox couples such as the cations FeIII/FeII at the electrode decreases. Negatively charged redox systems such as Fe(CN)<sub>6</sub>III/II and IrCl<sub>6</sub>III/II exhibit a more distinct, opposite effect [8, 10]. These authors suggested that the negative surface charge density due to the oxygen terminations affects the potential at the reaction plane so as to accelerate reactions involving positively charged species, and to decelerate those involving negatively charged species. A similar behaviour was noticed by Alehashem *et al* in the case of Fe(CN)<sub>6</sub>III/II at diamond before and after etching [6]. However, they attributed the increased reversibility of the system to a disordering effect of the etching treatment on the microstructure of the *sp*<sup>2</sup> species present on diamond. The increase in *sp*<sup>2</sup> disorder corresponded to an increased activity of BDD towards redox reactions in solution.

As already said, a comparison of results between different laboratories is quite difficult owing to the wide divergence in quality of the diamond films. The table below (Table 7.1) summarises the values of the reaction rate constants for the redox couples ferri/ferrocyanide (Fe(CN)<sub>6</sub>III/II) and benzoquinone/hydroquinone (Q/H<sub>2</sub>Q) at diamond electrodes. The values calculated are spread out over the relatively wide range of three orders of magnitude, from 10<sup>-5</sup> to 10<sup>-2</sup> cm s<sup>-1</sup>.

**TABLE 7.1.** Reaction rate constants,  $k^0$ , found in the literature for the redox reactions ferri/ferrocyanide, Fe(CN)<sub>6</sub>III/II, and benzoquinone/hydroquinone, Q/H<sub>2</sub>Q, at boron-doped diamond.

Fe(CN) <sub>6</sub> III/II $k^0$ [cm s <sup>-1</sup> ]	Q/H <sub>2</sub> Q $k^0$ [cm s <sup>-1</sup> ]	Ref.
10 <sup>-5</sup> -1.4x10 <sup>-4</sup>	-	[11]
10 <sup>-5</sup> -10 <sup>-4</sup>	-	[12]
1.4x10 <sup>-4</sup>	3.5x10 <sup>-7</sup>	[13]
10 <sup>-4</sup> -10 <sup>-3</sup>	10 <sup>-6</sup> -10 <sup>-5</sup>	[14]
0.02-0.05	-	[2, 15]

Where the transfer coefficients,  $\alpha_{\text{red}}$  and  $\beta_{\text{ox}}$ , of the reactions have been calculated, values lower than 0.5 and a sum of  $\alpha + \beta$  lower than unity were found [13].

## 1.2. Results obtained in this work

In the present work, boron-doped diamond electrodes have been subjected to different surface modifications, and the electrochemical properties of the electrodes have been investigated and compared with those reported in the literature.

### *BDD surface treatment*

As-grown polycrystalline boron-doped diamond ( $\text{BDD}_{\text{ag}}$ ) electrodes had a rather high film quality. Cyclic voltammetry revealed a rather high surface activity of the  $\text{BDD}_{\text{ag}}$ . The potential-dependent voltammetric charge recorded in inert solutions was typical of electrode surfaces on which surface redox couples were active. The capacitance values calculated were higher than the usual capacitance of a double layer ( $10 \mu\text{F cm}^{-2}$ ). A contribution of a pseudocapacitance due to these surface redox couples could explain the order of magnitude of the experimental values of capacitance and their dependence on the applied potential.

As-grown boron-doped diamond ( $\text{BDD}_{\text{ag}}$ ) electrodes were also tested in the presence of outer-sphere (ferri/ferrocyanide,  $\text{Fe}(\text{CN})_6^{\text{III/II}}$ ) and inner-sphere (benzoquinone/hydroquinone,  $\text{Q}/\text{H}_2\text{Q}$ ) electron-transfer reactions. The  $\text{BDD}_{\text{ag}}$  electrode exhibited a rather low electroactivity towards both redox reactions. The sum of the transfer coefficients ( $\alpha_{\text{red}} + \beta_{\text{ox}}$ ) was lower than unity, indicating that the diamond's behaviour differed from that of a metallic electrode material. The reaction rate constants for both the outer and the inner-sphere reaction were several orders of magnitude lower than the values typically calculated at metal electrodes. A slow kinetics of the charge-transfer process was noticed.

As-grown  $\text{BDD}_{\text{ag}}$  electrodes were polarised anodically under different conditions, and the properties of electrodes were also examined after these treatments. Mildly polarised diamond electrodes ( $\text{BDD}_{\text{mild}}$ ) did not reveal any changes in crystal structure or morphology relative to as-grown electrodes ( $\text{BDD}_{\text{ag}}$ ). The level of surface oxygen (determined by XPS measurements) increased, however, the surface activity of these electrodes was lower than that of as-grown diamond. The voltammetric charge and the capacitance were one order of magnitude lower. Part of the redox functions present on the surface were eliminated by the anodic polarisation. Similar deactivation effects were recorded towards the outer-sphere



and inner-sphere redox reaction,  $\text{Fe}(\text{CN})_6\text{III/II}$  and  $\text{Q}/\text{H}_2\text{Q}$ , respectively. The redox couples were less reversible on diamond after anodic treatment of the surface. The transfer coefficients,  $\alpha_{\text{red}}$  and  $\beta_{\text{ox}}$ , were lower than 0.5, while the rate constants were just slightly lower than at as-grown electrodes.

The deactivation effect was much more evident after strong anodic treatment of the surface ( $\text{BDD}_{\text{severe}}$  and  $\text{BDD}_{\text{AcOH}}$ ). Morphological investigations by SEM indicated important changes in the crystal size and shape. The surface activity was strongly reduced. Featureless voltammograms typical of the absence of all surface redox transitions were recorded in both cases. The small values of voltammetric charge and of capacitance were typical of a double layer. No contribution of a pseudocapacitance was noticed. The reversibility of the outer-sphere and inner-sphere redox system,  $\text{Fe}(\text{CN})_6\text{III/II}$  and  $\text{Q}/\text{H}_2\text{Q}$ , respectively, decreased further.

Anodic oxidation of diamond electrodes was a way of creating aliphatic diamond-oxygen bonds on the polycrystalline diamond surface, as confirmed by the increase in the O/C ratio. For some authors [7, 10, 16], these C-O functions would create a dipole distribution on the surface that is able to hinder redox reactions of negative charged molecules such as those of the ferri/ferrocyanide and benzoquinone/hydroquinone couples investigated. This effect alone, however, could not explain the decrease in activity of the electrode surface after anodic treatment. The elimination of  $sp^2$  carbon by anodic oxidation was the most probable cause of surface deactivation.

#### *Graphite deposition on BDD electrodes*

Graphite particles were deposited on the diamond surface by wiping the diamond surface over a graphite foil, which had the effect of restoring the initial properties of as-grown boron-doped diamond ( $\text{BDD}_{\text{ag}}$ ) electrodes. The influence of the graphite loading on the diamond properties was also investigated. Deposition of graphite increased the surface activity, as shown by the voltammetric charge and capacitance values. The  $sp^2$  coverage on diamond was calculated for different deposition steps. An  $sp^2$  coverage of 3.6% was found for an as-grown diamond ( $\text{BDD}_{\text{ag}}$ ) electrode, while the coverage was only 1.3% for a mildly polarised electrode ( $\text{BDD}_{\text{mild}}$ ). The reversibility of outer-sphere and inner-sphere redox couples ( $\text{Fe}(\text{CN})_6\text{III/II}$  and  $\text{Q}/\text{H}_2\text{Q}$ , respectively) increased with the graphite loading. It can be said that the electrode's behaviour approached that of a metal electrode.

The oxygen evolution reaction was also investigated on diamond and diamond-graphite composite electrodes. It was noticed that the onset overpotential

decreased by almost 1 V, however, the stability of the graphite coverage was extremely low under the conditions of oxygen evolution, and with every new cycle the graphite loading decreased until the  $sp^2$  deposit had completely vanished. This was evidence for the instability of graphite particles under the conditions of oxygen evolution, and thus for the possibility of eliminating them as  $CO_2$  by simple anodic oxidation of the diamond surface.

*Electrochemical oxidation of EDTA on BDD electrodes*

Anodically treated diamond, in fact, behaved like an ‘non-active’ material. The surface did not exhibit any surface redox transitions, and a very stable response of the electrodes was recorded under all working conditions. The high overpotential for water discharge on diamond leads to the formation of free hydroxyl radicals at the diamond surface. It is the high reactivity of such mediators which explains the high current efficiencies obtained in the electrochemical oxidation of organic compounds at diamond in the potential region of water decomposition. In Chapter 5, an example of applications of boron-doped diamond electrodes was described in which the electrochemical oxidation of ethylenediaminetetraacetic acid (EDTA) was investigated. The potentials applied during the experiments were such as to assure elimination of the  $sp^2$  species from the surface and to obtain a completely ‘non-active’ diamond electrode. The possible effects of graphite present on a diamond surface could not be investigated under these harsh working conditions. However, the general conclusion can be drawn that  $sp^2$  species present on diamond act as charge-transfer promoters on the polycrystalline surface. Their elimination then leads to the drop in electrode activity and to the kinetic slow-down of charge-transfer processes at the diamond electrode.

In order to interpret these observations, a comprehensive model has been proposed [17-20]. Figure 7.2 illustrates the reaction scheme in acidic media, where M designates an active site at the anode surface. The first step in all cases is the discharge of water molecules to hydroxyl radicals (reaction a). The electrochemical and chemical activity of hydroxyl radicals strongly depends on the nature of the electrode material used.

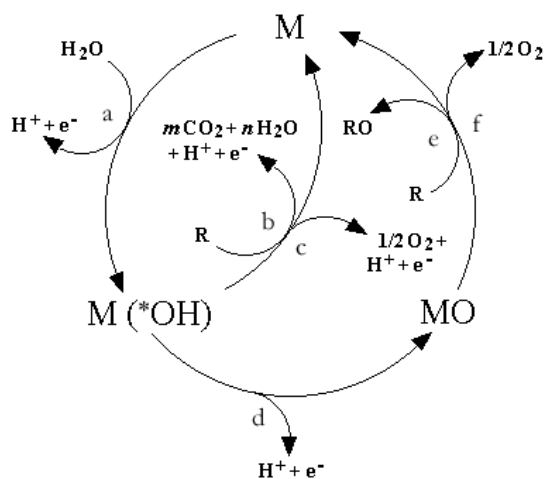
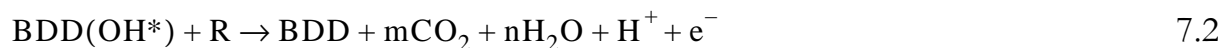


**FIGURE 7.2.** Mechanistic scheme of anodic oxidation of organic compounds with simultaneous oxygen evolution on *non-active* anodes (reactions a, b and e) and on *active* anodes (reactions a, c, d and f). (a) water discharge to hydroxyl radicals,  $OH^*$ ; (b) combustion of the organic compound,  $R$ , *via* hydroxyl radicals; (c) oxygen evolution by electrochemical oxidation of hydroxyl radicals; (d) formation of the higher metal oxide,  $MO$ ; (e) partial (selective) oxidation of the organic compound; (f) oxygen evolution by chemical decomposition of the higher metal oxide.

Diamond electrodes have been defined as ‘non-active’ electrodes. In fact, they do not provide any catalytically active site for the adsorption of reactants and/or products in aqueous media. Intermediates such as hydroxyl radicals produced by water decomposition at ‘non-active’ anodes (reaction a in Fig. 7.2) are considered to be involved in the oxidation of organics in aqueous media. The first reaction is the electrochemical discharge of water leading to hydroxyl radical formation (reaction a, Fig. 7.2):



These hydroxyl radicals are then consumed by two competing reactions: combustion of organics (reaction b in Fig. 7.2 with  $M = BDD$ ):



and oxygen evolution (reaction c in Fig. 7.2 with  $M = BDD$ ):

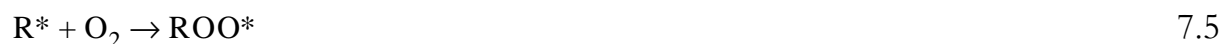


Dioxygen very probably also participates in the combustion of organics according to the following reaction scheme:

1) Formation of organic radicals, R\*, by a hydrogen abstraction mechanism:



2) Reaction of the organic radical with dioxygen:



3) Further abstraction of a hydrogen atom with the formation of an organic hydroperoxide (ROOH):



Since the organic hydroperoxides are relatively unstable, decomposition of such intermediates often leads to molecular breakdown and formation of subsequent intermediates with lower carbon numbers. These scission reactions continue rapidly until the organic substance has been completely transformed to CO<sub>2</sub> and H<sub>2</sub>O.

#### *Iridium-modified BDD electrodes*

For a better understanding of the phenomenon of charge-transfer promotion, the BDD surface was modified by the deposition of IrO<sub>2</sub> nanoparticles. Cyclic voltammetry indicated an increased surface activity due to the surface redox couples Ir(III)/(II) and Ir(VI)/(IV) which are active at different values of potential. Different IrO<sub>2</sub> loadings  $\Gamma$  were investigated ( $\Gamma = 1$  corresponds to 10<sup>15</sup> molecules IrO<sub>2</sub> cm<sup>-2</sup>), and the electrode's capacitance was found to increase with increasing loading. The reversibility of the redox couples ferri/ferrocyanide (Fe(CN)<sub>6</sub>III/II) and benzoquinone/hydroquinone (Q/H<sub>2</sub>Q) investigated also increased with increasing IrO<sub>2</sub> loading on the diamond, just as already found in the case of graphite deposition on diamond. The presence of IrO<sub>2</sub> also affected the overpotential of the oxygen evolution reaction (there was a 1-V decrease of the onset potential value).

Particular attention was paid to the oxidation of organic compounds on BDD and BDD-IrO<sub>2</sub> electrodes under the conditions of water discharge. The model proposed by Fóti *et al* [21] distinguishes between the behaviour of BDD and of BDD-IrO<sub>2</sub> electrodes towards oxidation of organic compounds in the potential region of water decomposition. According to this model, diamond is an '*non-active*' material which does not participate directly in the oxidation process. Hydroxyl radicals formed during water discharge are the active mediators involved in the oxidation of organic compounds on diamond electrodes. The high overpotential for

the water discharge process is due to weak bonding existing between diamond and the radical species formed during water decomposition. However, these weak interactions with the diamond surface are responsible for the high activity of the hydroxyl radicals, which leads to complete electrochemical combustion of the organic substances. A very high current efficiency was obtained in this process.

The deposition of  $\text{IrO}_2$  completely masks the diamond's activity, and the properties of the  $\text{IrO}_2$ /electrolyte interface now determine the behaviour of the resulting composite BDD- $\text{IrO}_2$  electrodes.  $\text{IrO}_2$  has been defined as an 'active' electrode material which itself takes part in the oxidation process of organic substances [21]. The  $\text{IrO}_3/\text{IrO}_2$  surface redox couples are the "oxidising intermediates" involved in the oxidation process. The hydroxyl radicals formed during water discharge strongly interact with the  $\text{IrO}_2$  surface and form the higher oxide  $\text{IrO}_3$ . This causes a decrease in the overpotential for water discharge to the values typical for iridium dioxide electrodes. However, the fact that the oxidation reaction is now mediated by a surface redox couple is responsible for the lower current efficiencies obtained in the oxidation of organic compounds. This behaviour can also be attributed to the BDD- $\text{IrO}_2$  electrodes when considering a BDD surface as an inert substrate.

The calculated rate constant values of the investigated reactions (ferri/ferrocyanide,  $\text{Fe}(\text{CN})_6\text{III/II}$  and benzoquinone/hydroquinone,  $\text{Q}/\text{H}_2\text{Q}$ ) are shown in the Table 7.2.

**TABLE 7.2.** Reaction rate constants,  $k^0$ , obtained experimentally for the redox reactions ferri/ferrocyanide,  $\text{Fe}(\text{CN})_6\text{III/II}$ , and benzoquinone/hydroquinone,  $\text{Q}/\text{H}_2\text{Q}$ , at BDD and modified BDD electrodes.

electrodes	$\text{Fe}(\text{CN})_6\text{III/II}$ $k^0$ [ $\text{cm s}^{-1}$ ]	$\text{Q}/\text{H}_2\text{Q}$ $k^0$ [ $\text{cm s}^{-1}$ ]
<b>BDD<sub>ag</sub></b>	$5 \times 10^{-4}$	$7 \times 10^{-5}$
<b>BDD<sub>mild</sub></b>	$8 \times 10^{-5}$	$2 \times 10^{-5}$
<b>BDD<sub>severe</sub></b>	$9 \times 10^{-5}$	$6 \times 10^{-5}$
<b>BDD<sub>AcOH</sub></b>	$3 \times 10^{-5}$	$1 \times 10^{-6}$
<b>BDD-g<sub>l</sub></b>	$8 \times 10^{-5}$	$8 \times 10^{-5}$
<b>BDD-g<sub>h</sub></b>	$1 \times 10^{-4}$	$2 \times 10^{-4}$
<b>BDD-<math>\text{IrO}_2</math> <math>\Gamma = 0.6</math></b>	$2 \times 10^{-3}$	$6 \times 10^{-6}$
<b>BDD-<math>\text{IrO}_2</math> <math>\Gamma = 6.4</math></b>	$3 \times 10^{-3}$	$3 \times 10^{-5}$

A phenomenological model has been proposed in the present work in order to explain the changes in the properties of diamond occurring after surface treatments, and the analogies existing between graphite-modified and IrO<sub>2</sub>-modified BDD electrodes. The experimental results found in the literature and those obtained in this work have been considered.

---

## 2. The phenomenological model

For *p*-type diamond, the flat-band potential,  $E_{fb}$ , is close to the valence-band potential,  $E_v = -5.6$  eV, as shown in Figure 7.3 [1]. A band-gap potential,  $E_g$ , of 5.5 eV places the conduction-band potential,  $E_c$ , at -0.1 eV. According to semiconductor theory, in this band gap between -5.6 eV and -0.1 eV (which corresponds to the range of electrode potentials between -4.6 and 1 V *vs* SHE), all reduction processes should be hindered. However, many redox systems are electrochemically active in this potential region. In Fig. 7.3, the redox couples investigated in this work are placed according to their apparent equilibrium potentials.

A particular charge carrier distribution was assumed to compensate for the expected lack of electroactivity in the band-gap region (Fig. 7.3) in order to explain the electrochemical activity of diamond. Because of the high doping level of about  $10^{20}$  to  $10^{21}$  boron atoms cm<sup>-3</sup> (the semiconductor-metal transition occurs at  $2 \times 10^{20}$  atoms cm<sup>-3</sup>), the diamond electrodes investigated could be considered as degenerate *p*-type semiconductors. The presence of  $sp^2$  species can also contribute to the promotion of charge transfer. The high overpotentials at which the reactions occur, and the  $\alpha_{red}$  and  $\beta_{ox}$  values which are smaller than 0.5, can be explained by an insufficient density of these charge carriers on the diamond surface. The behaviour of the diamond electrodes approaches that of metal materials, only when the diamond surfaces are modified by the deposition of materials such as graphite or IrO<sub>2</sub>. Contrary to the simple picture of semiconductor materials, the electroactivity of diamond is tied to the charge carrier concentration at the surface and not only to that in the bulk of the film (doping level). Since the boron level in the bulk of the material is not altered by the deposition of conductive particles (*i.e.*, IrO<sub>2</sub> or graphite) on the diamond surface, only changes in the electronic configuration at the electrode/electrolyte interface can justify the recorded changes in electrode behaviour. In Figure 7.3, the boron doping band is shown close to the valence band that is responsible for the electrical conductivity in the bulk of the film. Charge carrier bands are distinguished as being due to surface states created on the diamond

surface. These charge carriers can influence the charge-transfer process at the electrode/electrolyte interface.

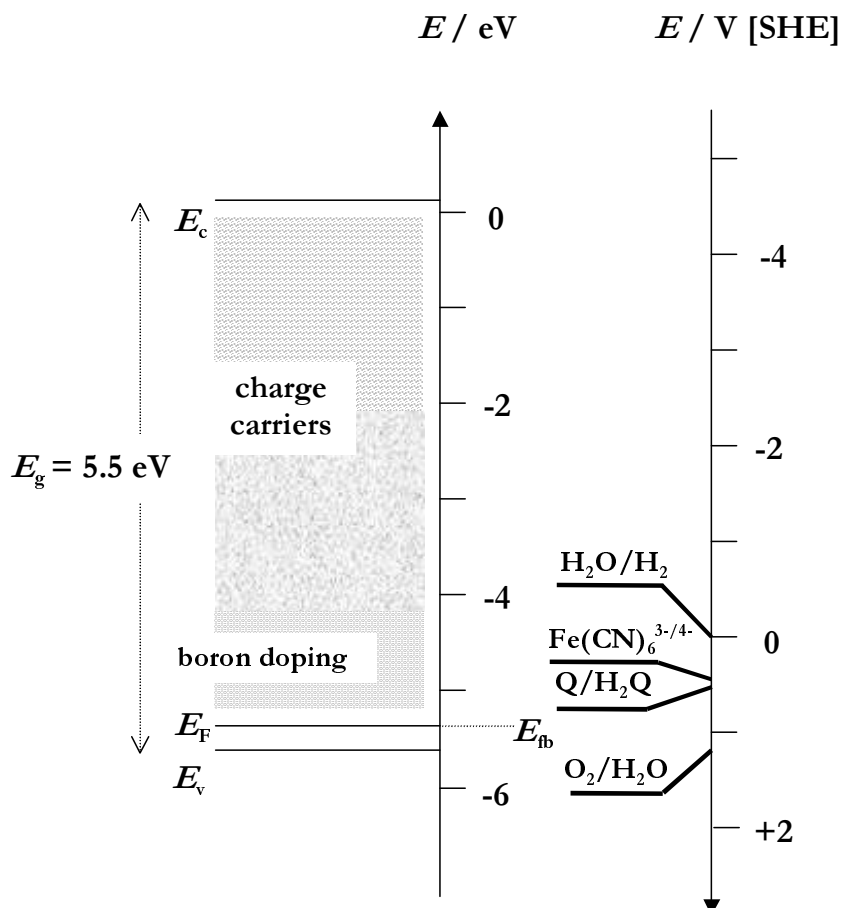


**FIGURE 7.3.** Energy diagram of the boron-doped diamond/aqueous electrolyte interface with the flat-band energy,  $E_{fb}$ , in the presence of different redox couples.  $E_F$  = Fermi-level energy,  $E_v$  = valence-band energy,  $E_c$  = conduction-band energy,  $E_g$  = band-gap energy. pH = 0.

The phenomenological model in Fig. 7.4 provide a better explanation for the charge-transfer phenomena occurring at the electrode/electrolyte interface when an overpotential ( $\eta_{app}$ ) is created at the boron-doped diamond (BDD) in an electrolyte with a dissolved redox couple. Because the diamond film can be considered as a degenerate  $p$ -type semiconductor material (boron levels of  $10^{20}$ - $10^{21}$  boron atoms  $\text{cm}^{-3}$ ), the interface with the electrolyte is a contact of the type: degenerate  $p$ -type semiconductor/electrolyte (Case 1 in Fig. 7.4). Usually, in semiconductor electrodes a potential drop occurs across the space-charge layer below the semiconductor

surface due to the low carrier density [22]. Because of the rather low carrier density in the film and because of the presence of the Helmholtz layer in the electrolyte close to the diamond surface, such a potential drop ( $\eta_{\text{BDD}}$  in Fig. 7.4.1) can be supposed to exist across the space-charge layer of diamond. The linear potential drop,  $\eta$ , occurs across the Helmholtz layer. It is on account of this potential drop,  $\eta_{\text{BDD}}$ , across the diamond film, which constitutes an overpotential loss when looking from the viewpoint of driving force for the reaction at the electrode/solution interface, that the high overpotentials,  $\eta_{\text{app}}$ , usually involved in a redox reaction on diamond can be explained ( $\eta_{\text{app}} = \eta + \eta_{\text{BDD}}$ ).

Case 2 in Figure 7.4 describes the behaviour of a metal/electrolyte interface (*i.e.*, IrO<sub>2</sub> electrode in solution). In metals, the electron density is very high, so that at a metal/electrolyte interface only the potential drop across the Helmholtz layer,  $\eta$ , exists, as shown in Fig 7.4.2. In this case the overpotential applied is fully available for driving charge transfer in the reaction ( $\eta_{\text{app}} = \eta$ ) [23].

For composite materials such as BDD-graphite or BDD-IrO<sub>2</sub>, Case 3 should be considered in which two interfaces are present. The first contact (contact A of Case 3 in Fig. 7.4) is typical of a degenerate *p*-type semiconductor/metal interface. A charge distribution layer in the metal is absent, and because of the degenerate-semiconductor character of diamond, a charge depletion in the semiconductor as in Case 1 of Figure 7.4 is not possible. An ohmic junction can be assumed to be present where any potential loss in the junction point is avoided. The second interface is of the type of metal/electrolyte (Case 2 or contact B of Case 3 in Fig. 7.4). In this case, too, all of the applied potential is used to drive the charge-transfer process ( $\eta_{\text{app}} = \eta$ ). This second (metal/electrolyte) interface wholly determines the electrochemical properties of materials such as BDD-IrO<sub>2</sub> and composite BDD-graphite electrodes. The diamond surface in contact with the solution (Case 3 in Fig. 7.4) does not contribute to the charge-transfer reaction, which is because of the high overpotential that should be applied in order to compensate the potential loss in the BDD ( $\eta_{\text{app}} = \eta + \eta_{\text{BDD}}$ ). According to the model, the deposit particles (graphite or IrO<sub>2</sub>) behave as charge-transfer promoters on the BDD surface. The relation already used in previous chapters (Chapters 4 and 6) can be applied in a more general way:  $k_{\text{deposit}}^0 \gg k_{\text{diamond}}^0$ , where the deposited particles in this case are IrO<sub>2</sub> or graphite particles.



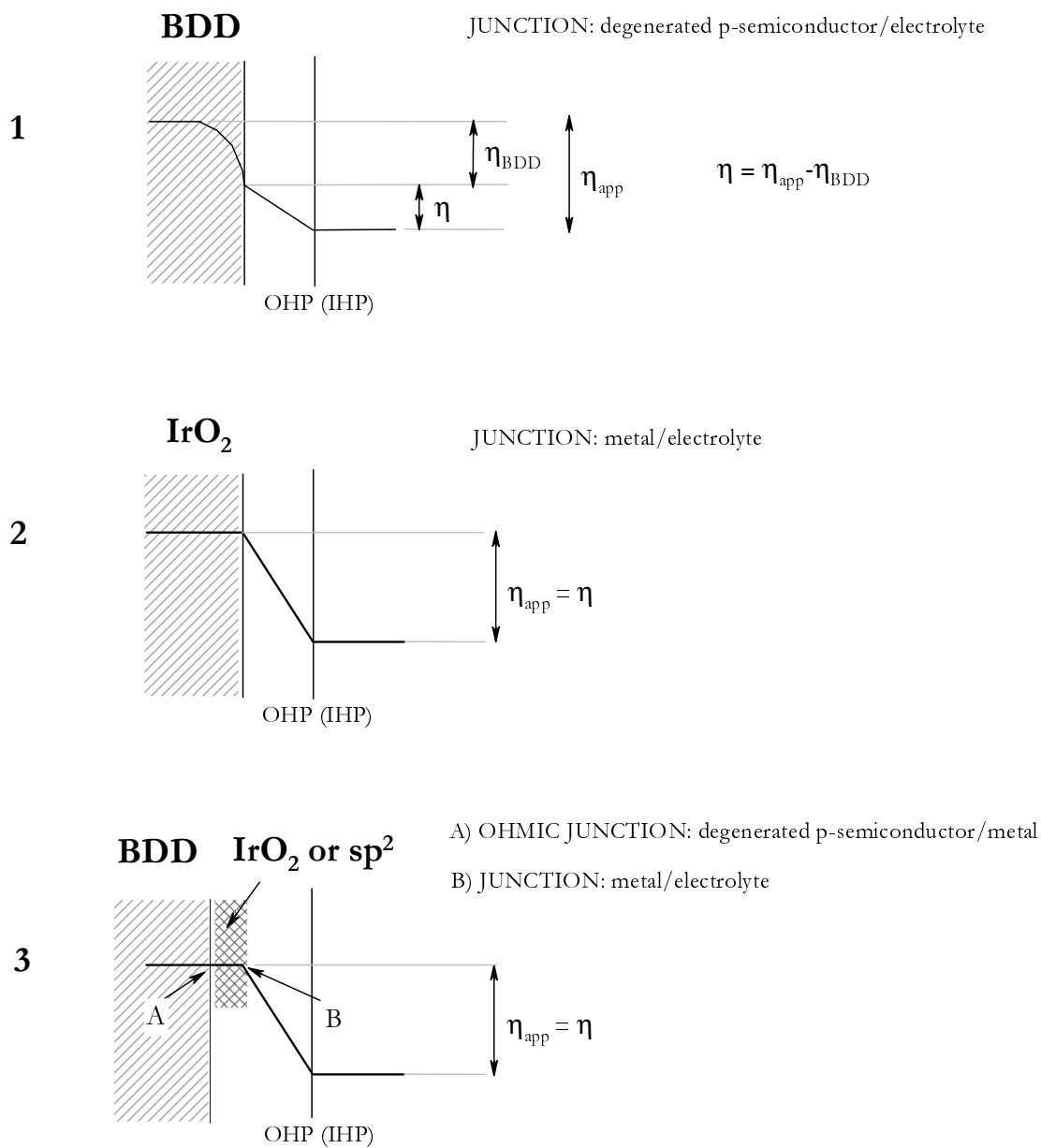


**FIGURE 7.4.** Profiles of potential at the electrode/electrolyte interface for three different cases: 1) Junction degenerate *p*-type semiconductor/electrolyte (BDD/electrolyte); 2) junction metal/electrolyte (IrO<sub>2</sub>/electrolyte); 3) double junction: A) ohmic junction degenerate *p*-type semiconductor/metal (BDD/IrO<sub>2</sub> or BDD/*sp*<sup>2</sup>) and B) junction metal/electrolyte (IrO<sub>2</sub>/electrolyte or *sp*<sup>2</sup>/electrolyte).  $\eta_{app}$  = applied overpotential,  $\eta_{BDD}$  = overpotential loss in the degenerate *p*-type semiconductor (BDD),  $\eta$  = overpotential for electron transfer. The dotted line corresponds to the Outer Helmholtz Plane (OHP) or to the Inner Helmholtz Plane (IHP), depending on the reaction investigated (outer-sphere or inner-sphere reaction).

The redox reaction investigated can occur on both the diamond and the deposited particles, however, because of the very slow kinetics of the reaction on diamond, the electrode's behaviour is typical of the deposited particles. The experimental results obtained can be explained in terms of the model just described. Electrochemical reactions have very slow kinetics on boron-doped diamond electrodes, but redox processes can occur on diamond in spite of its supposed semiconductor character. Because of the rather high charge density on its surface due to boron doping ( $> 10^{21}$  boron atoms  $\text{cm}^{-3}$ ), to the non-diamond ( $sp^2$ ) carbon, and more generally to surface species, boron-doped diamond can be defined as a degenerate semiconductor material. This distribution of charges on the surface promotes processes of electron transfer across the diamond/electrolyte interface. By deposition of particles on the diamond surface (graphite or  $\text{IrO}_2$ ), this surface charge density increases further until a perfectly metallic behaviour is reached. Since the charge transfer processes occur on the deposited particles with a lower overpotential than on diamond sites, surface-modified diamond electrodes exhibit the electrochemical properties of the deposited material. The possibilities which thus exist, for influencing the electrochemical properties of diamond by increasing or decreasing the charge density on its surface, make diamond a very versatile material.

Because of the inertness of diamond and its high chemical and electrochemical stability, it is possible in particular to investigate without any interference the electrochemical properties of many materials deposited on its surface. This possibility offers new prospects for the electrochemistry of dispersed nanoparticle materials which take advantage of their enhanced electrocatalytic activity. The specific case of  $\text{IrO}_2$  on diamond which was studied in the present work shows how the improved electrocatalytic properties of the highly dispersed  $\text{IrO}_2$  particles on diamond can be used for electroanalytical purposes, even when the  $\text{IrO}_2$  loadings are very small. Because of the considerable decrease of the overpotential for oxygen evolution found after  $\text{IrO}_2$  deposition, one can obtain a low-overpotential electrode for oxygen evolution and for the partial oxidation of organic compounds in electrosynthetic processes.

### 3. References

1. G. M. Swain, A. B. Anderson, and J. C. Angus, *MRS Bull.*, **23** (1998) 56.
2. M. C. Granger, M. Witek, J. Xu, J. Wang, M. Hupert, A. Hanks, M. D. Koppang, J. E. Butler, G. Lucazeau, M. Mermoux, J. W. Strojek, and G. M. Swain, *Anal. Chem.*, **72** (2000) 3793.
3. H. B. Martin, A. Argoitia, J. C. Angus, and U. Landau, *J. Electrochem. Soc.*, **146** (1999) 2959.
4. I. P. Hayward, K. J. Baldwin, D. M. Hunter, D. N. Batchelder, and G. D. Pitt, *Diamond Relat. Mater.*, **4** (1995) 617.
5. J. Rosa, J. Pangrác, M. Vanecek, V. Vorlicek, M. Nesladek, K. Meykens, C. Quaeys, and L. M. Stals, *Diamond Relat. Mater.*, **7** (1998) 1048.
6. S. Alehashem, F. Chambers, J. W. Strojek, G. M. Swain, and R. Ramesham, *Anal. Chem.*, **67** (1995) 2812.
7. D. A. Tryk, K. Tsunozaki, T. N. Rao, and A. Fujishima, *Diamond Relat. Mater.*, **10** (2001) 1804.
8. I. Yagi, H. Notsu, T. Kondo, D. A. Tryk, and A. Fujishima, *J. Electroanal. Chem.*, **473** (1999) 173.
9. E. Popa, H. Notsu, T. Miwa, D. A. Tryk, and A. Fujishima, *Electrochem. Solid-state Lett.*, **2** (1999) 45.
10. H. Notsu, I. Yagi, T. Tatsuma, D. A. Tryk, and A. Fujishima, *J. Electroanal. Chem.*, **492** (2000) 31.
11. R. Ramesham, *Sensor and Actuators B*, **50** (1998) 131.
12. Y. V. Pleskov, Y. E. Evstefeeva, M. D. Krotova, V. V. Elkin, V. M. Mazin, V. Y. Mishuk, V. P. Varnin, and I. G. Teremetskaya, *J. Electroanal. Chem.*, **455** (1998) 139.
13. A. D. Modestov, Y. E. Evstefeeva, Y. V. Pleskov, V. M. Mazin, V. P. Varnin, and I. G. Teremetskaya, *J. Electroanal. Chem.*, **431** (1997) 211.
14. N. G. Ferreira, L. L. G. Silva, E. J. Corat, and V. J. Trava-Airoldi, *Diamond Relat. Mater.*, **11** (2002) 1523.
15. J. Xu and G. M. Swain, *Anal. Chem.*, **70** (1998) 1502.
16. H. Notsu, I. Yagi, T. Tatsuma, D. A. Tryk, and A. Fujishima, *Electrochem. Solid-state Lett.*, **2** (1999) 522.
17. C. Comninellis and A. D. Battisti, *J. Chim. Phys.*, **93** (1996) 673.
18. C. Comninellis, *Electrochim. Acta*, **39** (1994) 1857.
19. O. Simond, V. Shaller, and C. Comninellis, *Electrochim. Acta*, **42** (1997) 2009.
20. G. Fóti, D. Gandini, Ch. Comninellis, A. Perret, and W. Haenni, *Electrochem. Solid-state Lett.*, **2** (1999) 228.

21. G. Fóti and C. Comninellis, in *Modern Aspects of Electrochemistry*, Vol. 37 (B. E. Conway, R. E. White, and C. G. Vayenas, eds.), Plenum Press, New York, in press.
22. R. Memming, in *Comprehensive Treatise of Electrochemistry*, Vol. 7 (B. E. Conway, J. O. M. Bockris, E. Yeager, S. U. M. Khan, and R. E. White, eds.), Plenum Press, New York, 1983, p. 529.
23. P. Allongue, in *Modern Aspects of Electrochemistry*, Vol. 23 (B. E. Conway, J. O. M. Bockris, E. Yeager, S. U. M. Khan, and R. E. White, eds.), Plenum Press, New York, 1992, p. 239.

---

---

## Curriculum Vitae

### Ilaria Duo

2, Eugène Grasset  
CH-1006 Lausanne

Italian  
5 June 1972  
Single

### Education

---

- 1999 to date     **Chemistry Department of the EPF in Lausanne, Switzerland**  
Ph.D. on the electrochemical characterization of diamond surfaces
- 11/1997         **Chemistry Department of the University of Ferrara, Italy**  
Diploma cum laude in Chemistry (equivalent to Masters)

### Professional Experience

---

- 2002            **University of Tokyo, Japan**  
Internship of 3 months on industrial applications of diamond electrodes  
Set-up of a system for electrochemical treatment of industrial wastewater
- 1998-1999     **Montell polyolefins SpA (now Basell) in Ferrara, Italy**  
Position in the quality control laboratory  
Physical and chemical tests for quality control of polymers in accordance to ISO 9000
-

---

## Publications

1. G. Fóti, P.-A. Michaud, **I. Duo**, B. Marselli, M. Panizza, and Ch. Comninellis, "Modern aspects of electrochemistry", Editors: B.E. Conway, R.E. White, and C.G. Vayenas, Plenum Press, New York (submitted)
2. F. Montilla, E. Morallón, **I Duo**, Ch. Comninellis, and J.L.Vázquez, *Electrochim. Acta* (submitted)
3. L. Ouattara, T. Diaco, **I. Duo**, M. Panizza, G. Fóti, and Ch. Comninellis, *J. Electrochem. Soc.*, **150**(2) (in press)
4. **I. Duo**, S. Ferro, A. De Battisti, and Ch. Comninellis, "Catalysis at nanoparticles surfaces", Editors: A. Wieckowski, E.R. Savinova, and C.G. Vayenas. Marcell Dekker Inc., New York (in press)
5. M.A. Rodrigo, P.-A. Michaud, **I. Duo**, M. Panizza, G. Cerisola, and Ch. Comninellis, *J. Electrochem. Soc.*, **148**(5) (2001) D60
6. M. Panizza, **I. Duo**, P.-A. Michaud, G. Cerisola, and Ch. Comninellis, *Electrochem. Solid-state Lett.*, **3**(12) (2000) 550
7. M. Panizza, **I. Duo**, P.-A. Michaud, G. Cerisola, and Ch. Comninellis, *Electrochem. Solid-state Lett.*, **3**(9) (2000) 429
8. **I. Duo**, P.-A. Michaud, W. Haenni, A. Perret, and Ch. Comninellis, *Electrochem. Solid-state Lett.*, **3**(7) (2000) 325
9. S. Ferro, A. De Battisti, **I. Duo**, Ch. Comninellis, W. Haenni, and A. Perret, *J. Electrochem. Soc.*, **147**(7) (2000) 2614
10. D. Gandini, P.-A. Michaud, **I. Duo**, E. Mahé, W. Haenni, A. Perret, and Ch. Comninellis, *New Diamond and Front. Carbon Technol.*, **9**(5) (1999) 303

## Presentations

1. **I. Duo** and Ch. Comninellis, "Electrochemical oxidation of organic compounds on BDD and BDD- $\text{IrO}_2$  electrodes" 53<sup>rd</sup> Annual Meeting of the International Society of Electrochemistry (ISE), Düsseldorf, Germany (September 2002)
  2. **I. Duo**, Ch. Comninellis, T. A. Ivandini, R. Kawasaki, K. Honda, T. N. Rao, and A. Fujishima, "Direct Electrochemical oxidation of Cu-EDTA on BDD electrodes" The 5<sup>th</sup> International Mini-Symposium on Diamond Electrochemistry and Related Topics, Tokyo, Japan (March 2002)
  3. **I. Duo**, Ch. Comninellis, W. Haenni, and A. Perret, "Deposition of nanoparticles of iridium dioxide on a synthetic boron-doped diamond surface" Joint International ECS-ISE Meeting, San Francisco, California (September 2001)
-

- 
4. **I. Duo** and Ch. Comninellis, “*Nanoparticles on BDD surfaces*” The 4<sup>th</sup> International Workshop Diamond Electrodes, Braunschweig, Germany (May 2001)
  5. **I. Duo**, P.-A. Michaud, Ch. Comninellis, W. Haenni, and A. Perret, “*Electrochemical oxidation of simple carboxylic acids on synthetic diamond electrodes*” 51<sup>st</sup> Annual Meeting of the International Society of Electrochemistry (ISE), Warsaw, Poland (September 2000)
  6. **I. Duo** and Ch. Comninellis, “*Activation of boron-doped diamond electrodes with IrO<sub>2</sub> and Pt clusters*”, The 3<sup>rd</sup> International Workshop Diamond Electrodes, Neuchâtel, Switzerland, (June 2000)
-